

PROGRAMA DE DOCTORADO EN INFORMÁTICA

TESIS DOCTORAL

Contribuciones a la gestión óptima de recursos en aplicaciones solares térmicas: CSP y desalación

PhD THESIS

Towards optimal resource management in solar thermal applications: CSP and desalination



Escuela Internacional de
DOCTORADO
Universidad de Almería



UNIVERSIDAD
DE ALMERÍA

AUTOR / AUTORA

JUAN MIGUEL SERRANO RODRÍGUEZ

DIRECTOR / A / ES / AS

LIDIA ROCA SOBRINO

PATRICIA PALENZUELA ARDILA

UNIVERSIDAD DE ALMERÍA

Escuela Internacional de Doctorado de la Universidad de Almería

Almería, 2025

Towards optimal resource management in solar thermal applications

PhD Thesis

**Towards optimal resource management in solar thermal applications:
CSP and desalination**

Juan Miguel Serrano Rodríguez

November 25, 2025

University of Almería

Some rights reserved

 This work is available under the Creative Commons Attribution 3.0 IGO license (CC BY 3.0 IGO) <http://creativecommons.org/licenses/by/3.0/igo>. Under the Creative Commons Attribution license, you are free to copy, distribute, transmit, and adapt this work, including for commercial purposes, under the following conditions:

- ▶ Attribution—Please cite the work as follows: Serrano Juan Miguel, Roca Lidia , Palenzuela Patricia. November 25, 2025. Towards optimal resource management in solar thermal applications: CSP and desalination DOI: [10.1596/XXX](https://doi.org/10.1596/XXX). License: Creative Commons Attribution CC BY 3.0 IGO
- ▶ Translations—if you create a translation of this work, please add the following disclaimer along with the attribution: This translation was not created by Serrano J.M and should not be considered an official Serrano J.M translation. Serrano J.M shall not be liable for any content or error in this translation.
- ▶ Adaptations—if you create an adaptation of this work, please add the following disclaimer along with the attribution: This is an adaptation of an original work by Serrano J.M. Views and opinions expressed in the adaptation are the sole responsibility of the author or authors of the adaptation and are not endorsed by Serrano J.M.
- ▶ Third-party content—Serrano J.M does not necessarily own each component of the content contained within the work. Serrano J.M therefore does not warrant that the use of any third-party-owned individual component or part contained in the work will not infringe on the rights of those third parties. The risk of claims resulting from such infringement rests solely with you. If you wish to re-use a component of the work, it is your responsibility to determine whether permission is needed for that re-use and to obtain permission from the copyright owner. Examples of components can include, but are not limited to, tables, figures, or images.

Available at

DOI: [10.1596/XXX](https://doi.org/10.1596/XXX)

Main repository: <https://github.com/juan11iguel/my-thesis/blob/main>

Mirror repository: <https://github.com/juan11iguel/my-thesis>

Colophon

This document was typeset with the help of KOMA-Script and \TeX using the kaobook class.
The source code of this book class is available at: <https://github.com/fmarotta/kaobook>

Publisher

First printed in November 25, 2025 by University of Almería

Acknowledgements

Test test test

Juanmi

Preface

The present manuscript is the result of a PhD thesis research work carried out at the Plataforma Solar de Almería, Spain, under the supervision of Dr. Lidia Roca and Dr. Patricia Palenzuela and is ascribed to the Computer Science Doctorate Program at the University of Almería. The research was funded by a scholarship from CIEMAT, a public research organization attached to the Ministry of Science, Innovation and Universities.

The research work was developed within the framework of several national and international research projects, including the European Union's Horizon 2020 research and innovation programme *SFERA-III – Solar Facilities for the European Research Area* (823802) and *Water Mining – Next generation water-smart management systems* (869474), as well as the national project *SOLhycool – Hybrid cooling solutions for water saving in solar thermal applications* (PID2021-126452OA-I00).

Different parts of the research work to be presented in the following, were developed during international stays. In a combined short-stay at the Cyprus Institute (Nicosia, Cyprus - 2023) and attendance to the EDS conference in Limassol, it was matured and presented the initial *Proposal for a standard methodology for performance evaluation in multi-effect distillation processes* under the supervision of Dr. Marios Georgiou (EEWRC). A year later (February – June 2024), the main research stay at the Universidade Federal de Santa Catarina (UFSC), in Florianópolis (Brazil) took place under the supervision of Dr. Julio E. Normey-Rico. There it was completed the *Hybrid model of a solar desalination system, composed of finite state machines coupled to data-driven and first-principles models*. Finally, at the end of the contractual relationship with CIEMAT, in 2025, a one-month stay at the Technische Universität Chemnitz financed by the Erasmus program served to advance the work in *Evaluation and comparison of annual simulations of different cooling alternatives for a case study CSP plant* which would culminate with its presentation at the SolarPACES conference in September 2025.

This manuscript has been prepared with an intention of making it accessible to a non-expert audience, however, it is primarily aimed at researchers and professionals in the fields of renewable energy and water treatment, with the technical parts of the document delving into thermodynamic, mathematical modelling and optimization concepts. The content is structured to provide a comprehensive understanding of the topics discussed, while also being approachable for those who may not have a deep technical background in these areas.

The text is divided into four parts where each contains a number of chapters.

PART ONE introduces the context and motivation of the thesis, the research plan, including the main contributions of this research work, and ends with an introduction of the main research topics used to develop this research work. This introductory part is then followed by two parts detailing the main contributions, where each part is a complete unit: it describes the problem, presents the proposed solutions and analyses the obtained results.

PART Two is devoted to the cooling of the power block in Concentrated Solar Power (CSP) plants, with a focus on the optimal management of the water resource through the modelling and optimization of alternative combined cooling systems.

PART THREE centers around thermal desalination processes, particularly multi-effect distillation. First by analyzing the separation process from a thermodynamic and qualitative perspective in order to standardize its evaluation and later in the part, the process is integrated with a variable energy source: solar thermal energy and its operation is modelled and optimized to manage the solar resource, maximizing fresh water generation and advancing the state of research in this area.

PART FOUR completes the manuscript with a recapitulation of the main conclusions and findings, as well as a discussion on potential future research directions in the studied topics and presents the derived scientific contributions.

Summary

This research encompasses two complementary studies on two intrinsically linked resources: water and energy. The first part focuses on the efficient management of water resources for power generation, while the second explores the efficient use of solar energy for clean water production.

CONCENTRATED SOLAR POWER (CSP) is poised to be a crucial contributor to the energy transition away from fossil fuels. The first phase of this transition is well underway, driven by the massive deployment of low-cost and non-dispatchable renewable technologies such as wind and solar photovoltaics. However, the second and more challenging phase, which involves achieving large-scale dispatchable renewable generation, is still ahead. CSP stands out as a renewable and scalable dispatchable technology with the potential to outcompete combined-cycle and coal-fired power plants.

One of the key challenges in CSP systems lies in cooling the power block, which is typically associated with high water consumption. The first part of this research is therefore dedicated to the efficient management of water resources in CSP plants. An optimal water management strategy is proposed for CSP systems that integrate novel combined cooling configurations. To this end, the annual performance of different cooling alternatives is evaluated for a commercial 50 MW_e CSP plant, Andasol-II, located in southern Spain. Specifically, three cooling systems, all modelled and validated, are compared: the plant's existing Wet Cooling Tower (WCT), and two variants of a novel Combined Cooler (CC) system with dry cooler capacities of 75 % and 100 % of the nominal thermal load of the WCT system.

For each alternative, plant operation is optimized under the same water-scarcity scenario using a multi-stage optimization framework. This framework minimizes the cooling cost, encompassing both electricity and water expenses, while ensuring that the cooling demand is satisfied. The key challenge lies in effectively managing the limited water resource. Results show that the integration of the CC can reduce specific cooling costs by up to 80 % and annual water consumption by about 48 %, with 38 % savings during the driest months. These benefits arise primarily from reduced reliance on costly alternative water sources. The CC alternatives also provide more stable and cost-effective operation throughout the year compared to the WCT, which is highly sensitive to water availability.

THERMAL DESALINATION, particularly Multi-Effect Distillation (MED), can play an important role in mitigating water scarcity. These systems use thermal and electrical energy to separate seawater or contaminated feedwater into fresh water and concentrated brine. Although it may not become the dominant desalination technology, it is well suited for specific applications. Its competitiveness can be improved by leveraging opportunities such as brine mining or industrial wastewater treatment, which enhance both economic feasibility and environmental benefits.

To expand their applicability, MED systems must improve in two directions: (i) by enhancing efficiency through wider operating ranges, or (ii) by adapting to low-temperature applications in which their heat demands can be partially or fully met using low-exergy sources such as waste heat or solar thermal energy. However, the true cost of thermal energy, and consequently the performance of such systems, is often difficult to quantify, particularly because there is no unified set of criteria for evaluating their performance.

To address this challenge, this research proposes a standardized methodology for evaluating the performance of MED processes, which can also be extended to other thermal separation technologies. The method covers key aspects such as instrumentation requirements, process control, and the suitability of performance metrics. It also includes uncertainty quantification and an algorithm for automatic steady-state detection. The proposed approach enhances the reliability and robustness of experimental evaluations under variable conditions. Experimental results confirm that the methodology is both reliable and consistent, enabling fair comparisons of MED systems across different operating scenarios.

The experimental campaign includes evaluations at high Top Brine Temperatures (TBTs). Results analyzed using several performance metrics and scale formation risks demonstrate that the MED process can operate at high TBTs without significant scaling and can achieve higher concentrations. However, no substantial improvements in thermal performance or reconcentration capacity are observed unless specific design modifications are introduced.

Finally, a novel operational strategy is proposed to enable the seamless, autonomous, and optimal integration of a solar-driven MED system. The method explicitly determines when to start and stop each subsystem while considering a two-day prediction horizon. This allows the optimization to account not only for immediate performance but also for the effect of present decisions on future production. The approach is based on an experimentally validated system model

that includes the electrical consumption of each component, combined with the most comprehensive data-driven MED model currently available in the literature. The control architecture follows a hierarchical three-layer structure, in which the upper operational layer solves a Mixed Integer Non-Linear Programming problem aimed at maximizing water production while minimizing operating costs. Results from a week-long system simulation are compared with two alternative strategies, a baseline rule-based operation and a fixed-schedule optimized operation. The proposed method significantly increases system performance by 32 % relative to the heuristic baseline and by 21 % relative to the fixed-schedule strategy. These gains arise from the proposed method ability to fully exploit the temporal flexibility provided by the thermal storage while accounting for operational costs.

Resumen

Esta investigación abarca dos estudios complementarios sobre dos recursos intrínsecamente vinculados: el agua y la energía. La primera parte se centra en la gestión eficiente de los recursos hídricos para la generación eléctrica, mientras que la segunda explora el uso eficiente de la energía solar para la producción de agua limpia.

LA ENERGÍA SOLAR DE CONCENTRACIÓN (CSP) está destinada a desempeñar un papel crucial en la transición energética hacia el abandono de los combustibles fósiles. La primera fase de esta transición está bien encaminada, impulsada por el despliegue masivo de tecnologías renovables de bajo coste y no gestionables, como la eólica y la solar fotovoltaica. Sin embargo, la segunda y más desafiante fase, que implica lograr una generación renovable gestionable a gran escala, no se ha alcanzado. La CSP se posiciona como una tecnología renovable y escalable con capacidad gestionable y el potencial de superar a las plantas de ciclo combinado y de carbón.

Uno de los principales desafíos en los sistemas CSP radica en la refrigeración del bloque de potencia, la cual suele asociarse con un alto consumo de agua. Por ello, la primera parte de esta investigación se dedica a la gestión eficiente de los recursos hídricos en plantas CSP. Se propone una estrategia óptima de gestión del agua que integra configuraciones de refrigeración combinada novedosas. Con este fin, se evalúa el rendimiento anual de diferentes alternativas de refrigeración para una planta comercial de 50 MW_e CSP, Andasol-II, ubicada en el sur de España. En concreto, se comparan tres sistemas de refrigeración, todos ellos modelados y validados: el sistema húmedo WCT existente en la planta, y dos variantes de un novedoso sistema de refrigeración combinada (CC) con capacidades de enfriador seco del 75 % y del 100 % de la carga térmica nominal del sistema WCT.

Para cada alternativa, la operación de la planta se optimiza bajo el mismo escenario de escasez de agua utilizando un método de optimización multi-etapa. Este método busca minimizar el coste de refrigeración, que incluye gastos de electricidad y agua, garantizando al mismo tiempo que se satisfaga la demanda de refrigeración dadas unas condiciones de entorno. El desafío clave radica en gestionar eficazmente el recurso hídrico limitado. Los resultados muestran que la integración del CC puede reducir los costes específicos de refrigeración hasta en un 80 % y el consumo anual de agua en alrededor del 48 %, con un ahorro del 38 % durante los meses más secos. Estos beneficios surgen principalmente de la menor dependencia de fuentes de agua alternativas y su alto coste asociado. Las alternativas CC también ofrecen una operación más estable y rentable a lo largo del año en comparación con la WCT, que es altamente sensible a la disponibilidad de agua.

LA DESALACIÓN TÉRMICA, en particular la Destilación Multiefecto (MED), puede desempeñar un papel importante en la mitigación de la escasez de agua. Estos sistemas utilizan energía térmica y eléctrica para separar agua de mar o agua contaminada en agua dulce y salmuera concentrada. Aunque no se posicione como la tecnología de desalación dominante, es muy adecuada para otras aplicaciones. Su competitividad puede mejorarse aprovechando oportunidades como la minería de salmuera o el tratamiento de aguas residuales industriales, que mejoran tanto la viabilidad económica como los beneficios ambientales.

Para ampliar su aplicabilidad, los sistemas MED deben mejorar en dos direcciones: (i) aumentando su eficiencia mediante rangos de operación más amplios, o (ii) adaptándose a aplicaciones de baja temperatura en las que sus demandas térmicas puedan satisfacerse parcial o totalmente mediante fuentes de baja exergía, como el calor residual o la energía solar térmica. Sin embargo, el coste real de la energía térmica y, en consecuencia, el rendimiento de estos sistemas, suele ser difícil de cuantificar, en particular porque no existe un conjunto unificado de criterios para evaluar su desempeño.

Para abordar este desafío, esta investigación propone una metodología estandarizada para evaluar el rendimiento de los procesos MED, la cual también puede extenderse a otras tecnologías de separación térmica. El método abarca aspectos clave como los requisitos de instrumentación, el control del proceso y la idoneidad de las métricas de rendimiento. También incluye la cuantificación de incertidumbre y un algoritmo para la detección automática del estado estacionario. El enfoque propuesto mejora la fiabilidad y la robustez de la evaluación de la operación bajo condiciones variables. Los resultados experimentales, obtenidos en una planta piloto real, confirman que la metodología es confiable y consistente, lo que permite comparaciones justas entre sistemas MED bajo diferentes escenarios operativos.

La campaña experimental incluye evaluaciones a altas temperaturas de salmuera en el primer efecto (TBT). Los resultados, analizados mediante diversas métricas de rendimiento y riesgos de formación de incrustaciones, demuestran que el proceso MED puede operar a altas TBTs sin incrustaciones significativas en las superficies de intercambio y puede

alcanzar mayores concentraciones. Sin embargo, no se observan mejoras sustanciales en el rendimiento térmico o la capacidad de reconcentración, a menos que se introduzcan modificaciones específicas en el diseño.

Finalmente, se propone una estrategia de operación novedosa que permite la integración autónoma y óptima de un sistema MED alimentado con energía solar. El método determina explícitamente cuándo iniciar y detener cada subsistema, considerando un horizonte de predicción de dos días. Esto permite que la optimización tenga en cuenta no solo el impacto inmediato de las decisiones presentes, sino también el efecto sobre la producción futura. El enfoque se basa en un modelo del sistema validado experimentalmente que incluye el consumo eléctrico de cada componente, combinado con el modelo MED basado en datos más completo disponible actualmente en la literatura. La arquitectura de control sigue una estructura jerárquica de tres niveles, en la que la capa superior, la capa de planificación de la operación, resuelve un problema de programación no lineal mixto (Mixed Integer Non-Linear Programming (MINLP) por sus siglas en inglés) destinado a maximizar la producción de agua mientras se minimizan los costes de operación. Los resultados de una simulación del sistema durante una semana se comparan con dos estrategias alternativas: una operación simple basada en reglas y una operación optimizada con un plan de operación fijo. El método propuesto aumenta significativamente el rendimiento del sistema en un 32 % en relación con la alternativa heurística y en un 21 % comparado con la estrategia de plan de operación fijo. Estas ganancias se deben a la capacidad del método propuesto para aprovechar al máximo la flexibilidad temporal que ofrece el almacenamiento térmico, al tiempo que se tienen en cuenta los costes de operación.

Contents

Acknowledgements	iii
Preface	v
Summary	vii
Resumen	ix
Contents	xi
INTRODUCTION	1
1 Context	3
2 Research plan	7
2.1 Hypothesis	7
2.2 Objectives	7
2.3 Contributions	8
2.4 Implementation software tools	10
3 Automation overview: modelling, optimization and control	11
3.1 Modelling and simulation	11
3.1.1 First principle modelling	13
3.1.2 Data-driven modelling	13
3.1.3 Discrete modelling by means of Finite-State Machines (FSMs)	18
3.1.4 Forecasting and combinatory nature of FSMs	19
3.1.5 Performance metrics	19
3.2 Optimization	20
3.2.1 Non-Linear Programming (NLP) problems	21
3.2.2 MINLP problems	22
3.2.3 A discussion on constraint handling	22
3.2.4 Multi-objective optimization	23
3.2.5 Optimization algorithms	24
3.3 Control	28
3.3.1 PID controllers	29
3.4 Hierarchical control	29
I OPTIMAL WATER AND ELECTRICITY MANAGEMENT IN A COMBINED COOLING SYSTEM	31
4 Solar thermal energy and water	35
4.1 Concentrated solar thermal	35
4.1.1 CSP: Concentrated Solar Power	36
4.1.2 A brief history of CSP: from the hype to unrealized potential	37
4.2 Cooling and water use	38
4.2.1 Conventional condenser cooling technologies	39
4.2.2 Non-conventional cooling: Combined / hybrid cooling	42
4.2.3 Selection of the cooling technology	45
5 Combined cooling pilot plant at Plataforma Solar de Almería	47
5.1 Plant description	48
5.2 Experimental campaigns	48
5.2.1 Physical model calibration campaigns	49
5.2.2 Data-driven models training campaigns	50
5.2.3 Models validation campaigns	50

6 Modelling of a combined cooling system	51
6.1 Wet cooler	51
6.1.1 Physical model	52
6.1.2 Generating synthetic data for surrogate WCT Model	53
6.1.3 Model interface	54
6.2 Dry cooler	54
6.2.1 Physical model	54
6.2.2 Generating synthetic data for surrogate Dry Cooler (DC) model	55
6.2.3 Model interface	55
6.3 Other components and outputs	56
6.3.1 Surface condenser	56
6.3.2 Electrical consumption	56
6.3.3 Mixers	57
6.3.4 Valves	57
6.4 Complete system	57
7 Optimization of a combined cooling system	59
7.1 Environment description	61
7.2 Static optimization	61
7.2.1 Dry cooler	62
7.2.2 Wet cooler	63
7.2.3 Combined cooler	64
7.3 Horizon optimization	66
7.3.1 A discussion on solving the optimization problem	67
7.3.2 Proposed solution: Decomposition-based multi-objective optimization with trajectory planning	68
8 Validation in the combined cooling pilot plant	71
8.1 Modelling	71
8.1.1 Wet cooler model alternatives comparison and validation	71
8.1.2 Dry cooler model alternatives comparison and validation	73
8.1.3 Surface condenser model	75
8.1.4 Complete system model validation	76
8.2 Control and optimization results	78
8.2.1 Choosing an optimization algorithm	78
8.2.2 Simulation results	80
8.2.3 Experimental validation	83
9 Annual analysis: Andasol-II CSP plant	89
9.1 Environment definition	90
9.1.1 Water context	90
9.1.2 Thermal load	90
9.1.3 Prices context	91
9.2 Cooling alternatives comparison	91
II ENERGY MANAGEMENT IN MED PROCESSES DRIVEN BY VARIABLE ENERGY SOURCES	95
10 Thermal desalination	99
10.1 Water crisis	99
10.2 Brine concentration and mining	100
10.3 Overview of Desalination Technologies	101
10.3.1 Mechanical Technologies	101
10.3.2 Thermal Technologies	101
10.3.3 Thermal desalination timeline and comparison with Reverse Osmosis (RO)	102
10.4 (Variable) Energy sources for thermal separation processes	104
10.4.1 Solar thermal	104
10.4.2 Waste heat	105
11 SolarMED pilot plant	107
11.1 Solar field	108
11.2 Thermal storage	108
11.3 Multi-Effect Distillation	109

12 Hybrid modelling of a solar driven MED system	113
12.1 Introduction	113
12.2 Dynamic modelling. Process variables	113
12.2.1 Solar field	113
12.2.2 Thermal storage	118
12.2.3 Heat exchanger	122
12.2.4 MED	124
12.3 Discrete modelling. Operation state	129
12.3.1 Heat generation and storage subsystem (sfts)	129
12.3.2 Separation subsystem (med)	129
12.3.3 Validation	131
12.4 Complete system model	132
12.4.1 Validation	133
13 Performance evaluation in MED processes	137
13.1 Process analysis	140
13.2 Performance metrics	141
13.2.1 Separation metrics	141
13.2.2 Energetic metrics	142
13.2.3 Exergetic metrics	144
13.3 Instrumentation	145
13.3.1 Key Process Variables (KPVs)	145
13.3.2 Instrumentation requirements	146
13.3.3 Uncertainty determination	148
13.4 Monitoring and process control	148
13.4.1 Monitoring: steady-state identification	148
13.4.2 Control system	150
13.5 Methodology validation in an experimental campaign	152
14 Towards the optimal coupling and operation of a solar driven MED system	161
14.1 Introduction	161
14.2 Problem description	163
14.2.1 Implementation discussion	165
14.4 Operation plan layer description	167
14.4.1 Candidate problems generation	167
14.4.2 Update times generation	168
14.5 Operation optimization layer description	170
14.6 Alternative strategies. Heuristic approach	171
14.7 Optimization results	172
14.7.1 Candidate problems generation	172
14.7.2 Choosing an algorithm	172
14.7.3 Choosing a candidate problem	173
14.7.4 Simulation results	173
14.7.5 Operation and performance comparison between strategies	175
CONCLUSIONS AND OUTLOOK	179
Conclusions	181
Outlook and future work	184
Derived scientific contributions	188
APPENDIX	191
A MED Performance Evaluation	193
A.1 Uncertainty estimation through first-order Taylor series approximation	193
A.1.1 Specific Thermal Energy Consumption (STEC)	193
A.1.2 Specific Electrical Energy Consumption (SEEC)	193
A.1.3 Performance Ratio	193
A.1.4 Waste heat performance ratio	194
A.1.5 Recovery ratio	194
A.1.6 Concentration factor	194

A.2	Exergy calculations	194
A.3	Separation metrics calculation	195
A.4	Control system and steady state identification parameters	196
B	MED First-Principles Model	199
B.1	Nomenclature	199
	B.1.1 Calibration mode	201
	B.1.2 Simulation mode	202
B.2	Implementation	202
B.3	Validation	204
	Bibliography	207
	Nomenclature	219

List of Figures

1.1	Shareholders-driven apocalysis	3
1.2	Annual global mean temperature anomalies relative to a pre-industrial (1850–1900) baseline.	
	Source: State of the Global Climate. World Meteorological Organization (UN) [3]	4
1.3	Extreme weather-related events map. Source: [7]	5
1.4	Aerial view of the pilot plants at Plataforma Solar de Almería (PSA)	6
3.1	Dynamic response (reaction curve) of a process output to changes in its inputs'	13
3.2	Illustration of Gaussian Process Regression. (a) Prior samples drawn from a Gaussian Process with zero mean and smooth covariance, representing the prior belief before observing any data. (b) Posterior samples and mean after conditioning on two observations, showing reduced uncertainty near the observed points. Source: Rasmussen <i>et al.</i> [38]	
3.3	ANN model configurations	15
3.4	Considered ANN architectures	16
3.5	FSM representation of a traffic light	17
3.6	Evolution of different traffic-light FSMs	18
3.7	Constrained optimization problem. The goal is to minimize $y = f(x)$ with the two continuous decision variables x_1 and x_2 constrained to $g(x)$. The problem is NLP with a convex solution-space. Source: Wang <i>et al.</i> [47]	19
3.8	Simulated Annealing. Example illustrating the effect of cooling schedule on the performance of simulated annealing. The problem is to rearrange the pixels of an image so as to minimize a certain potential energy function, which causes similar colors to attract at short range and repel at a slightly larger distance. The elementary moves swap two adjacent pixels. These images were obtained with a fast cooling schedule (left) and a slow cooling schedule (right), producing results similar to amorphous and crystalline solids, respectively. Source: Wikipedia	21
3.9	Illustration of optimization runs for two algorithms	25
3.10	Particle Swarm Optimization concept. Each particle adjusts its velocity based on its own experience and that of neighboring particles to explore the search space and converge towards optimal solutions. Source: Pagmo 2.19.1 documentation	26
3.11	Control diagrams	27
3.12	Hierarchical control architecture	28
4.1	Two main Concentrated Solar Thermal (CST) technologies	30
4.2	Solar tower CSP plant. Source: NREL [72]	35
4.3	Levelized Cost of Electricity (LCOE) evolution and capacity predictions	36
4.4	Water consumption comparison between thermal power generation technologies	38
4.5	38
4.6	39
4.7	Different hybrid/combined coolers configurations	40
5.1	PSA combined cooling system facility	44
5.2	Back view of the WCT	47
5.3	Layout of combined cooling systems pilot plant at PSA.	48
6.1	Control volume in the exchange area of a wet cooling tower arrangement. Variables are described in the Nomenclature section. Source: Serrano <i>et al.</i> [116].	49
6.2	Complete model diagram of the combined cooling system	52
6.3	Inputs-outputs block diagram of the main model components	58
7.1	Block diagram of the optimization scheme including environment components	60
7.2	Diagram of the dry cooler only cooling problem	62
7.3	Diagram of the wet cooler only cooling problem	63
7.4	Diagram of the combined cooler and condenser problem	64
7.5	Pareto fronts in different representative scenarios (top) and detailed power and hydraulic distribution for a specific scenario (bottom)	65
7.6	Visualization of a constrained search space for two decision variables	67

7.7	Proposed methodology. Decomposition-based multi-objective optimization with trajectory planning	68
8.1	Experimental results for the Me number as a function of $\dot{m}_{wct}/\dot{m}_{wct,air}$	71
8.2	WCT Models performance regression	72
8.3	Air side Nusselt number vs air side Reynolds number for the air cooled heat exchanger	73
8.4	DC Models performance regression	75
8.5	Surface condenser validation	75
8.6	Combined cooler model validation	76
8.7	Samples distribution visualization for synthetic dataset generation.	77
8.8	Horizon optimization – path selection subproblem. Fitness evolution comparison	79
8.9	Horizon optimization results in three different seasons	81
8.10	Detailed simulation results comparison: horizon vs static. CC-horizon	82
8.11	Implementation of the optimization strategy in the real facility. Hierarchical control	83
8.12	Horizon optimization strategy results. Experimental validation results at pilot plant.	87
9.1	Andasol I, II and III	89
9.2	Specific cooling costs comparison	91
9.3	Annual simulation results for the different studied alternatives optimized	93
10.1	Global water stress map. [1ex]Source: Statista. [1ex]	100
10.2	Desalination technologies used at plants worldwide in 2019 [1ex]Source: Panagopoulos et al. [142]	103
10.3	Greenhouse Gas (GHG)s emissions per cubic meter of freshwater produced Source: Panagopoulos et al. [142].	104
10.4	Desalination technologies coupled with renewable energy sources at plants worldwide. Source: Panagopoulos et al. [142]	104
11.1	Solar-driven Multi-Effect Distillation (SolarMED) process diagram	108
11.2	109
11.3	MED plant at PSA with open effects for maintenance	109
11.4	Single effect distillation unit schematic diagram	110
11.5	Piping and Instrumentation Diagram (P&ID) representative of the MED-PSA plant with the installed instrumentation, Key Process Variables (KPVs), and implemented control loops (ANSI/ISA 5.1-2022).	111
12.1	Solar field process diagram.	114
12.2	Solar field and thermal storage electrical characterization tests.	116
12.3	Solar field flow rate for different pump configurations and their associated power consumption. [1ex]	116
12.4	117
12.5	Thermal storage process diagram.	119
12.6	121
12.7	Heat exchanger process diagram.	123
12.8	Heat exchanger model validation for a particular test.	124
12.9	MED process diagram.	126
12.10	MED Gaussian-Process Regression (GPR) model regression for different outputs.	127
12.11	128
12.12	Finite-state machines for the different subsystems	130
12.13	SolarMED FSM states evolution during a test on 20230703	131
12.14	Complete SolarMED model architecture.	133
12.15	134
13.1	Ryznar Stability Index (RSI) of seawater at different temperatures and concentrations	139
13.2	Inputs and outputs variables in an MED process. The dash line delimits the control volume	141
13.3	P&ID with the required instrumentation, KPVs, and basic control loops (ANSI/ISA 5.1-2022) required in an MED plant	147
13.4	Sensitivity index results for different variables. Useful to assess the impact of the different measured variables uncertainty on the performance metrics. KPVs are shown in bold notation	147
13.5	Diagram of the steady-state identification procedure	149
13.6	Flowchart of finite state machines for plant start-up (left) and shutdown (right)	152
13.7	153
13.8	154
13.9	Condenser outlet temperature controller implementation	155

13.10	RSI values as a function of temperature and concentration before (left) and after (right) pretreatment using nanofiltration.	155
13.11	Scaling assessment during high TBT operation	157
13.12	Per effect comparison between low and high TBT operation points	158
14.1	Decision tree resulting from the combinatorial nature of the integer part of the optimization problem. Text in nodes represents system states.	166
14.2	Proposed optimization strategy architecture	167
14.3	Operation mode updates time distribution. The thick-yellow line illustrates the irradiance.	168
14.4	Proposed nNLP methodology computation timeline. (1) Operation plan start-up evaluation. (2) Start of operation optimization evaluation train. (3) System operation start. (4) Operation plan shutdown evalutaion and (5) System operation end.	169
14.5	Operation plan layer (start-up) candidate problem generation results for specific dates	172
14.6	Fitness evolution comparison for a representative start-up problem.	173
14.7	SolarMED nNLP optimization strategy results	174
14.8	Daily key variables differences comparison	176
14.9	Operation schedule comparison	176
14.10		177
14.11	Alternative configurations for variable energy source(s) driven MED processes.	187
B.1	Overall schematic of the MED model with inputs, outputs, main variables and components	200
B.2	MED model <i>calibration mode</i> diagram with inputs and outputs	201
B.3	MED model <i>simulation mode</i> diagram with inputs and outputs	202
B.4	Detailed schematic of a single cell in the MED containing the effect or evaporator (left) and the preheater (right)	202
B.5	Detailed schematic of a single cell in the MED with the effect's equations.	203
B.6	Detailed schematic of a single cell in the MED with the energy source side equations and internal effect condensate flashing.	203
B.7	Detailed schematic of a single cell in the MED with the preheater's equations.	204
B.8	Detailed schematic of a single cell in the MED with distribution lines for the energy source side and generated steam. Also, auxiliary elements like demister and preheater-effect distribution line geometry.	204
B.9	Heat transfer coefficients comparison between <i>calibration mode</i> and <i>simulation mode</i> for the validation set	205
B.10		206

List of Tables

5.1	Characteristics of instrumentation	48
5.2	Main characteristics of the Air-Cooled Heat Exchanger (ACHE) dry cooler at the pilot plant	49
5.3	Main characteristics of the surface condenser at the pilot plant	49
5.4	Experimental campaigns performed at the CC pilot plant	50
8.1	Bounds and discretization of the model WCT input variables.	72
8.2	Summary table of the prediction results obtained with the different modelling approaches studied.	73
8.3	Bounds and discretization of the model input variables.	74
8.4	Summary table of the prediction results obtained with the different modelling approaches studied.	74
8.5	Performance metrics obtained with the complete (CC) and component (Cnt) models	77
8.6	Static optimization algorithm comparison results	79
8.7	Box-bounds for the decision variables.	83
8.8	Low-level control loops	84
9.1	Andasol-II plant main characteristics	89
11.1	MED plant at PSA specifications and nominal operating conditions	110
11.2	MED plant available experimental data range.	110
11.3	Characteristics of the instrumentation installed at MED-PSA unit (^a value of the measured temperature in °C, ^b of reading, ^c full scale).	111
12.1	Summary table of the prediction results obtained with the solar field model for different test days and sample times.	118
12.2	Summary table of the prediction results obtained with the thermal storage model for different test days and sample times.	122
12.3	Summary table of the prediction results obtained with the heat exchanger model for different test days and sample times.	125
12.4	Models parameters	129
12.5	Solar Field and Thermal Storage subsystem (sfts) FSM states definitions. \wedge represents the logical AND operator.	129
12.6	Separation subsystem (med) FSM states definitions. \wedge represents the logical AND operator, \exists represents that at least one meets the condition, and \forall represents that all meet the condition.	131
12.7	Summary table of the prediction results obtained with the SolarMED model for different test days, sample time set to 400s and different prediction horizons.	136
13.1	Ryznar Stability Index (RSI) values and their interpretation in terms of scaling and corrosion risk [187].	140
13.2	Experimental campaign design specifications	152
13.3	Measured variables and performance metrics for some operation points of the experimental campaign. The values are expressed as mean \pm standard deviation with a coverage factor of 2 (95% confidence interval). D is the duration of the steady state period.	156
14.1	Operation plan layer. Degrees of freedom assignment.	168
A.1	Parameters for the steady-state detection algorithm, where <i>s.u.</i> represents that the parameter has the same units to the related variable	197
A.2	Parameters for the Proportional-Integral-Derivative controller (PID) based process control, where <i>i.u.</i> represents the input variable units, and <i>o.u.</i> the output units.	197

INTRODUCTION

Should I kill myself or have a cup of coffee?

Albert Camus

Technological development has undeniably improved material conditions for an important part of humanity. Over the past century, innovations in energy, medicine, transport, and communication have contributed to longer life expectancy, higher productivity, and broader access to goods and services. This has however been strongly correlated with major CO₂ emissions. For a time it was at least possible to argue that this rise in emissions was tied to an—unequal—overall improvement in material well-being of *some* societies.

However, this trend has been reversed. Seven out of ten people live in countries where economic inequality has increased over the past 30 years, and nearly half of the world's wealth—46%—is concentrated in the hands of just 1% of the population [1].

We find ourselves in a paradoxical situation: as the planet becomes increasingly uninhabitable, social inequalities continue to deepen. The overall outlook is far from encouraging. Technological progress no longer serves to enhance collective well-being¹ or to effectively build a sustainable future. Instead, the relentless pursuit of endless economic growth—fueled by unchecked consumption, short-term profit seeking, and a shareholder-driven economy dominated by speculation—is propelling us ever closer to catastrophic climate collapse.

One of the main drivers in this direction, consequence of this unchecked growing economy prioritization, is the abuse in use of fossil fuels. Despite the finite nature of fossil fuels, the problem today is not scarcity, but excess—an abundance sufficient to fill the atmosphere with greenhouse gases² at levels incompatible with life. The Paris Agreement has a long-term temperature goal which is to keep the rise in global surface temperature to well below 2 °C above pre-industrial levels. The agreement also states that preferably the limit of the increase should only be 1.5 °C.

A 2024 report from the World Meteorological Organization (WMO) finds an 86% chance that global average temperatures will exceed 1.5 °C above pre-industrial levels in at least one of the next five years (see Figure 1.2), and a one per cent chance of one of those years exceeding 2 °C of warming [3].

Our dependence on fossil fuels is proving lethal, and this is manifesting in multiple ways:

- ▶ As of 2024, CO₂ emissions continue to increase, albeit more slowly than in the past. Yet this continued growth has pushed global emissions to another record high [4].
- ▶ Between 1999 and 2020, coal-related particulate matter (PM_{2.5}) caused an estimated 460,000 deaths in the United States alone [5].
- ▶ Plastic production has *more than doubled* in the last two decades [6]. Only a small fraction of this plastic is recycled, and even then, only a limited number of times³
- ▶ Studies covering nearly 750 extreme weather-related events and trends (see Figure 1.3) show that 83% have been influenced by human-induced climate change [7].

Even within this grim context, financial logic seems to prevail. Private investors, motivated not by moral concern but by the growing profitability of renewables, are now turning towards cleaner technologies⁴. Yet at the same time, a new wave of governments has emerged that, despite overwhelming evidence, promotes a return to fossil fuels: leaders who exploit crises to sow confusion and advance regressive agendas⁵. If previous climate measures were insufficient and



Figure 1.1: "Yes, the planet got destroyed. But for a beautiful moment in time, we created a lot of value for shareholders"

Source: Tom Toro – The New Yorker

[1]: Sayer (2016), *Why We Can't Afford the Rich*

1: not that it ever did for a significant amount of people [2]

2: great efforts are also being made in filling both hydrosphere and lithosphere with plastics

[3]: Organization (2025), *State of the Global Climate 2024*

[4]: IEA (2025), *Global Energy Review 2025*

[5]: Henneman et al. (2023), "Mortality Risk from United States Coal Electricity Generation"

[6]: Geyer et al. (2017), "Production, Use, and Fate of All Plastics Ever Made"

3: As environmental engineer **Jenna Jambeck** from the University of Georgia notes, "What's the best way to manage waste? To not produce it in the first place."

4: The private sector is driving the energy transition, providing three-quarters of global clean energy investment. However, to meet scale investment in renewables to at least USD₂₀₂₅ 1.4 trillion per year in 2025–2030, more than doubling the invested in 2024 [8]

5: Two examples

- President Trump Prioritizes Fossil Fuel Development and Rolls Back Climate Action in Energy [9]

- Confusion over the causes of the blackout intensifies the ideological battle between renewables and nuclear power [10]

Global mean temperature 1850-2024

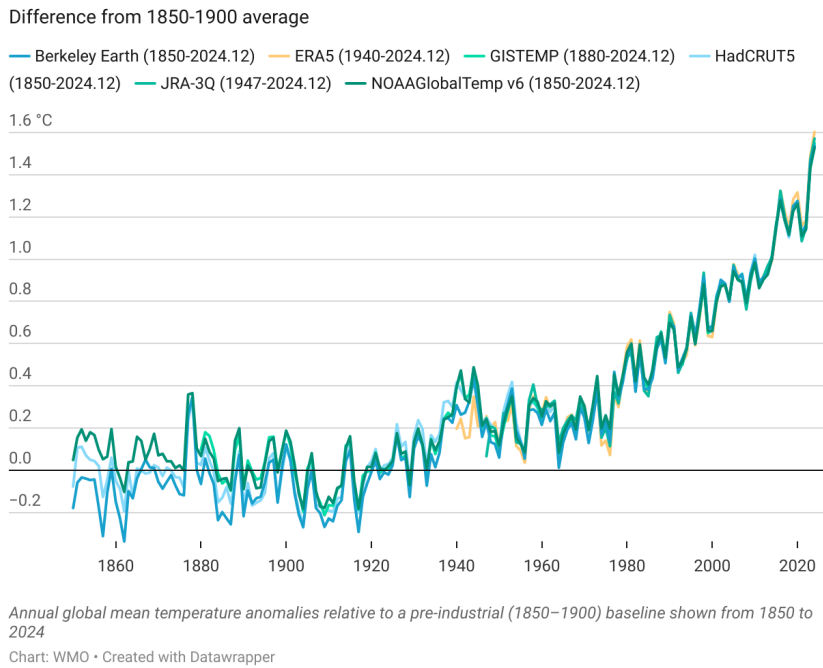


Figure 1.2: Annual global mean temperature anomalies relative to a pre-industrial (1850–1900) baseline. Source: State of the Global Climate, World Meteorological Organization (UN) [3]

[11]: Amelie (2025), “The Future of Climate Migration”

State health services and pensions are run down and replaced by private health insurance and private pensions. You’re on your own, free to choose, free to lose... Instead of seeing ourselves as members of a common society... we are supposed to see ourselves as competing individuals with no responsibility for anyone else.

Andrew Sayer
In Why We Can't Afford the Rich

often reduced to symbolic agreements with limited implementation (e.g. Paris Agreement), the current political landscape shows an even more concerning trend: *open denialism*. This fuels widespread disenchantment. Society has become increasingly alienated. Trust in collective institutions, including science, is eroding, while conspiracy theories gain traction and shape public opinion. As a result, genuine and complex challenges are neglected, while artificial or symbolic issues dominate public discourse. In Europe and elsewhere, racism and exclusionary politics are resurging, often presented as responses to fabricated threats. Yet the true challenge lies ahead: in the coming decades, climate change is expected to displace millions, as vast regions of the planet become increasingly incompatible with human life [11].

THE QUESTION remains whether societies will respond with solidarity and structural transformation, or with further division and denial.

Where this research work fits in the current context

After discussing the global environmental challenges of our time, and setting aside their complex socio-political dimensions, the focus can now narrow to a more specific and concrete contribution. The work presented here does not solve such grand challenges, nowhere near, but rather contributes within a limited scope: developing and optimizing technologies that improve the sustainable management of two interconnected resources, energy and water, in two solar-driven processes. A central element of this contribution is the digitalization of these systems, enabling advanced modelling, prediction, and optimization tools that are essential for improving the performance and operational efficiency of solar-based technologies.

This research is therefore structured in two complementary parts. The first addresses the efficient management of water resources for power generation in Concentrated Solar Power (CSP) plants, through the optimization of a novel

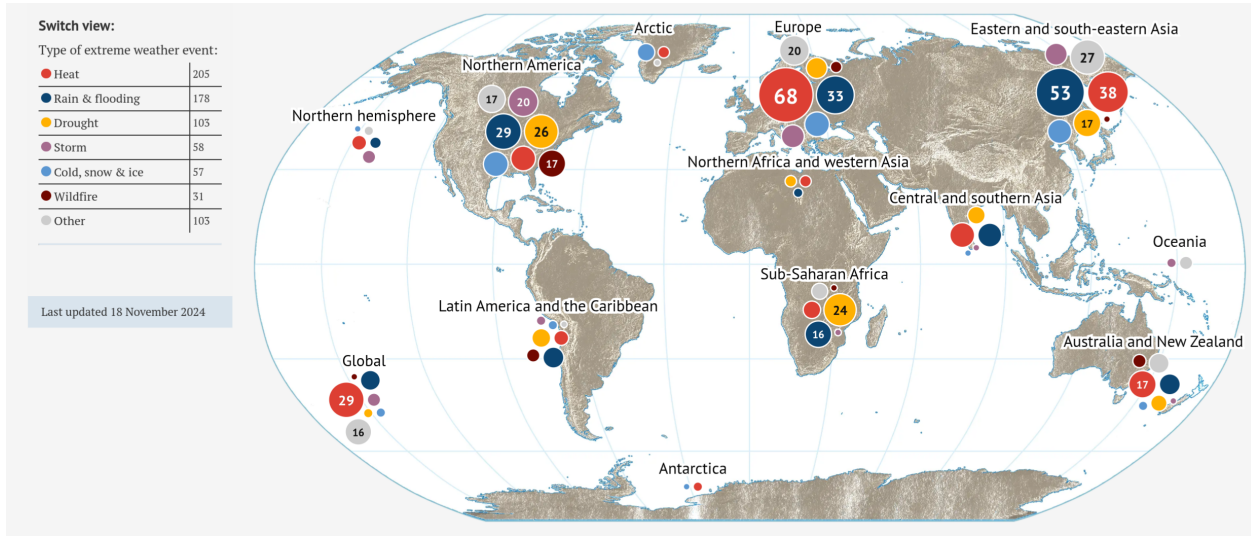


Figure 1.3: Extreme weather-related events map. Source: [7]

combined cooling system. The second explores the efficient use of solar energy for clean water production in a solar-driven multi-effect distillation system with thermal storage, focusing once again on operational optimization.

In an era where almost every idea seems to have been expressed before, originality rarely lies in invention alone, but in the creative integration of existing concepts into meaningful, purposeful solutions. For this reason, implementation plays an increasingly central role even—and perhaps especially—in applied scientific research. Implementation should not remain hidden; it should be shared, documented, and made accessible, allowing others to replicate, verify, and build upon it [12].

Accordingly, the complete implementations of both studies are made available in open repositories, alongside most of the code and supplementary material used to develop this manuscript. The developed work has an important experimentation component involving the facilities shown in Figure 1.4. Most experimental and simulated results follow the Findable, Accessible, Interoperable, Reusable (FAIR) data principles⁶ [13], ensuring transparency, accessibility, and reproducibility.

Further details are provided in Section 29 (Derived scientific contributions).

[12]: Hicks et al. (2015), "Bibliometrics"

6: And made public at time of publication of this manuscript. The rest may follow soon after

[13]: Wilkinson et al. (2016), "The FAIR Guiding Principles for Scientific Data Management and Stewardship"

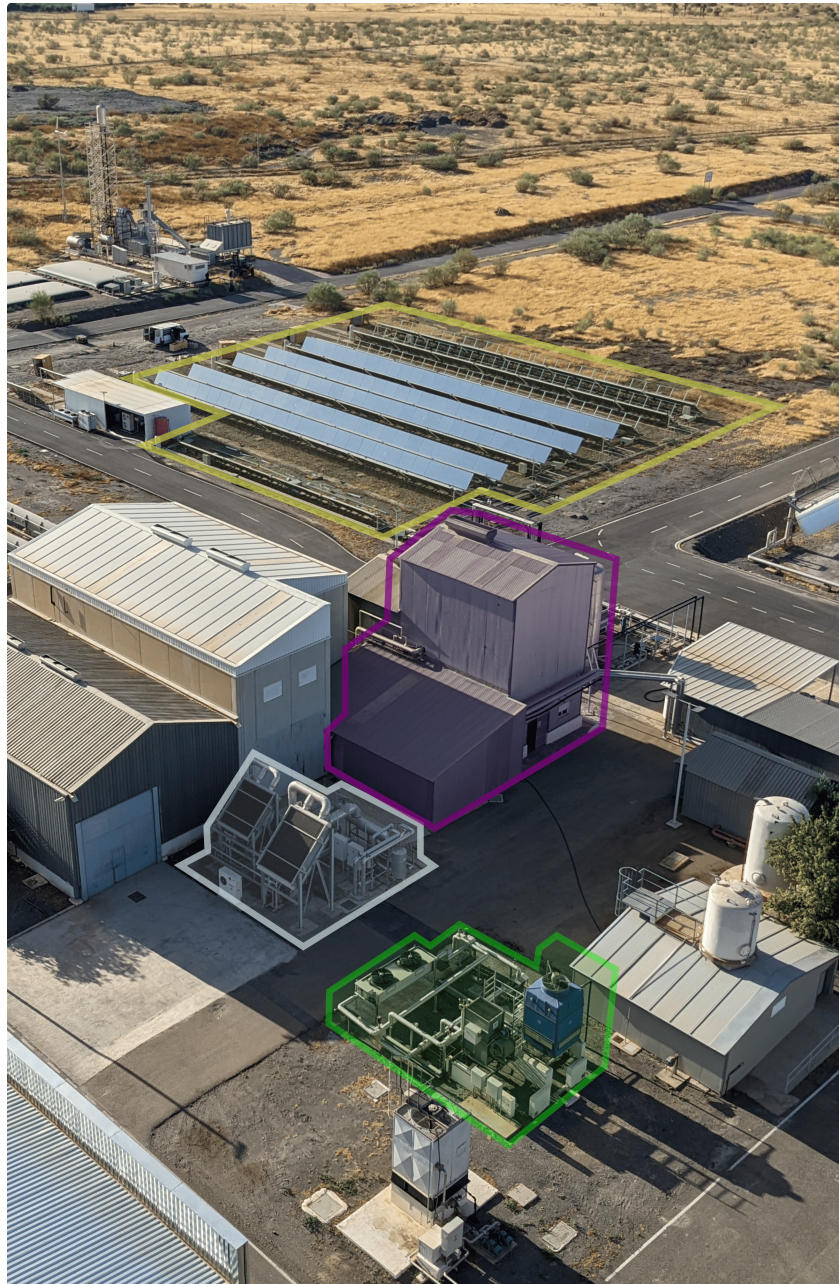


Figure 1.4: Aerial view of the pilot plants at Plataforma Solar de Almería (PSA), Spain. The developments presented in this thesis have been developed and validated around two test-rigs: a Combined Cooling System (CCS) and a Solar-driven Multi-Effect Distillation (SolarMED) pilot plant. In the picture, the solar field, the source of energy for all processes, is highlighted in yellow. Below it in purple is the building containing the Multi-Effect Distillation (MED) plant. The bottom two boxes (gray and green) delineate the area of the CCS plant. In gray the condenser and Air-Cooled Condenser (ACC) and in green the combined cooler composed by the Air-Cooled Heat Exchanger (ACHE) and Wet Cooling Tower (WCT) components.

2.1 Hypothesis

The purpose of this thesis is to investigate the following hypotheses:

- i) The selection of the cooling solution in a CSP plant is strongly dependent on the specific location of the plant, particularly on its weather conditions and water resources. Restricting the cooling choice to only dry or only wet options penalizes the overall system performance.
- ii) Hybrid or combined cooling systems are a technically feasible compromise between purely wet or dry systems, but they have seen limited deployment due to the increased complexity in design and operation. A general optimization methodology for these alternative cooling solutions could promote their broader adoption.
- iii) Thermal desalination has an important role in addressing water scarcity, not necessarily as the dominant desalination technology, but by targeting specific applications where it can complement other mature processes. These include value-added approaches such as brine mining, as well as the recovery and treatment of industrial and mining wastewater streams where thermal methods offer clear advantages.
- iv) To serve these niche but increasingly relevant applications, thermal desalination (with emphasis on MED) must evolve in a sustainable and decarbonized direction. This requires, on the one hand, improving efficiency and expanding operational ranges, and on the other, adapting to low-temperature contexts where its heat demand can be met—partially or fully—using alternative sources such as low-energy waste heat or solar thermal energy. While efficiency improvements are largely a design challenge, the present work contributes directly to the second aspect by developing methods that optimize the operation of solar-driven thermal desalination systems.

2.2 Objectives

The specific objectives set out to fulfil in the present research work are divided into two main blocks, each corresponding to one of the main contributions of the thesis¹. The first block (**O1**) focuses on the development of a methodology for the modelling and optimization of combined cooling systems, while the second block (**O2**) is centered around MED systems coupled with solar thermal plants.

1: And matches the parts in this manuscript

- O1.1** Model and validate various components of combined cooling systems, as well as their integration into a complete combined system.
- O1.2** Propose a methodology for optimizing combined cooling systems.
- O1.3** Experimental validation of the proposed methodology.
- O1.4** Perform a simulation-based analysis of a representative case study comparing different cooling alternatives and integrating the proposed methodology.

- O2.1** Analyze the current performance indices and evaluation criteria used in thermal desalination processes.

2.1 Hypothesis	7
2.2 Objectives	7
2.3 Contributions	8
2.4 Implementation software tools	10

- O2.2 Establish a standardized experimental evaluation framework for thermal desalination processes using consistent performance criteria.
- O2.3 Design and assess basic control loops, as well as identify stable operating conditions to ensure the reliability of experimentally obtained evaluation criteria.
- O2.4 Experimentally evaluate improvements (e.g., nanofiltration pretreatment) that enhance efficiency and/or reduce costs in solar desalination systems.
- O2.5 Model and simulate multi-effect desalination plants coupled with solar thermal systems.
- O2.6 Propose a methodology to optimize the operation of solar desalination processes based on selected performance criteria.
- O2.7 Evaluate hierarchical control structures aimed at optimizing desalination processes coupled with solar plants.
- O2.8 Demonstrate that the proposed hierarchical control structures improve the performance indices of desalination plants coupled with solar thermal systems.

2.3 Contributions

[14]: Asfand et al. (2020), "Thermodynamic Performance and Water Consumption of Hybrid Cooling System Configurations for Concentrated Solar Power Plants"

[15]: Mdallal et al. (2024), "Modelling and Optimization of Concentrated Solar Power Using Response Surface Methodology"

[16]: Hu et al. (2018), "Thermodynamic Characteristics of Thermal Power Plant with Hybrid (Dry/Wet) Cooling System"

[17]: Tang et al. (2013), "Study on Operating Characteristics of Power Plant with Dry and Wet Cooling Systems"

[18]: Asvapoositkul et al. (2014), "Comparative Evaluation of Hybrid (Dry/Wet) Cooling Tower Performance"

[19]: Barigozzi et al. (2014), "Performance Prediction and Optimization of a Waste-to-Energy Cogeneration Plant with Combined Wet and Dry Cooling System"

[20]: Martín et al. (2013), "Optimal Year-Round Operation of a Concentrated Solar Energy Plant in the South of Europe"

[21]: Martín (2015), "Optimal Annual Operation of the Dry Cooling System of a Concentrated Solar Energy Plant in the South of Spain"

[22]: Wiles et al. (1978), *Description and Cost Analysis of a Deluge Dry/Wet Cooling System*.

[23]: Zaloudek et al. (1976), *Study of the Comparative Costs of Five Wet/Dry Cooling Tower Concepts*

[24]: Rohani et al. (2021), "Optimization of Water Management Plans for CSP Plants through Simulation of Water Consumption and Cost of Treatment Based on Operational Data"

Over the years, numerous studies have compared wet and dry cooling systems for CSP plants. Most of these works focus on sensitivity analyses of selected operating parameters [14–19]. A smaller number have addressed the optimization of individual component operation to improve overall cooling system performance. In Martin et al. [20, 21], they optimized the year-round operation of the cooling system (wet in [20] and dry in [21]) in a CSP plant. However, both of their studies relied on monthly average data, which obscure significant daily temperature variations —often exceeding 10 °C— that coincide with peak power production and substantially affect cooling system performance.

In contrast, there has been little discussion in the literature regarding the operational strategies of combined cooling systems. For water-enhanced dry cooling and parallel configurations, the commonly proposed strategy [22–24] is to prioritize the dry section until the condenser pressure reaches a predefined threshold, at which point the wet units are activated. While this approach is simple and robust, it leaves significant performance potential untapped.

Several additional considerations arise when developing an effective operation strategy for combined cooling systems:

- ▶ Humidity is typically higher at night, when ambient temperatures are lower. This partially mitigates the limitations of dry cooling and makes it less unfavorable.
- ▶ The wet cooling section should be fully leveraged when water is plentiful, given its superior efficiency and lower operational cost.
- ▶ The availability and dynamic cost of alternative water sources should be incorporated into the decision process.
- ▶ The operation of combined cooling systems is inherently complex and requires a strategy that, at a minimum, ensures reliable satisfaction of the cooling demand, and ideally, minimizes the total operating cost.

This research work investigates the optimization of different cooling system configurations, focusing on their two main resource consumptions: electricity and water. The optimization problems are formulated to minimize the total cost of cooling a prescribed thermal load, with cost defined as the combined use of these two resources. The thermal load itself is treated as an external requirement and is therefore excluded from the decision space. This work addresses existing gaps in the literature and, for the first time, presents an actual optimization of the operation of a combined cooling system within the context of CSP applications.

Regarding the MED process, its future in desalination and brine concentration applications depends on both its technical development and its integration with other technologies [25, 26]. Performance evaluation plays a central role in this development. Although efforts have been made to propose performance metrics for multi-effect evaporation, there is currently neither consensus on which metrics are the most appropriate [27] nor a standardized methodology for experimental evaluation. The only existing standard for MED processes addresses cost structures and determinants rather than performance assessment [28].

This research proposes a standardized methodology for evaluating the performance of MED processes, which can also be extended to other thermal separation technologies. The method addresses key aspects such as instrumentation requirements, process control, and the suitability of various performance metrics, including the uncertainties associated with their determination. In addition, an algorithm has been developed for the automatic detection of steady-state operation, improving the reliability and robustness of evaluations under variable conditions. Furthermore, the plant is evaluated for the first time at high Top Brine Temperatures (TBTs) using the proposed methodology. The results are analyzed using multiple performance metrics, and the scale formation risk is quantified via the Ryznar Stability Index (RSI).

A MED plant, like any thermal separator, requires both heat and electricity. While electricity costs can be directly assigned, the cost of thermal energy depends on its source. When the heat is supplied by a variable source such as solar (or waste) heat, the situation becomes more complex: solar availability is intermittent, and the operation and efficiency of the solar field are closely linked to how the MED load is managed. This coupling is further complicated by the presence of thermal storage, which allows temporal shifting of heat usage and introduces additional operational decisions.

These promising low-exergy heat sources require high-level optimization systems capable of managing fluctuating operating conditions in order to integrate them with MED processes. Most existing literature on the automatic control of solar-driven MED systems focuses on low-level control strategies, typically employing simple control loops with either Proportional-Integral-Derivative controller (PID) controllers [29] or Model Predictive Control (MPC) schemes [30], whose primary goal is to maintain temperature setpoints –usually at the heat source inlet. A number of works have also addressed the optimization of the MED process in isolation [31, 32]. However, optimizing the MED subsystem independently neglects its coupling with the energy supply and storage systems.

Several studies have addressed this broader problem at varying levels of complexity. González *et al.* [30] proposed a receding-horizon optimal control strategy with economic objectives –maximizing water production while minimizing electricity costs– but relied on a simplified linear model that optimized only the solar field flow, keeping the MED inlet temperature constant. The most advanced optimization efforts in the literature, however, have been developed for Membrane Distillation (MD) rather than MED. Gil *et al.* [33] recognized that a solar MD plant operates through distinct modes (e.g., solar field heating, thermal storage charging, and MD operation), dictated by solar and thermal conditions. However, in their work, the transitions between these modes were hardcoded in the control rules, meaning that the choice of when to start or stop each subsystem was not treated as a decision variable but as part of the environment.

In many studies, either the decision space is too limited, the models are overly simplified, or key variables are treated as uncontrollable. Moreover, thermal storage decouples heat usage from solar availability, within certain limits, making the timing of subsystem operation –both solar field and thermal separator– critical for maximizing system performance over multiple days. Using a fixed irradiance threshold to trigger startup is therefore suboptimal, as it ignores the

[25]: Ghenai *et al.* (2021), “Performance Analysis and Optimization of Hybrid Multi-Effect Distillation Adsorption Desalination System Powered with Solar Thermal Energy for High Salinity Sea Water”

[26]: Son *et al.* (2020), “Pilot Studies on Synergistic Impacts of Energy Utilization in Hybrid Desalination System”

[27]: Burgess *et al.* (2000), “Solar Thermal Powered Desalination: Membrane versus Distillation Technologies”

[28]: Pinto *et al.* (2017), “Desalination Projects Economic Feasibility”

[29]: Roca *et al.* (2008), “Solar Field Control for Desalination Plants”

[30]: González *et al.* (2014), “Economic Optimal Control Applied to a Solar Seawater Desalination Plant”

[31]: Carballo *et al.* (2018), “Optimal Operating Conditions Analysis for a Multi-Effect Distillation Plant According to Energetic and Exergetic Criteria.”

[32]: Chorak *et al.* (2017), “Experimental Characterization of a Multi-Effect Distillation System Coupled to a Flat Plate Solar Collector Field”

[30]: González *et al.* (2014), “Economic Optimal Control Applied to a Solar Seawater Desalination Plant”

[33]: Gil *et al.* (2019), “Hybrid NMPC Applied to a Solar-powered Membrane Distillation System”

state of thermal storage and forecasts of future solar availability, which could enable more flexible and efficient operation.

In this work, the operation of a solar-driven MED system is optimized with these aspects explicitly accounted for. The formulation includes decision variables for starting and stopping each subsystem and considers a two-day prediction horizon. This enables the optimization to balance current performance with the impact of present decisions on future operation. The method is based on an experimentally validated system model that includes the electrical consumption of each component, coupled with a comprehensive data-driven MED model.

2.4 Implementation software tools

2: Isaac Newton in a letter to Robert Hooke in 1676, acknowledging that his discoveries were built on the work of others; also the title of the fourth studio album by English rock band Oasis

[34]: Biscani et al. (2020), “A Parallel Global Multiobjective Framework for Optimization: Pagmo”

[35]: Marcellos et al. (2021), *PyEqulon*

Software development for this research relies on a variety of tools. Just as scientific knowledge is built on the shoulders of giants², software similarly builds upon thousands of—mostly open-source—tools. Listing every tool used would be impractical, so only the most relevant ones are presented below:

- ▶ [PyGMO](#) (Mozilla Public License Version 2.0) [34] is a Python library for massively parallel optimization. It provides a unified interface for optimization algorithms and problems, facilitating deployment in parallel environments.
- ▶ [GPy](#) (BSD-3-Clause License) is a Gaussian Process Regression framework written in Python, developed by the Sheffield Machine Learning group.
- ▶ [pytransitions](#) (MIT License) is a lightweight, object-oriented state machine implementation in Python with many extensions. Created by Tal Yarkoni and maintained by Alexander Neumann.
- ▶ [simple-pid](#) (MIT License) provides a simple and fast PID controller implementation in Python. Created by Martin Lundberg.
- ▶ [Apache Airflow](#) (Apache 2.0 License). A platform to programmatically author, schedule, and monitor workflows.
- ▶ [PyEqulon](#) (BSD 3-Clause License) [35] is a Python package for automatic speciation calculations of aqueous electrolyte solutions.
- ▶ Statistics and Machine Learning Toolbox (proprietary MATLAB license) provides functions and apps to describe, analyze, and model data, including tools for machine learning such as classification, regression, clustering, and dimensionality reduction.

Automation overview: modelling, optimization and control

3

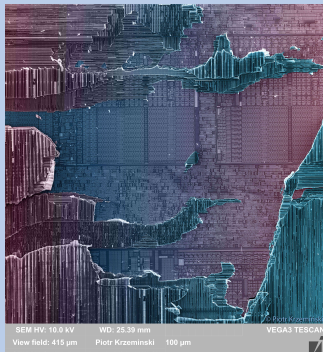
Automation, and particularly process automation, is a multidisciplinary technology that, by integrating various fields of knowledge, aims to develop autonomous systems capable of operating with minimal human intervention, using resources efficiently, adapting to changing conditions, and ensuring safety and reliability.

This chapter provides an overview of the main aspects of automation, focusing on modelling, optimization and control which are particularly relevant to the development of this research work. These three pillars are essential for the development of advanced automation systems and are widely used in the industry. The chapter is structured as follows: first, an overview of modelling techniques is presented, including first-principles and data-driven approaches. Then, optimization methods are discussed, covering both single-objective and multi-objective optimization. Finally, control strategies are reviewed, with a focus on PID and hierarchical control.

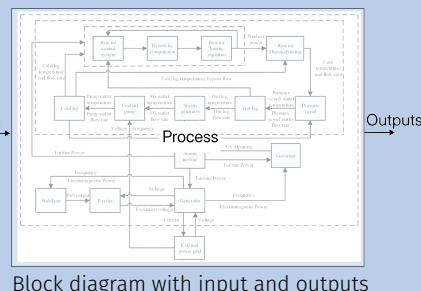
Dealing with complexity

Real systems are complex, with many elements interconnected. We first need to simplify them into simpler blocks or levels of abstraction that we can work with. These blocks or boxes have inputs and outputs, internally they hide some complexity, but from our abstraction we only care that we give some input to them, they perform some transformation, and then they return some output. These then can be interconnected to form a complex network or structure representing the real process.

This layering is common in many different fields, for example, processors are made up by thousands of layers, with modern processors going from city-like structures in the upper layers while reaching atomic scales in the lowest layers.



Zoomed-in microprocessor.
Source: [stylishpirate - Reddit](#)



Block diagram with input and outputs

3.1 Modelling and simulation

Models are useful approximations for the real-world, more precisely a mathematical representation of real-world systems. A model can depict a system at different levels of abstraction depending on the intended use. Models are useful in many applications [36]:

3.1 Modelling and simulation	11
3.1.1 First principle modelling	13
3.1.2 Data-driven modelling	13
3.1.3 Discrete modelling by means of Finite-State Machines (FSMs)	18
3.1.4 Forecasting and combinatory nature of FSMs	19
3.1.5 Performance metrics	19
3.2 Optimization	20
3.2.1 Non-Linear Programming (NLP) problems	21
3.2.2 Mixed Integer Non-Linear Programming (MINLP) problems	22
3.2.3 A discussion on constraint handling	22
3.2.4 Multi-objective optimization	23
3.2.5 Optimization algorithms	24
3.3 Control	28
3.3.1 PID controllers	29
3.4 Hierarchical control	29

[36]: Sokolowski et al. (2011), *Principles of Modeling and Simulation*

- ▶ Forecasting. They are used to predict the value of a variable at some time in the future.
- ▶ Simulation. Oftentimes experimentally evaluating real-world systems is impractical or infeasible, either because it is costly, time-consuming, or deteriorate the system, among other factors. Simulating a model enables the repeated observation of a system with just an associated computational cost.
- ▶ Control and optimization. In order to compute the optimal input to give to a real system, many control strategies are model-based, that is, they assess how inputs given to the real system will affect it by first evaluating them in a model.
- ▶ Via analysis, they enable to draw conclusions, verify and validate the research, and make recommendations in order to support decision-making.

Sensitivity analysis

Sensitivity analysis is one of the possible analysis tools. It involves systematically assessing how variations in input parameters impact the model outputs. One of the methods used in this research work is the Sobol method [37], which is a variance-based approach. This method decomposes the total variance of the model output into contributions from individual input parameters and their interactions.

All real world systems are fundamentally dynamical systems, that is, they evolve over time. For example a fluid flowing over a plane wing, the spread of a disease, the climate of a planet, the stock market, planets moving around the solar system. This behavior takes place continuously with respect to time for most physical systems, and can be described using differential equations. An alternative discrete representation can be achieved by performing a transformation from the continuous space to a discrete space sampling data at discrete time intervals and is described by difference equations. For an infinitesimal small time interval they are equivalent. In practice, the discrete representation is a simplification of continuous systems.

An example of the position (y) of an object free-falling by gravity could be represented:

- ▶ In a dynamic continuous space as $\frac{d^2y(t)}{dt^2} = -g$
- ▶ or with a discrete representation (sample time Δt and velocity v): $y_{k+1} = y_k + v_k \Delta t - \frac{1}{2}g(\Delta t)^2$

When a dynamic system is left unchanged for a sufficiently long period and an equilibrium is established between its inputs and outputs, it eventually reaches a stable or steady state. As long as the inputs remain constant, the outputs will also remain constant (visualized in Figure 3.1). Thermodynamic processes are often analyzed under these equilibrium conditions, since the main interest is typically the stable relationship between a given set of inputs and the resulting outputs, rather than the detailed trajectory of how the system evolves from one state to another. This approach makes it possible to evaluate the long-term performance of the system.

In many cases, a dynamic system can be approximated as a steady-state system if the transitions between equilibrium states are either negligible or irrelevant to the problem at hand. Such simplifications are appropriate when the system is expected to operate mostly under stable conditions, and the transient dynamics do not significantly affect performance. For example, in thermodynamic analyses, transient behavior is frequently treated as noise when evaluating efficiency or energy balances. This is especially valid for systems with fast dynamics —where

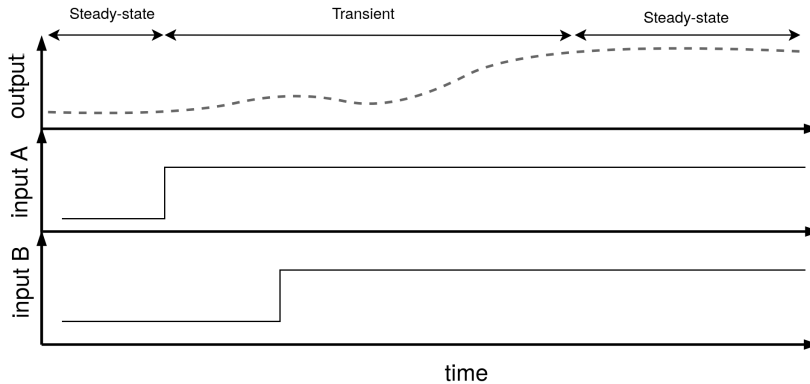


Figure 3.1: Dynamic response (reaction curve) of a process output to changes in its inputs'

transients settle within seconds—and that are only occasionally disturbed, meaning the system spends most of its time operating near steady state.

A model can be an incomplete and possibly incorrect representation of the phenomenon under study. This typically occurs when information about the phenomenon is lacking or when very complex processes are being modeled—such as biological systems that change their dynamics over time, or large-scale stochastic processes like climate, where small errors can propagate exponentially. All these factors contribute to uncertainty in modeling. Uncertainty is generally classified as aleatory or epistemic [36]. Aleatory uncertainty arises from inherent randomness in the system and is typically addressed through probabilistic or stochastic methods, though in some cases it may be simplified or ignored. Epistemic uncertainty, on the other hand, stems from incomplete knowledge, modeling assumptions, or limited data.

[36]: Sokolowski et al. (2011), *Principles of Modeling and Simulation*

Given a real-world scenario, the first step is to identify a problem to model, make reasonable assumptions about the process and collect data, choose a modelling approach, test the assumptions, refine the model as necessary and finally fit the model to data if appropriate. Two main categories of modelling exist: first-principle and data-driven, explained in the following.

3.1.1 First principle modelling

First-principle modelling¹ is an approach to representing a system by starting from the fundamental laws of nature—such as conservation of mass, energy, and momentum; Newton's laws of motion; thermodynamics; or chemical kinetics. In this framework, the model equations are derived from established physical, chemical, or biological principles that govern the system's behavior.

1: also called white-box modelling or physics-based modelling

The resulting models typically take the form of differential and algebraic equations, which describe how system states evolve over time as a function of inputs and parameters. Such models are valuable because they provide physical interpretability, can be extrapolated beyond measured operating points, and allow deeper insight into how design or operating conditions affect performance. However, they often require detailed process knowledge, accurate parameter estimation, and can become computationally intensive for complex systems.

3.1.2 Data-driven modelling

Data-driven modelling refers to the construction of models that rely primarily on measured or simulated data, rather than on explicit knowledge of the underlying physical laws. The central idea is to capture patterns, correlations, and dependencies in input-output data and use them for prediction, control, or

optimization. Unlike first-principle models, which are built from conservation laws and mechanistic equations, data-driven models treat the system as a black box, with little or no prior assumptions about its internal structure.

A large class of data-driven techniques can be framed within supervised learning, where the model learns a mapping from inputs to outputs based on labeled training data. Supervised learning methods are commonly divided into regression and classification problems: classification predicts discrete categories, while regression focuses on continuous quantities. In this research work the focus is mainly on regression approaches, since most engineering systems require the prediction of continuous variables such as temperatures, pressures, flows, or performance indices.

Data-driven regression models can range from simple, interpretable structures—such as polynomial regressions—to highly flexible nonlinear machine learning models such as Gaussian process regression or artificial neural networks. Each comes with its own trade-offs between accuracy, interpretability, data requirements, and computational cost. In the following, we discuss some representative examples of these approaches.

Data-driven approaches are particularly useful when: adequate experimental or simulated data is available, predictions are needed mainly within the range of observed data and simplicity and speed are prioritized over detailed physical interpretability.

Polynomial models

Polynomial models of arbitrary order approximate system behavior by expressing outputs as polynomial functions of the inputs. The degree of the polynomial determines how flexibly the model can capture nonlinear relationships: lower-order polynomials give simple trends, while higher-order ones can represent more complex patterns but risk overfitting and poor extrapolation outside the training range.

Polynomial regression is one of the most widely used empirical parametric-modeling techniques because it is easy to implement, computationally efficient, and provides closed-form solutions for the estimated coefficients. Despite its simplicity, it often delivers sufficiently accurate approximations for engineering applications.

Use cases include curve fitting, surrogate models for optimization problems, quick approximations in control design, and empirical correlations.

Gaussian Process Regression

A Gaussian Process (GP) is a powerful and flexible non-parametric model that defines a distribution over functions instead of assuming a specific functional form (such as a straight line in linear regression). In this framework, any possible function could explain the data, but functions that are *smoother* or *closer* together in input space are more likely. It consists of a collection of random variables, any finite number of which have a joint Gaussian (normal) distribution [38].

Gaussian-Process Regression (GPR) provides a flexible and probabilistic approach to modeling unknown functions. Consider a simple one-dimensional regression problem, mapping an input variable x to an output $f(x)$. In Figure 3.2 (a), several sample functions are drawn from a *prior* Gaussian Process, which expresses the assumed characteristics of functions before any data are observed. This prior favors smooth functions with an average (mean) value of zero across the input space². The shaded region represents the variability of

[38]: Rasmussen et al. (2006), *Gaussian Processes for Machine Learning*

2: Although the individual functions shown may not have a zero mean, the average of many such samples at any fixed x would approach zero

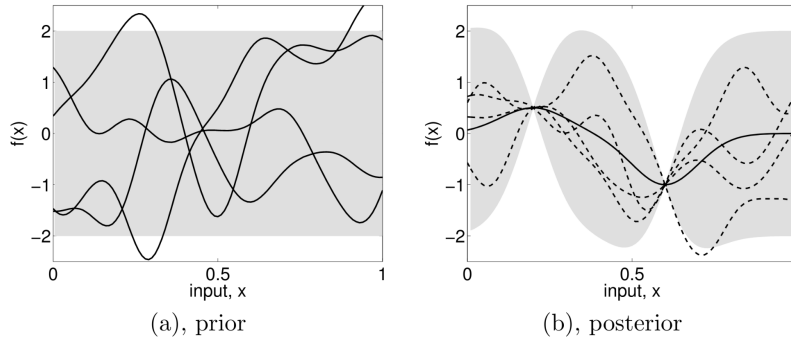


Figure 3.2: Illustration of Gaussian Process Regression. (a) Prior samples drawn from a Gaussian Process with zero mean and smooth covariance, representing the prior belief before observing any data. (b) Posterior samples and mean after conditioning on two observations, showing reduced uncertainty near the observed points.

Source: Rasmussen et al. [38]

these functions, corresponding to twice the pointwise standard deviation, which in this case is constant across x .

When a small dataset $\mathcal{D} = \{(x_1, y_1), (x_2, y_2)\}$ is observed, the process is updated to consider only functions consistent with these observations. This is illustrated in Figure 3.2 (b). The dashed lines represent sample functions that agree with the data, and the solid line indicates their mean. The uncertainty, represented by the shaded area, decreases near the observed points and remains higher where data are unavailable. This updated distribution is the *posterior* Gaussian Process, obtained by combining the prior assumptions with the observed data through Bayesian inference [39].

The choice of the prior, and particularly of the covariance (or kernel) function determines the characteristics of the functions the GP can represent, such as smoothness, amplitude, or characteristic length-scale (*i.e.* its shape)³. Adjusting the kernel parameters controls how quickly the functions vary with x , thereby tailoring the model to the data properties. In practice, learning with Gaussian Processes involves identifying the kernel and parameter values that best describe the observed data.

[39]: Gelman et al. (2013), *Bayesian Data Analysis, Third Edition*

3: Options such as the Squared Exponential (RBF) kernel produce smooth functions, while linear or periodic relationships can be captured using other kernels.

Artificial Neural networks

Artificial Neural Networks (ANNs), as the name suggests, have a behavior similar to biological neurons. Their structure is formed by a succession of layers, each one composed by nodes (or neurons) and they receive as input the output of the previous layer. This process is subsequently repeated until the final layer which has a number of neurons equal to the number of outputs [40].

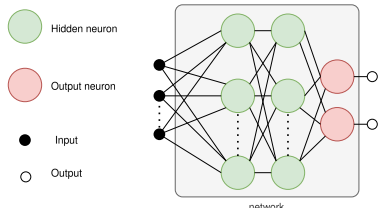
There are important aspects to be considered in the ANN model design, such as the model configuration, the network architecture and the network topology. They are discussed below.

[40]: Hagan et al. (2014), *Neural Network Design*

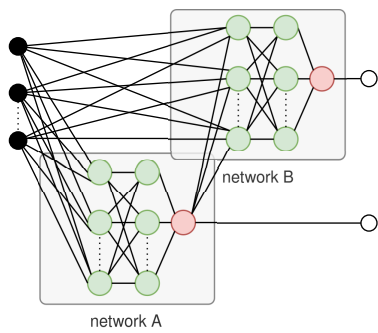
Model configuration. If the model has more than one output, several configurations are available for the implementation of the model as shown in Figure 3.3. The first one is a Multiple Inputs Multiple Outputs (MIMO) configuration, where a single network receives all the inputs and directly produces all predicted outputs. The second one is a cascade structure. This cascading approach involves training a network (*network A* in Figure 3.3 (b)) to predict one output using the available inputs. Subsequently, these inputs, along with the output from the first-output-predicting network, are fed into a second network (*network B* in Figure 3.3 (b)) that is in charge of forecasting the second output. This procedure can be repeated as many times as desired. A potential advantage of this configuration is that it may reduce the experimental data requirements to obtain satisfactory results. A third option is the combination of both configurations, where some networks may predict several outputs, while others are fed some of these outputs and subsequently use them as inputs.

Network architectures. Three network architectures have been explored in this research work:

4: Defined as $\text{logsig}(x) = 1/(1 + e^{-x})$, mapping any real input to a value between 0 and 1.



(a) MIMO configuration



(b) Cascade configuration

Figure 3.3: ANN model configurations

[41]: Beale et al. (2010), "Neural Network Toolbox"

5: The Z-score method rescales data so that each feature has a mean of 0 and a standard deviation of 1. It is computed as $z = \frac{x-\mu}{\sigma}$, where μ and σ are the feature's mean and standard deviation, respectively.

6: it refers to one complete pass of the entire training dataset through a learning algorithm during the training process of a model

[42]: Hamm et al. (2007), "Comparison of Stochastic Global Optimization Methods to Estimate Neural Network Weights"

1. Feed Forward (FF) network - Figure 3.4 (a). This is the base network architecture, where different layers are added sequentially and the flow of information is unidirectional. The transfer function adopted in the hidden layers is the differentiable Log-Sigmoid⁴, whereas the one employed in the output layer is a linear one with no saturations.
2. Cascade-forward (CF) network - Figure 3.4 (b). It is a variation on the feedforward network since it adds direct connections from the input and hidden layers to the output layer.
3. Radial Basis Function (RBF) network - Figure 3.4 (c). The transfer functions used in the first layer of the RBF network are different, they are local Gaussian like functions. Also, instead of multiplying by the weights, the distance between inputs and weights is computed and the bias is multiplied instead of added [40].

Network topology. Two-layer networks (one hidden and one output layer) can learn almost any input-output relationship, including non-linear ones. Adding more layers can improve the learning for more complex problems. However, increasing the number of layers or neurons per layer increases the training computational requirements, requires more data for a satisfactory model and can lead to overfitting. Therefore, the process usually starts with two layers and then the number of layers is increased if they do not perform satisfactorily [40].

Training process. The next important aspect to consider is the training process. For the FF and CF networks many Gradient- or Jacobian-based algorithms can be utilized like the Levenberg–Marquardt backpropagation algorithm [41]. It is a fast algorithm, ideal for multilayer networks with up to a few hundred weights and biases enabling efficient training. The training in this case is done in batches since sequential training is slower and does not produce better results. All data needs to be standardized applying methods like the Z-score normalization method⁵. The criteria established for deciding when to stop the training is the following one: when the performance on the validation set increases (worsens) for a number of iterations (also known as patience) or when the gradient is below a minimum (e.g. 1×10^{-7}) for a number of iterations or epochs⁶, or when a maximum number of epochs is reached (e.g. 1000). Finally, the selected network parameters are those of the best epoch.

For each network architecture, the training process is repeated a number of times (ten times is the recommended practice if the computational requirements allow it, since it guarantees reaching a global optimum with a high degree of confidence [42]). The optimal architecture and training is then selected according to a performance function evaluated with normalized values (e.g. Mean Squared Error (MSE) explained in a later section).

In the case of the RBF network, the training method consists in two stages which treats the two layers of the RBF network separately. The first layer weights and biases are tuned based on the orthogonal least squares method [40], while for the second layer are computed in one step using a linear least-squares algorithm. During training, neurons are added to the first layer (e.g. in increments of 20) trying to minimize a performance metric (e.g. MSE) to some goal. Finally, a parameter called spread is used to set the first layer biases. Larger values of this parameter promote a smoother approximation of the training data (more generalization), conversely, lower values provide a more exact fit to the training data.

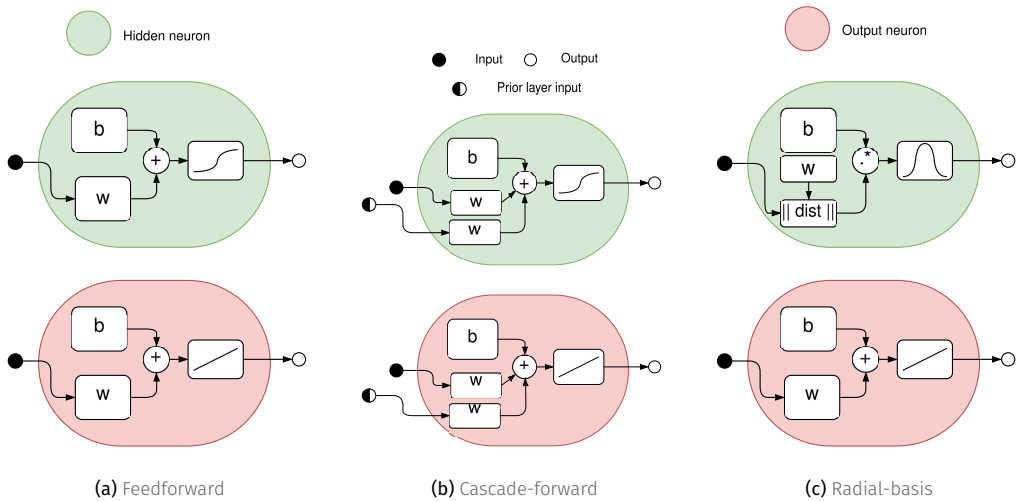


Figure 3.4: Considered ANN architectures

Other machine learning methods

- **Random Forest.** A random forest for regression is a method that combines many decision trees to make more accurate and stable predictions. A decision tree is a model that splits the data into smaller and smaller groups based on input features, creating a set of simple rules that lead to a prediction at the end of each branch. Each tree in a random forest is trained on a slightly different version of the data by randomly sampling both data points and features, and the forest's final prediction is obtained by averaging the outputs of all trees. As the number of trees increases, the prediction error stabilizes and approaches a fixed value. The performance of a random forest depends on how strong the individual trees are at predicting the target and how different they are from each other, and this balance allows the method to produce reliable predictions that are usually better than those of a single decision tree [43].
- **Gradient-boosting** builds a strong predictive model by combining many weak models, usually decision trees, in a sequential way. Each new tree is trained to correct the errors (residuals) made by the previous ensemble, using the gradient of a loss function to guide the improvements [44].

[43]: Breiman (2001), “Random Forests”

[44]: Friedman (2001), “Greedy Function Approximation”

Surrogate Data-driven models from first-principles models. Synthetic dataset generation

One important advantage that first-principles models have over data-driven is their scalability, that is, the ability to adapt a model developed and validated in a pilot-scale system, to a large scale one. This is true for many systems as long as the system configuration remains the same. This allows to study and analyze pilot scale plants and extrapolate the results to industrial-sized plants. In addition, these type of models are also capable of predicting the behavior of the modelled systems in conditions that have not been tested (e.g. different operating or environmental conditions), although the reliability of the model could be lowered if these conditions move away from those experimentally used for some parameter calibration.

On the contrary, data-driven models are very specific to the system and operating ranges they are trained for. That is why training/calibrating a data-driven model

with a synthetic dataset generated from the evaluation of the first-principles model is common practice to obtain a surrogate model that can then be used in a larger range of operating conditions and that provides superior computational performance.

The process of generating samples from a first-principles model to train a data-driven model is called synthetic dataset generation. It consists of running the first-principles model for a set of input parameters, which can be selected randomly or following a specific distribution, and then using the outputs of the first-principles model as the training data for the data-driven model.

The first step is to define the input parameters and their ranges. This can be done by selecting the most relevant parameters for the system and determining their ranges based on the system's operating conditions. The next step is to generate a set of input parameters, which can be done using different methods such as Latin Hypercube Sampling, Monte Carlo Sampling, Sobol Sampling, or simply grid sampling [37, 45, 46]. These methods allow generating a set of input parameters that cover the entire range of the input parameters and ensure that the generated samples are representative of the system's behavior. Once the input parameters are defined, the first-principles model is run for each set of input parameters, and the outputs of the model are recorded. Finally, the recorded outputs are used to train the surrogate data-driven model.

[37]: Nossent et al. (2011), "Sobol'sensitivity Analysis of a Complex Environmental Model"

[45]: McKay et al. (1979), "A Comparison of Three Methods for Selecting Values of Input Variables in the Analysis of Output from a Computer Code"

[46]: Saltelli et al. (2000), *Sensitivity Analysis*

3.1.3 Discrete modelling by means of FSMs

Up to this point, the discussion has focused on the modeling of continuous systems, in which changes evolve smoothly over time and are typically described by differential equations. In contrast, discrete or event-driven modeling deals with systems whose states change only at distinct moments, triggered by the occurrence of specific events

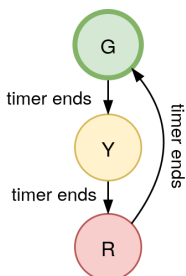
There are many ways of modeling the behavior of these systems, and the use of state machines is one of the oldest and best known. State machines allow us to think about the "state" of a system at a particular point in time and characterize the behavior of the system based on that state⁷.

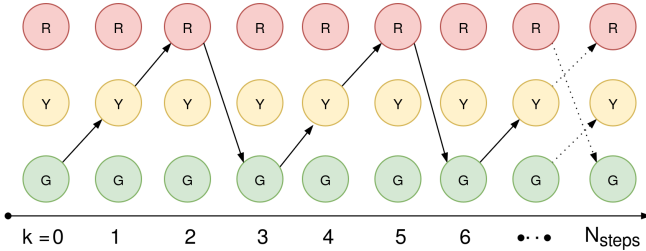
For example, a traffic light (see Figure 3.5) can be described as a finite state machine with three primary states: *green*, *yellow*, and *red*. In each state, the traffic light has a well-defined behavior (allowing vehicles to pass, warning them to slow down, or stopping them completely). The transitions between states are also clearly defined: green changes to yellow, yellow to red, and red back to green. Some transitions are possible, while others are not (e.g., green cannot jump directly to red without first passing through yellow).

So, a finite state machine is a model of behavior composed of a finite number of states and *transitions* between those states. Within each state and transition some *action* can be performed. A state machine needs to start at some *initial state*. Finite refers to a machine that has a limited number of possible states and at any given time it will be in one of those states. Its core components are described hereinafter:

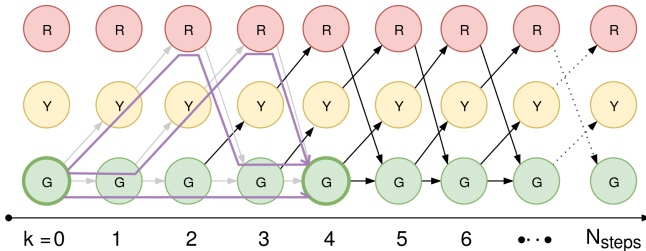
- ▶ **State.** A state represents a particular condition or stage in the machine. It represents a distinct mode of behavior or phase in a process.
- ▶ **Transition.** This is the process or event that causes the state machine to change from one state to another.
- ▶ **Action.** Specific operation or task that is performed when a certain event happens i.e. a state is entered, exited, or during a transition.
- ▶ **Model.** A stateful structure that holds information about the state of the machine. It gets updated during transitions and defines actions.

Figure 3.5: FSM representation of a traffic light





(a) Simple traffic light



(b) Traffic light with push-button

Figure 3.6: Evolution of different traffic-light FSMs assuming the timer takes one step to complete.

- **Machine.** This is the entity that manages and controls the model, states, transitions, and actions. It's the conductor that orchestrates the entire process of the state machine.

3.1.4 Forecasting and combinatory nature of FSMs

A traffic light is a simple example of a deterministic state machine, because its transitions are triggered by a single predictable input —the timer—and therefore its future trajectory is entirely fixed. From any given state, there is only one possible next step, so the entire cycle can be anticipated with certainty (see Figure 3.6 (a)). Many real systems, however, are not that simple. When the set of inputs that can trigger transitions is larger and each input leads to different successor states, the system no longer has just one linear trajectory but many possible ones. In such cases, the behavior of the machine can be represented as a branching tree, where each node corresponds to a state and each branch corresponds to a possible input event. This can be illustrated for the traffic light example if a push-button is added (see Figure 3.6 (b)). The state will be green-light unless the push-button is triggered. Starting from an initial state, evaluating now the possible paths that yield in an arbitrary final state given a number of steps becomes a combinatory problem.

This branching has important implications: while the machine is still finite in the number of states, the number of possible sequences of states over the horizon grows rapidly as more steps are considered. After just a few transitions, the tree of possible futures can expand exponentially.

3.1.5 Performance metrics

For models to be useful they need to accurately represent the real process. In order to quantitatively assess how good a model represents a real system different performance metrics are used. Four performance metrics are described: coefficient of determination (R^2), Root Mean Squared Error (RMSE), Mean Absolute Error (MAE) and Mean Absolute Percentage Error (MAPE).

8: also known as features
9: also referred as target

Coefficient of determination. Regression estimates the relationship between input variables⁸ and a continuous output variable⁹. R^2 is a direct measure of regression. It measures the proportion of the variance in the predicted variable that can be attributed to the independent variable(s), in this case the considered system inputs. Values close to one indicate a better prediction accuracy. It is calculated as follows:

$$R^2 = 1 - \frac{\sum_{i=1}^n (y_i - \hat{y}_i)^2}{\sum_{i=1}^n (y_i - \bar{y})^2},$$

where y_i is the measured or observed value for the output variable, in the i -th observation, \hat{y}_i is the estimated value of the same variable and n is the total number of observations. Finally, \bar{y} is the mean value of the experimental values.

Root Mean Square Error. RMSE is a statistical measure of the difference between the values predicted by a model and the observed values. It is calculated as the square root of the mean of the squared differences between the predicted and observed values, and it has its units.

$$\text{RMSE} = \sqrt{\frac{1}{n} \sum_{i=1}^n (y_i - \hat{y}_i)^2}$$

Mean Absolute Error. It represents the average absolute difference between predicted and measured values.

$$\text{MAE} = \frac{1}{n} \sum_{i=1}^n |y_i - \hat{y}_i|$$

Mean Absolute Percentage Error. As the MAE, it calculates the difference between the predicted and the actual values, but in this case it does so in relative terms:

$$\text{MAPE} = \frac{1}{n} \sum_{i=1}^n \left| \frac{y_i - \hat{y}_i}{y_i} \right| \times 100\%$$

3.2 Optimization

Optimization consists on finding the best solution, i.e. the optimal solution, to a problem under given circumstances. At its core, optimization seeks to determine the values of decision variables that minimize (or maximize) an objective function while respecting a set of constraints. These problems arise in diverse domains such as operations research, economics, energy systems, and machine learning, where they enable the systematic allocation of resources, the design of efficient processes, and the balancing of trade-offs between competing goals.

A general expression to define an optimization problem is:

$$\min_{\mathbf{x}, \mathbf{e}; \theta} J = f(\mathbf{x}, \mathbf{e}; \theta) \quad \text{s.t.} \quad g_i(\mathbf{x}) \leq 0, \quad i = 1, \dots, m \quad (3.1)$$

where \mathbf{x} is the vector of decision variables, \mathbf{e} the vector of environment variables, θ the list of parameters, $f(\mathbf{x})$ is the objective function to be minimized, and $g_i(\mathbf{x})$ are the constraints of the problem. The objective function is a scalar

function that maps the decision variables to a real number, representing the cost or performance of the system. The constraints are functions that restrict the feasible region of the problem, defining the set of values that the decision variables can take. The optimization problem is to find the values of the decision variables that minimize the objective function while satisfying the constraints.

Regarding the constraints, they can be categorized in two types depending whether they can be evaluated before evaluating the objective function or not:

- ▶ **Bounds** or box-bounds. These are constraints that limit the range of the decision variables, such as

$$x_i \in [l_i, u_i], \quad i = 1, \dots, n$$

where l_i and u_i are the lower and upper bounds of the decision variable x_i , respectively. They can be evaluated before evaluating the objective function.

- ▶ **Constraints**. These are constraints that restrict the feasible region (also known as domain) of the problem, such as

$$g_i(\mathbf{x}) \leq 0, \quad i = 1, \dots, m$$

where $g_i(\mathbf{x})$ are the constraint functions that depend on the decision variables \mathbf{x} , and m is the number of constraints. Its value can only be known after evaluating the problem.

These described components of an optimization problem are visualized in Figure 3.7.

3.2.1 NLP problems

A NLP problem refers to a *nonlinear programming* formulation in which both the objective function $f(\mathbf{x})$ and the constraint functions $g_i(\mathbf{x})$ can be nonlinear. These problems are generally more difficult to solve than linear programming (LP) problems, since the feasible region may be non-convex and the objective function may have multiple local minima. Solution techniques for NLP include gradient-based methods, sequential quadratic programming, interior-point methods, and heuristic approaches when derivatives are unavailable or the problem is highly non-convex.

Optimization concepts

- ▶ **Decision variables (\mathbf{x})**. These are the variables that can be controlled or adjusted in order to optimize the objective function.
- ▶ **Environment variables (\mathbf{e})**. These are the variables that cannot be controlled or adjusted, but they can affect the objective function and the constraints.
- ▶ **Objective function ($f(\mathbf{x})$)**. This is the function that needs to be minimized or maximized. It represents the goal of the optimization problem.
- ▶ **Constraints ($g(\mathbf{x})$)**. These are the restrictions or limitations that need to be satisfied in order to find a feasible solution. They can be equality or inequality constraints.
- ▶ **Search-space ($\mathcal{X} \subseteq \mathbb{R}^n$)**. This is the set of all possible values of the decision variables that satisfy the bounds.
- ▶ **Feasible region ($\mathcal{F} \subseteq \mathcal{X}$)**. This is the set of all possible values of the decision variables that satisfy the constraints. The optimal solution must lie within this region.
- ▶ **Optimal solution ($\mathbf{x}^* \in \mathcal{F}$)**. This is the set of values of the decision vari-

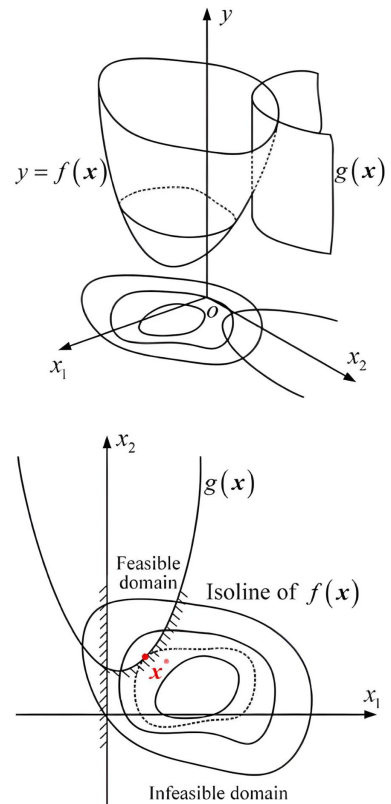


Figure 3.7: Constrained optimization problem. The goal is to minimize $y = f(\mathbf{x})$ with the two continuous decision variables x_1 and x_2 constrained to $g(\mathbf{x})$. The problem is NLP with a convex solution-space.
Source: Wang et al. [47]

ables that minimize or maximize the objective function while satisfying all the constraints.

- ▶ **Convexity.** A problem is convex if both the objective function and the feasible region are convex. Convex problems have a single global optimum, which can be found efficiently using various optimization algorithms. Non-convex problems may have multiple local optima, making them more challenging to solve.

3.2.2 MINLP problems

A Mixed Integer Non-Linear Programming (MINLP) problem, extends the NLP formulation by introducing integer (often binary) decision variables alongside continuous ones. The presence of discrete variables significantly increases the complexity of the problem, as the feasible set becomes combinatorial in nature, often leading to an exponential growth in the search space. MINLP problems naturally arise in many engineering problems where decisions such as on/off states, integer quantities, or logical relations must be combined with nonlinear models. Typical solution strategies include branch-and-bound, branch-and-cut, outer approximation, and decomposition methods.

As an example, consider the following MINLP problem:

$$\begin{aligned} \min_{x,y} \quad & (x - 3)^2 + y \\ \text{s.t.} \quad & x^2 \leq y, \\ & x \in \mathbb{R}, \quad y \in \{0, 1\}. \end{aligned} \tag{3.2}$$

In this formulation, x is a continuous variable, while y is binary. The feasible set is determined not only by the nonlinear constraint $x^2 \leq y$ but also by the discrete choice of y , which switches the constraint on or off depending on its value.

A common strategy for tackling MINLPs is by integer *relaxation*, in which the integer constraints on some variables are relaxed to continuous domains (e.g., replacing $y \in \{0, 1\}$ with $y \in [0, 1]$). The relaxed problem becomes a standard NLP, which is typically easier to solve. The solution of this relaxation can then be used to guide exact methods such as branch-and-bound or to construct valid lower bounds in global optimization algorithms. However, this is flawed in assuming the best solution of the relaxed problem is close to the full MINLP problem solution, or that the relaxed problem contains relevant information in its gradient.

3.2.3 A discussion on constraint handling

There are two main approaches to handle constraints in optimization problems:

- ▶ **Penalty methods.** These methods add a penalty term to the objective function to penalize the violation of the constraints. The penalty term is usually a function of the constraint violation, and it is added to the objective function to form a new objective function that is minimized. The penalty term can be linear or non-linear, and it can be adjusted during the optimization process to ensure that the constraints are satisfied. The main advantage of penalty methods is that they allow to handle constraints in a flexible way, and they can be used with any optimization algorithm. However, they can also lead to suboptimal solutions if the penalty term is not properly tuned, and they can also lead to numerical instability if the penalty term is too large.

- ▶ **Constraint handling methods.** These methods handle the constraints directly, by either rejecting solutions that violate the constraints or by modifying the optimization algorithm to ensure that the constraints are satisfied. The main advantage of constraint handling methods is that they guarantee that the constraints are satisfied, and they can also lead to better solutions than penalty methods. However, they can also be more complex to implement, and they can also lead to numerical instability if the constraints are too restrictive. Specific constraint-handling capable algorithms are required to solve these type of problems.

By using inequality constraints, the optimization algorithm is forced to find the best solution that satisfies these constraints. However, in problems with a horizon window, this would require returning a value of the constraint for each step within the horizon, thereby producing a large vector of inequality constraints and increasing the problem's dimension (*i.e.* its complexity). On the other hand, returning a single aggregated value for the entire episode provides much less information to the algorithm about which decisions violate the constraints and when. As a result, the optimizer may struggle to adapt its decision variables effectively and could fail to converge, or require an unfeasibly large number of objective function evaluations¹⁰.

Finally, non constraint-handling capable algorithms can be wrapped with constraint handling methods to solve problems with constraints [48], where they basically implement some type of penalty method.

¹⁰: Here, “unable” refers to requiring an unfeasible number of objective function evaluations, *i.e.*, too much time.

[48]: Farmani et al. (2003), “Self-Adaptive Fitness Formulation for Constrained Optimization”

3.2.4 Multi-objective optimization

When an optimization problem involves only one objective function, the task is called single-objective optimization. In contrast, when multiple objectives must be optimized simultaneously, the problem becomes one of multi-objective optimization. A key difference is that in the multi-objective case, objectives are often conflicting: improving one objective typically requires sacrificing performance in another [49]. As Johan Löfberg illustrates in the [YALMIP documentation](#):

It is impossible to design a car which is as light as possible, as cheap as possible, as fast as possible, and as durable as possible, all at the same time. In the end, the solution to the obviously multi-objective task of designing a car, will be a compromise. Multi-objective optimization is about finding the set of non-bad compromises, which is called the Pareto-optimal solutions.

Two main approaches are commonly used to address multi-objective problems [49]:

- ▶ Scalarization (or decomposition) methods, where the multi-objective problem is converted into a sequence of single-objective problems by combining objectives into one, for example using weighted sums or penalty methods. Each run of a single-objective solver yields one trade-off solution, so multiple runs with different scalarizations are required to approximate the Pareto set.
- ▶ Population-based methods, such as evolutionary algorithms¹¹, which evolve a set of solutions in parallel. Because they operate on a population rather than a single solution, these methods naturally approximate the entire Pareto front within a single run, capturing multiple trade-offs between conflicting objectives.

[49]: Deb (2011), “Multi-Objective Optimisation Using Evolutionary Algorithms: An Introduction”

¹¹: Described in the following section

3.2.5 Optimization algorithms

Optimization algorithms are methods designed to find the best solution to a problem by minimizing or maximizing an objective function under given constraints. Two categories are distinguished: local and global.

Local optimization

For convex problems and gradient-based methods, they typically use derivative information to guide the search efficiently.

[50]: Wächter et al. (2006), “On the Implementation of an Interior-Point Filter Line-Search Algorithm for Large-Scale Nonlinear Programming”

[51]: Kolda et al. (2003), “Optimization by Direct Search: New Perspectives on Some Classical and Modern Methods”

- ▶ **Interior Point OPTimizer (IPOPT)** [50] is a numerical optimization algorithm for large-scale NLP problems. It uses a primal-dual interior-point method, solving a sequence of barrier subproblems to handle inequality constraints while maintaining feasibility. At each iteration, IPOPT computes a Newton-type step by solving the sparse Karush-Kuhn-Tucker system, simultaneously updating primal and dual variables. Line search and barrier parameter updates ensure convergence, even for non-convex problems. It is highly efficient with sparse derivative matrices.
- ▶ **Compass search** [51] is a derivative-free local optimization method belonging to the class of direct search algorithms. At each iteration, the algorithm evaluates the objective function by probing in coordinate directions (north, south, east, west in two dimensions, or along each axis in higher dimensions) from the current point. If a trial move in any direction improves the objective, the algorithm accepts the move and continues from the new point; otherwise, the step size is reduced, and the process repeats. It is a slow but sure local optimization algorithm.
This algorithm is illustrated in Figure 3.9 (b).

Gradient-free global optimization

Global optimization: The holy grail!
60% of the time it works every time.

Johan Löfberg
Creator of YALMIP

12: they try to optimize a problem by iteratively trying to improve a candidate solution with regard to a given measure of quality

[52]: Holland (1992), *Adaptation in Natural and Artificial Systems*

[53]: Rechenberg (1989), “Evolution Strategy”

[54]: Schwefel (1981), *Numerical Optimization of Computer Models*

13: Crossover does exist in ES but plays a secondary role compared to GAs

Global gradient-free optimization refers to a family of optimization methods that aim to find the best solution to a problem without relying on gradient information. These methods are especially useful when the objective function is non-differentiable, noisy, discontinuous, or available only through expensive simulations where derivatives are impossible or impractical to compute. Unlike local optimization methods that may get trapped in nearby minima, global approaches search the entire solution space to increase the chances of finding the true global optimum.

Genetic Algorithms (GAs) and Evolutionary Strategies (ESs) are both part of the evolutionary computation family¹², but they emphasize different mechanisms. GAs, introduced by Holland [52], are inspired by biological evolution and work mainly with populations of candidate solutions represented as strings, often binary. They rely heavily on crossover (recombining parts of two solutions) along with mutation and selection, and are frequently applied to discrete or combinatorial problems. In contrast, ES, pioneered by P. Bierent, I. Rechenberg, and H. Schwefel in the 60s [53, 54], were designed for continuous optimization tasks and emphasize mutation as the primary search operator. A defining feature of ES is self-adaptation: not only the solutions but also the mutation parameters (such as step sizes or covariance structures) evolve over time, allowing the algorithm to adjust its own search dynamics¹³.

Genetic Algorithms versus Evolutionary Strategies

An interesting reflection from Francesco Biscani and Dario Izzo [34]:

Approximately during the same decades as Evolutionary Strategies were studied, a different group led by John Holland, and later by his student David Goldberg, introduced and studied an algorithmic framework called “genetic algorithms” that were, essentially, leveraging on the same idea but introducing also crossover as a genetic operator. This led to a few decades of confusion and discussions on what was an evolutionary strategy and what a genetic algorithm and on whether the crossover was a useful operator or mutation only algorithms were to be preferred.

Local versus gradient-free global optimization

When suitable, local optimization algorithms are generally preferable to heuristic approaches, as they typically achieve higher precision with far fewer function evaluations and offer more reliable convergence properties. Heuristic methods, in contrast, often demand significantly larger computational effort and may still fail to reach the desired solution quality. Their use should therefore be limited to situations where gradient information is unavailable or the problem structure prevents the application of more efficient local techniques.

Some of the algorithms presented here can theoretically, for any given finite problem, terminate with a global optimal solution as their parameters enable for a more extensive search. This theoretical result, however, is not particularly helpful, since the time required to ensure a significant probability of success will usually exceed the time required for a complete search of the solution space.

The focus is to try different algorithms and find the best alternative that, given a particular problem, can consistently find good solutions given some computational budget.

The following global optimization algorithms have been used in this research work:

- ▶ **(N+1)-ES Simple Evolutionary Algorithm (SEA)** [34, 53, 54]. Basic evolutionary strategy algorithm, where a population of individuals at each generation produces one offspring by randomly and uniformly mutating its best individual within the given bounds. Should the offspring be better than the worst individual in the population it will substitute it.
- ▶ **Simple Genetic Algorithm (SGA)** [52], [34]. Basic genetic algorithm where a population of individuals evolves through selection, crossover, and mutation. New offspring are generated by combining the genetic material of selected parents, and the population is updated by replacing less fit individuals with the newly created ones.
- ▶ **Covariance Matrix Adaptation Evolution Strategy (CMA-ES)** [55, 56], [34] iteratively samples candidate solutions from a multivariate normal distribution whose parameters are adapted over time. The distribution mean is updated toward successful candidate solutions, while the covariance matrix is incrementally adjusted to increase the likelihood of previously successful search directions, a process that can be interpreted as a natural gradient descent and as an iterated principal component analysis of successful steps. In addition, CMA-ES maintains two evolution paths that track the correlation between consecutive steps: one path accelerates

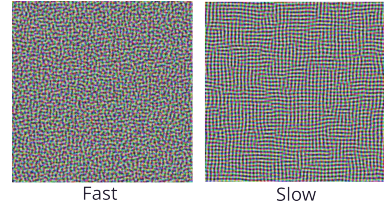


Figure 3.8: Simulated Annealing. Example illustrating the effect of cooling schedule on the performance of simulated annealing. The problem is to rearrange the pixels of an image so as to minimize a certain potential energy function, which causes similar colors to attract at short range and repel at a slightly larger distance. The elementary moves swap two adjacent pixels. These images were obtained with a fast cooling schedule (left) and a slow cooling schedule (right), producing results similar to amorphous and crystalline solids, respectively.

Source: [Wikipedia](#)

[34]: Biscani et al. (2020), “A Parallel Global Multiobjective Framework for Optimization: Pagmo”

[53]: Rechenberg (1989), “Evolution Strategy”

[54]: Schwefel (1981), *Numerical Optimization of Computer Models*

[52]: Holland (1992), *Adaptation in Natural and Artificial Systems*

[55]: Hansen (2006), “The CMA Evolution Strategy”

[56]: Gendreau et al. (2010), *Handbook of Metaheuristics*

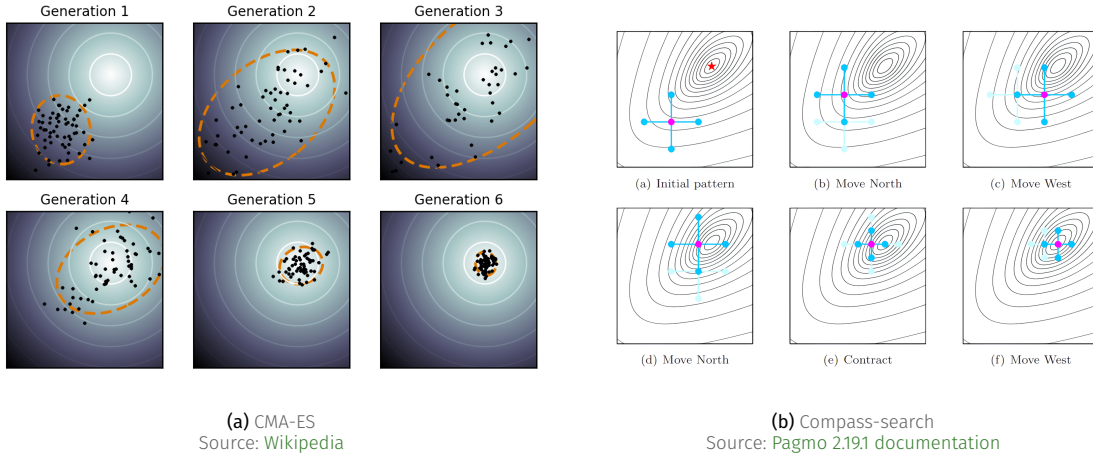


Figure 3.9: Illustration of optimization runs for two algorithms. In CMA-ES (a) it shows the covariance matrix adaptation on a simple two-dimensional problem. The spherical optimization landscape is depicted with solid lines of equal f -values. It shows how the distribution (dotted line) of the population (dots) changes during the optimization. On this simple problem, the population concentrates over the global optimum within a few generations.

the adaptation of the covariance matrix by reinforcing favorable directions, while the other provides a robust mechanism for step-size control. This dynamic adaptation of both the covariance structure and step size allows CMA-ES to balance exploration and exploitation effectively, prevent premature convergence, and achieve fast progress toward optima even in high-dimensional, ill-conditioned, or nonconvex landscapes. The algorithm is illustrated in Figure 3.9 (a).

[57]: Schlüter et al. (2009), "Extended Ant Colony Optimization for Non-Convex Mixed Integer Nonlinear Programming"

[58]: Kennedy et al. (1995), "Particle Swarm Optimization"

[59]: Gad (2022), "Particle Swarm Optimization Algorithm and Its Applications"

[60]: Storn et al. (1997), "Differential Evolution – A Simple and Efficient Heuristic for Global Optimization over Continuous Spaces"

[61]: Brest et al. (2006), "Self-Adapting Control Parameters in Differential Evolution"

[62]: Elsayed et al. (2011), "Differential Evolution with Multiple Strategies for Solving CEC2011 Real-World Numerical Optimization Problems"

► **Extended Ant Colony Optimization (GACO)** [57], [34]. Ant Colony Optimization (ACO) is a class of optimization algorithms inspired by the foraging behavior of ants. Artificial ‘ants’ explore a parameter space representing all possible solutions, recording their positions and solution quality. Similar to real ants laying pheromones to guide others, simulated ants use this information so that future iterations increasingly focus on better solutions. An extended version called Extended ACO [57] generates new solutions using a multi-kernel Gaussian distribution based on pheromone-like values derived from previous solution quality. Solutions are ranked using an oracle penalty method. Extended ACO can handle box-bounded single-objective problems, both constrained and unconstrained, with continuous or integer variables.

► **Particle Swarm Optimization (PSO)** [58, 59], [34] is a population-based, derivative-free optimization algorithm inspired by the collective behavior of bird flocks. Each particle represents a candidate solution and moves through the search space with a velocity influenced by its personal best position and the global or neighborhood best positions. Through iterative updates of positions and velocities, the swarm balances exploration and exploitation to converge toward optimal solutions. The algorithm is illustrated in Figure 3.10.

► **Self-adaptive Differential Evolution (SADE)** [60–62], [34]. In the original differential evolution algorithm [60], at each iteration, new candidate solutions are generated by combining the weighted difference of randomly selected individuals with another individual from the population. This mutation step is followed by crossover to increase diversity, and selection ensures that only the better solutions survive. Many different proposals have been made to self-adapt both the crossover probability and the differential weight parameters of the original differential evolution algorithm. The used optimization library [34] implements two different mechanisms-Brest et al. [61] and Elsayed et al. [62] - together with their

own addition.

- ▶ **Simulated annealing - Corana's version (SA)** [63], [34, 56] is a stochastic, derivative-free optimization algorithm inspired by the annealing process in metallurgy. The defining feature of simulated annealing is its use of a temperature parameter that decreases gradually during the search. The algorithm begins with a high initial temperature, allowing it to explore the search space freely and accept worse solutions with higher probability. As the temperature is reduced according to an annealing schedule specified by the user, the algorithm increasingly focuses on low-energy (or low-cost) regions and eventually behaves like a steepest descent method. This cooling process helps the system move from broad exploration toward fine-grained exploitation. Corana's version of SA introduces coordinate-wise temperature adaptation, where each variable has its own temperature schedule, and the step size is adjusted based on the success rate of previous moves. This allows the algorithm to adaptively balance exploration and exploitation for each dimension, improving convergence on high-dimensional or rugged landscapes. The algorithm is illustrated in Figure 3.8.
- ▶ **(Improved) Harmony Search (IHS)** [64], [34] inspired by the improvisation process of musicians, each musician represents a decision variable where each note corresponds to a value, and the aim is to achieve the best possible harmony –analogous to finding the global optimum. In practice, every member of the population contributes to the search. At each iteration, a new solution is generated and, if it performs better than the worst individual in the population, it replaces it. The number of fitness function evaluations is therefore equal to the number of iterations. An improved version in Biscani et al. [34] of HS introduces dynamic parameters: the probability of reusing values from the decision vector is adjusted linearly, while the mutation rate decreases exponentially over time. These refinements are designed to balance exploration and exploitation more effectively¹⁴.

In this research work the two problems that are going to be presented on each part are non linear and non-convex. One of them also includes constraints. Meta-algorithms enable adapting algorithms that would otherwise be limited to certain types of problems. This is achieved by wrapping them with the so-called meta-algorithm. In this study two meta-algorithms are used:

- ▶ **Monotonic Basin Hopping (MBH)** [34] is an optimization algorithm that combines local search with stochastic exploration. It repeatedly perturbs candidate solutions within a neighborhood and applies a local optimization algorithm to find nearby minima. If the best solution improves, it is updated; otherwise, the search resets. This iterative approach allows the algorithm to escape local minima and efficiently explore the landscape in search of the global optimum.
- ▶ **Self-adaptive fitness formulation for constrained optimization (CSTR-SA)** [48]. The self-adaptive constraint-handling meta-algorithm allows any single-objective unconstrained algorithm to solve constrained problems. It adapts its parameters based on the current population, using a penalty approach that accounts for constraint violations. Each individual is evaluated by both objective value and normalized constraint infeasibility, and the population is evolved using the wrapped algorithm with penalized objectives. The best individuals are reinserted immediately, influencing the next generation, making this approach compatible with non-generational evolutionary algorithms.

[63]: Corana et al. (1987), "Minimizing Multi-modal Functions of Continuous Variables with the "Simulated Annealing" Algorithm—Corrigenda for This Article Is Available Here"

[64]: Geem et al. (2001), "A New Heuristic Optimization Algorithm"

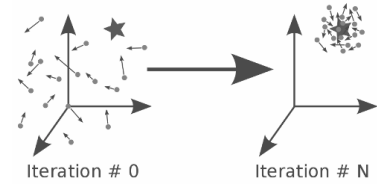


Figure 3.10: Particle Swarm Optimization concept. Each particle adjusts its velocity based on its own experience and that of neighboring particles to explore the search space and converge towards optimal solutions.
Source: Pagmo 2.19.1 documentation

14: While HS has demonstrated competitive results, it has also been criticized for its metaphor: the musical analogy adds little explanatory value and may obscure the algorithm's mechanics, which in essence resemble those of ESs or GAs, relying on concepts such as mutation and crossover.

[48]: Farmani et al. (2003), "Self-Adaptive Fitness Formulation for Constrained Optimization"

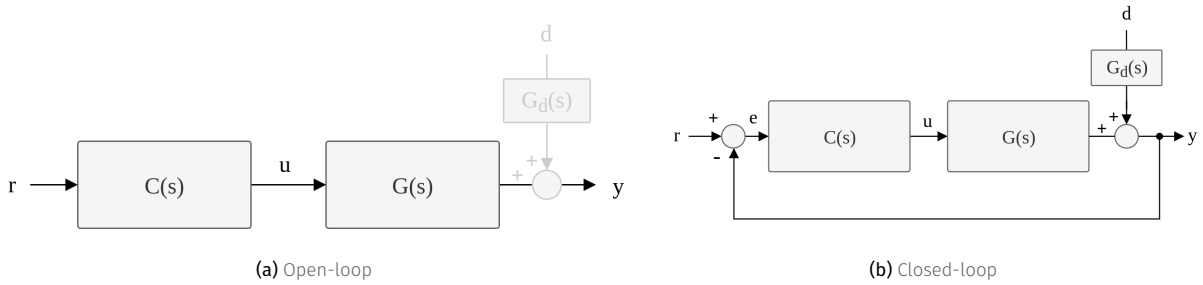


Figure 3.11: Control diagrams

3.3 Control

Controllers are mechanisms that allow us to manipulate the behavior of a system. While modeling and simulation provide a way to passively describe and predict how a system evolves, controllers take the next step by actively influencing the system in order to promote a desired behavior. In this way, controllers are fundamental to turning a passive system description into an autonomous system capable of regulating itself and achieving specific goals.

The general workflow of control engineering is: start with a dynamical system of interest, develop a mathematical model that captures its essential behavior, and then design a control policy that drives the system toward the desired performance. Depending on how this is achieved, different types of control strategies can be distinguished:

- ▶ Passive control: The desired behavior is embedded into the design of the system itself, without requiring active intervention. For example, designing a building with proper thermal insulation ensures it maintains stable indoor temperatures without external control actions.
 - ▶ Active control: The controller actively supplies energy or signals to the system in order to adjust its behavior. Active control can be further classified into:
 - Open-loop control: A sequence of control actions (or a predefined trajectory) is computed in advance and applied to the system without measuring its actual response. This approach is simple but fragile, since it assumes the system will behave exactly as predicted.
 - **Closed-loop (feedback) control:** The controller continuously measures the outputs of the system and adjusts its actions based on the observed behavior. This feedback mechanism allows the system to autonomously correct deviations and respond to changes in real time.

Feedback control, in particular, offers several fundamental advantages over open-loop strategies:

- ▶ Robustness to uncertainty: Real systems are never perfectly known –models are approximations, and parameters may vary. Feedback allows the controller to adapt its actions on the fly, reducing the impact of modeling errors.
 - ▶ Rejection of disturbances: External disturbances, whether measurable or not, can affect the system output. Feedback enables the controller to partially or fully counteract these disturbances.
 - ▶ Stability enhancement: A system that is unstable when uncontrolled (open-loop) can often be stabilized through properly designed feedback, ensuring safe and predictable behavior.

In short, control theory provides a framework that transforms dynamical systems from passive entities into actively regulated, autonomous ones. Through feedback, controllers achieve robustness, disturbance rejection, and stability.

3.3.1 PID controllers

A PID controller is one of the most widely used feedback control strategies in engineering¹⁵ because it combines three complementary mechanisms that work together to regulate a system effectively [66]. The proportional term (P) generates a control action directly proportional to the instantaneous error $e(t)$, which is the difference between the desired setpoint and the actual process variable; this provides an immediate response that reduces deviations. However, proportional action alone often leaves a steady-state error, which is corrected by the integral term (I). By integrating the error over time, the integral term accumulates past deviations and adjusts the control signal until the steady-state error is eliminated, ensuring that the system output eventually matches the setpoint exactly. While proportional and integral actions ensure responsiveness and accuracy, they may lead to sluggishness or overshoot if the system changes rapidly. To address this, the derivative term (D) predicts future behavior by considering the rate of change of the error, effectively damping oscillations and improving stability by anticipating trends before they cause large deviations. Together, these three terms balance immediate reaction, long-term correction, and predictive adjustment, resulting in the general PID control law¹⁶:

$$u(t) = K \left(e(t) + \frac{1}{T_i} \int_0^t e(t) dt + T_d \frac{de(t)}{dt} \right), \quad (3.3)$$

where K is the proportional gain, T_i the integral time, and T_d the derivative time. By tuning these parameters appropriately, the PID controller can be adapted to a wide variety of dynamic systems, offering both robustness and simplicity, which explains its success and popularity in industrial and scientific applications. PI controllers are sufficient for many control problems, particularly when process dynamics are benign and the performance requirements are modest. This is the case of the processes of this research work. However, some enhancements can be applied to extend the basic PID scheme:

- ▶ **Anti-windup on the integral action:** prevents the integrator from accumulating error when the actuator saturates, avoiding overshoot and slow recovery once the control signal returns within bounds.
- ▶ **Feedforward:** improves disturbance rejection and setpoint tracking by adding a direct control action based on measurable inputs or known process dynamics, reducing the burden on the feedback loop.
- ▶ **Gain scheduling:** adapts controller parameters to changing operating conditions, maintaining performance and stability across a wide range of process regimes. It compensates for nonlinearities and varying dynamics by switching or interpolating between different sets of controller gains based on the current operating point or system state.

3.4 Hierarchical control: how optimization and control come together

Ideally, a centralized solution would handle both low-level process control tasks and higher-level resource management and distribution optimization. However, this is rarely the case. For instance, planning the optimal distribution of resources on a monthly basis may require solving a complex optimization problem,

¹⁵: Honorable mention here to MPC control, not used in this research work but widely used in the industry for complex and effective process control, it shares many similarities to the optimization just described above and the reader is referred to Camacho et al. [65]

¹⁶: Hägglund et al. (2006), *Advanced PID Control*

16: In ideal form, other representations exist like the parallel representation

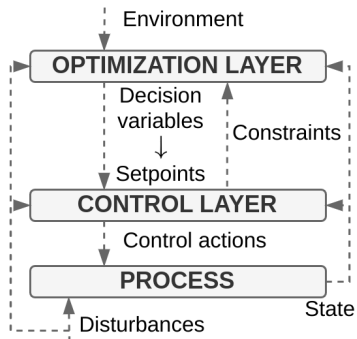


Figure 3.12: Hierarchical control architecture

[67]: Scattolini (2009), “Architectures for Distributed and Hierarchical Model Predictive Control – A Review”

17: depends on the particular problem, they can get very complex too

often with a combinatorial component. Such optimization is computationally expensive, so it is typically addressed using simplified process models with long sampling periods, and the computation of new decisions is performed only occasionally.

In contrast, low-level process control requires frequent updates of control actions that must be computed quickly. A single centralized system attempting to address both high- and low-level problems would therefore face major challenges. Moreover, in large-scale systems, any failure of this centralized solution could compromise many—often critical—processes. For these reasons, decentralized and distributed approaches are often preferred.

In such approaches, complexity is divided among different agents (or layers). Each agent has a limited, problem-specific set of responsibilities. Various architectures exist for managing the information exchange between these agents. Summarizing, the factors that justify the need of a decentralized solution are [67]:

- ▶ Different time scales between low- (in the order of seconds) and high-level (in the order of hours) layers
- ▶ Different dynamic behavior: usually fast for regulatory control, slow or static for upper layers.
- ▶ Different computing requirements: complex resource optimization compared to generally more straightforward process control¹⁷
- ▶ Decoupling between optimization and critical process control

In this research work, a hierarchical two-layer control architecture is adopted as visualized in Figure 3.12. At the upper layer, a Real-Time Optimization (RTO) determines the optimal operating conditions with respect to an economic performance metric, using a detailed but pseudo-dynamic nonlinear physical model of the system. The lower layer relies on a simpler linear dynamic model, often derived through identification experiments, to design regulators such as MPC or PID controllers that ensure the RTO targets are met, while also providing bottom-up feedback on constraints and performance. Although the RTO model is inherently static, it should be periodically updated through reconciliation procedures to account for slow disturbances. Consistency must be maintained between the models used in the upper and lower control layers, and the steady-state optimization should ensure that the computed input and output references are both feasible and as close as possible to the desired setpoints [67].

Part I

OPTIMAL WATER AND ELECTRICITY MANAGEMENT IN A COMBINED COOLING SYSTEM

Of all humanity's instruments, the most wondrous, no doubt, is the book. The other instruments are extensions of his body. The microscope, the telescope, are extensions of his sight; the telephone is the extension of his voice; then we have the plow and the sword, extensions of the arm. But the book is something else altogether: the book is an extension of memory and imagination.

//

De los diversos instrumentos del hombre, el más asombroso es, sin duda, el libro. Los demás son extensiones de su cuerpo. El microscopio, el telescopio, son extensiones de su vista; el teléfono es extensión de la voz; luego tenemos el arado y la espada, extensiones de su brazo. Pero el libro es otra cosa: el libro es una extensión de la memoria y de la imaginación.

Jorge Luis Borges

TL;DR

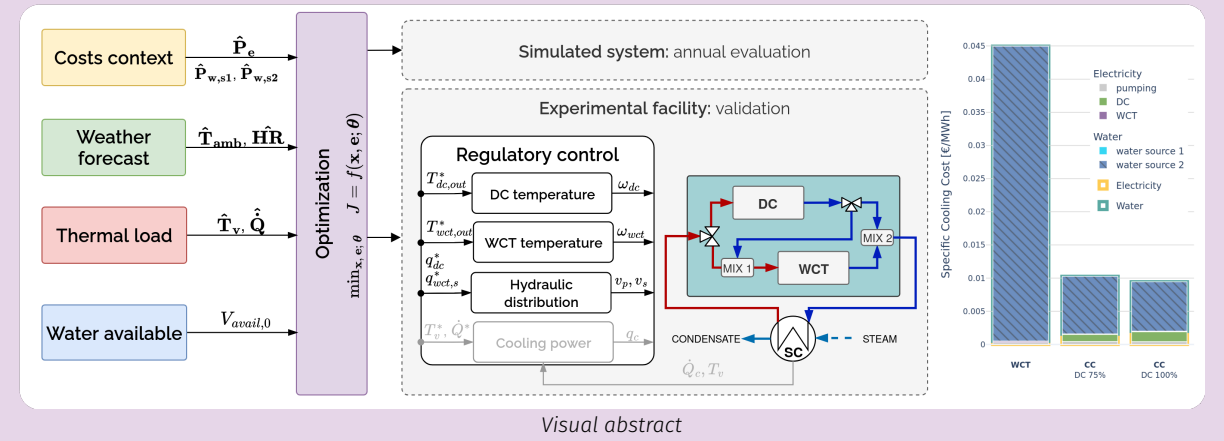
This part of the thesis addresses the challenge of reducing water consumption in Concentrated Solar Power (CSP) plants through a hybrid cooling concept combining dry and wet technologies. The broader context of concentrated solar thermal power and its dependence on water resources is introduced, motivating more water-efficient cooling solutions. An experimental Combined Cooler (CC) pilot plant at Plataforma Solar de Almería (PSA) is then presented, comprising a Wet Cooling Tower (WCT) and a Dry Cooler (DC) integrated with a surface condenser in a flexible-hydraulic circuit.

A steady-state modelling framework is developed for the main components of the combined cooler. Two complementary strategies are considered: physics-based first-principles models with broad applicability, and several data-driven approaches (artificial neural networks, Random Forest, Gradient Boosting, and Gaussian Process Regression). To combine the generality of physical models with the speed of data-driven surrogates, Gaussian Process models are trained on synthetic data generated by first-principles simulations. This yields fast, scalable surrogate models with high predictive accuracy, achieving mean absolute errors below 0.97 °C for key temperatures and 19.4 L/h for water consumption when validated against 24 experimental tests over a wide operating range.

Building on this framework, a two-stage multi-objective optimization strategy is proposed to minimize daily cooling cost—electricity and water—under limited water availability while ensuring the required cooling duty. At each time step, a multi-objective problem generates a Pareto front between cost and water use; a second-stage optimization selects an optimal path across the horizon. Pilot-plant validation shows very good agreement between optimized and measured operation. The results highlight the strong sensitivity of dry cooling to ambient temperature, the wet cooler's compensating role when dry cooling reaches its limits, and the systematic prioritization of water savings, including periods of dry-only or series operation. Tests also show that the optimized strategies remain valid for extended quasi-steady periods, and that upper-layer predictions can support low-level control (e.g. feed-forward actions), improving robustness when re-optimization is delayed.

The methodology is then applied to a case study of a commercial 50 MW_e CSP plant with 8 h of storage (Andasol-II, southern Spain). Three cooling configurations are compared under a water-scarcity scenario using annual simulations: the existing wet-only WCT, and two CC variants with dry-cooler capacities of 75 % and 100 % of the nominal wet load. For each configuration, operation is optimized using the proposed framework. The combined-cooler options reduce specific cooling costs by up to 80 % and annual water consumption by about 48 %, with 38 % savings during the driest and hottest months. These gains stem mainly from reduced reliance on expensive alternative water sources. The CC configurations also show more stable and predictable annual costs than the water-sensitive wet-only reference.

The analysis underscores the importance of evaluating cooling concepts over representative annual conditions rather than relying on aggregated averages, and confirms that water availability can become the dominant constraint and cost driver, especially where alternative sources are costly. Although no strategy can fully resolve the mismatch between peak cooling demand and water scarcity in hot-dry seasons, the results demonstrate substantial potential for improved water management through optimized hybrid-cooling operation. The proposed framework is generic and adaptable to other plant designs, locations, and resource scenarios, supporting informed decisions for more sustainable CSP plants.



Part structure

This part is structured as follows: first in Chapter 4 (Solar thermal energy and water) a context of concentrated solar thermal technologies is provided and their relationship with the water resource, specifically for the case of CSP. Then, the experimental Combined Cooling System (CCS) pilot at PSA is presented in Chapter 5. The methodology for modelling and optimizing the operation of the system are described in Chapter 6 and Chapter 7, respectively. The validation with experimental data is shown in Chapter 8. Finally, Chapter 9, describes and analyzes the results of the annual simulations performed for a commercial CSP plant, Andasol-II, using the proposed cooling system.

Solar thermal energy and water

TL;DR

In the pursuit of eliminating reliance on fossil fuels sources for energy generation and replacing them by renewable sources, Concentrated Solar Power (CSP) has proven to be a reliable contributor. In particular, in providing much needed energy storage, dispatchability and ensuring grid stability.

However, water availability emerges not only as a technical constraint but also as a planning and policy issue. CSP deployment in water-stressed regions is strongly dependent on innovative cooling solutions, policy incentives, and careful water resource management to ensure sustainable operation without compromising water security for local communities.

Ideally, negligible raw water would be needed to operate a CSP plant and it should be achieved with no increase in the Levelized Cost of Electricity (LCOE). The most water demanding component is the cooling of the power block, and currently this water saving can be achieved with dry cooling and an increase of 7% in the LCOE. A compromise solution can be reached by using hybrid cooling solutions together with water preservation strategies. Further savings can be achieved by optimizing the operation of the hybrid cooler and take full advantage of its flexibility towards optimal resource management.

4.1 Concentrated solar thermal	35
4.1.1 CSP: Concentrated Solar Power	36
4.1.2 A brief history of CSP: from the hype to unrealized potential	37
4.2 Cooling and water use	38
4.2.1 Conventional condenser cooling technologies	39
4.2.2 Non-conventional cooling: Combined / hybrid cooling	42
4.2.3 Cooling technology selection	45

4.1 Concentrated solar thermal

Concentrated Solar Thermal (CST) technologies use heliostats or mirrors to reflect and concentrate solar radiation onto a receiver. There, the radiation is captured as heat, also known as thermal energy. They can be classified in different ways¹, using temperature, two broad groups can be identified.

The first group includes lower-temperature systems operating below 400 °C. These are typically used for applications such as power generation, district heating, cooling, and desalination. It is worth noting that most industrial heat demand lies within this relatively low-temperature range of 100–400 °C [68]. This segment of CST is also the most technically mature. Over the past decades, considerable progress has been made in line-focus technologies such as parabolic

1: With some parameters being correlated; for example, higher operating temperatures generally mean higher concentration factors

[68]: Schoeneberger et al. (2020), “Solar for Industrial Process Heat”



(a) Parabolic trough pilot plant at PSA



(b) Gemasolar 20MW_e-15h central tower CSP plant in Sevilla, Spain.
Source: Wikipedia

Figure 4.1: Two main Concentrated Solar Thermal (CST) technologies. In (a) collector rows positioned facing each other for cinematographic purposes

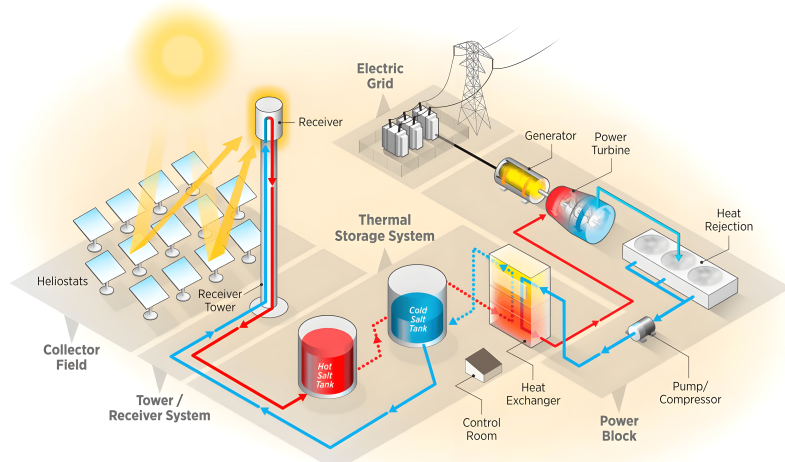


Figure 4.2: Solar tower CSP plant. Source: NREL [72]

2: Flat-plate collectors, though non-concentrating also deserve mention here, as they remain the most widely deployed solar thermal technology [69]

[70]: Thonig et al. (2023), "Concentrating Solar Technology Policy Should Encourage High Temperatures and Modularity to Enable Spillovers"

[71]: Mehos et al. (2020), "Concentrating Solar Power Best Practices Study"

3: In the context of the industrial life-cycle (ILC) [76], the formative phase considers the period in which a technology and its industry and innovation system are still immature and need to grow and develop

[73]: Pfenninger et al. (2014), "Potential for Concentrating Solar Power to Provide Baseload and Dispatchable Power"

[74]: Binz et al. (2017), "Toward Technology-Sensitive Catching-Up Policies"

[75]: Lilliestam et al. (2021), "The Near- to Mid-Term Outlook for Concentrating Solar Power: Mostly Cloudy, Chance of Sun"

[77]: Mir Artigues et al. (2019), *The Economics and Policy of Concentrating Solar Power Generation*

troughs (see Figure 4.1 (a)) and linear Fresnel collectors². Although these systems have reached a high level of development, their potential for significant further cost reduction is relatively limited.

The second group comprises high-temperature systems operating above 600 °C. These rely on point-focus technologies, most notably central receiver systems similar to the one shown in Figure 4.1 (b). They can reliably operate below 600 °C but above —and using a Brayton cycle— are still under development. They show promising potential for higher-value applications, including solar-driven chemical processes (such as aviation fuel production) and the provision of high-grade industrial heat in sectors like cement manufacturing [70]. Central receiver technology, however, remains at an earlier stage of commercial maturity. Fewer plants have been built, and many existing installations employ a mix of technical approaches [71].

4.1.1 CSP: Concentrated Solar Power

In a concentrated solar power plant, power is generated with a power-cycles such as Rankine or Brayton. The principle of operation is very similar to conventional thermal power plant, however, the working fluid is heated up not by combusting/burning a fossil fuel, but as mentioned, by concentrating solar energy as shown in Figure 4.2.

By coupling CSP with thermal storage —Figure 4.2 - *Thermal Storage System*—electricity can be generated after sundown or even days later, for example during adverse weather periods. Because of this ability, CSP is one of the few renewable electricity technologies that can generate fully dispatchable or fully baseload power at very large scale [73]. Finally, the exhaust steam from the turbine —Figure 4.2 - *Power block*— is directed to a condenser, where its latent heat of vaporization is transferred to the available cooling medium.

CSP is an engineering-heavy, complex technology, with each project being different and tailored to both the environment in which it stands and the requirements of each single offtaker [74]. This means, that despite its relative long history, is still in its formative phase [75]³. As CSP is not yet competitive with other new generation, and especially not with operating and depreciated generators, it requires policy support to be economically viable [77]. This is due to its irregular historical development.

4.1.2 A brief history of CSP: from the hype to unrealized potential

At one point, CSP was seen as the leading alternative for large-scale solar energy. Ambitious visions and bold initiatives—such as the Desertec project—played a key role in generating immediate excitement around the technology [78]. However, the political consequences of raising expectations that were ultimately unmet proved significant. In Europe, this disillusionment contributed to CSP becoming politically sidelined for many years [78]. Additionally, around 2010–2012 the cost crossover with Photovoltaic (PV) occurred and from there the PV cost advantage only increased [79]. Many investments shifted from CSP to the more straightforward and profitable PV technology.

The development of CSP has been marked by alternating periods of rapid expansion and sharp decline, largely shaped by national policy support. In the 1980s, California's incentives led to the construction of nine CSP plants totaling around 350 MW_e, but the withdrawal of support caused the bankruptcy of the main developer of solar thermal electric projects, *Luz*, in 1991, resulting in a 15-year global pause in new projects. A second growth phase began in 2007 with feed-in tariffs in Spain and temporary backing in the US, leading to the construction of about 50 plants, mostly supplied by Spanish and German companies. However, the end of policy support in both countries around 2013 led to a sharp slowdown, with construction activity in 2016 at just one-third the 2012 level, and many firms exiting the sector. CSP remained commercially active mainly through projects in Morocco and South Africa, although costs increased and future prospects dimmed. Momentum returned in 2016 when China introduced a new feed-in tariff aimed at 5 GW_e of capacity, sparking renewed global interest. Optimism was further strengthened by major projects launched in Dubai and Morocco in 2018–2019. The near- to mid-term outlook for CSP is very uncertain but there are several positive developments concerning the global value chain and cost development. The market and policy outlook is bleak with the risk of a complete loss in many markets for CSP [75].

Setting realistic targets may ultimately be more effective than raising expectations that cannot be met. CSP remains a valuable technology for the energy transition—though likely at a smaller scale than initially envisioned, and over a longer timeframe. Several studies highlight its potential role in a zero-carbon or near zero power system [80]. For instance, the International Energy Agency (IEA)'s Net Zero by 2050 report projects that the global CSP capacity should reach 73 GW_e by 2030 and 281 GW_e by 2040 [81]. Likewise, International Renewable Energy Agency (IRENA) envisions several hundred gigawatts of CSP by 2050, contributing to grid stability alongside a projected 8500 GW_e of solar PV and 6000 GW_e of wind capacity [82]. These projections suggest that CSP can play a complementary role to PV and wind by providing dispatchable, on-demand renewable electricity—further enabling intermittent renewable alternatives. However, even at these more modest levels, CSP deployment would need to accelerate rapidly (see Figure 4.3 (a)). To meet the IEA's 2030 target, the global CSP fleet—standing at just 6 GW_e in 2021—would need to expand more than tenfold in under a decade [83]. So far this is not happening, CSP technology remains niche with only 7 plants coming online in the 2020–2023 period [79] and is unlikely to become a globally important contributor to power system balancing in the next decade [83]. However, things might be changing: 4 new plants came online in 2024, the costs of new CSP stations have decreased rapidly in the last years, 77 % from 2010 to 2024, including a 46 % reduction from 2023 to 2024 (see Figure 4.3 (b)). In terms of LCOE, it means that CSP has improved from 0.402 \$₂₀₂₄/kWh to below 10 cents (0.092 \$₂₀₂₄/kWh) making it competitive with new fossil fuel power stations [79] and the Chinese CSP project pipeline includes 37 future and ongoing projects, with a total capacity of 4.8 GW_e [84].

[78]: Schmitt (2018), "Why Did Desertec Fail?"

[79]: IRENA (2025), *Renewable Power Generation Costs in 2024*

[75]: Lilliestam et al. (2021), "The Near- to Mid-Term Outlook for Concentrating Solar Power: Mostly Cloudy, Chance of Sun"

[80]: Bonilla et al. (2022), "Feasibility and Practical Limits of Full Decarbonization of the Electricity Market with Renewable Energy"

[81]: IEA (2021), "Net Zero by 2050 - A Roadmap for the Global Energy Sector"

[82]: IRENA (2024), "World Energy Transitions Outlook 2024: 1.5°C Pathway"

[83]: Lilliestam et al. (2023), "Scaling up CSP"

[79]: IRENA (2025), *Renewable Power Generation Costs in 2024*

[84]: Alliance (2024), *Blue Book of China's Concentrating Solar Power Industry 2024*

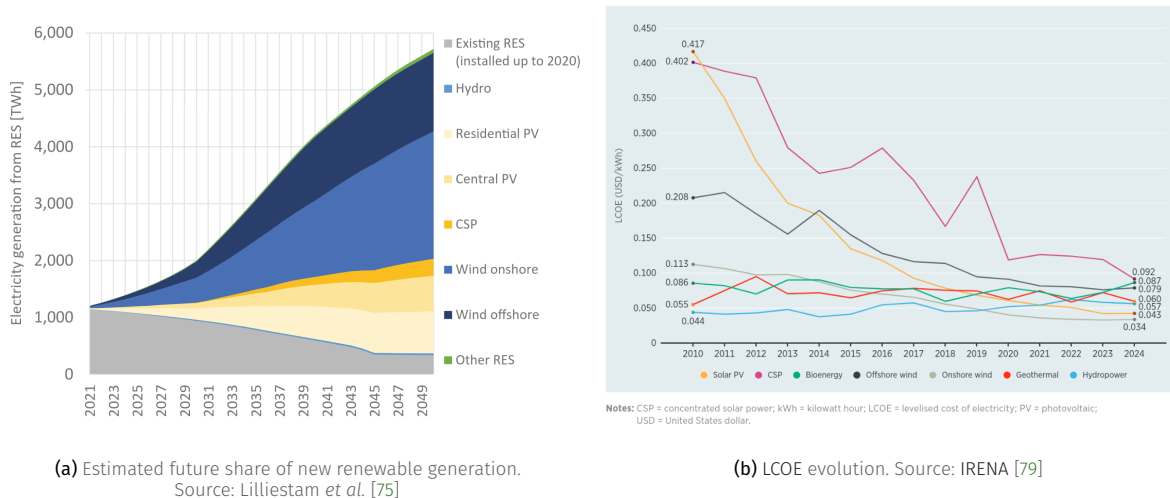


Figure 4.3: LCOE evolution and capacity predictions for different renewable technologies. Share is dominated by variable renewable energies and CSP is the fifth largest contributor, serving as a “gap filler” for the system flexibility of the EU electricity system [85]

4.2 Cooling and water use

The successful deployment of CSP plants depends on several key factors: high annual direct normal irradiance, adequate land availability, and sufficient water resources. However, while the first two are typically found in arid regions as shown in Figure 4.5, the availability of water is often limited. In such locations, the source of raw water is usually restricted to groundwater or limited surface water bodies such as rivers, lakes, wells, or artificial reservoirs.

A CSP plant consumes water for various purposes, with the most significant demand coming from the cooling of the power block⁴. The power output and efficiency of a thermal power plant are strongly influenced by the operating temperature and pressure conditions at the condenser, which are directly linked to the turbine backpressure, and in turn to the cooling system.

In addition to cooling, water is also required for other plant operations, including [24]:

- ▶ Mirror cleaning (1.3 % of total water consumption)
- ▶ Boiler blowdown (1.4 %)
- ▶ Miscellaneous uses, auxiliary equipment cooling, and general infrastructure and staff needs.

In wet-cooled CSP plants, cooling water accounts for over 95 % of the total water consumption, which can be further broken down into evaporation: 77.8 % and blowdown and drift: 19.1 % [24].

Although CSP plants share a similar power cycle with other thermal power technologies, their water consumption patterns differ (see Figure 4.4). This is due to their unique capacity factor, operating schedule, and particularly their strong dependency on weather conditions, which contrasts with the more stable operation of fossil-fired plants. Conventional thermal power plants (e.g. coal, gas, or nuclear) are often sited near reliable freshwater sources, such as rivers or lakes, allowing them to utilize wet cooling without severe resource constraints. These plants are not tied to solar availability and can prioritize water access in their location decisions. CSP plants, however, must prioritize solar access and land availability and thus have less flexibility in selecting sites with abundant water.

4: When wet cooling is used, further explained in the following

[24]: Rohani et al. (2021), “Optimization of Water Management Plans for CSP Plants through Simulation of Water Consumption and Cost of Treatment Based on Operational Data”

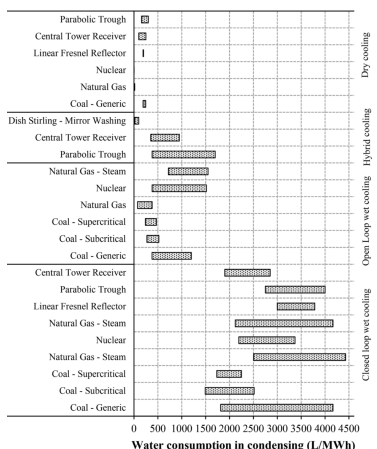


Figure 4.4: Water consumption comparison between CSP and other thermal power generation technologies.

Source: Aseri et al. [86]

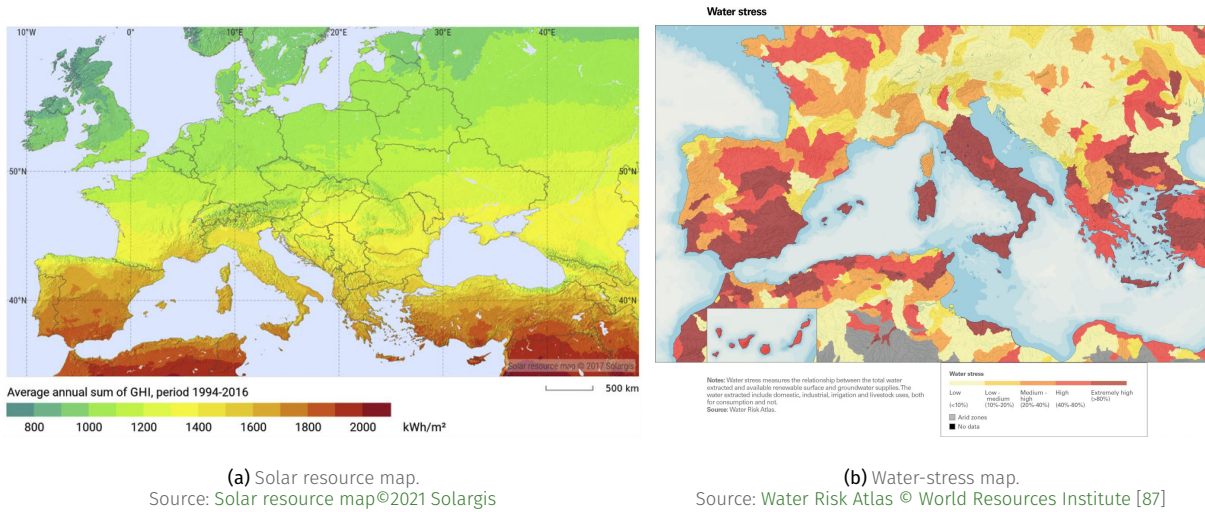


Figure 4.5: Greater potential for solar-powered processes takes place in water-scarce regions

4.2.1 Conventional condenser cooling technologies

To date, the conventional systems used to remove excess heat from CSP plants are either wet (water-cooled) or dry (air-cooled), each with distinct characteristics and trade-offs regarding water usage, thermal performance, and cost.

Reminder: Cooling thermodynamic concepts

- ▶ The *cooling range* refers to the temperature drop experienced by the cooling water as it circulates through the condenser. The greater the better.
- ▶ The *approach* of the cooler is the temperature difference between the cooler outlet and the lowest attainable cooling medium temperature, which varies depending on the cooling technology used.
- ▶ The Initial Temperature Difference (ITD) is the temperature difference between the hot fluid entering the cooler and the reference sink (e.g., dry-bulb temperature) at the cooler inlet.
- ▶ Terminal Temperature Difference (TTD) represents the difference between the outlet temperatures of the cooling and the cooled fluids.

Wet cooling

Water has traditionally been used as the cooling medium in wet cooling technology due to its high heat capacity and the possibility of reuse. In power plants, the steam exiting the turbine is condensed in a surface condenser, where cooling water circulates through tubes and absorbs the latent heat of the steam. The warmed cooling water is then returned to the cooling system for heat rejection, in closed-loop systems, or returned to the body of water in open-loop (*i.e.* once-through) systems. In CSP plants, closed-loop systems are predominantly used and analyzed in the remaining text.

Wet cooling towers function as heat rejection devices by bringing warm water from the condenser into direct contact with air. As part of the water evaporates, it absorbs heat from the remaining liquid, thereby lowering its temperature. The cooled water is then recirculated back to the condenser, completing the loop.

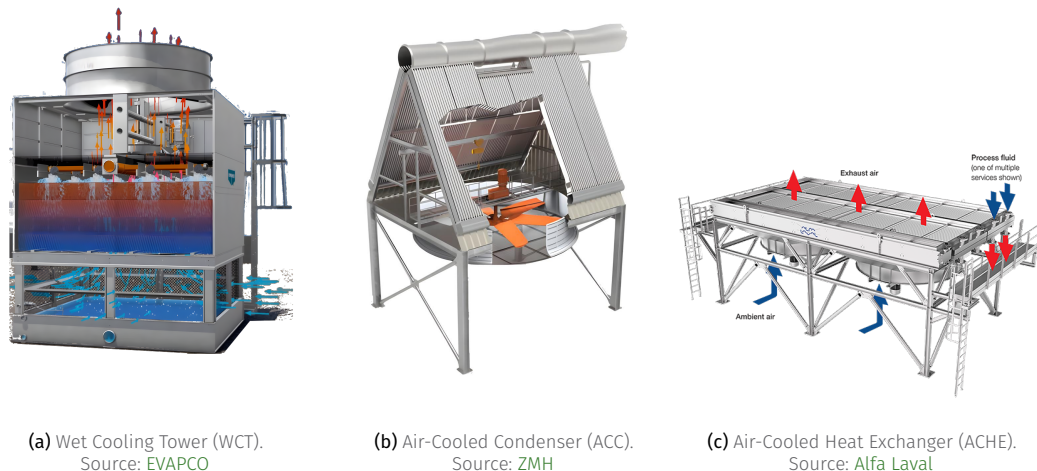


Figure 4.6: Conventional cooling technologies

[88]: Meldrum et al. (2013), "Life Cycle Water Use for Electricity Generation"

[89]: Colmenar-Santos et al. (2014), "Water Consumption in Solar Parabolic Trough Plants"

This process is highly efficient, but it also leads to water losses from evaporation, drift, and blowdown.

Wet cooling technology requires a substantial amount of water (1.8–4 l/kWh) for condenser cooling since heat is rejected to the atmosphere through evaporative cooling [88]. While a small share of heat is removed through sensible air-to-water heat transfer, 80–90 % of the cooling is achieved through the latent heat of vaporization [89].

Land availability for cooling systems is often constrained, particularly in central receiver plants where the solar field surrounds the receiver and requires unobstructed space for heliostat placement. For this reason, compact wet cooling designs using forced-draft towers are predominantly employed, such as the example shown in Figure 4.6 (a).

CSP plants next to the sea, why not?

Building CSP plants near the sea is generally not recommended. Although seawater could serve as an unlimited resource for once-through steam condensation, solar radiation is typically lower in coastal areas, land prices are higher, and the salty environment accelerates corrosion, which can significantly reduce optical efficiency. However, if a suitable site is

found and feasible mitigation measures are implemented, CSP with seawater cooling or CSP+D(esalination) plants could be a viable option [93]

Wet cooling main characteristics

- ▶ Water consumption: 1.8–4 l/kWh [88]
- ▶ Parasitic load: $\approx 0.0165 \text{ kW/KWh}$ or 0.165 % average annual consumption [90].
- ▶ Wet cooling consumes similar power along the year but increases its water consumption in the hotter months [20].
- ▶ CSP plants with wet cooling towers consume as much as $1.7 \times 10^6 \text{ m}^3$ per year of operation [24].
- ▶ Greater available approach, since the lowest attainable temperature is the wet-bulb temperature.
- ▶ 55 % of CSP plants worldwide make use of wet cooling technology for condenser cooling [91, 92]

Dry cooling

In dry cooling, heat is rejected to the surroundings by convection via extended or finned surfaces or tubes arranged in a row, and each row consists of numerous cells [94]. In this type of cooling, the warm water and the ambient air do not have direct contact with each other (as in wet cooling). Because air is a poor

[94]: Turchi (2010), *Parabolic Trough Reference Plant for Cost Modeling with the Solar Advisor Model (SAM)*

heat transfer medium, the condenser must operate at a higher temperature and pressure to drive heat out efficiently. This sensitivity to ambient air temperature leads to elevated turbine back-pressure, specially during hot weather, reducing thermal efficiency and power output compared to wet cooling systems. Dry cooling systems can be broadly categorized as direct or indirect [95].

In direct systems, turbine exhaust steam is delivered straight to an Air-Cooled Condenser (ACC) (see Figure 4.6 (b)), where heat rejection to the environment occurs in a single step. The steam is condensed inside finned tubes by ambient air blown across the exterior finned surfaces arranged in A-frame (forced draft) or delta (induced draft) configuration. This process relies on latent heat transfer and can employ either mechanical or natural draft designs. ACCs have been used for nearly 70 years, and were pioneered in regions as diverse as Western Europe, South Africa and the Middle East. The largest ACC units in operation is in South Africa (Medupi) with six fossil-fuel driven 800 MW_e units on ACCs [96].

In indirect systems, steam first condenses in a separate condenser, which may be either a conventional shell-and-tube surface condenser or a barometric condenser⁵ (direct-contact type), where steam meets a spray of cooling water. The resulting warm cooling water is then circulated to an Air-Cooled Heat Exchanger (ACHE) (see Figure 4.6 (c)) for final heat rejection to the atmosphere. This arrangement introduces an additional heat exchange stage, so the Air-Cooled Heat Exchanger (ACHE) handles only sensible heat transfer, requiring greater heat exchange surface area but being less sensitive to fluctuations in ambient temperature.

A prominent example of an indirect dry cooling configuration is the Heller system, named after its inventor Prof. H. Heller in Hungary in the 1940's [97, 98]. In the direct-contact Heller system, steam from the turbine condenses in a barometric condenser, and the resulting warm cooling water is cooled in an ACHE before recirculation. Thermal performance is generally comparable to that of an ACC, but mechanically driven Heller systems tend to have higher specific electrical consumption because, in addition to fan power, extra pumping power is required to overcome the jet condenser's added pressure drop [99].

If an indirect-contact surface condenser is used instead of a barometric condenser, the setup is generally less efficient than both ACCs and the direct-contact condenser Heller configuration because it introduces a Terminal Temperature Difference (TTD) (TTD ≈ 3–4 °C versus ≈ 0.3 °C for barometric condenser), resulting in lower overall cycle efficiency.

There remains challenges with natural draft dry cooling towers compatibility with CSP. For example, in central receiver systems, their significant size (> 70 m tall, > 60 m) would obstruct the heliostat field. A possible alternative is fan-assisted natural draft systems, which reduce tower height while retaining some benefits of natural draft operation [100]. Heller systems have been operating for decades in 17 power plants including the largest indirect dry cooled combined cycle power plant with 3x777 MW_e dry towers at Gebze-Adapazari combined cycle (Turkey) [100].

Unlike wet cooled plants, the dry cooled plants require minimal waterside infrastructure and other related components. None dedicated to the cooling such as water supply network, evaporation ponds, storage ponds, biological cooling water treatment. As a consequence, for the dry-cooled plants, capital and operation and maintenance costs of these components are negligible [96].

However, a recent review on condenser cooling technologies [86] shows that a dry-cooled Parabolic Trough (PT) based plant would deliver 3–10% less annual electricity output and would cost 4 % to 10 % more than a wet-cooled plant resulting in 2 % to 19 % increase in LCOE. It was also observed that due to large differences in operating temperature of power cycle (560 °C for Solar Tower (ST) based plants and 391 °C for PT based plants), the reduction in net electricity

[95]: Maulbetsch (2004), *Comparison of Alternate Cooling Technologies for U.S. Power Plants: Economic, Environmental, and Other Tradeoffs*

[96]: Maulbetsch (2012), *Economic Evaluation of Alternative Cooling Technologies*

⁵: Also known as jet condenser or contact condenser.

[97]: Jászay (1958), "Indudustrial Review-Aus Der Industrie. The Air-Cooled Condensing Equipment" System Heller" a Comprehensive Survey"

[98]: Balogh et al. (2006), "Heller's Indirect Approach Widens Applicability of Dry Cooling"

[99]: Mil'man et al. (2020), "Air-Cooled Condensing Units in Thermal Engineering (Review)"

[100]: Andras et al. (2005), "Advanced Heller System Technical Characteristics"

[86]: Aseri et al. (2022), "Condenser Cooling Technologies for Concentrating Solar Power Plants"

[95]: Maulbetsch (2004), *Comparison of Alternate Cooling Technologies for U.S. Power Plants: Economic, Environmental, and Other Tradeoffs*

output for ST based plants is less as compared to PT based plants (Sau et al., 2016). It should be noted that many of these analysis were made for first generation CSP with no thermal storage, which is an outdated technology. The inclusion of thermal energy storage in the dry or hybrid cooling plant (six hours of storage capacity) can reduce the overall penalty of LCOE considerably: 8.1% to 6.3% for dry-cooled as compared to wet-cooled plants [86]. According to Maulbetsch et al. [95], the *breakeven* water cost at which wet and dry cooling have the same annual costs (for situations in which the rest of the base case values and assumptions apply) is between 2.00 and 3.00 USD₂₀₀₂/kgal.

Dry cooling main characteristics

- ▶ Capital cost ratio ranges from 4.5 times at a hot, arid site to about 3.5 times at more moderate weather [95].
- ▶ Electrical consumption: 1.5 to 5 times wet cooling, 0.05–0.06 kWe/kWh
- ▶ Penalty up to 25% during the hottest hour of the year [95] and 5–6% average annual parasitic consumption [21, 86, 101].
- ▶ Limited approach, constrained by the dry-bulb temperature, worsened if an indirect contact surface condenser is used.
- ▶ 24% of commercial CSP plants make use of this technology [91, 92].
- ▶ Most new plants expected to be built in the next years will make use of dry cooling [84].

NOTE: Comparisons are made relative to wet cooling

[22]: Wiles et al. (1978), *Description and Cost Analysis of a Deluge Dry/Wet Cooling System*.

[23]: Zaloudek et al. (1976), *Study of the Comparative Costs of Five Wet/Dry Cooling Tower Concepts*

[102]: Hu (1976), *Engineering and Economic Evaluation of Wet/Dry Cooling Towers for Water Conservation*

[103]: Loscutoff (1975), *Preliminary Evaluation of Wet/Dry Cooling Concepts for Power Plants*

4.2.2 Non-conventional cooling: Combined / hybrid cooling

While energy efficiency has long been a priority, water conservation only began receiving significant attention in recent years. This is reflected in the large number of wet-cooled CSP plants built in the past. Today, some of these plants face growing scrutiny and competition for water resources, as many regions of the world experience prolonged periods of water stress. In response, a third alternative is gaining traction: hybrid or combined cooling technologies, which integrate the advantages of different cooling methods (wet and dry) into a single, innovative system. The concept has been explored since the 1970s [22, 23, 102, 103] and regained momentum in the following decades [95, 96], although early studies primarily focused on fossil-fuel and nuclear thermal power plants. Over the past decade, interest sparked in evaluating hybrid cooling solutions specifically for concentrated solar power systems.

Terminology: Combined vs Hybrid Cooling

In the literature, two terms are commonly used to describe cooling systems that integrate both wet and dry components: *hybrid* and *combined*.

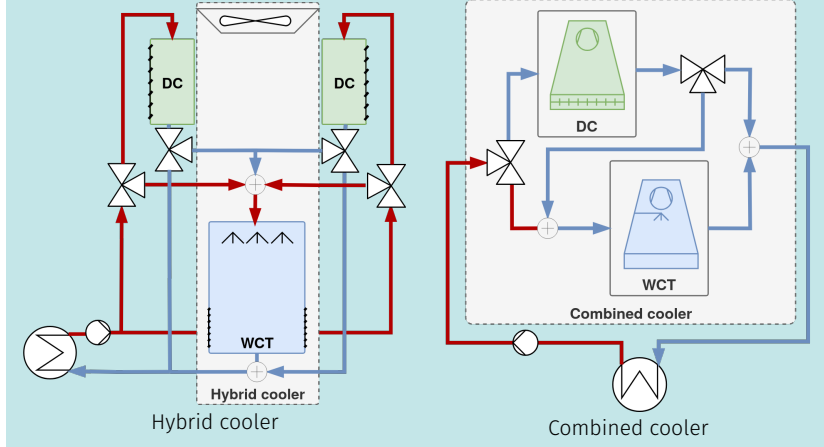
Hybrid systems refer to configurations where the dry and wet cooling components are integrated into a single physical unit. An example is a cooling tower with two sections –an upper dry section followed by a wet section that can be activated as needed.

Combined systems consist of separate, independent dry and wet units connected by a hydraulic circuit. Each component is physically distinct and operates independently.

From a thermodynamic perspective, hybrid and combined systems are functionally equivalent. However, hybrid systems tend to be more compact

due to their integrated design, while combined systems offer greater flexibility in component layout and maintenance. Additionally, combined systems are often easier to implement in practice, as the individual dry and wet components are commercially available off the shelf unlike hybrid units, which may require custom design and manufacturing.

These differences are not all that important, so the two terms can be used interchangeably.



Many heterogeneous hybrid/combined coolers can be found comprising different components with different arrangements:

1. Water-enhanced dry cooling. A dry cooler (usually ACC) switchable to wet (deluge condenser cell). In the deluged condenser configuration, dry-cooling is prioritized until a certain backpressure is reached. When this happens water is sprayed wetting the exchanging surfaces, which now act equivalently to the packing bed in a wet cooling tower [22–24, 103, 104]. The overall heat transfer rates are improved since now the transfer mechanism is air to the water film that evaporates, but air-metal contact is lost, effectively disabling the dry-cooling mechanism. In this configuration is either one or the other. Still, because the nominal cooling capacity of such systems is usually achieved by assembling multiple smaller cells, it is possible to operate them in parallel. In practice, this means that some cells can remain in dry mode (or even be designed exclusively for dry operation), while others can be switchable to wet mode when needed. See Figure 4.7 (a) for an example of such system.
2. Dry cooler (usually ACC) + WCT in parallel [19, 96, 105]. In this configuration part of the vapor is directed to an ACC while the rest goes to a surface condenser cooled by a wet cooling tower. Each cooler can be sized independently. A commercial example of such system can be seen in Figure 4.7 (b).
3. Surface Condenser (SC) + ACHE + WCT in series.
4. SC + (ACHE+WCT) in series-parallel [16, 18, 106]. The series-parallel configuration is interesting since it offers the greatest degree of flexibility, at the cost of adding two heat transfer processes in series, at a minimum (SC→ACHE), and three if in series configuration: SC→ACHE→WCT. Though this last one is intended and not so problematic since the wet cooling has a higher Initial Temperature Difference (ITD) (in this case, the difference between outlet temperature from dry cooler and wet bulb temperature). Flexibility is provided by the almost continuous flexible hydraulic configuration: only series, only parallel, any configuration in between or only one of the systems. But also in the design, each cooler can be sized independently⁶. This allows to optimize the system adhoc for each particular

[22]: Wiles et al. (1978), *Description and Cost Analysis of a Deluge Dry/Wet Cooling System*.

[23]: Zaloudek et al. (1976), *Study of the Comparative Costs of Five Wet/Dry Cooling Tower Concepts*

[24]: Rohani et al. (2021), “Optimization of Water Management Plans for CSP Plants through Simulation of Water Consumption and Cost of Treatment Based on Operational Data”

[103]: Loscutoff (1975), *Preliminary Evaluation of Wet/Dry Cooling Concepts for Power Plants*

[104]: Golkar et al. (2019), “Determination of Optimum Hybrid Cooling Wet/Dry Parameters and Control System in off Design Condition”

[19]: Barigozzi et al. (2014), “Performance Prediction and Optimization of a Waste-to-Energy Cogeneration Plant with Combined Wet and Dry Cooling System”

[96]: Maulbetsch (2012), *Economic Evaluation of Alternative Cooling Technologies*

[105]: Barigozzi et al. (2011), “Wet and Dry Cooling Systems Optimization Applied to a Modern Waste-to-Energy Cogeneration Heat and Power Plant”

[16]: Hu et al. (2018), “Thermodynamic Characteristics of Thermal Power Plant with Hybrid (Dry/Wet) Cooling System”

[18]: Asvapoositkul et al. (2014), “Comparative Evaluation of Hybrid (Dry/Wet) Cooling Tower Performance”

[106]: Palenzuela et al. (2022), “Experimental Assessment of a Pilot Scale Hybrid Cooling System for Water Consumption Reduction in CSP Plants”

6: Specially in the combined cooler case, in the hybrid alternative it might not be as straightforward

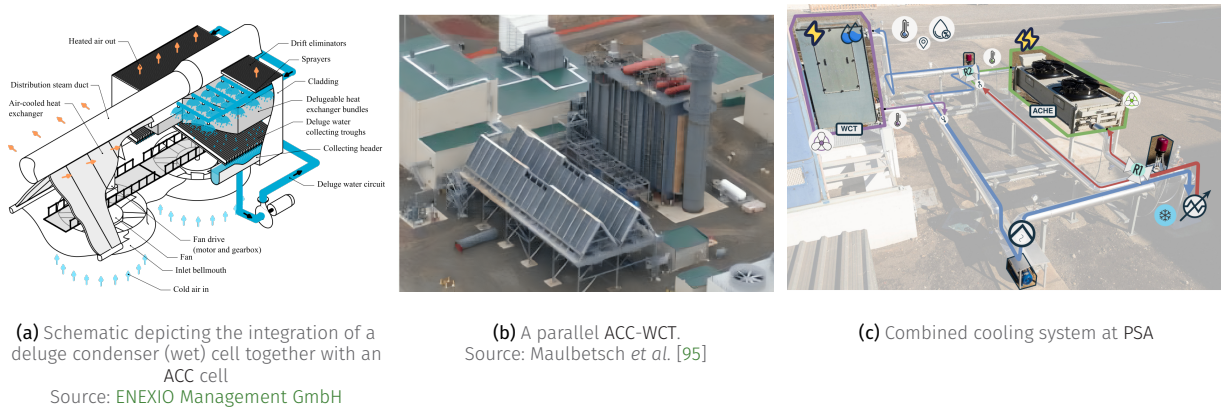


Figure 4.7: Different hybrid/combined coolers configurations

deployment by running simulations with the expected operation conditions and prioritizing more the wet or the dry component. An example of such system is shown in Figure 4.7 (c).

From a literature review a few conclusions can be drawn:

- ▶ Air flow rates are very different between dry and wet systems, so any design needs to allow independent regulation of each. In the combined configuration (separate coolers) this is easily achieved since they have independent fans. On the other hand for hybrid systems with a single shared fan louvers can be used to regulate the air flow through each section [18].
- ▶ Corrosion might be a problem in the deluged condenser, if so, plastic exchange surfaces might have to be used, further decreasing already low heat transfer coefficients.
- ▶ If dry and wet systems share the condenser *i.e.* the hydraulic circuit. A direct contact jet-condenser type cannot be used, since the power cycle requires high-quality water and large amounts would need to be constantly replenished because of the wet cooler evaporation.
- ▶ If the dry cooler is going to be the main cooling source throughout the year, options that combine an ACHE with a surface condenser, are going to penalize the dry cooling component compared to alternatives like the ACC or Heller system -both with or without delugement or a parallel only configuration.
- ▶ On the contrary, during operation systems that allow combinations of series-parallel configurations provide the greatest potential to adapt the cooling system to the changing operation and ambient conditions. The series configuration is a water conservative configuration while still being able to maintain the required backpressure despite adverse conditions. The parallel configuration maximizes cooling capacity but is more water intensive.

Hybrid/combined cooling technology generally requires larger infrastructure as it comprises of components of both wet and dry cooling technologies, though much smaller water side infrastructure [24]. Also, the potential for water reuse for a hybrid system according to Rohani et al. [24] can amount to 23% of the total raw water consumption (mainly due to blowdown). An important part of this water can be treated and reused without significantly increasing the production costs: up to 14% reduction with the same production cost or even slightly reduced.

[24]: Rohani et al. (2021), "Optimization of Water Management Plans for CSP Plants through Simulation of Water Consumption and Cost of Treatment Based on Operational Data"

These systems are a compromise between full-wet and full-dry systems. Due to their heterogeneity depending on the prioritized objective their costs and consumptions can be closer to one or the other. Such systems can be sized for a range of desired water savings. The systems are normally considered for annual water use targets from 15 % to 85 % of that used by a wet cooling system. Outside that range, they are normally not economically attractive. When even less water than this is available, water-enhanced dry systems might be the better option [95]. For some configurations (when using indirect dry cooling) they can get more expensive than the standalone ACC alternative [96]. Finally, the inclusion of thermal energy storage in the hybrid cooled plant (six hours of storage capacity) can reduce the overall penalty of LCOE from 6.4 % to 3.2 % compared to wet-cooled plants [86].

Hybrid cooling main characteristics

1. Capital cost: 2–3.5x [96]
2. Penalty: 1–3 %, 2–8 % in LCOE [86],
3. Just one commercial CSP plant makes use of this technology [107]

NOTE 1: Due to the novelty and heterogeneity of these systems, values can change significantly.

NOTE 2: Comparisons are made relative to wet cooling.

[86]: Aseri et al. (2022), "Condenser Cooling Technologies for Concentrating Solar Power Plants"

4.2.3 Selection of the cooling technology

Selection of condenser cooling technology can affect the financial as well as technical viability of CSP plants. These differences between technologies are dependent on the environmental conditions (local water cost, local temperature, etc.). Except for extreme cases: no water availability making a dry cooler the only choice or plenty water availability throughout the year leading to the obvious decision of a wet cooler, this is not a trivial decision. Dry cooling is increasingly used in CSP projects, even though they typically come with higher capital costs and reduced thermodynamic performance, particularly in hot weather for the dry only alternative. These systems trade water savings for lower efficiency, making the choice of cooling technology a critical design decision that balances technical, economic, and environmental considerations.

Selecting the cooling technology is not trivial, especially if a hybrid cooler is chosen. The relative capability of the wet and dry systems is the primary determinant of the system cost. This, in turn, depends on: the amount of water available for cooling and the value of plant output during the hottest hours of the year compared to the average value over the entire year. As a general rule, the more water available for cooling, the cheaper and more efficient is the cooling system. If the amount of water available is between 15% and 85% of that required for an all-wet system, the capital cost of a hybrid system will be intermediate between the costs of an all-wet and an all-dry system [95]. Also, environment context and costs structures are strongly dependent on the particular location and affect decision-making. Annual simulations of the different cooling alternatives should be performed using weather data for the particular location, local water availability throughout the year, and performing a techno-economical analysis in order to make an informed decision.

So far most systems make use of either wet cooling (55 % worldwide) or dry (24 %)⁷ [91], but it is likely that some hybrid cooling configuration would be the optimal choice in most situations where a wet only alternative is used⁸ due to their adaptive nature and flexible operation. Currently, few commercial plants make use of hybrid cooling technologies. An example of a series, integrated, hybrid system providing significant water conservation exists at the San Juan Generating Station in Farmington, New Mexico. It consists of a conventional,

[95]: Maulbetsch (2004), *Comparison of Alternate Cooling Technologies for U.S. Power Plants: Economic, Environmental, and Other Tradeoffs*

7: the remaining 21 % is unknown, but likely to be either of the conventional technologies

[91]: Thonig et al. (2023), *CSP.Guru* 2023-07-01

8: and probably in some dry only ones too

shell-and-tube steam condenser coupled to a hybrid tower with an air-cooled dry section on top which discharges into a wet cooling tower beneath. For CSP, the only known plant to make use of this technology is the Crescent Dunes Solar Energy Project, a 110 MW_e concentrated solar power station equipped with 1.1 GWh of molten-salt thermal energy storage. This plant makes use of the described parallel configuration (ACC + WCT) [107]. Also, within the *MinWaterCSP* project, a full scale pilot hybrid plant consisting of an air cooled deluged condenser was successfully built and tested in Stellenbosch, South Africa [108].

[107]: SPX (2012), *SPX Awarded Contract to Supply Parallel Condensing System For Crescent Dunes Solar Energy Project near Tonopah, Nevada*

[108]: GmbH (2020), *Blog #29 – Full Scale Testing in Stellenbosch, South Africa | MinwaterCSP*

Combined cooling pilot plant at Plataforma Solar de Almería

5

TL;DR

In this chapter a detailed description of the combined cooling pilot plant at PSA is provided including a Piping and Instrumentation Diagram (P&ID) diagram and the methodology followed to perform the experimentation and data-processing. Several experimental campaigns have been performed to characterize the different components of the pilot plant and the complete system, at a wide range of operating conditions. Combined, 198 tests are processed most of which are openly available in public repositories.

5.1	Plant description	48
5.2	Experimental campaigns	48
5.2.1	Physical model calibration campaigns	49
5.2.2	Data-driven models training campaigns	50
5.2.3	Models validation campaigns	50

Introduction

The combined cooling pilot plant at Plataforma Solar de Almería (PSA) —see Figure 5.1— is a unique facility that integrates a wet cooling tower and a dry cooler¹ in a flexible hydraulic configuration. It allows for the study and validation of different cooling configurations, models, and control and optimization strategies. The pilot plant was installed at PSA in June 2019 as part of the WASCOP project (*Water Saving for Solar Concentrated Power*), within the Horizon 2020 (H2020) program. The main goal of the project was the development of innovative technologies for water management in CSP plants.

This chapter describes the plant in Section 5.1 (Plant description) and the experimental campaigns carried out in Section 5.2 (Experimental campaigns).

1: Both provided by Hamon D'Hondt

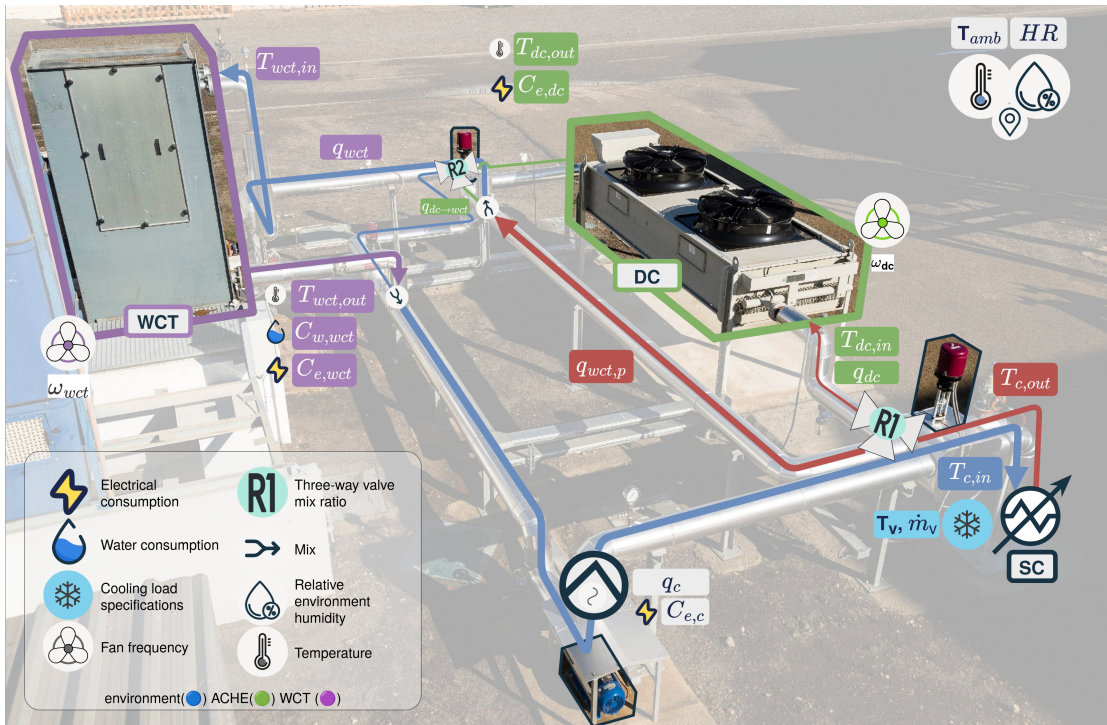


Figure 5.1: PSA combined cooling system facility

5.1 Plant description



Figure 5.2: Back view of the WCT

Table 5.1: Characteristics of instrumentation (^a value of the temperature in °C, ^b of reading, ^c full scale, ^d mean value).

Measured variable	Instrument	Range	Measurement uncertainty
Water temperature (TT-001... TT-007)	Pt100	0-100 °C	0.03 + 0.005·T ^a
Cooling water flow rate (FT-001...FT-003)	Vortex flow meter	9.8 - 25 m ³ /h	± 0.65 % o.r. ^b
Water flow rate (FT-004)	Paddle wheel flow meter	0.05-2 m ³ /h	± 0.5 % of F.S ^c + 2.5 % o.r.
Condensate water flow rate (FT-006)	Coriolis flow meter	0.1-0.3 m ³ /h	< 0.1 %
Ambient temperature	Pt1000	-40 - 60 °C	± 0.4 @20 °C
Relative humidity	Capacitive sensor	0-98 %	± 3 % o.r @20 °C
Air velocity	Impeller anemometer	0.1-15 m s ⁻¹	± 0.1 m s ⁻¹ + 1.5 % o.r
Outlet air temperature	Pt100	-20-70 °C	± 0.5 °C
Outlet air humidity	Capacitive sensor	0-100 %	± 2 %

5.2 Experimental campaigns

With the aim of characterizing and developing models for this novel facility several experimental campaigns have been carried out over the years.

The normative framework followed to carry out the experiments, in order to ensure stable conditions, has been the standards UNE 13741 [109] and the Spanish CTI [110]. These standards specify the test duration and the allowed variations of the most representative ambient and operating magnitudes (water flow rate, heat load, cooling tower range, wet-bulb and dry-bulb temperatures and wind velocity) during the tests —specific to WCT and extended to the other components. Although the duration of the test should not be less than one hour according to the standards, due to the low capacity of the components in the PSA pilot plant and the operational experience, the duration of the tests has been reduced to up to 30 minutes. Once stable conditions are maintained during the defined interval time, the average and deviations values of each measurement are calculated in order to check that they are within the allowable limits of the norm, which finally lead to a valid steady-state operating point.

Specifically, 11 experimental campaigns have been conducted at the pilot plant, which have been classified according to its goal. Table 5.4 summarizes these

[109]: UNE (2004), *Thermal Performance Acceptance Testing of Mechanical Draught Series Wet Cooling Towers*

[110]: CTI (2000), *Code Tower, Standard Specifications. Acceptance Test Code for Water Cooling Towers*

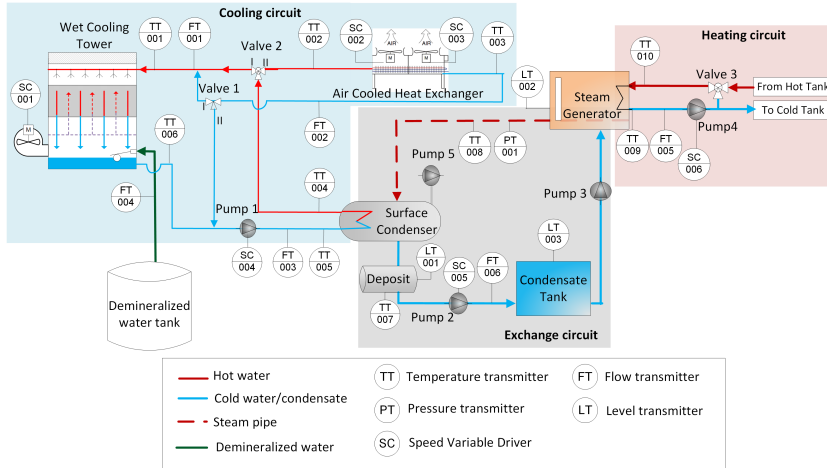


Figure 5.3: Layout of combined cooling systems pilot plant at PSA.

experimental campaigns, describing the Design of Experiments (DoE) employed and indicating the number of tests conducted under steady-state conditions. The ranges of the variables involved in the experiments are also indicated, with those used to define the DoE for each test campaign shown in bold.

5.2.1 Physical model calibration campaigns

- **WCT-fan.** The aim of this campaign was to fit a function (mapping) that relates the air mass flow rate at the outlet of the tower, $\dot{m}_{wct,air}$, with the frequency of the fan, ω_{wct} . Air velocity and temperature were measured at 8 different fan speed levels, ranging from 30 % to 100 % in 10 % increments (see Table 5.4 – *WCT-fan*). Sensors measuring the air velocity, temperature and relative humidity at the outlet area of the wet cooling tower are not permanently installed in the plant. Portable sensors were used instead in some experiments to characterize them. They were measured at the outlet area of the cooling tower —using the sensors listed in Table 5.1 and at the top of the tower in Figure 5.2. The outlet area was divided into 9 quadrants and the above mentioned magnitudes were registered at the center of each quadrant. The obtained values were averaged to determine the mean velocity, temperature and relative humidity used in the air mass flow rate calculation.
- **DC-fan.** The aim of this campaign was to fit a function (mapping) that relates the air mass flow rate at the outlet of the DC, $\dot{m}_{dc,air}$, with the frequency of the fan, ω_{dc} (see Table 5.4 – *DC-fan*). Air velocity and temperature were measured at 10 different fan speed levels, ranging from 11 % to 100 % in 10 % increments. The ACHE fan area was divided into eight quadrants, and measurements were taken at the center of each quadrant. The recorded values were then averaged to obtain the mean air velocity and temperature, which were used to calculate the air mass flow rate.
- **WCT-cal.** The experimental campaign was designed to calibrate the physical model by focusing on the Merkel number, which depends on the water-to-air mass flow ratio².
- **DC-cal.** An experimental campaign (*DC-cal*) was designed and performed to calibrate the Nusselt number correlation as described in Section 6.2.1.
- **SC-cal.** Designed to calibrate the global heat transfer coefficient, U_{dc} , as a function of inlet water temperature, $T_{c,in}$ and water flow rate, q_{dc}

Table 5.2: Main characteristics of the ACHE dry cooler at the pilot plant

Concept	Value	Unit
Number of tubes ($n_{dc,tb}$)	60	-
Number of passes per tube ($k_{dc,tb}$)	3	-
Tube length ($l_{dc,tb}$)	3.6	m
Outer tube diameter ($D_{dc,o}$)	12.7	mm
Inner tube diameter ($D_{dc,i}$)	9.4	mm
Tube material	Copper	-
Fin thickness	0.21	mm
Fin spacing	2.4	mm
Fin material	Aluminum	-

Table 5.3: Main characteristics of the surface condenser at the pilot plant

Concept	Value	Unit
Number of tubes	96	-
Number of passes per tube	4	-
Tube length	3	m
Outer tube diameter	21.34	mm
Tube thickness	2.08	mm
Thermal cond. of the tube wall	50	W/(m·K)
Tube-side inlet pressure	5	bar
Tube-side fouling	$1.72 \cdot 10^{-5}$	$\text{m}^2 \cdot \text{K}/\text{W}$

2: Further explained in Section 6.1.1

Table 5.4: Experimental campaigns performed at the CC pilot plant, where GD- n_1 - n_2 refers to the spatial grid distribution (n_1) around the fan with n_2 measurements in each quadrant ($n_1 \times n_2$ measurements); BB- n_1 - n_2 denotes a Box-Behnken design with n_1 variables and n_2 levels; and FF- n_1 -...- n_i indicates a full factorial design with i variables, each with n_i levels.

Features	Physical model calibration					Data-driven models training		Validation			
	WCT-fan	WCT-cal	DC-fan	DC-cal	SC-cal	WCT-tr	DC-tr	WCT-val	DC-val	SC-val	CC-val
DoE	GD-6-8	FF-2-2-2-2	GD-8-10	BB-4-3	BB-3-3	-	-	FF-2-2-2-2	BB-4-3	BB-3-3	FF-2-2-3
N_{tests}	48	17	80	27	15	115	137	17	27	15	24
T_{amb} (°C)	20-23	31-41	26	12 - 29	-	9-39	9-39	15-29	13 - 32	-	12 - 37
HR (%)	-	13-40	-	-	-	10-87	-	15-29	-	-	14 - 63
\dot{m}_v (kg/h)	-	-	-	-	118 - 328	-	-	-	-	133 - 287	200 - 310
\dot{Q}_c (kW)	-	-	-	-	78 - 216	-	-	-	-	88 - 187	132 - 202
q_c (m³/h)	-	-	-	-	10 - 24	-	-	-	-	10 - 24	18 - 24
q_{dc} (m³/h)	-	-	-	5 - 25	-	-	5-24	-	5 - 24	-	5 - 24
q_{wct} (m³/h)	-	8-22	-	-	-	6-23	-	6-22	-	-	6 - 24
$T_{dc,in}$ (°C)	-	-	-	35 - 41	-	-	31-54	-	31 - 42	-	33 - 54
$\Delta T_{dc,in-out}$ (°C)	-	-	-	2 - 7	-	-	1-13	-	2 - 9	-	1 - 11
T_v (°C)	-	-	-	-	36 - 56	-	-	-	-	36 - 56	36 - 57
$T_{wct,in}$ (°C)	-	31-49	-	-	-	33-41	-	35-40	-	-	33 - 54
$\Delta T_{wct,in-out}$ (°C)	-	6-18	-	-	-	2-16	-	4-11	-	-	4-11
w_{dc} (%)	-	-	11 - 100	11 - 76	-	-	11-100	-	11 - 98	-	11 - 100
w_{wct} (%)	30-100	25-100	-	-	-	21-93	-	21-48	-	-	21 - 87

5.2.2 Data-driven models training campaigns

The data required for data-driven models depends on several factors such as the complexity of the model and the diversity of the inputs. With the aim of obtaining reliable data-driven models, data collected over several years of operation were used for model training.

WCT-tr and DC-tr refer to the data collected to tune the WCT and DC data-driven models, respectively.

5.2.3 Models validation campaigns

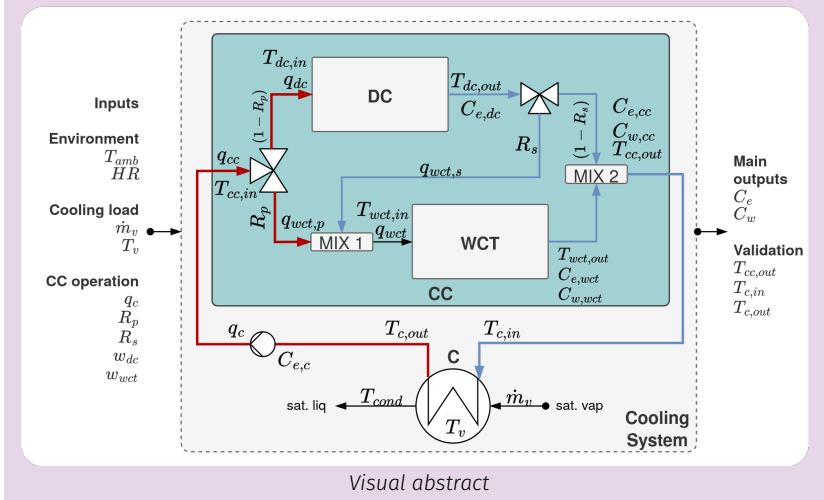
The experimental campaigns designed for the thermal model's calibration were repeated to validate the models of WCT (WCT-val), DC (DC-val) and SC (SC-val). An additional experimental campaign was designed and performed to validate the complete model of the CC system (CC-val).

6

Modelling of a combined cooling system

TL;DR

This chapter describes the steady-state modelling of the different components of a combined cooling system. Different alternatives are presented: from physical models to data-driven approaches, including the generation of surrogate data-driven models trained using synthetic data from a physical model. Finally, it is shown how they are integrated into a complete system model.



6.1	Wet cooler	51
6.1.1	Physical model	52
6.1.2	Surrogate model	53
6.1.3	Model interface	54
6.2	Dry cooler	54
6.2.1	Physical model	54
6.2.2	Surrogate model	55
6.2.3	Model interface	55
6.3	Other components and outputs	56
6.3.1	Surface condenser	56
6.3.2	Electrical consumption	56
6.3.3	Mixers	57
6.3.4	Valves	57
6.4	Complete system	57

Introduction

In order to study the potential advantages of making use of a combined cooling system, it is first necessary to develop the modelling of its components. Since the objective is performance prediction, this chapter focuses on the steady state modelling of the combined cooler main components, *i.e.* the Wet Cooling Tower (WCT), the Dry Cooler (DC) and the Surface Condenser (SC). More specifically, the aim is to develop two modelling strategies: that based on physical equations and that based on black box data-driven models.

First, in Section 6.1 a physical model for the WCT is described followed by a methodology to generate a synthetic dataset for data-driven surrogate models. In Section 6.2 the same structure is followed for the DC-type ACHE. Other first-principles model components are presented in Section 6.3: the surface condenser, mixers, and the electrical consumption. Finally, all components are integrated in Section 6.4 to form the complete model of the combined cooling system. The individual component and the CCS model sections are completed with a model interface block.

6.1 Wet cooler

The static models presented in this section have been developed to predict two main outputs, the water temperature at the outlet of the WCT, $T_{wct,out}$, and the

1: \dot{m}_{wct} in terms of mass flow rate

2: In the case of the physical model, internally the fan speed is converted into the air mass flow rate ($\dot{m}_{wct,air}$) with an empirical correlation.

water consumed due to evaporation losses, $C_{w,wct}$. The inputs variables required are: the cooling water flow rate (\dot{q}_{wct})¹, the water temperature at the inlet of the WCT ($T_{wct,in}$), the ambient temperature (T_{amb}), the ambient relative humidity (HR) and the cooler fan speed (ω_{wct})²

6.1.1 Physical model

The Poppe theory is used for the thermal performance evaluation of the WCT. This approach is preferred for applications in which an accurate determination of the outlet air state is required. As the water consumption is of paramount importance in CSP plants, it is suitable for integration into analysis/optimization frameworks for CSP plant cooling strategies.

In the case of cooling towers, the Merkel number is a dimensionless parameter widely recognized as a performance key indicator. It is commonly employed in experimental characterization, numerical simulations, and optimization studies. This parameter can be evaluated through several theoretical approaches, including the original Merkel formulation [111], the effectiveness-Number of Transfer Units (NTU) method [112], and the more comprehensive Poppe model [113].

[111]: Merkel (1925), "Verdunstungskühlung"

[112]: Jaber et al. (1989), "Design of Cooling Towers by the Effectiveness-NTU Method"

[113]: Poppe et al. (1991), "Berechnung von Rückkühlwerken"

[114]: Kloppers et al. (2005), "A Critical Investigation into the Heat and Mass Transfer Analysis of Counterflow Wet-Cooling Towers"

[115]: Navarro et al. (2022), "Critical Evaluation of the Thermal Performance Analysis of a New Cooling Tower Prototype"

Several investigations have compared the previously mentioned theories for thermal performance evaluation of wet cooling towers. Some examples include the works of [114, 115]. These investigations generally conclude that the Poppe method offers a more accurate representation of the physics of the problem, as it enables the prediction of moist air properties and the quantification of evaporative water losses. Consequently, the Poppe method is recommended for applications in which an accurate determination of the outlet air state is required.

According to the Poppe theory [113], the governing equations for heat and mass transfer in the transfer region of the wet cooling tower assuming a one dimensional problem. This is illustrated in the control volume shown in Figure 6.1 where the red and green dashed lines indicate the fill and air-side control volumes, respectively.

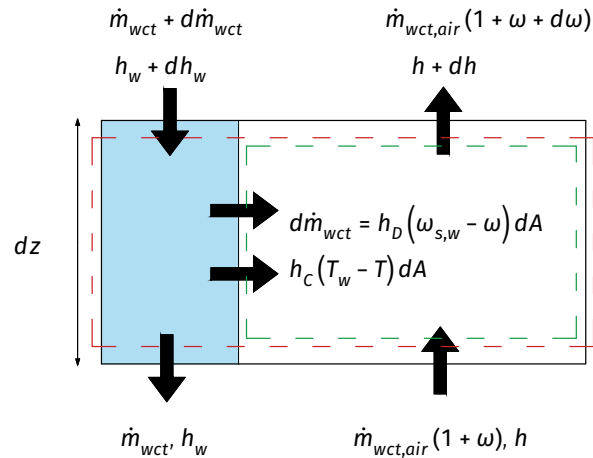


Figure 6.1: Control volume in the exchange area of a wet cooling tower arrangement. Variables are described in the Nomenclature section.

Source: Serrano et al. [116].

The major following equations for the heat and mass transfer obtained are [114, 115]:

$$\frac{d\omega}{dT_w} = \frac{c_{p_w} \frac{\dot{m}_{wct}}{\dot{m}_{wct,air}} (\omega_{s_w} - \omega)}{(h_{s_w} - h) + (Le - 1)[(h_{s_w} - h) - (\omega_{s_w} - \omega)h_v] - (\omega_{s_w} - \omega)h_w}, \quad (6.1)$$

$$\frac{dh}{dT_w} = c_{p_w} \frac{\dot{m}_{wct}}{\dot{m}_{wct,air}} \left[1 + \frac{(\omega_{s_w} - \omega)c_{p_w} T_w}{(h_{s_w} - h) + (Le - 1)[(h_{s_w} - h) - (\omega_{s_w} - \omega)h_v] - (\omega_{s_w} - \omega)h_w} \right], \quad (6.2)$$

$$\frac{d Me}{dT_w} = \frac{c_{p_w}}{(h_{s_w} - h) + (Le - 1)[(h_{s_w} - h) - (\omega_{s_w} - \omega)h_v] - (\omega_{s_w} - \omega)h_w}, \quad (6.3)$$

Le is the Lewis number, ω is the humidity ratio (kg/kg), h is the enthalpy and c_p the specific heat.

where the evolution of key variables such as the humidity ratio (Equation 6.1), air enthalpy (Equation 6.2), and the Merkel number (Equation 6.3) along the fill height is obtained by numerically solving the set of differential equations using a fourth-order Runge-Kutta algorithm. Secondly, the Merkel number of a wet cooling tower is not a constant value but varies with the operating conditions. When plotted against the water-to-air mass flow ratio (defined as the ratio between the water and air mass flow rates within the tower) it typically follows a straight, decreasing trend in logarithmic coordinates. As suggested by ASHRAE [117], this behavior is often expressed through a single correlation that depends on the water-to-air mass flow ratio:

$$Me = c \cdot \left(\frac{\dot{m}_{wct}}{\dot{m}_{wct,air}} \right)^{-n} \quad (6.4)$$

Here, c and n are empirical coefficients that depend on the specific design of the cooling tower. These coefficients can be determined through experimental data fitting.

6.1.2 Generating synthetic data for surrogate WCT Model

The first pair of input variables for the WCT synthetic dataset generation are the wet bulb temperature (T_{wb}) and the difference between this temperature and the system inlet temperature (ΔT_{wb-in}). The wet bulb temperature—the most relevant thermodynamic variable for the WCT performance—is used instead of the ambient temperature or the relative humidity. Using both the ambient temperature and the relative humidity would lead to a larger than necessary input space with many duplicate samples, as the wet bulb temperature is a function of both variables. The second pair of input variables are the cooling water flow rate (q_{wct}) and, following the reasoning from the physical model, the air to water mass flow ratio ($\dot{m}_{wct,air}/\dot{m}_{wct}$), since it is a key parameter in defining the operating conditions of the tower. From the resulting 2D grid, valid combinations are obtained by calculating the air mass flow rate and finding if a valid fan speed can be obtained using an air mass flow rate to fan speed empirical correlation.

Finally, all valid thermodynamic and operational combinations are merged into a comprehensive sample set, enabling detailed system evaluations across a realistic and constrained input space³

3: See Section 6

6.1.3 Model interface

Model 6.1: Wet cooling tower

$$T_{wct,out}, C_{e,wct}, C_{w,wct} = \text{wct model}(q_{wct}, \omega_{wct}, T_{amb}, HR, T_{wct,in}; \theta_{wct})$$

$$C_{e,wct} = \text{electrical consumption}(\omega_{wct})$$

6.2 Dry cooler

Similar to the WCT model, static models are used to predict, this time, one output: the water temperature at the outlet of the DC, $T_{dc,out}$. The inputs variables required are similar to the WCT: the cooling water flow rate (q_{dc})⁴, the water temperature at the inlet of the DC ($T_{dc,in}$), the ambient temperature (T_{amb}) and the cooler fan speed (ω_{dc})⁵.

6.2.1 Physical model

The modelling of air-cooled heat exchangers can involve different levels of complexity. A common simplification is to assume a constant effectiveness or overall heat transfer coefficient. However, such models cannot capture the influence of relevant operating conditions, such as water or air flow rates, which significantly affect both the transferred heat and the power consumption. For preliminary designs, it is common to rely on empirical models based on experimental correlations available in the open literature [118]. While this approach accounts for operating conditions, it must be applied with caution when used outside the range of the original correlations. Furthermore, it can be challenging to find correlations for relatively complex geometries. To partially address these limitations, other models adjust certain parameters through component tests while still preserving the main physics of the problem, primarily by obtaining a Nusselt number (Nu) correlation for a specific configuration as a function of the Reynolds (Re) and Prandtl (Pr) numbers.

The DC (ACHE-type) in the pilot-plant is modelled using the standard heat exchanger equations [119]: heat transferred from the hot fluid (water), heat transferred to the cold fluid (air), and the heat transfer expressed through the overall heat transfer coefficient and the logarithmic mean temperature difference.

$$\dot{Q}_{dc,released} = \dot{m}_{dc} \cdot c_{p,w} \cdot (T_{dc,in} - T_{dc,out}), \quad (6.5)$$

$$\dot{Q}_{dc,absorbed} = \dot{m}_{dc,air} \cdot c_{p,air} \cdot (T_{dc,air,out} - T_{amb}), \quad (6.6)$$

$$\dot{Q}_{dc,transferred} = U_{dc} \cdot A_{dc} \cdot F \cdot LMTD, \quad (6.7)$$

$$\dot{Q}_{dc,released} = \dot{Q}_{dc,absorbed} = \dot{Q}_{dc,transferred} \quad (6.8)$$

where \dot{Q} represents the heat transfer rate *i.e.*, the thermal power, F is the correction factor for the Logarithmic Mean Temperature Difference (LMTD), which is calculated for a cross flow heat exchanger with three tube rows and three tube passes [120], and the product of the overall heat transfer coefficient and

[118]: Zhang et al. (2024), "Preliminary Analysis of a Parabolic Trough Concentrating Solar Power System Integrated with Radiative Cooling"

[119]: Yunus A. Cengel et al. (2014), *Heat and Mass Transfer*

[120]: Kröger (2004), *Air-Cooled Heat Exchangers and Cooling Towers*

the heat exchange area is calculated from:

$$U_{dc} \cdot A_{dc} = \left(\frac{1}{A_{dc,i} \cdot h_i} + \frac{\ln(D_{dc,tb,o}/D_{dc,tb,i})}{2 \cdot \pi \cdot k_{dc,tb} \cdot L_{dc,tb} \cdot n_{dc,tb}} + \frac{1}{A_{dc,o} \cdot h_o} \right)^{-1}, \quad (6.9)$$

being h_o the convective heat transfer coefficient for the external surface of a single horizontal tube, $D_{tb,o}$ the outer tube diameter, $D_{tb,i}$ the inner tube diameter, $k_{dc,tb}$ the thermal conductivity of the tube wall material, and h_i the convective heat transfer coefficient for the water inside the tube⁶.

The convective heat transfer coefficient on the internal side (cooling water), h_i , is calculated using Gnielinski's correlation [121], assuming uniform flow distribution in the tubes and negligible roughness. The convective heat transfer coefficient on the external surface (air), h_o , cannot be easily calculated from correlations in the open literature due to the geometry involved (tube arrays with transversal plate fins). It can be determined experimentally with a campaign covering a wide range of operating conditions to then fit the experimental data to an equation that relates the air side Nusselt number and the air side Reynolds number, as follows:

$$\text{Nu}_a = G \cdot \text{Re}_{air}^m \cdot \text{Pr}_{air}^{0.36}, \quad (6.10)$$

where $\text{Nu}_a = h_o \cdot L_{dc,tb} / k_{dc,tb}$, and G and m are parameters to be determined by fitting to experimental data, and the exponent for the Prandtl number, Pr , is assumed to be the same value as that proposed by Zukauskas for staggered tube banks [122]⁷.

6: See their values in Table 5.2

[121]: Volker Gnielinski (1976), "New Equations for Heat and Mass Transfer in Turbulent Pipe and Channel Flow"

6.2.2 Generating synthetic data for surrogate DC model

Similar to the wet cooling tower case, setting absolute values for both the inlet temperature and the environment temperature will lead to many unfeasible combinations ($T_{dc,in} \leq T_{db}$). So instead, values are generated for the temperature difference, therefore, a 2D grid is constructed using combinations of ambient/dry-bulb temperature (T_{amb}) and the difference between inlet and ambient temperature (ΔT_{amb-in}). For each valid temperature pair ($T_{amb}, T_{dc,in}$), additional independent variables (q_{dc}, ω_{dc}) are combined via a cartesian product, resulting in a full multidimensional grid of plausible operating points. This systematic procedure ensures a dense and uniform sampling across all relevant input dimensions. Finally, infeasible combinations are filtered based on physical constraints.

[122]: Kakac et al. (1986), *Handbook of Single-Phase Convective Heat Transfer*

7: The system design characteristics needed for applying this methodology for the pilot plant are listed in Table 5.2.

6.2.3 Model interface

Model 6.2: Dry cooler

$$T_{dc,out} = \text{dc model}(q_{dc}, \omega_{dc}, T_{amb}, T_{dc,in}; \theta_{dc})$$

$$C_{e,dc} = \text{electrical consumption}(\omega_{dc})$$

θ_{dc} are the model parameters such as the area (A_{dc}), that can be found in Table 5.2.

6.3 Other components and outputs

6.3.1 Surface condenser

The surface condenser is a heat exchanger that condenses steam into water, assuming that all the vapor that enters the condenser (at saturated conditions), leaves it as saturated liquid, it can be modelled similar to the dry cooler by applying the first law of thermodynamics, which states that the heat lost by the steam (*released*) is equal to the heat gained by the cooling water (*absorbed*), and equal to the heat transferred by the condenser heat transfer surfaces (*transferred*).

Model 6.3: Surface condenser

$$T_{c,in}, T_{c,out} = \text{condenser model}(\dot{m}_c, T_v, \dot{m}_v; \theta_c)$$

$$\dot{Q}_c = \dot{m}_v \cdot (h_{sat.vap} - h_{sat.liq})$$

$$\dot{Q}_c = \dot{m}_c \cdot c_p \cdot (T_{c,out} - T_{c,in})$$

$$\dot{Q}_c = U_c \cdot A_c \cdot LMTD$$

$$LMTD = \frac{T_{c,out} - T_{c,in}}{\ln\left(\frac{T_v - T_{c,in}}{T_v - T_{c,out}}\right)}$$

θ_c are the model parameters such as the condenser area (A_c), that can be found in Table 5.3.

Being \dot{m}_c the condenser cooling water flow rate, T_v the vapor temperature inside the condenser and \dot{m}_v its flow rate. U_c , the overall heat transfer coefficient, can be determined in a variety of ways. One of them is given by:

$$U_c \cdot A_c = \left(\frac{1}{A_{c,i} \cdot h_i} + \frac{R_{c,if}}{A_{c,i}} + \frac{\ln(D_{c,tb,o}/D_{c,tb,i})}{2 \cdot \pi \cdot k_{c,tb} \cdot L_{c,tb} \cdot n_{c,tb}} + \frac{1}{A_{c,o} \cdot h_o} + \frac{R_{c,of}}{A_{c,o}} \right)^{-1}, \quad (6.11)$$

where $R_{c,if}$ and $R_{c,of}$ are the fouling resistances (inside and outside, respectively). The shell-side heat transfer coefficient h_o is estimated once again using the Nusselt method [123] for laminar-flow condensation over a horizontal tube bundle ($0 < Re < 30 \times 10^6$) including the Kern correction for condensate inundation, while the tube-side convective heat transfer coefficient for the water flow inside the tube bundle, h_i , is approximated using the Petukhov-Kirillov-Popov correlation for fully-developed turbulent flow through smooth circular tubes [124], valid within $0.5 < Pr < 10^6$ and $4000 < Re < 5 \times 10^6$.

[123]: Serth (2007), *Process Heat Transfer: Principles, Applications and Rules of Thumb*

[124]: Rohsenow et al. (1998), *Handbook of Heat Transfer*

6.3.2 Electrical consumption

For each component (e.g., the recirculated cooling water flow rate, cooler fan speed, etc.). electrical consumption is modelled with polynomial regressions of order 3 derived from experimental data:

Model 6.4: Electrical consumption

C_e = electrical consumption model($x; \theta$)

$$C_e = p_1 \cdot x^3 + p_2 \cdot x^2 + p_3 \cdot x + p_4$$

θ represents the model parameters, i.e., the polynomial coefficients (p_1, p_2, p_3, p_4).

where C_e represents the electrical consumption, and x is the input variable. The coefficients p_i correspond to a polynomial regression and must be calibrated individually for each component.

6.3.3 Mixers

Fluids are mixed at the inlet of the WCT and at the outlet of the combined cooler (MIX 1 and MIX 2 in Figure 6.2, respectively). The mixers outlet flow ($q_{mix,out,i}$) and temperature ($T_{mix,out,i}$) can be determined with a simple mass and energy balances from its inlets streams ($q_{mix,in}, T_{mix,in}$):

Model 6.5: Mixer model

$$q_{mix,out}, T_{mix,out} = \text{mixer model}(q_{mix,in,1}, T_{mix,in,1}, q_{mix,in,2}, T_{mix,in,2})$$

$$q_{mix,out} = q_{mix,in,1} + q_{mix,in,2}$$

$$T_{mix,out} = T_{mix,in,1} \cdot \frac{c_p(T_{mix,in,1})}{c_p(T_{out,i})} \frac{q_{mix,in,1}}{q_{mix,out,i}} +$$

$$T_{mix,in,2} \cdot \frac{c_p(T_{mix,in,2})}{c_p(T_{out,i})} \frac{q_{mix,in,2}}{q_{mix,out,i}}$$

where $c_p(\cdot)$ is the specific heat, which can be assumed to be the same for the mixing temperature differences of this type of system.

6.3.4 Valves

The two divergent three-way valves (see Figure 6.2) are modeled using the distribution ratio R as inputs, so the mass flow rate at the outlets of each valve can be easily estimated as $q_{out,1} = R \cdot q_{in}$ and conversely $q_{out,2} = (1 - R) \cdot q_{in}$. Where R is a value in the range [0, 1], which implicitly includes the non-linearities of the valve.

6.4 Complete system

The complete model of the combined cooling system integrates the models of the WCT and DC, along with the surface condenser and the mixers, as defined in Model 6.6 (Complete system). The full diagram, including all variables, is shown in Figure 6.2.

The system can be solved with the provided inputs ($q_c, R_p, R_s, \omega_{dc}, \omega_{wct}, T_{amb}, HR, T_v, \dot{m}_v$) as follows. First, the flow rates through the different paths are determined from the recirculation flow (q_c) and the valve positions (R_p, R_s).

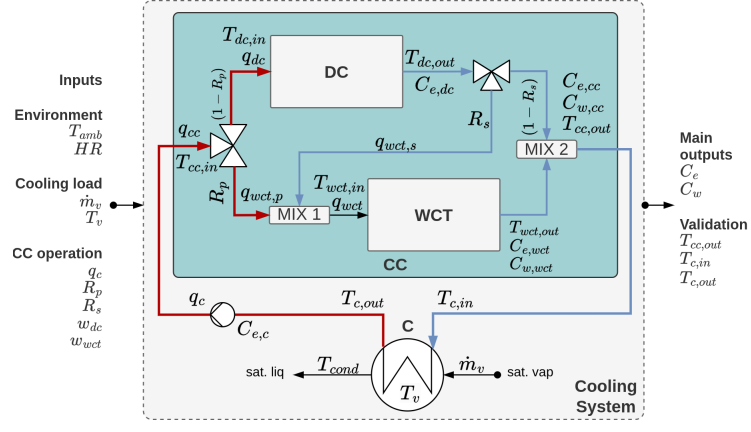


Figure 6.2: Complete model diagram of the combined cooling system

Next, the condenser model is evaluated, yielding the remaining input needed to fully specify the dry cooler, namely its inlet temperature ($T_{dc,in} = T_{c,out}$). The inlet and outlet temperatures for the wet cooler are then obtained by evaluating the mixers using the dry-cooler outlet temperature ($T_{dc,out}$) together with the combined-cooler outlet temperature, which equals the condenser inlet temperature ($T_{cc,out} = T_{c,in}$). Finally, the wet cooling tower is evaluated: given its inlet temperature ($T_{wct,in}$, from the first mixer) and fan speed (ω_{wct}), its outlet temperature ($T_{wct,out}$) and water consumption ($C_{w,wct}$) are obtained. A consistency check is performed requiring that the wet-cooler outlet temperature matches the value obtained from the second mixer.

If no convergence is achieved, the process can either be repeated iteratively changing the condenser vapor temperature (T_v) until the system converges to a valid equilibrium steady-state. Or alternatively, a flag can be set to indicate that the current input combination is not feasible.

Model 6.6: Combined cooling system

θ_{cc} represents the parameters of the different components (condenser area, heat transfer coefficients, number of tubes in the ACHE, etc.)

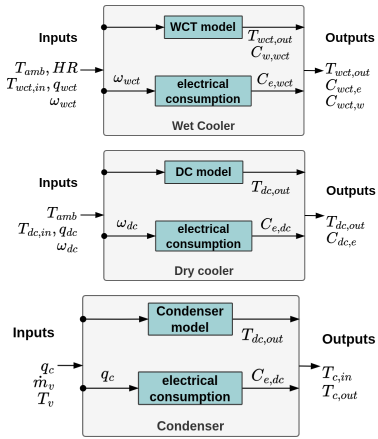


Figure 6.3: Inputs-outputs block diagram of the main model components

$$\begin{aligned}
 T_{cc,out}, C_e, C_w, T_{c,in}, T_{c,out} &= ccs \text{ model}(q_c, R_p, R_s, \omega_{dc}, \omega_{wct}, T_{amb}, HR, T_v, \dot{m}_v; \theta_{cc}) \\
 T_{cc,in} &= T_{c,out} \\
 T_{dc,in} &= T_{cc,in} \\
 q_{dc} &= q_c \cdot (1 - R_p) \\
 q_{wct,p} &= q_c \cdot R_p \\
 q_{wct,s} &= q_{dc} \cdot R_s \\
 T_{c,in}, T_{c,out} &= \text{condenser model}(q_c, \dot{m}_v, T_v; \theta_c) \\
 T_{dc,out}, C_{e,dc} &= \text{dc model}(q_{dc}, \omega_{dc}, T_{amb}, T_{dc,in}; \theta_{dc}) \\
 q_{wct}, T_{wct,in} &= \text{mixer model}(q_{wct,p}, T_{cc,in}, q_{wct,s}, T_{dc,out}) \\
 q_{cc}, T_{cc,out} &= \text{mixer model}(q_{wct}, T_{wct,out}, q_{dc}, T_{dc,out}) \\
 T_{wct,out}, C_{e,wct}, C_{w,wct} &= \text{wct model}(q_{wct}, \omega_{wct}, T_{amb}, HR, T_{wct,in}; \theta_{wct}) \\
 C_{e,c} &= \text{electrical consumption}(q_c; \theta_{c,e}) \\
 C_{e,dc} &= \text{electrical consumption}(\omega_{dc}; \theta_{dc,e}) \\
 C_{e,wct} &= \text{electrical consumption}(\omega_{wct}; \theta_{wct,e}) \\
 C_e &= C_{e,dc} + C_{e,wct} + C_{e,c}; C_w = C_{w,wct}
 \end{aligned}$$

Optimization of a combined cooling system

TL;DR

This chapter describes optimization problems for a combined cooling system as well as different optimization strategies propositions to solve them. The objective is to minimize the daily cost of operation made up by the electricity and water costs, while ensuring the cooling demand is met. The key challenge is to manage the limited water resource. From the studied alternatives, this can only be effectively achieved by the proposed two-stage horizon optimization strategy.

7.1	Environment description	61
7.2	Static optimization	61
7.2.1	Dry cooler	62
7.2.2	Wet cooler	63
7.2.3	Combined cooler	64
7.3	Horizon optimization	66
7.3.1	Problem discussion	67
7.3.2	Proposed solution	68

Introduction

Over the years, various studies have compared wet and dry cooling systems for CSP plants. Most of these works are limited to studying the effect of some operating parameters via a sensitivity analysis [14–19]. Nonetheless, several have focused on improving cooling system performance through optimization of the individual component operation. Among them, the works from Martín *et al.* stand out. In [20] they were the first to optimize the year-round operation of a CSP system not only considering the cooling side (a WCT) but also integrating the power block. The problem was formulated as a multiperiod Non-Linear Programming (NLP) problem with the cooling system air flow rate and outlet temperature as decision variables. They showed that the obtained complex problem can feasibly be solved and an average water consumption of 2.1 l/kWh was obtained with the least efficient month amounting to 2.5 l/kWh. In [21] the same strategy was applied this time for a dry cooling alternative (ACC) and formulating the optimization as a multiperiod Mixed Integer Non-Linear Programming (MINLP) problem. This integer extension to the problem was done to account for the addition of a new decision variable: the discrete number of units and fans that make up the ACC *i.e.* their active state. The problem was solved via relaxation of the integer variables and after evaluating the annual operation they found that the optimized dry cooler consumed around 5 % of the total generated power compared to 3.44 % of the wet alternative, and increasing a cent the LCOE (0.16 vs. 0.15 €/kWh, respectively). A limitation of both studies is the use of monthly average values, which masks the significant daily temperature variations—often exceeding 10°C—that coincide with peak power production and can have a substantial impact on cooling system performance.

Little discussion can be found in the literature regarding the operation strategy of combined cooling systems. For water-enhanced dry cooling and parallel configurations, the proposed operation strategy [22–24] consists on always prioritizing the dry sections up until a set value in the condenser pressure is reached, in which case the wet units are activated. This strategy offers a simple and robust solution but leaves a lot of performance on the table.

In Maulbetsch *et al.* [96], a parallel combined system is analyzed, where the operation strategy is set as follows: At some temperature, the condensing pressure achieved will raise above a desired limit. For ambient temperatures above that level, both systems are operated at full design fan power. When the condensing pressure is below that limit, the capacity of the wet section is reduced to maintain it while the dry section is operated at full capacity. At lower temperature where the dry section can maintain the condensing pressure by

[14]: Asfand *et al.* (2020), “Thermodynamic Performance and Water Consumption of Hybrid Cooling System Configurations for Concentrated Solar Power Plants”

[15]: Mdallal *et al.* (2024), “Modelling and Optimization of Concentrated Solar Power Using Response Surface Methodology”

[16]: Hu *et al.* (2018), “Thermodynamic Characteristics of Thermal Power Plant with Hybrid (Dry/Wet) Cooling System”

[17]: Tang *et al.* (2013), “Study on Operating Characteristics of Power Plant with Dry and Wet Cooling Systems”

[18]: Asvapoositkul *et al.* (2014), “Comparative Evaluation of Hybrid (Dry/Wet) Cooling Tower Performance”

[19]: Barigozzi *et al.* (2014), “Performance Prediction and Optimization of a Waste-to-Energy Cogeneration Plant with Combined Wet and Dry Cooling System”

[20]: Martin *et al.* (2013), “Optimal Year-Round Operation of a Concentrated Solar Energy Plant in the South of Europe”

[21]: Martin (2015), “Optimal Annual Operation of the Dry Cooling System of a Concentrated Solar Energy Plant in the South of Spain”

[22]: Wiles *et al.* (1978), *Description and Cost Analysis of a Deluge Dry/Wet Cooling System*.

[23]: Zaloudek *et al.* (1976), *Study of the Comparative Costs of Five Wet/Dry Cooling Tower Concepts*

[24]: Rohani *et al.* (2021), “Optimization of Water Management Plans for CSP Plants through Simulation of Water Consumption and Cost of Treatment Based on Operational Data”

itself, the wet system is no longer operated. Finally, at even lower temperatures, the fan power is gradually reduced on the dry section.

One inherent limitation that no optimization strategy can fully overcome is the seasonal mismatch between ambient temperature and water availability. In many locations, ambient temperatures are lowest —favoring dry cooling— during times of the year when water is most abundant —favoring wet cooling. The opposite occurs during hot, dry summer periods, when cooling demand is highest but water becomes a scarce resource. Many studies report annual water savings figures, but this does not offer a complete picture and can be misleading, as it may mask poor performance during critical periods. Reducing water use during times of abundance, while failing to achieve significant savings during water-scarce periods, does not represent an optimal solution —even if total annual water consumption appears lower.

The Increasing Variability of Rainfall

Water scarcity, stress, and climate change are typically portrayed through a lens of averages and trends. But this is seldom an adequate representation of water availability throughout much of the world, where deviations from trends are widespread and are growing more frequent, as witnessed by the increased frequency of floods and droughts. Adapting to rainfall variability is often much more challenging than accommodating long-term trends because of the unpredictable duration of a deviation, its uncertain magnitude, and its unknown frequency. With climate change, deviations from trends are projected to become more pronounced and more frequent. Inter-annual variability in particular is expected to pose a large threat in some of the world's driest regions.

Source: Uncharted Waters: The New Economics of Water Scarcity and Variability [125]

Significant cost savings can be achieved with increasing water availability, either from the specification of a smaller condenser or by lowering operating turbine exhaust pressures (increasing the wet ratio). In conclusion, there remains significant potential for improved water management through optimized system operation, particularly when resource availability is explicitly considered in the decision-making process:

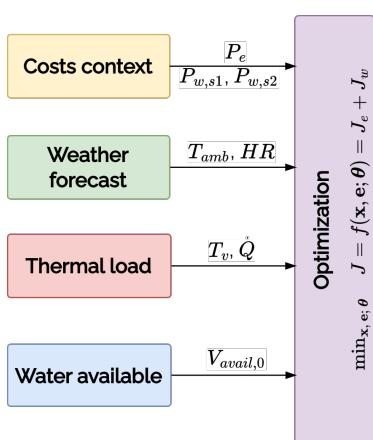


Figure 7.1: Block diagram of the optimization scheme including environment components

1: Although the proposed methodology is applicable to any system requiring thermal load cooling, particular emphasis is placed on water resource availability, given its critical importance in solar thermal applications. See Section 4.2 (Cooling and water use)

- ▶ Humidity is higher at night where ambient temperatures are lower, partially alleviating the limitations of the dry system and making it less unfavorable.
- ▶ Take full advantage of the cheaper and more efficient wet cooling when water is plentiful.
- ▶ Consider the availability of alternative water sources and their dynamic costs.
- ▶ When using a combined cooling system its operation is not trivial but inherently becomes more complex; thus requiring an operation strategy to, at a minimum, robustly satisfy the cooling demand, but preferably also minimize the cost of operation.

This chapter analyzes the optimization of different cooling system configurations, focusing on their two primary resource consumptions: electricity and water. The optimization problems are formulated to minimize the total cost of cooling a thermal load, with cost defined as the combined use of these two resources. The thermal load is treated as an external requirement and is therefore excluded from the decision space. This work addresses existing limitations in the literature and presents, for the first time, an actual optimization of the operation of a combined cooling system in the context of CSP applications.¹

This chapter is organized as follows: Section 7.1 (Environment description) introduces the context by describing the key variables involved, including cost factors,

weather forecasts, thermal load, and water resource availability. Section 7.2 (Static optimization) presents the first optimization approach, focusing on static problems for the dry cooler, wet cooler, and their combined configurations. Section 7.3 (Horizon optimization) introduces a shrinking horizon optimization strategy applied to the combined cooler, optimizing its performance over a prediction horizon. This final section also explores the nature of the problem and outlines the proposed methodology for its resolution.

7.1 Environment description

The environment for the optimization problems includes the following components (See Figure 7.1):

1. **Costs context** There are mainly two operational costs associated with the cooling system: electricity (J_e) and water (J_w). In a system that generates electricity, such as a CSP plant, this is electricity that could otherwise be sold to the market, so the associated price (P_e) is the pool market price. As for the water, two sources are considered: the water price from source 1 is denoted as $P_{w,s1}$, and from source 2 as $P_{w,s2}$, being $P_{w,s1} < P_{w,s2}$.
2. **Weather conditions** The weather variables that have an impact on the cooling system are the ambient temperature (T_{amb}) and the relative humidity (HR) since they set the dry and wet bulb temperatures.
3. **Thermal load** The thermal load is defined either by a vapor flow rate (\dot{m}_v) or a thermal power (\dot{Q}), which enters the condenser at a temperature T_v^2 .
4. **Water resource availability** Two sources of water are assumed to be available, one of them, the cheaper one coming from a dam/reservoir is limited in volume (V_{avail}). This cheaper source (s_1) is prioritized until it is depleted, when the more expensive alternative source (s_2) is used:

$$C_{w,s1,i} = \frac{\min(V_{avail,i}, C_{w,i} \cdot T_s)}{T_s}, \quad (7.1)$$

$$C_{w,s2,i} = C_{w,i} - C_{w,s1,i}, \quad (7.2)$$

$$V_{avail,i} = V_{avail,i-1} - C_{w,s1,i} \cdot T_s, \quad (7.3)$$

2: Vapor can also be referred as steam, usually steam is used when the vapor performs work, like in a turbine.

where i represents the step. At every step the amount used from each source is estimated and the source 1 availability is updated accordingly. C_w represents the flow rate of water consumed and T_s is the sample time at which steps are computed.

7.2 Static optimization

Static optimization problems are defined in a particular instant, given an environment. Decisions are made without considering past states or actions, nor their impact on future states.

From a process perspective this also characterizes the cooling process, except for the water resource availability, being the only variable that depends on the previous state, *i.e.* is not static. Each time a static problem is evaluated, it begins with a specific initial water volume ($V_{avail,0}$) for that step. After solving the problem, this volume must be updated before proceeding to the next step. As a result, evaluating multiple consecutive steps requires a sequential approach.

Reminder: Optimization problem definition

The general optimization function is defined as:^a

$$\min_{\mathbf{x}, \mathbf{e}; \boldsymbol{\theta}} J = f(\mathbf{x}, \mathbf{e}; \boldsymbol{\theta}) \quad \text{s.t.} \quad g_i(\mathbf{x}) \leq 0, \quad i = 1, \dots, m$$

where \mathbf{x} is the decision vector, \mathbf{e} represents the environment, and $\boldsymbol{\theta}$ contains the fixed parameters.

^a See Section 3.2 (Optimization)

In order to streamline the problem formulation, a general combined cooling system model is used for every scenario. This unified model incorporates both the dry and wet coolers, as well as the shared surface condenser. For cases where only one cooler is used, the other can be effectively disabled by setting its associated variables to zero and configuring the hydraulic circuit to prevent water circulation through it.

7.2.1 Dry cooler

In the first case study, the optimization focuses exclusively on the dry cooler. Consequently, all variables and terms associated with the wet cooler, as well as water resource management, are omitted from the formulation, making the problem completely static³. This configuration is illustrated in Figure 7.2 and the problem is defined as follows:

3: Achieved by setting $R_p = 0$ and $R_s = 0$. See Section 6.4 (Complete system) for reference

See Section 6.2 (Dry cooler) for a detailed description of the dry cooler and Section 6.3.1 (Surface condenser) for the condenser model.

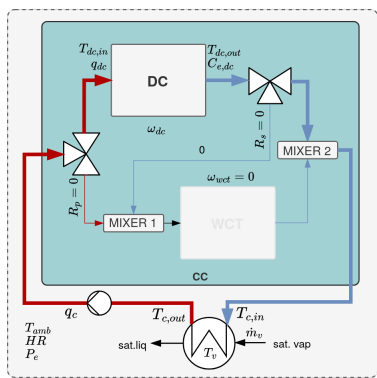


Figure 7.2: Diagram of the dry cooler only cooling problem

Problem 7.1: DC - static

$$\min_{\mathbf{x}, \mathbf{e}; \boldsymbol{\theta}} J = f(\mathbf{x}, \mathbf{e}; \boldsymbol{\theta}) = C_e \cdot P_e$$

with:

$$T_{dc,out}, C_e, T_{c,in}, T_{c,out} = \text{ccs model}(q_c, \omega_{dc}, T_{amb}, T_v, \dot{m}_v)$$

- Decision variables

$$\mathbf{x} = [q_c, \omega_{dc}]$$

- Environment variables

$$\mathbf{e} = [T_{amb}, P_e, T_v, \dot{m}_v]$$

- Fixed parameters

$$\boldsymbol{\theta} = [R_p = 0, R_s = 0, \omega_{wct} = 0]$$

subject to:

- Box-bounds

$$\begin{aligned} &\cdot \omega_{dc} \in [\underline{\omega}_{dc}, \bar{\omega}_{dc}] \\ &\cdot q_c \in [\underline{q}_c, \bar{q}_c] \end{aligned}$$

- Constraints

$$\begin{aligned} &\cdot |T_{dc,out} - T_{c,in}| \leq \epsilon_1 \\ &\cdot |Q_{dc} - Q_{c,released}| \leq \epsilon_2 \\ &\cdot T_{c,out} \leq T_v - \Delta T_{c-v,min} \end{aligned}$$

The cost of cooling (J) is equivalent to the cost of electricity (J_e), which in turn is the product of the electricity price (P_e) and the electricity consumption (C_e). Only two decision variables are defined, the cooling water recirculation flow rate (q_c) and the dry cooler fan speed (ω_{dc}). Any two pair of values for these variables that satisfy the bounds do not necessarily yield a feasible solution. This is why three constraints are introduced, the first one ensures that the outlet cooler temperature matches the inlet condenser temperature (since they are directly connected), the second one ensures that the cooling duty of the dry cooler matches the one of the condenser while the last one ensures that the condenser outlet temperature respects the minimum temperature difference with the vapor temperature⁴.

7.2.2 Wet cooler

Conversely to the dry cooler, the wet cooler optimization problem is configured by setting $R_p = 1$, effectively disabling the dry cooler. In this case, water associated variables are included in the problem formulation⁵:

Problem 7.2: WCT – static

$$\min_{\mathbf{x}, \mathbf{e}; \boldsymbol{\theta}} J = f(\mathbf{x}, \mathbf{e}; \boldsymbol{\theta}) = J_e + J_w$$

with:

$$\begin{aligned} J_e &= C_e \cdot P_e \\ J_w &= C_{w,s1} \cdot P_{w,s1} + C_{w,s2} \cdot P_{w,s2} \\ C_{w,s1} &= \min(V_{avail}/T_s, C_w) \\ C_{w,s2} &= C_w - C_{w,s1} \end{aligned}$$

$$T_{wct,out}, C_e, C_w, T_{c,in}, T_{c,out} = \text{ccs model}(q_c, \omega_{wct}, T_{amb}, HR, T_v, \dot{m}_v)$$

- Decision variables

$$\mathbf{x} = [q_c, \omega_{wct}]$$

- Environment variables

$$\mathbf{e} = [T_{amb}, HR, P_e, P_{w,s1}, P_{w,s2}, V_{avail}, T_v, \dot{m}_v]$$

- Fixed parameters

$$\boldsymbol{\theta} = [R_p = 1, R_s = 0, \omega_{dc} = 0]$$

subject to:

- Box-bounds

$$\begin{aligned} \cdot \omega_{wct} &\in [\underline{\omega}_{wct}, \bar{\omega}_{wct}] \\ \cdot q_c &\in [\underline{q}_c, \bar{q}_c] \end{aligned}$$

- Constraints

$$\begin{aligned} \cdot |T_{wct,out} - T_{c,in}| &\leq \epsilon_1 \\ \cdot |\dot{Q}_{wct} - \dot{Q}_{c,released}| &\leq \epsilon_2 \\ \cdot T_{c,out} &\leq T_v - \Delta T_{c-v,min} \end{aligned}$$

4: In order to better comprehend why mismatches between cooler and condenser can exist, the reader is referred to Section 6.4 (Complete system)

5: See Section 6.1 (Wet cooler) for a detailed description of the wet cooler and condenser model.

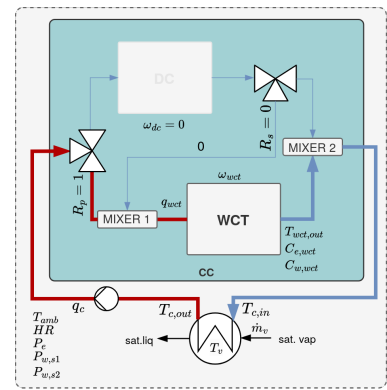


Figure 7.3: Diagram of the wet cooler only cooling problem

In this version of the problem, the decision vector is composed by the recirculation flow rate, but now the fan speed of the wet cooler (ω_{wct}) is included.

The cost of cooling now includes the cost of water (J_w) and its availability is updated using the water consumption (C_w) as described in Equations 7.1–7.3. The environment now includes the air relative humidity and water prices.

7.2.3 Combined cooler

The last static optimization problem is the combined cooler, which incorporates both the dry and wet coolers, as well as the condenser. Here the hydraulic distribution is not fixed but is part of the decision variables, allowing the optimization to determine the optimal distribution between the two coolers. The problem is defined as follows⁶:

6: See Section 6.4 (Complete system) for a detailed description of the combined cooler and condenser model.

Problem 7.3: CC - static

$$\min_{\mathbf{x}, \mathbf{e}; \boldsymbol{\theta}} J = f(\mathbf{x}, \mathbf{e}; \boldsymbol{\theta}) = J_e + J_w$$

with:

$$J_e = C_e \cdot P_e$$

$$J_w = C_{w,s1} \cdot P_{w,s1} + C_{w,s2} \cdot P_{w,s2}$$

$$C_{w,s1} = \min(V_{avail}/T_s, C_w)$$

$$C_{w,s2} = C_w - C_{w,s1}$$

$$T_{cc,out}, C_e, C_w, T_{c,in}, T_{c,out} = \text{ccs model}(q_c, R_p, R_s, \omega_{dc}, \omega_{wct}, T_{amb}, HR, T_v, \dot{m}_v)$$

- Decision variables

$$\mathbf{x} = [q_c, R_p, R_s, \omega_{dc}, \omega_{wct}]$$

- Environment variables

$$\mathbf{e} = [T_{amb}, HR, P_e, P_{w,s1}, P_{w,s2}, V_{avail}, T_v, \dot{m}_v]$$

subject to:

- Box-bounds

$$\begin{aligned} & \cdot \omega_{dc} \in [\underline{\omega}_{dc}, \bar{\omega}_{dc}] \\ & \cdot \omega_{wct} \in [\underline{\omega}_{wct}, \bar{\omega}_{wct}] \\ & \cdot q_c \in [\underline{q}_c, \bar{q}_c] \\ & \cdot R_p \in [0, 1] \\ & \cdot R_s \in [0, 1] \end{aligned}$$

- Constraints

$$\begin{aligned} & \cdot |T_{cc,out} - T_{c,in}| \leq \epsilon_1 \\ & \cdot |\dot{Q}_{cc} - \dot{Q}_{c,released}| \leq \epsilon_2 \\ & \cdot T_{c,out} \leq T_v - \Delta T_{c-v,min} \end{aligned}$$

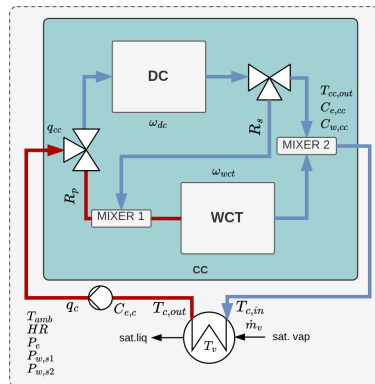


Figure 7.4: Diagram of the combined cooler and condenser problem

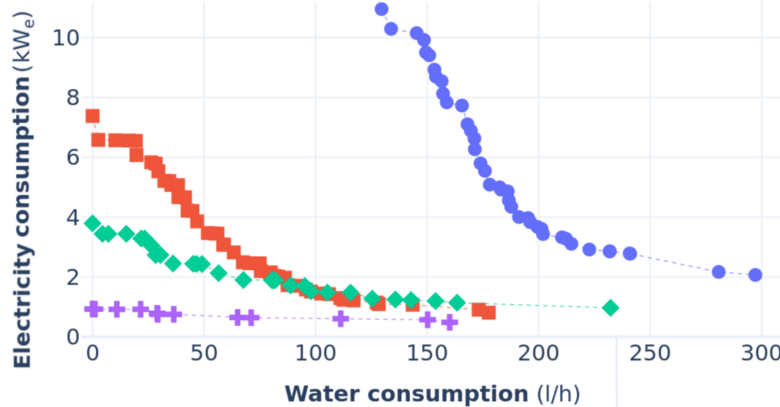
Since any given decision variables do not necessarily yield a feasible solution, the same three constraints as in the previous problems are included to ensure the proper operation of the system. The decision vector now includes the recirculation flow rate, the fan speeds of both coolers, and the hydraulic distribution variables (R_p and R_s). The environment variables remain unchanged with respect to the previously presented wet cooler case.

To better understand the combined cooler static optimization problem, Figure 7.5 illustrates the various ways a combined cooler⁷ can meet a specific cooling load under four diverse scenarios: two different environment conditions and

7: Particularly for the pilot plant described in Chapter 5

Pareto fronts in different representative scenarios

- ● - (I) | 20050623 | $T_{amb}=30.0\text{ }^{\circ}\text{C}$, HR=40 %, $T_v=42.0\text{ }^{\circ}\text{C}$, $\dot{Q}=200\text{ kW}_{th}$
- ■ - (II) | 20050623 | $T_{amb}=30.0\text{ }^{\circ}\text{C}$, HR=40 %, $T_v=42.0\text{ }^{\circ}\text{C}$, $\dot{Q}=120\text{ kW}_{th}$
- ◆ - (III) | 20051221 | $T_{amb}=10.0\text{ }^{\circ}\text{C}$, HR=70 %, $T_v=42.0\text{ }^{\circ}\text{C}$, $\dot{Q}=200\text{ kW}_{th}$
- + - (IV) | 20051221 | $T_{amb}=10.0\text{ }^{\circ}\text{C}$, HR=70 %, $T_v=42.0\text{ }^{\circ}\text{C}$, $\dot{Q}=120\text{ kW}_{th}$



Reminder: Pareto front

When dealing with multiple objectives where no single solution is optimal, but improvements in one objective lead to trade-offs in others, a set of points is obtained that represents the best trade-offs between the objectives —known as a Pareto front^a.

^a See Section 3.2.4 (Multi-objective optimization)

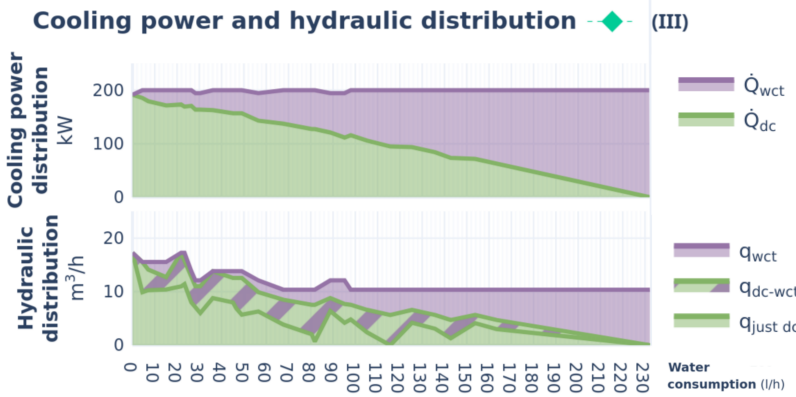


Figure 7.5: Pareto fronts in different representative scenarios (top) and detailed power and hydraulic distribution for a specific scenario (bottom)

cooling loads. The optimal operating points are evaluated in terms of the two consumptions: electricity (C_e) and water (C_w) and form the Pareto front.

In **Case I**, which presents the highest water and electricity consumptions, it can be observed that the water consumption is always above zero. This indicates that the use of the WCT is essential, as the DC alone is not capable of cooling the nominal thermal load at $42\text{ }^{\circ}\text{C}$, during summer conditions. If the system operates only with the DC, the vapor temperature (*i.e.* turbine backpressure) would rise, negatively impacting the power cycle performance of a CSP plant. Maintaining the same ambient conditions, when the thermal power is reduced (**Case II**), it becomes feasible to operate using only the DC, although with a high parasitic load (7.4 kW_e). By combining the DC with the WCT, electricity consumption can be reduced by half, with water consumption remaining below 50 l/h. Under more favorable winter conditions (**Cases III and IV**), the DC alone becomes more efficient as demonstrated by the significant reduction in electricity demand. Still, when coupled with the WCT, electricity consumption can decrease by about 35 % at full thermal load, with a limited water consumption of 50 l/h. At reduced thermal load the additional benefit of the WCT becomes negligible, making this the only case where operating with DC alone is more favorable.

The figure also details the optimal cooling power and hydraulic distribution for **Case III**. The background color represents the distribution of cooling power:

green indicates a greater contribution from the dry cooler, while purple indicates a greater contribution from the wet cooler. To avoid water consumption, steam must be cooled exclusively using the DC. At the other extreme, to minimize electricity consumption, only the WCT should be used. At intermediate optimal points, both systems are combined. This is achieved by series configurations at prioritized dry cooling and progressively increasing parallel configurations for predominantly WCT use. As expected, the cooling water flow rate (Figure 7.5 - *Hydraulic distribution*) is higher ($17 \text{ m}^3/\text{h}$) for a drier operation, since the reduced temperature component of the cooling driving force is limited and therefore needs to be compensated with a higher flow. Higher compared to the wet operation and its inherently higher temperature difference available, allowing for a better (lower) flow of $10 \text{ m}^3/\text{h}$. In Figure 7.5 - *Cooling power distribution* it is also interesting to highlight how the series-parallel flexibility of the system enables it to achieve almost a continuous division of the cooling power from full dry to full wet, at least for this particular case.

7.3 Horizon optimization

8: Bold notation is used to indicate that the variable is an array and not a single value, e.g. \mathbf{x}

The problem structure is very similar to the static alternative, the main difference is that now the decision and environment vectors are composed not from the expected value for the optimization step, but an array of values from the current optimization step (i) until the end of the prediction horizon (n_{steps})⁸:

Problem 7.4: CC - horizon

$$\min_{\mathbf{x}, \mathbf{e}; \boldsymbol{\theta}} J = f(\mathbf{x}, \mathbf{e}; \boldsymbol{\theta}) = \sum_{i=1}^{n_{\text{steps}}} (J_{e,i} + J_{w,i}) \cdot T_s$$

with:

for $i = 1 \dots n_{\text{steps}}$:

$$\begin{aligned} J_{e,i} &= C_{e,i} \cdot P_{e,i} \\ J_{w,i} &= C_{w,s1,i} \cdot P_{w,s1,i} + C_{w,s2,i} \cdot P_{w,s2,i} \\ C_{w,s1,i} &= \min(V_{\text{avail},i}/T_s, C_{w,i}) \\ C_{w,s2,i} &= C_{w,i} - C_{w,s1,i} \\ V_{\text{avail},i} &= V_{\text{avail},i-1} - C_{w,s1,i} \cdot T_s \\ T_{cc,out,i}, C_{e,i}, C_{w,i}, T_{c,out,i} &= f(q_{c,i}, R_{p,i}, R_{s,i}, \omega_{dc,i}, \omega_{wct,i}, T_{amb,i}, HR_i, T_{v,i}, \dot{m}_{v,i}) \end{aligned}$$

► Decision variables

$$\mathbf{x} = [\mathbf{q}_c, \mathbf{R}_p, \mathbf{R}_s, \boldsymbol{\omega}_{dc}, \boldsymbol{\omega}_{wct}]$$

$$\text{where } \mathbf{x} = [x_{1,1}, \dots, x_{1,n_{\text{steps}}}, \dots, x_{n_x,n_{\text{steps}}}]$$

► Environment variables

$$\mathbf{e} = [T_{amb}, HR, \mathbf{P}_e, \mathbf{P}_{w,s1}, \mathbf{P}_{w,s2}, V_{\text{avail},0}, T_v, \mathbf{m}_v]$$

$$\text{where } \mathbf{e} = [e_{1,1}, \dots, e_{1,n_{\text{steps}}}, \dots, e_{n_e,n_{\text{steps}}}]$$

subject to:

► Box-bounds

$$\begin{aligned} \cdot \boldsymbol{\omega}_{dc} &\in [\underline{\omega}_{dc}, \overline{\omega}_{dc}] \\ \cdot \boldsymbol{\omega}_{wct} &\in [\underline{\omega}_{wct}, \overline{\omega}_{wct}] \end{aligned}$$

- $\mathbf{q}_c \in [q_c, \bar{q}_c]$
- $R_p \in [0, 1]$
- $R_s \in [0, 1]$
- Constraints, $\forall i = 1 \dots n_{\text{steps}}$:
 - $|T_{cc,out,i} - T_{c,in,i}| \leq \epsilon_1$
 - $|\dot{Q}_{cc,i} - \dot{Q}_{c,released,i}| \leq \epsilon_2$
 - $T_{c,out,i} \leq T_{v,i} - \Delta T_{c-v,min}$

Although this formulation allows for an arbitrarily long prediction horizon, in practice it is limited to the number of steps for which reliable forecasts of the environmental variables are available. In this study, water availability is allocated on a daily basis; therefore, the prediction horizon begins at the current time when the optimization is launched and extends it until the end of the operation day.

Remark 7.3.1 A fixed sample time (T_s) is assumed, although the formulation can be adapted to handle variable sample times if the problem data are provided as time series with non-uniform time steps.

7.3.1 A discussion on solving the optimization problem

As defined, the CCS problem decision vector is composed by five variables that are direct inputs on the process, *i.e.* decision variables represent actuators in the system. As explained in Section 6.4, not every combination of these variables yields a feasible solution. In the real system, this implies that stable operation would not be achieved for such a set of inputs⁹. To check for feasible operation the three mentioned constraints are introduced. However, this increases the complexity of the solution space significantly, since the solution space will not be continuous, but as seen in Figure 7.6, it will be formed by islands of feasible solution space regions separated by infeasible regions. This means that finding a feasible solution is not trivial, and the optimization algorithm will need to explore the solution space-a global search algorithm-in an attempt to find the global minimum.

For one single step (equivalent to the static Problem 7.3), most global search algorithms with multiple runs are able to consistently find the global optima. Local gradient-based algorithms are not suitable in this case because of its sensitivity to the initial solution and often converge to local minima, even when coupled with other techniques such as Generalized Monotonic Basin Hopping [126].

The problem becomes significantly more complex when the prediction horizon is extended, the decision vector grows five-fold for each additional step in the prediction horizon, and the optimization algorithm is tasked with finding a feasible solution for this much larger decision vector, in a very complex solution space, at once for all steps. The chances of finding a feasible solution decrease significantly, and this was reflected during implementation in the failure to find a single feasible solution. Even when providing an initial guess composed by the static problem solutions for each step in a 24 steps horizon, the returned solution was that same initial guess.

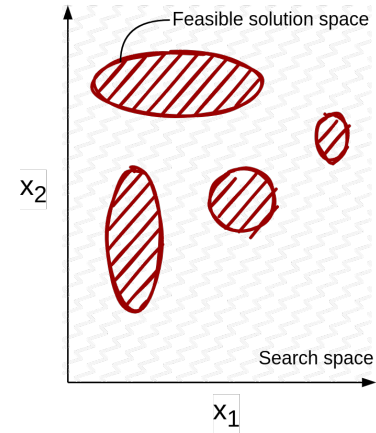


Figure 7.6: Visualization of a constrained search space for two decision variables

9: Either the system would be overcooled, causing the vapor pressure and temperature to decrease until a new equilibrium is reached, or undercooled, leading them to increase instead

[126]: Wales et al. (1997), "Global Optimization by Basin-Hopping and the Lowest Energy Structures of Lennard-Jones Clusters Containing up to 110 Atoms"

7.3.2 Proposed solution: Decomposition-based multi-objective optimization with trajectory planning

10: Alternative wording: Pareto front chaining, multi-step Pareto optimization, path planning on Pareto surfaces.

11: This is akin to a pathfinding or the traveling salesman problem over the Paretos set

A two-stage optimization strategy is proposed to solve a multi-step decision problem¹⁰. At each step of the prediction horizon, a multi-objective optimization problem is independently solved, yielding a Pareto front. A global optimization problem is then formulated to select a path through the sequence of Pareto fronts, minimizing a cumulative objective *i.e.* the cost of cooling¹¹.

The methodology is illustrated in Figure 7.7 and its components are described in the following sections.

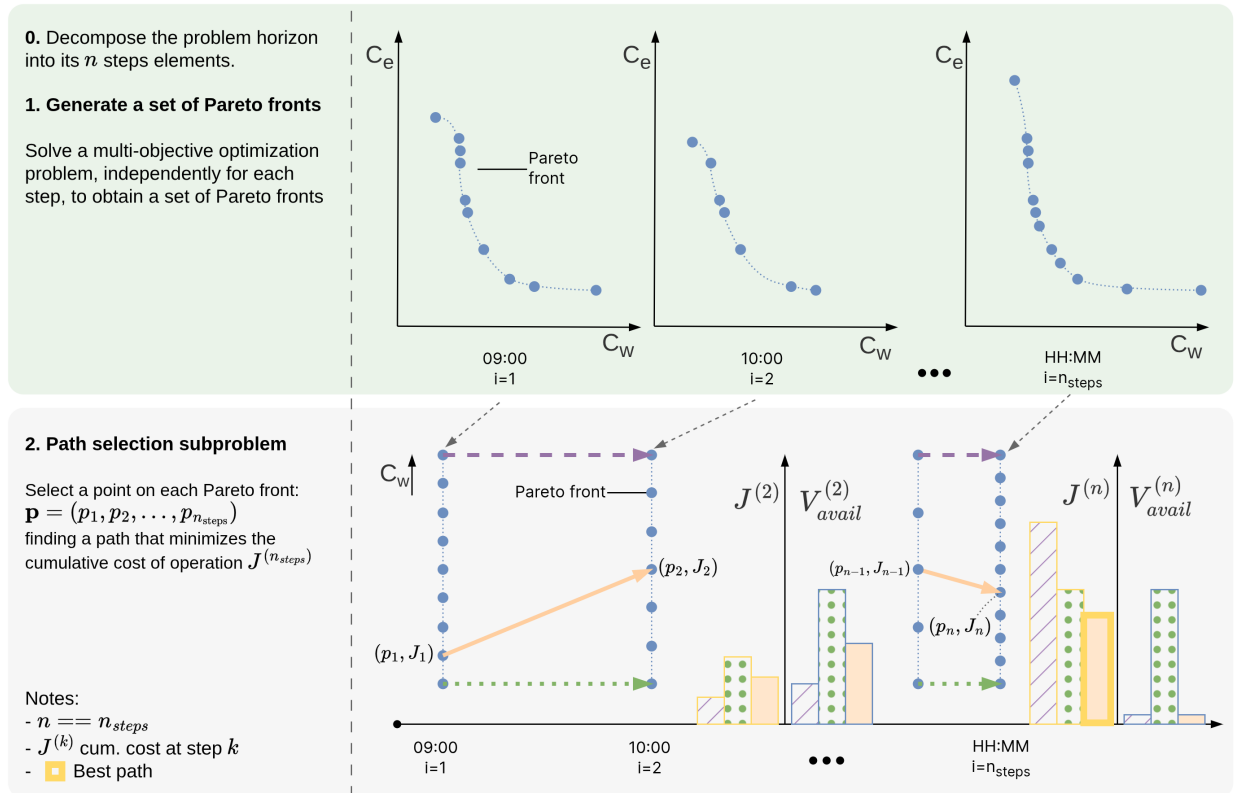


Figure 7.7: Proposed methodology. Decomposition-based multi-objective optimization with trajectory planning. Blue-dots (•) represent points on the Pareto front. Three paths are illustrated: a water-greedy dash-purple (—) path, a water-conservative green-dotted path (..) and an optimized-approach solid-orange path (—).

Solving the multi-objective optimization problems

To limit the complexity of the problem, the decision space can be reduced by one variable by analyzing how the complete model is solved and described in Section 6.4 (Complete system); firstly, the condenser can be solved just by using the recirculation flow rate (q_c), it follows the dry cooler by adding the first valve ratio (R_p) and dry cooler fan speed (ω_{dc}). The only remaining component to solve is the wet cooler. The wet cooler inlet conditions ($q_{wct}, T_{wct,in}$) can be determined by using the second valve ratio (R_s). As for the outlet conditions, from the condenser evaluation, its inlet temperature is known and it sets the value of the combined cooler outlet temperature ($T_{cc,out}$), which in turn is the

result of the mixing from the DC and WCT outlet temperatures ($T_{dc,out}$ and $T_{wct,out}$, respectively).

The result of this analysis is that the wet cooler fan speed is not a decision variable anymore, but an output of the model, which can be computed by inverting the wet cooler model, where an outlet temperature is provided as input, and the fan speed is computed as an output. Summarizing, the decision vector can be reduced from five to four variables:¹²

$$\mathbf{x} = [q_c, R_p, R_s, \omega_{dc}]$$

More importantly, now the optimization algorithm does not need to find a set of five inputs that produce a feasible solution in a complex solution space, but only four values from which a feasible wet cooling tower fan speed exists¹³, thus greatly simplifying the solution-space complexity.

A straightforward approach to solve the multi-objective optimization is to do a grid-search over the decision space, evaluating the model for every combination of decision variables, and then storing only the points for which a feasible ω_{wct} exists. This approach is not recommended for large decision spaces, but for the four-dimensional decision space and with a model that can be evaluated in fractions of a second, it is feasible.

Next, the Pareto front is computed from the feasible points, which are evaluated in terms of the two consumptions: electricity (C_e) and water (C_w). By definition, the Pareto front is the set of points that cannot be improved in one objective without worsening the other, and it is computed by checking for each point if there is another point that is better in both objectives, and if so, it is removed from the set of feasible points. The remaining points form the Pareto front. This process is repeated for each step in the horizon, resulting in a set of Pareto fronts as visualized in Figure 7.7–1.

Path selection subproblem

The path selection subproblem is a combinatorial optimization problem over a layered, dynamic-weighted directed graph. Each layer corresponds to a time step in the prediction horizon, and each node within a layer represents a point on the corresponding Pareto front. The objective is to find a path $\mathbf{p} = (p_1, p_2, \dots, p_{n_{steps}})$, where p_i is the selected node at time step i , that minimizes the total cumulative cost J along the path. Each layer weight (i.e., the water cost component) is dynamic—that is, it depends on the trajectory followed to reach that layer. The problem can be formulated as:

$$\min_{\mathbf{p}, e} \quad J = \sum_{i=1}^{n_{steps}} J_i(p_i, V_{avail,i-1}). \quad (7.4)$$

The step cost contribution J_i depends on both the consumptions (i.e. electricity and water) of the node p_i , as well as on a dynamic cost function determined by the traversed path. In particular, the water cost component is correlated with the water resource availability ($J_{w,i} = f(V_{avail,i-1})$ ¹⁴). The step associated cooling cost is:

$$J_i = P_{e,i} \cdot C_e(p_i) + P_{w,s1,i} \cdot C_{w,s1}(p_i, V_{avail,i-1}) + P_{w,s2,i} \cdot C_{w,s2}(p_i, V_{avail,i-1}), \quad (7.5)$$

where:

12: This reasoning works only for a system with this particular configuration. A different combined cooler layout would require a different analysis.

13: i.e. within its bounds $\omega_{wct} \in [\underline{\omega}_{wct}, \overline{\omega}_{wct}]$

14: See Equations 7.1–7.3

- ▶ $C_e(p_i), C_{w,sx}(p_i, V_{avail,i-1})$: electricity and water consumption (from s_1 and s_2) at node p_i .
- ▶ $P_{e,i}, P_{w,sx,i}$: prices for electricity and water (from s_1 and s_2) at step i .

This dynamic cost function introduces path-dependency into the cost function, and makes the problem non-trivial to solve via simple shortest path algorithms. Nonetheless, its calculation is straightforward and can be performed almost instantly, thus making it suitable for dynamic programming, graph search (like Dijkstra or A*), or metaheuristics such as genetic algorithms.

The subproblem is illustrated in Figure 7.7–2. Each layer corresponds with the Pareto front of a step in the horizon and each node, blue-dot (•), represents a point in the particular step Pareto and is associated with a dynamic cost (J_i). Sequentially traversing the layers selecting one point per layer up to a certain layer, yields the cumulative cost up to that step ($J^{(i)}$). Three paths are illustrated in Figure 7.7–2. The dash-purple (- -) path is a path that chooses nodes with a high water use¹⁵, so in the first split it can be seen it achieves the lowest cost of cooling ($J^{(2)}$), but also leaves the least water available for the next steps ($V_{avail}^{(2)}$), resulting in a higher total cost of cooling at the end of the horizon ($J = J^{(n)}$). On the other hand, the green-dotted path (..) selects the nodes with the lowest water use, this translates in a consistently higher cost of operation and leaving some water available at the end of the horizon. Because of the formulation of the problem, this is sub-optimal since this unused water is considered lost. Finally, the solid-orangey path (—) is a compromise between the two, it uses water efficiently, leaving no water available at the end of the horizon and minimizing the overall cost of cooling.

15: In Figure 7.7, nodes are ordered with increasing values of C_w from bottom to top.

Validation in the combined cooling pilot plant

TL;DR

This chapter presents the modelling and optimization results for the combined cooling pilot plant. First calibration and training results of various modelling approaches, followed by validation of the complete integrated model. The best performing data-driven model, the Gaussian-Process Regression (GPR) is calibrated using synthetic data from the first-principle models. This surrogate and on-demand model that can be adapted to the particular case study, while still being fast and efficient in terms of computational resources achieves a Mean Absolute Error (MAE) below 0.97 °C for temperatures and 194 l/h for water consumption. In the second part of the chapter, the proposed optimization strategies are compared. The horizon optimization alternative, which is also validated experimentally, shows superior performance.

8.1 Modelling	71
8.1.1 Wet cooler model alternatives comparison and validation	71
8.1.2 Dry cooler model alternatives comparison and validation	73
8.1.3 Surface condenser model	75
8.1.4 Complete system model validation	76
8.2 Control and optimization	78
8.2.1 Choosing an optimization algorithm	78
8.2.2 Simulation results	80
8.2.3 Experimental validation	83

8.1 Modelling

The system consists of two main components, the WCT and the DC, which are modelled using different approaches and compared. The alternatives considered are:

1. A first-principles approach, described in Section 6.1.1 and Section 6.2.1 for the WCT and DC, respectively.
2. Artificial Neural Network (ANN), as introduced in Section 3, with different network architectures: Feedforward, Cascade-forward, and Radial Basis.
3. Random Forest, described in Section 6.
4. Gradient Boosting, described in Section 6.
5. Gaussian Process Regression, described in Section 3.1.2.

In addition, the physical model of the surface condenser is validated. Finally, the selected modelling alternative is integrated with the remaining system components (Section 6.3) and validated at the system level in Section 8.1.4 (Complete system model validation).

8.1.1 Wet cooler model alternatives comparison and validation

Physical model

As explained in Section 5.2, three experimental campaigns have been performed. Using data from the fan calibration tests (Table 5.4 – *WCT-fan*), a function (mapping) is fitted that relates the air mass flow rate at the outlet of the tower, $\dot{m}_{wct,air}$, with the fan speed, ω_{wct} :

$$\dot{m}_{wct,air} = -0.0014\omega_{wct}^2 + 0.1743\omega_{wct} - 0.7251. \quad (8.1)$$

And with data from the calibration campaign (Table 5.4 – *WCT-cal*), the Merkel performance number, Me. Figure 8.1 shows the variation of the Merkel number as a function of the water-to-air mass flow ratio ($\dot{m}_w/\dot{m}_{wct,air}$). As can be seen, the Me decreases with $\dot{m}_w/\dot{m}_{wct,air}$ values following a linear trend on log-log

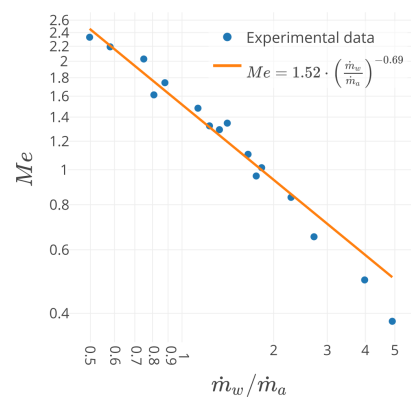


Figure 8.1: Experimental results for the Me number as a function of $\dot{m}_w/\dot{m}_{wct,air}$

scale. Following the correlation for the Merkel number of a wet cooling tower described in Section 6.1.1, the parameters c and n obtained from the data fitting are 1.52 and 0.69, respectively.

Data-driven

In order to generate the data-driven from first-principles alternative, the most relevant input variables identified in Section ?? are discretized using a fixed number of resolution steps (n in Table 8.1) for each variable, within ranges based on expected operating conditions, as defined in Table 8.1.

Table 8.1: Bounds and discretization of the model WCT input variables.

x	Units	lb	ub	n
T_{amb}	°C	3	50	7
ΔT_{amb-in}	°C	3	30	7
q_{dc}	m ³ /h	0.00	1.00	5
w_{dc}	%	11.00	99.18	10
w_{wct}	%	21.00	93.42	10

Figure 8.7 (a) shows the generated input space distribution. The upper plot shows the frequency distribution of the samples while the lower one the actual values per input, where the x-axis represents the samples and the y-axis the values for each of the input variables.

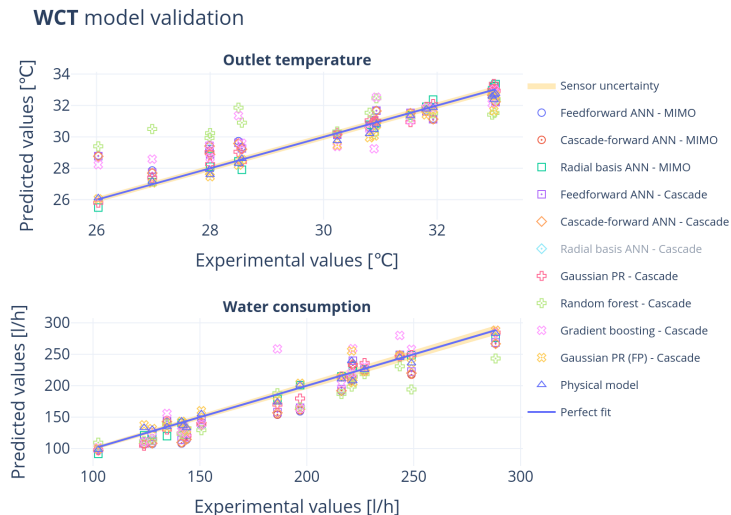


Figure 8.2: WCT models performance comparison between the different modelling approaches.



1: Described in Section 3.1.5

Validation

The results of each modelling alternative and its comparison can be visualized in Figure 8.2. It shows the results obtained with the models using the validation dataset (Table 5.4 – WCT-val). In Table 8.2, the performance of the studied modelling approaches are included for the different performance metrics¹ where T represents the performance metric value for the training / calibration dataset and V for the validation one.

In both the figure and the table, there are two Gaussian PR models: one trained using the experimental data (labeled as *Gaussian PR*) and the second is the surrogate model trained using the synthetic data from the physical model (labeled as *Gaussian PR (FP)*).

Comparing the physical model to the data-driven ones, it can be seen that there are three groups: gradient boosting and random forest alternatives underperform with R^2 values around 0.8 and some clear outliers in Figure 8.2. Artificial Neural Network (ANN) alternatives in general provide good results, specially the radial-basis architecture. Finally, the Gaussian Process Regression approach provides the best results among the data-driven alternatives, with R^2 values above 0.95 for both output variables. This advantage is maintained

even in the case of the surrogate model with R^2 values of 0.94 and 0.95 for the outlet temperature and water consumption, respectively. The physical model provides superior performance for both output variables: obtaining an Root Mean Squared Error (RMSE) of 0.33 °C and an R^2 of 0.98 for the temperature and in terms of water consumption, RMSE and R^2 (8.5 l/h and 0.97). This explains how the surrogate model is able to outperform many of the data-driven alternatives, as it provides a good approximation of the superior physical model. It achieves this with a fraction of the computational cost, vectorization support, limited need for experimental data (same as the physical model) and covering a wide input space.

Table 8.2: Summary table of the prediction results obtained with the different modelling approaches studied.

Predicted variable	Modelling alternative	Model config	Topology	Performance metric								Evaluation time (s)	
				R^2 (-)		RMSE (s.u.)		MAE (s.u.)		MAPE (%)			
				T	V	T	V	T	V	T	V		
$T_{wct,out}$ (°C)	Physical model	-	-	-	0.98	-	0.33	-	0.27	-	0.87	6.288	
	Feedforward ANN	MIMO	20-2	0.90	0.81	0.60	0.97	0.42	0.67	1.36	2.36	0.004	
	Cascade-forward ANN	MIMO	10-10-2	0.90	0.82	0.60	0.93	0.44	0.65	1.42	2.27	0.005	
	Radial basis ANN	MIMO	34-2	0.97	0.97	0.34	0.41	0.21	0.28	0.66	0.94	0.007	
	Feedforward ANN	Cascade	20-1	0.90	0.82	0.60	0.93	0.43	0.65	1.41	2.26	0.011	
	Cascade-forward ANN	Cascade	10-10-1	0.90	0.83	0.60	0.92	0.43	0.64	1.40	2.24	0.010	
	Radial basis ANN	Cascade	92-1	0.97	-1.44	0.33	3.45	0.10	2.12	0.32	743	0.009	
	Gaussian PR	Cascade	N/A	0.99	0.97	0.20	0.37	0.15	0.26	0.47	0.89	0.001	
	Random forest	Cascade	N/A	0.75	0.30	0.96	1.85	0.60	1.46	2.03	5.05	0.078	
	Gradient boosting	Cascade	N/A	1.00	0.68	0.00	1.24	0.00	0.95	0.01	3.29	0.015	
C_w (l/h)	Gaussian PR (FP)	Cascade	N/A	1.00	0.94	0.32	0.54	0.15	0.41	0.52	1.32	0.105	
	Physical model	-	-	-	0.97	-	8.47	-	6.74	-	3.74	6.288	
	Feedforward ANN	MIMO	20-2	0.92	0.83	14.77	21.58	11.98	18.64	9.91	10.75	0.004	
	Cascade-forward ANN	MIMO	10-10-2	0.92	0.84	15.47	20.90	12.51	17.84	10.48	10.22	0.005	
	Radial basis ANN	MIMO	34-2	0.99	0.97	5.58	9.34	3.81	7.47	3.23	4.68	0.007	
	Feedforward ANN	Cascade	20-1	0.92	0.88	15.00	18.45	11.97	15.77	10.20	8.92	0.011	
	Cascade-forward ANN	Cascade	10-10-1	0.92	0.85	15.01	20.34	12.11	17.66	10.00	10.18	0.010	
	Radial basis ANN	Cascade	33-1	0.99	0.93	4.99	14.28	3.45	10.14	2.68	6.22	0.009	
	Gaussian PR	Cascade	N/A	0.99	0.95	4.74	12.00	3.61	9.96	3.09	6.32	0.001	
	Random forest	Cascade	N/A	0.89	0.80	17.35	23.23	10.51	18.51	7.58	9.73	0.078	
	Gradient boosting	Cascade	N/A	1.00	0.77	0.24	25.07	0.07	17.21	0.05	9.55	0.015	
	Gaussian PR (FP)	Cascade	N/A	0.98	0.95	10.85	11.63	4.81	8.14	3.74	4.52	0.105	

s.u. stands for same units as the predicted variable

8.1.2 Dry cooler model alternatives comparison and validation

Physical model

The following $\dot{m}_{dc,air} - \omega_{dc}$ relation was obtained with the Table 5.4 – DC-fan dataset

$$\dot{m}_{dc,air} = 0.30195 \cdot \omega_{dc} - 1.02179. \quad (8.2)$$

The DC model uses this linear function to estimate the air mass flow rate, with the ω_{dc} input applied in the pilot plant.

Once the air mass flow rate is established, the set of 27 experimental points (see Table 5.4 – DC-cal) is used to fit the experimental data to Equation 6.10. To do so, Equations 6.5–6.9 were used to determine the air side heat transfer coefficient using the inlet and outlet water temperatures, the air inlet temperature, and the mass flow rates for both fluids as known values.

Figure 8.3 shows the measured air side Nusselt number as a function of the air side Reynolds number and the fitted equation as a straight line. The correlation (using Equation 8.3) fits 82 % of the data points with a deviation lower than 20 %.

$$Nu_a = 0.006411 \cdot Re_{air}^{0.9143} \cdot Pr_{air}^{0.36}. \quad (8.3)$$

DC Nusselt number validation

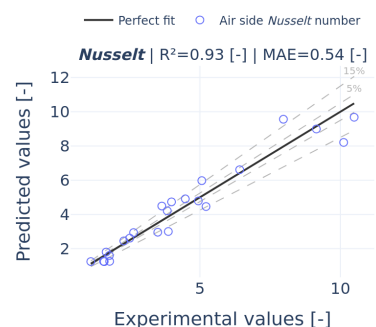


Figure 8.3: Air side Nusselt number vs air side Reynolds number for the air cooled heat exchanger

Data-driven

In order to generate the data-driven from first-principles alternative, the most relevant input variables identified in Section 6.2.2 are discretized using a fixed number of resolution steps for each variable, within ranges based on expected operating conditions, as defined in Table 8.3. Figure 8.7 (b) visualizes the generated input space distribution where it can be appreciated that the samples are well distributed across the entire input space.

Table 8.3: Bounds and discretization of the model input variables.

x	Units	lb	ub	n
T_{amb}	°C	3	50	7
$\Delta T_{amb-dc,in}$	°C	3	30	7
q_{dc}	m ³ /h	6	24	7
$T_{dc,in}$	°C	25	45	-
w_{dc}	%	11	99.18	6

2: Described in Section 3.1.5

Validation

The results of the different modelling alternatives for predicting the outlet temperature can be seen in Table 8.4 (with the validation dataset, Table 5.4 – DC-val). The table presents the performance of the physical and data-driven approaches in terms of the selected performance metrics².

Once again, two Gaussian Process Regression models are included: one trained directly with the experimental data (*Gaussian PR*) and the other acting as a surrogate trained with the synthetic data from the physical model (*Gaussian PR (FP)*)).

The physical model itself provides robust performance, with $R^2 = 0.98$ on the validation set and the lowest error metrics among the deterministic approaches (RMSE = 0.50 °C, MAE = 0.42 °C, and Mean Absolute Percentage Error (MAPE) = 1.28 %). Nevertheless, the Gaussian PR trained with experimental data surpasses this performance in all metrics: it achieves R^2 values of 0.99 for both training and validation, and substantially lower error indicators (RMSE = 0.24–0.32 °C, MAE = 0.19–0.25 °C). The surrogate version, Gaussian PR (FP), also delivers excellent results, nearly matching the experimental Gaussian PR model with R^2 values close to 1.00 and very low errors (RMSE = 0.03–0.53 °C, MAE = 0.02–0.44 °C). Importantly, this surrogate achieves such accuracy at an extremely low evaluation time (0.002 s), which is one order of magnitude faster than the physical model.

Among the machine learning alternatives, the feedforward and cascade-forward ANN architectures yield reasonable results, with validation R^2 values between 0.78 and 0.85. However, their errors (RMSE ≈ 1.37–1.62 °C and MAPE ≈ 3–4 %) are significantly higher than those of the Gaussian PR. Tree-based methods show mixed outcomes: random forest underperforms with validation $R^2 = 0.61$ and high prediction errors (RMSE = 2.17 °C, MAPE = 4.69 %), while gradient boosting achieves nearly perfect training performance but suffers from overfitting, with validation $R^2 = 0.86$ and errors similar to the ANN alternatives.

In summary, the Gaussian Process Regression models clearly outperform all other data-driven methods, consistently reaching R^2 values above 0.98 and very low error levels. The surrogate version (*Gaussian PR (FP)*) combines this predictive accuracy with extremely low computational cost, explaining its advantage over more complex architectures. The physical model, although slightly

Table 8.4: Summary table of the prediction results obtained with the different modelling approaches studied.

Predicted variable	Modelling alternative	Model config	Topology	Performance metric								Evaluation time (s)
				R^2 (-)		RMSE (s.u.)		MAE (s.u.)		MAPE (%)		
$T_{dc,out}$ (°C)	Physical model	-	-	-	0.98	-	0.50	-	0.42	-	1.28	0.035
	Feedforward ANN	-	20-1	0.77	0.78	1.42	1.62	1.13	1.18	3.29	3.85	0.005
	Cascade-forward ANN	-	10-10-1	0.78	0.85	1.39	1.37	1.12	1.02	3.23	3.24	0.007
	Gaussian PR	-	N/A	0.99	0.99	0.24	0.32	0.19	0.25	0.56	0.77	0.005
	Random forest	-	N/A	0.84	0.61	1.19	2.17	0.72	1.36	2.05	4.69	0.022
	Gradient boosting	-	N/A	1.00	0.86	0.00	1.31	0.00	0.86	0.00	2.92	0.035
	Gaussian PR (FP)	-	N/A	1.00	0.98	0.03	0.53	0.02	0.44	0.07	1.35	0.002

s.u. stands for same units as the predicted variable

DC model validation

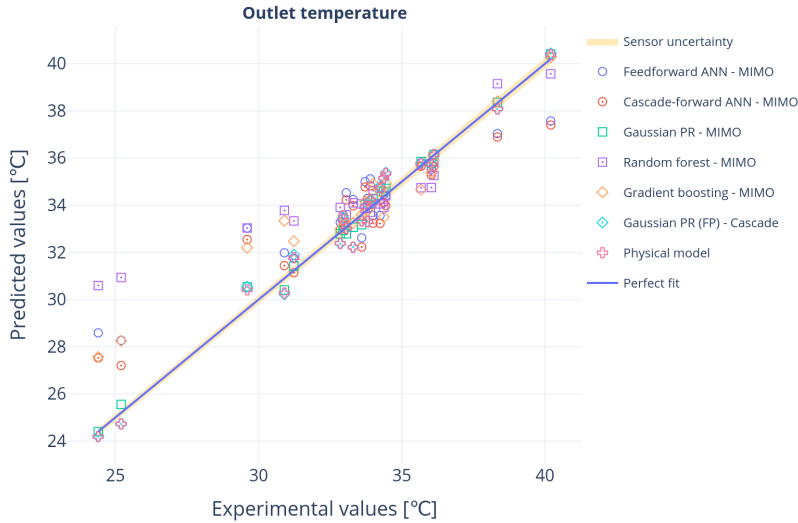


Figure 8.4: DC models performance comparison between the different modelling approaches.



less accurate than Gaussian PR, still offers solid results and remains a valuable benchmark for validating the data-driven approaches.

8.1.3 Surface condenser model

Following the same methodology as in the previous case, data from the model calibration campaign (see Table 5.4 – SC-cal) was used to calculate the global heat transfer coefficient, U_c , with Equation 6.11 together with the surface condenser manufacturer's specifications from Table 5.3. U_c is in this case calibrated as a function of the input variables $T_{c,in}$ and q_c , obtaining the following relation:

$$U_c = p_1 \cdot T_{c,in} + p_2 \cdot \dot{m}_{c,tb} + p_3 \cdot \dot{m}_{c,tb} \cdot T_{c,in} + p_4 + p_5 \cdot \dot{m}_{c,tb}^2 + p_6 \cdot T_{c,in}^2, \quad (8.4)$$

where $\dot{m}_{c,tb}$ is the water mass flow rate inside each condenser tube, $p_1=12.71$, $p_2=2.91$, $p_3=9.5 \cdot 10^{-3}$, $p_4=343.29$, $p_5=-1 \cdot 10^{-3}$ and $p_6=-4.83 \cdot 10^{-2}$, with each parameter, p_i , has units consistent with the variables involved.

Using the previous relation and equations from Model 6.3 and assuming that the water leaving the shell side of the condenser is saturated at temperature T_v , the surface condenser model can be solved to estimate $T_{c,out}$ and T_v . Otherwise if T_v is provided $T_{c,out}$ and $T_{c,in}$ can be estimated.

Validation

To validate this model, a different data set of 15 steady state tests (Table 5.4 – SC-val) has been used with the results depicted in Figure 8.4. The predicted outlet water temperature in the tubes shows good agreement with the experimental measurements, with a low MAE. In contrast, the prediction error is larger for the condensate water temperature at the shell-side outlet ($MAE = 1.86 \text{ }^\circ\text{C}$). This discrepancy may arise because the experimental outlet temperature does not exactly match the vapor saturation temperature (T_v), but is instead 0.1 to 1.7 $^\circ\text{C}$ subcooled.

Condenser model validation

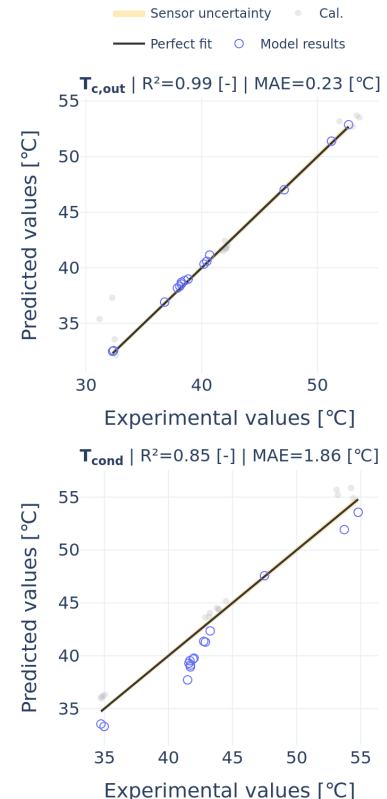


Figure 8.5: Surface condenser validation

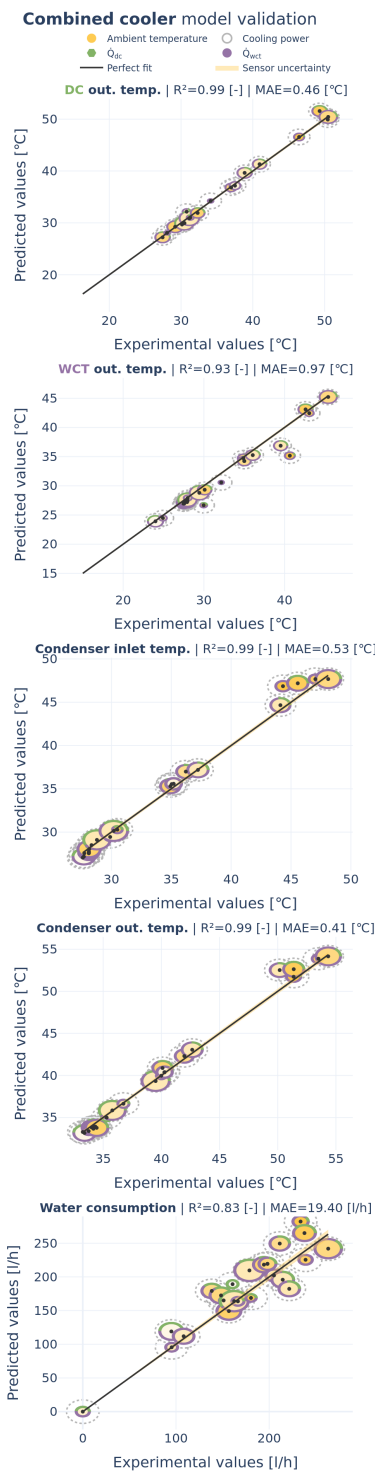


Figure 8.6: Complete combined cooler model validation.



8.1.4 Complete system model validation

For the proposed optimization strategy in Chapter 7 (Optimization of a combined cooling system), a model is required that is fast, reliable, and easily scalable to different system sizes.

First-principle models, while accurate and broadly applicable, have a much longer execution time compared to data-driven alternatives. This becomes a critical drawback for optimization, where the model must be evaluated many times within short time spans. In contrast, data-driven models can be executed orders of magnitude faster and their runtime remains nearly constant independently of the input conditions. However, they are limited to the specific system and operating conditions on which they were trained, and achieving robust performance typically demands significantly larger datasets.

The main strength of the physical models presented in this chapter lies in their generality: they can predict cooler operation under a wide range of conditions without retraining. Data-driven models, while faster and more suitable for vectorized evaluation, trade this generality for speed, restricting their use to the contexts for which they were developed and requiring significant data to achieve satisfactory results.

Therefore, as combining a wet cooler and a dry cooler into a combined cooler offers potential advantages compared to the individual systems, combining both modelling approaches is the chosen solution to model the system. The best performing data-driven model, the GPR is calibrated using synthetic data from the first-principle models, where physical models can be adapted to different scales and finally the surrogate data-driven model can be generated. This approach provides a way of having on-demand models that can be adapted to the particular case study, while still being fast and efficient in terms of computational resources.

The complete model of the combined cooler has been validated with a different dataset composed of 24 tests (see Table 5.4 – CC-val). The obtained outputs regression is shown in Figure 8.6. This figure compares the experimental results with the predicted values. To visualize the operational characteristics of each test, the data points are represented with the following information:

- ▶ The dashed circle represents the nominal cooling power ($200 \text{ kW}_{\text{th}}$).
- ▶ The filled circle represents the cooling power measured in the test relative to the nominal value. The closer it is to the dashed circle, the closer the cooling power is to the nominal one.
- ▶ The measured cooling power is achieved using a certain percentage of DC and WCT. These contributions are distinguished by green and purple, respectively. For example, if the ring is mostly green, it reflects that the cooling contribution from DC is predominantly larger than that from WCT.
- ▶ The filling color inside the circle represents the ambient temperature. From low temperature (no filling) to high ambient temperature (dark yellow).

With this representation, it can be observed that the model provides satisfactory results over a wide range of operating and ambient conditions. The outlet temperatures show a MAE lower than 0.97 °C, with the largest error occurring in $T_{wct,out}$, when the cooling power was far from the nominal value. This may be due to the need to improve the relation $\dot{m}_{air} - \omega_{wct}$ relationship at low flow rates. In the case of the water consumption, the tendency ($R^2=0.82$) of the predicted values follows the experimental ones, being the MAE 19.4 l/h.

A summary of the models' results is shown in Table 8.5. This table includes the performance metrics of each component simulated individually (Cnt column) and those obtained with the complete model (CC column).

Predicted variable	Performance metric					
	R^2 (-)		MAE (s.u.)		MAPE (%)	
	Cnt	CC	Cnt	CC	Cnt	CC
$T_{dc,out}$ ($^{\circ}\text{C}$)	0.99	0.98	0.29	0.46	0.90	1.17
$T_{wct,out}$ ($^{\circ}\text{C}$)	0.92	0.94	1.01	0.97	3.01	2.72
C_w (l/h)	0.87	0.82	16.55	19.40	10.42	11.03
$T_{c,out}$ ($^{\circ}\text{C}$)	0.98	0.99	0.23	0.41	1.51	1.00
$T_{c,in}$ ($^{\circ}\text{C}$)	-	0.99	-	0.53	-	1.52

Table 8.5: Performance metrics obtained with the complete (CC) and component (Cnt) models

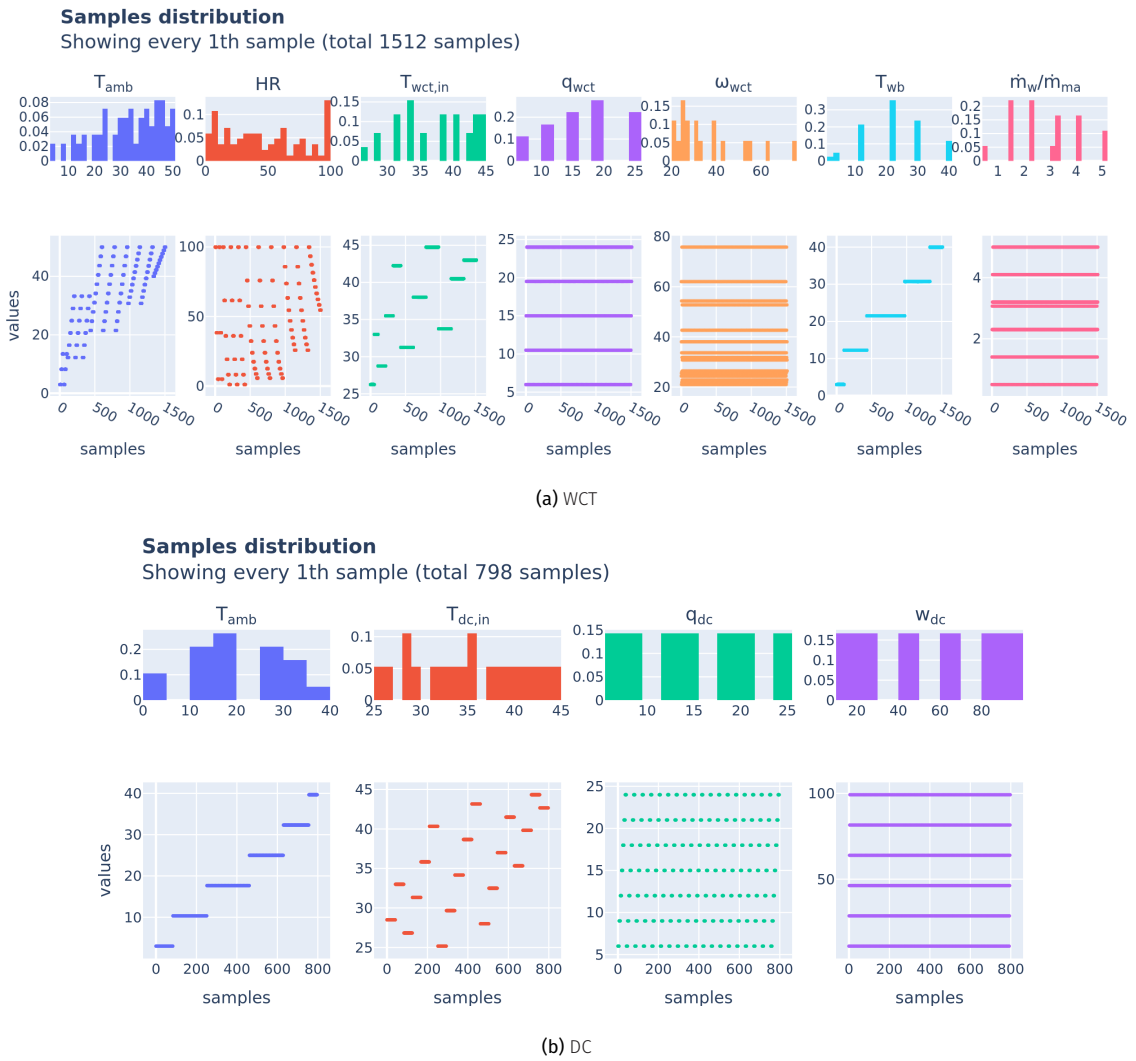


Figure 8.7: Samples distribution visualization for synthetic dataset generation.

8.2 Control and optimization results

Once the models of the main components of the system have been validated, the next step is to validate the optimization strategies proposed in Section ?? (??). First, an optimization algorithm is chosen by comparing different alternatives for each optimization alternative (*i.e.* static and horizon). Then, the two proposed variants for the combined cooler are compared in simulation for one representative operation period in the simulated pilot plant in order to see which one performs better in Section 8 (Comparing the static and horizon optimization strategies). Finally, the proposed horizon methodology is tested in the real facility, where planned changes are introduced in the operation schedule, in order to validate how the optimization strategy adapts to changing conditions.

8.2.1 Choosing an optimization algorithm

Static problems

For every static optimization problem (Problem 7.1, Problem 7.2, Problem 7.3) three different algorithms are tested: (N+1)-ES Simple Evolutionary algorithm with self-adaptive Constraint Handling (SEA-CSTR), Improved Harmony Search algorithm (IHS) and Differential Evolution with self-adaptive Constraint Handling algorithm (DE-CSTR). For each alternative the same number of objective function evaluations are given (800) but they are distributed differently depending on the algorithm:

- ▶ SEA-CSTR and DE-CSTR make use of the Self-Adaptive Constraint handling algorithm (CSTR-SA) wrapper algorithm, which allows them to the constrained problems. 10 iterations are performed for this wrapper algorithm, leaving 80 iterations to spare for the inner algorithm.
- ▶ For all alternatives, three values are tested for the initial population size: 50, 100 and 400 individuals³.
- ▶ Depending on the algorithm only one individual is evolved (IHS and (N+1)-ES Simple Evolutionary algorithm (SEA)) or the whole population (Differential Evolution algorithm (DE)). This means that 800 generations are available for IHS, 80 generations for SEA-CSTR and for DE-CSTR, 1 generation is available for the population of 50 individuals, while only the initial generation is for the population of 100 and 400 individuals.

3: The initial population fitness evaluation is not counted for the budget of objective function evaluations

Table 8.6 shows the results obtained, in terms of fitness at different stages in the evolution. From the results it can be seen that for all alternatives the best performing and most consistent algorithm is IHS. It converges quickly, provides stable results across different population sizes, and consistently reaches the best fitness values within the evaluation budget. The SEA-CSTR also shows competitive results, especially for small populations, but tends to converge more slowly. In contrast, the DE-CSTR is limited by the small number of generations available when larger populations are considered, leading to poorer performance and higher variability. Overall, the results indicate that the incremental evolution of a single individual, as in IHS, is better suited to the limited evaluation budget imposed in these static optimization problems.

Horizon optimization. Path selection

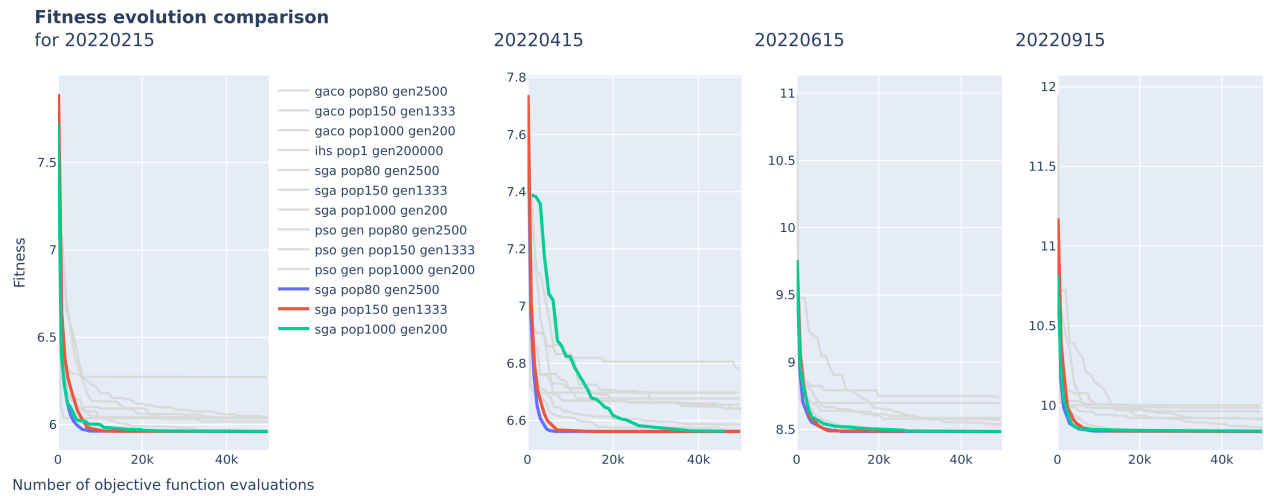
A methodology similar to the static comparison is used. This time the algorithms evaluated are: Generalized Ant Colony Optimization algorithm (GACO), Improved Harmony Search algorithm (IHS), Simple Genetic Algorithm (SGA) and Particle Swarm Optimization algorithm (PSO). Three different population sizes are tested

System	Algorithm	Parameters			Average fitness per obj. fun. evaluations			
		pop size	gen	wrapper algo iters	0	50	150	800
DC	IHS	50	800	N/A	1.28 ± 0.82	1.05 ± 0.29	0.80 ± 0.10	0.77 ± 0.09
		100	800	N/A	0.92 ± 0.18	0.87 ± 0.14	0.81 ± 0.11	0.77 ± 0.10
		400	800	N/A	0.81 ± 0.11	0.80 ± 0.11	0.79 ± 0.10	0.77 ± 0.10
	SEA-CSTR	50	80	10	1.19 ± 0.28	0.95 ± 0.11	0.79 ± 0.10	0.77 ± 0.09
		100	80	10	0.92 ± 0.13	0.86 ± 0.10	0.80 ± 0.10	0.77 ± 0.09
		400	80	10	0.82 ± 0.10	0.80 ± 0.10	0.78 ± 0.10	0.77 ± 0.09
	DE-CSTR	50	1	10	1.06 ± 0.40	0.97 ± 0.18	0.83 ± 0.10	1.04 ± 1.04
		100	0	10	0.95 ± 0.16	0.95 ± 0.16	0.95 ± 0.95	0.95 ± 0.95
		400	0	10	0.83 ± 0.10	0.83 ± 0.10	0.83 ± 0.83	0.83 ± 0.83
WCT	IHS	50	800	N/A	0.24 ± 0.08	0.18 ± 0.04	0.10 ± 0.00	0.07 ± 0.00
		100	800	N/A	0.12 ± 0.02	0.11 ± 0.01	0.08 ± 0.00	0.07 ± 0.00
		400	800	N/A	0.07 ± 0.00	0.07 ± 0.00	0.07 ± 0.00	0.07 ± 0.00
	SEA-CSTR	50	80	10	0.25 ± 0.04	0.16 ± 0.01	0.07 ± 0.00	0.06 ± 0.00
		100	80	10	0.17 ± 0.03	0.11 ± 0.00	0.07 ± 0.00	0.06 ± 0.00
		400	80	10	0.07 ± 0.00	0.07 ± 0.00	0.07 ± 0.00	0.06 ± 0.00
	DE-CSTR	50	1	10	0.29 ± 0.07	0.17 ± 0.02	0.09 ± 0.00	0.07 ± 0.07
		100	0	10	0.11 ± 0.00	0.11 ± 0.00	0.11 ± 0.11	0.11 ± 0.11
		400	0	10	0.07 ± 0.00	0.07 ± 0.00	0.07 ± 0.00	0.07 ± 0.07
CC	IHS	50	1000	N/A	0.77 ± 0.12	0.80 ± 0.11	0.77 ± 0.11	0.59 ± 0.11
		100	1000	N/A	0.70 ± 0.12	0.78 ± 0.10	0.82 ± 0.15	0.61 ± 0.13
		400	1000	N/A	0.79 ± 0.19	0.82 ± 0.21	0.80 ± 0.22	0.65 ± 0.16
	SEA-CSTR	50	100	10	0.92 ± 0.13	0.86 ± 0.14	0.74 ± 0.16	0.51 ± 0.10
		100	100	10	0.88 ± 0.16	0.82 ± 0.16	0.75 ± 0.21	0.62 ± 0.16
		400	100	10	0.84 ± 0.21	0.80 ± 0.18	0.74 ± 0.21	0.69 ± 0.19
	DE-CSTR	50	2	10	0.83 ± 0.16	0.79 ± 0.13	0.73 ± 0.14	0.56 ± 0.13
		100	1	10	0.82 ± 0.17	0.80 ± 0.13	0.77 ± 0.10	0.64 ± 0.13
		400	0	10	0.73 ± 0.16	0.73 ± 0.16	0.73 ± 0.16	0.73 ± 0.73

Table 8.6: Static optimization algorithm comparison results

(80, 150 and 1000) if the particular algorithm evolves more than one individual; the number of generations is calculated accordingly so that all alternatives have the same budget of objective function evaluations, equal to 200k evaluations⁴. The results are visualized in Figure 8.8, where there are different plots for different dates, the y-axis represents the fitness and the x-axis shows the number of objective function evaluations. The results show that consistently the SGA outperforms the alternatives, and particularly, the smaller population size (80) configuration followed very closely by the 150 population size configuration.

4: Only up to 50k evaluations is shown in the figure for clarity

**Figure 8.8:** Horizon optimization – path selection subproblem. Fitness evolution comparison for different algorithms in four different dates.

8.2.2 Simulation results

5: in simulation and at pilot-scale

6: This results figure structure is going to be repeated several times in the next sections.

7: Figure 8.9 - Weather conditions

8: i.e. plenty of water resource available, Figure 8.9 - Resources context

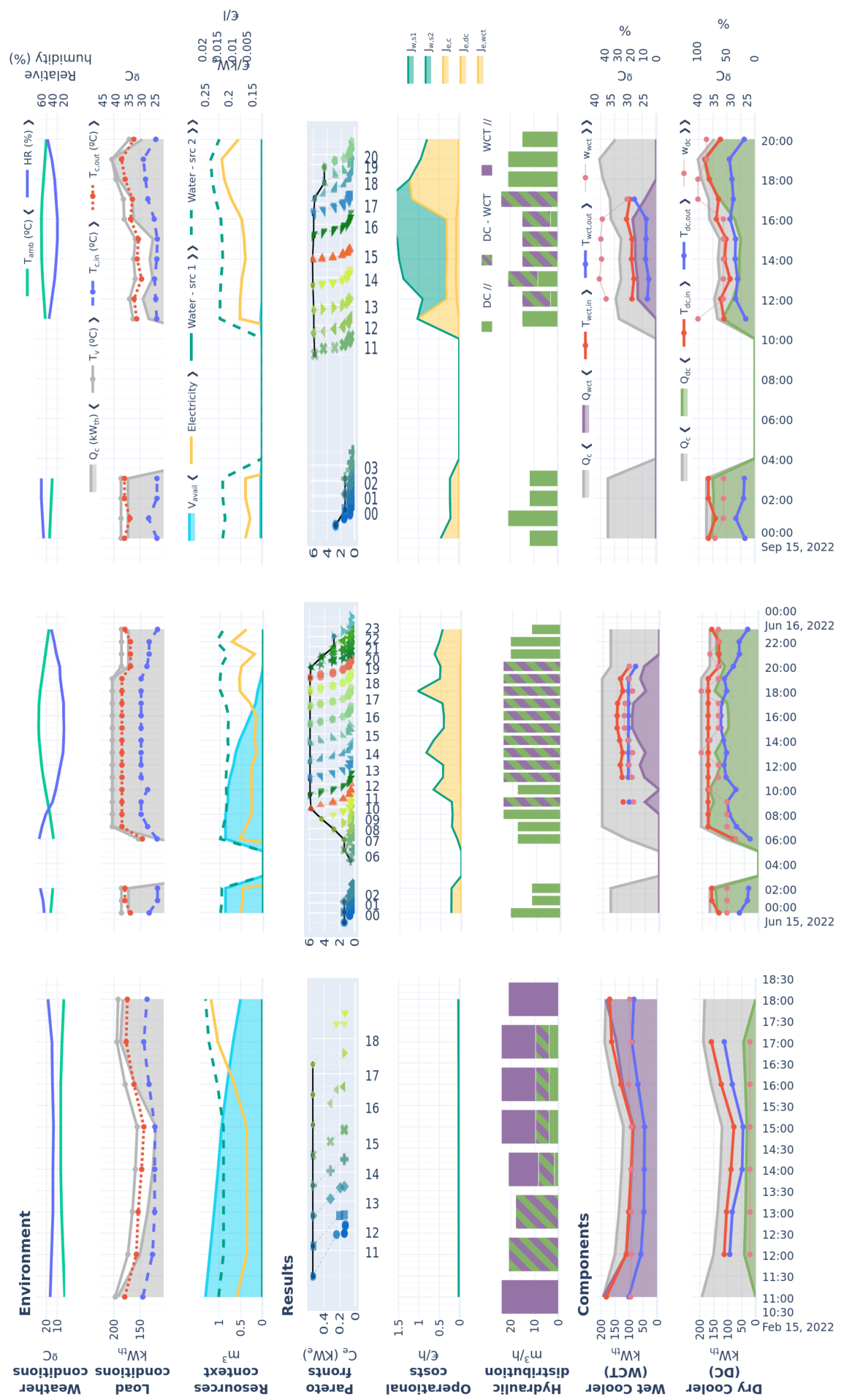
Figure 8.9 shows the optimization results⁵ for the horizon optimization strategy⁶. This is for the same three days in different months: 15-February, 15-June, 15-September, that is, different periods of the year. This means that three different environments are available, respectively: cold⁷ and wet⁸, moderate temperature and water availability; and finally hot and dry.

The cooling costs obtained in each scenario are displayed in Figure 8.9 - Operational costs. In yellow costs associated with electricity use while green for water associated costs.

In terms of hydraulic distribution, it can be observed that when the water resource is abundant (i.e. 15-February) the system relies mostly in the wet cooler and when combined with the dry cooler, is the only scenario where the parallel configuration is used. Both in the moderate (15-June) and hot-dry (15-September) scenarios, the system operates mostly in series, or using exclusively the dry cooler.

At the bottom of the figure, in the Components section, the cooling power provided by each cooler (\dot{Q}_{wct} / \dot{Q}_{dc}) is shown with respect to the total (\dot{Q}_c). It can be observed that in the cold and wet season the system relies mostly on the wet cooler with some assist from the dry cooler also boosted by the low ambient temperatures. In the moderate scenario the roles reverse, with the dry cooler providing most of the cooling power while the wet cooler is used only occasionally, at the central hours of the day where the ambient temperature is higher and the dry cooler is not able to cope with the full load. Finally, in the hot and dry scenario, the system tries to rely exclusively on the dry cooler. However, at the peak hours of the day, the dry cooler is not able to provide the full cooling load, and the wet cooler is used to supplement the cooling power (11:00 – 16:00).

Comparing the costs, in the cold and wet season (15-Feb) not zero but orders of magnitude cheaper cooling is obtained compared to the other two scenarios since the thermal load is lower and the wet system can be broadly used. In the moderately hot and dry season significant higher costs can be observed due to the extended use of the more expensive dry cooler. This is still cheaper than the hot and dry season, where on top of the already more expensive dry cooler cooling, the sparse wet cooler use and the lack of water resource significantly increase the cooling costs by 50 % compared to the moderate scenario.



Comparing the static and horizon optimization strategies

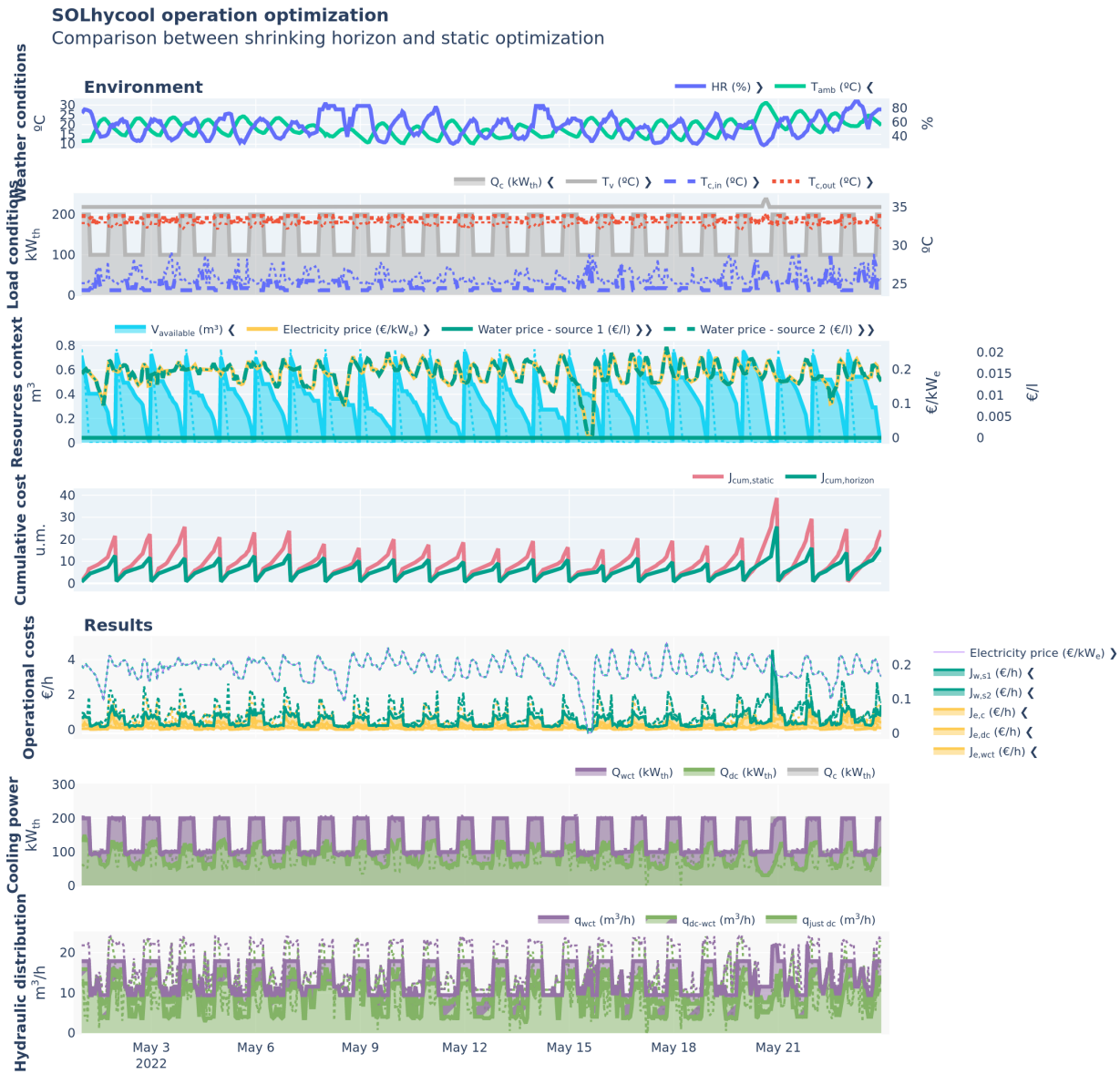


Figure 8.10: Simulation results for the horizon optimization compared to the static alternative. The horizon-based strategy is shown with solid lines (and filled areas where relevant), while the static strategy is represented with dotted lines in the same colors as the corresponding variables



Figure 8.10 shows the results obtained for a range of days (May 3 to May 21) with the two optimization alternatives: static and horizon, presented in Sections 7.2.3 and 7.3, respectively. Both are evaluated given the same environment, which is shown at the top of the figure. The horizon strategy is depicted with solid lines and/or filled areas. In comparison, the static results are included using

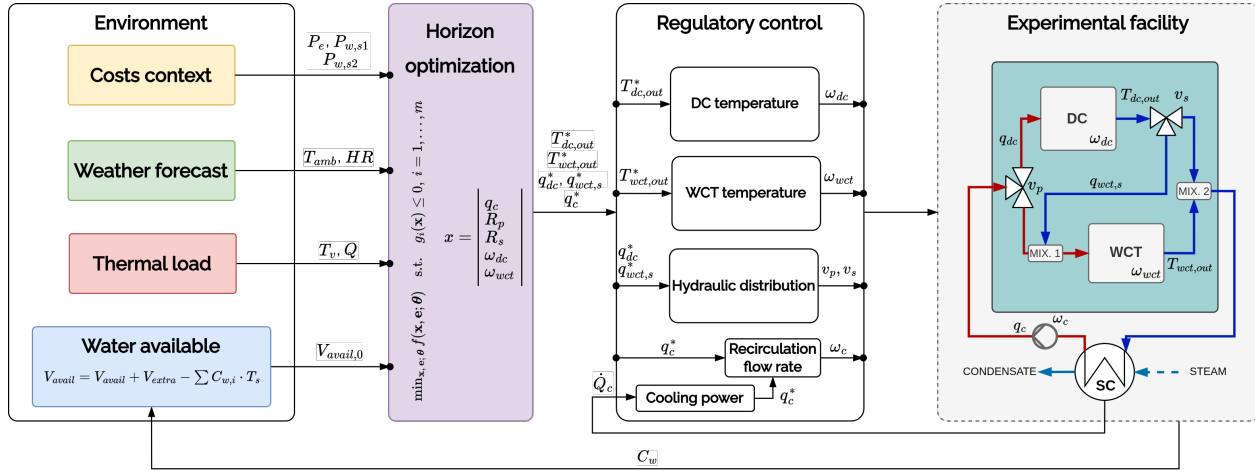


Figure 8.11: Implementation of the optimization strategy in the real facility. Hierarchical control

dotted lines with the same color for the compared variable. The results show that the horizon strategy consistently outperforms the static one in terms of cost (Figure 8.10 – Cumulative cost), with a cost advantage of more than 20 % and often above 50 %. This can be explained by how each strategy manages the water resource⁹: the static strategy tends to use a lot of water at the beginning of the day, when the ambient temperature is low, and then as the day progresses and the ambient temperature rises, it has less water available and is forced to use the alternative, more expensive water source. In contrast, the horizon strategy manages the water resource more efficiently, using it when it is most needed and preserving it for the times when it will be most beneficial.

9: See Figure 8.10 - Resources context – $V_{available}$

8.2.3 Experimental validation

A hierarchical control¹⁰ strategy has been implemented in order to validate the optimization strategy in the real facility. Figure ?? shows a diagram of the methodology, where the left side represents the upper layer with the proposed shrinking horizon optimization¹¹ and the right side shows the low-level regulatory control layer, which directly interfaces with the actuators and sensors of the facility.

10: See Section 3.4 (Hierarchical control)

Environment. The optimization environment was generated using weather forecasts obtained from the OpenWeather API [127]. Electricity cost data were taken from the 2022 Spanish market pool [128]. The water cost was defined as $P_{w,s2} = 0.03 \text{ €}/\text{m}^3$ for source 1, and $P_{w,s1} = 80 \times P_e = 8 \pm 5 \text{ €}/\text{m}^3$ for source 2.

11: See Section 7.3 (Horizon optimization)

The thermal load profile was created by fixing the vapor temperature at $T_y = 45^\circ\text{C}$ and generating an arbitrary cooling power based on the heat available from the flat-plate collector field—the system's heat source for the selected day. Finally, the initial available water volume was set to $V_{avail,0} = 0.4 \text{ m}^3$, after which it was updated dynamically according to the system's real-time consumption data.

Optimization layer. The optimization algorithm is run every 30 minutes, and generates a new set of results for the remaining operation time. The results of the optimization are then passed to the regulatory control layer by setting them as setpoints for the low-level control. The box-bounds for the decision variables are shown in Table 8.7. Since the low-level control layer actuates over the coolers fan speeds, instead of using ω_{dc} and ω_{wct} directly as setpoints, the would-be obtained outlet temperatures values ($T_{dc,out}$ and $T_{wct,out}$) are used

Table 8.7: Box-bounds for the decision variables.

x	Units	lb	ub
q_c	m^3/h	5.22	24.15
R_p	–	0.00	1.00
R_s	–	0.00	1.00
ω_{dc}	%	11.00	99.18
ω_{wct}	%	21.00	93.42

[127]: OpenWeather (2025), Current Weather and Forecast - OpenWeatherMap

[128]: de España (2025), Red Eléctrica – Negocio Eléctrico En España

Table 8.8: Low-level control loops

Controller	Control signal Variable	P&ID	Controlled signal Variable	P&ID	Controller parameters K_p	T_i (s)
TC-01	ω_{dc}	SC-02, SC-03	$T_{dc,out}$	TT-03	[−16.8, −3] %/°C	[30.2, 155.7]
TC-02	ω_{wct}	SC-01	$T_{wct,out}$	TT-06	−5.9 %/°C	78.0
FC-01	ω_c	SC-04	q_c	FT-06	0.9 %·(h·m ³)	1.3
FC-02	V_p	ZC-02	q_{dc}	FT-02	−1.18 %·h·m ^{−3}	4.3
FC-03	V_s	ZC-01	q_{dc-wct}	f(FT-01, FT-02, FT-03)	0.7 %·h·m ^{−3}	4.0

instead. This makes the strategy more robust, since as long as the outlet temperatures from the coolers are kept, and they will be since the fan speed is continuously regulated to achieve that, the correct condenser operation can be guaranteed, despite possible deviations.

The optimization algorithm is executed every 30 minutes and generates a new set of results for the remaining operation period. These results are then passed to the regulatory control layer, where they serve as setpoints for the low-level control. The box constraints for the decision variables are provided in Table 8.7.

Control layer. It is a regulatory layer with five control loops (see Table 8.8). The purpose of this layer is to track the setpoints calculated by the upper layer for the five controlled variables and maintain them near steady-state conditions around these references, even in the presence of disturbances such as variations in temperature or flow rate. Classical feedback loops with Proportional-Integral controller (PI) controllers have been used in this regulatory layer, which were tuned using the improved SIMC technique [129]. Table 8.8 shows the proportional gain, K_p , and the integral time, K_i , for each control loop. The ideal configuration of the PI controller has been implemented¹², including anti-windup mechanism and a sample time of one second. In the special case of the ACHE, due to its strong nonlinear dynamics, a Gain Scheduling scheme [66] has been implemented. For this purpose, a 3×3 matrix of regions has been defined to account for three levels: low, medium and high values in the three main variables involved (q_{dc}, ω_{dc} and ΔT_{in-amb}).

The optimization does not provide ω_{dc} and ω_{wct} as setpoints. Instead, it provides the expected corresponding outlet temperature values. This way the low-level control layer directly adjusts the fan speeds of the coolers in order to regulate the outlet temperatures ($T_{dc,out}$ and $T_{wct,out}$) to the setpoints provided. This approach increases the robustness of the control strategy: as long as the outlet temperatures of the coolers are maintained—and they are, since fan speeds are continuously regulated to achieve them—the proper operation of the condenser can be ensured, even in the presence of potential deviations due to modelling inaccuracies, external disturbances or uncertainty in the forecasted weather conditions.

Experimental results. In order to validate the optimization strategy, several tests were performed over different days. In particular Figure 8.12 visualizes one test carried out in the 1st August to analyze in this section. The objective of the test was twofold. For the first part of the test a set operation plan was established:

- ▶ \dot{Q} = Ramp up from 150 to 200 kW from 08:40 until 10:00, and hold the 200 kW value until the end of the test (13:00).
- ▶ T_v = 45 °C. Held constant throughout the experiment (08:40 – 13:00)

The objective was to validate that the optimized operation based on the provided predictions was effectively able to correctly manage resources and cool the thermal load with the predicted associated consumptions. During operation of a CSP plant changes to the operation plan can arise in response to changes in electricity market dynamics, or other unforeseen environment circumstances. At 10:20 a change is introduced in the operation plan to simulate this behavior, the thermal load was ramped down with a similar (inverse) profile to the initial one. This allows to verify the adaptability of the proposed strategy to changing conditions and is the second objective of the test.

[129]: Skogstad et al. (2012), “The SIMC Method for Smooth PID Controller Tuning”

12: i.e. $C(s) = K_p(1 + 1/(T_i \cdot s))$

[66]: Hägglund et al. (2006), *Advanced PID Control*

The operation strategy was as follows:

- ▶ Before the test and while the system starts up by generating vacuum in the surface condenser, the optimization layer was evaluated to have an initial perspective on the day operation and expected consumptions. If the operator was satisfied the provided values were used as reference and manually set to bring the system into stable operation after gradually increasing the thermal load.
- ▶ The optimization sample time was 20 minutes, it takes around that time to compute and is evaluated every 40 minutes.
- ▶ The thermal load was designed to change every 40 minutes, this means that for each optimization evaluation, two setpoint changes are provided to the regulatory control layer per optimization evaluation and thus predictions must be valid for those at least 40 minutes.
- ▶ For every optimization layer evaluation, first the environment is updated and then is provided as input to the optimization evaluation (see Figure 8.11).
- ▶ The low-level control layer has available the operation strategy for the whole horizon provided by the upper layer and following its schedule updates its setpoints.

Figure 8.12 is divided in several sections. In general solid lines represent measured (experimental) values, while the thin-dashed equivalent (same color) is the predicted value by the upper-optimization layer. This predicted value is provided by the latest evaluated optimization. The upper section of the figure displays the environment evolution (weather conditions, load conditions and resources context). They are followed by a comparison between predicted and actual results for: (a) distribution between cooling systems, in terms of flows (*hydraulic distribution*) and in terms of the assigned cooling power (*cooling power distribution*) and (b) individual cooler outputs in terms of temperature profile and water consumption in the wet cooler case. Finally, the right group of plots shows the low-level control layer performance for each control loop: coolers outlet temperature and flows.

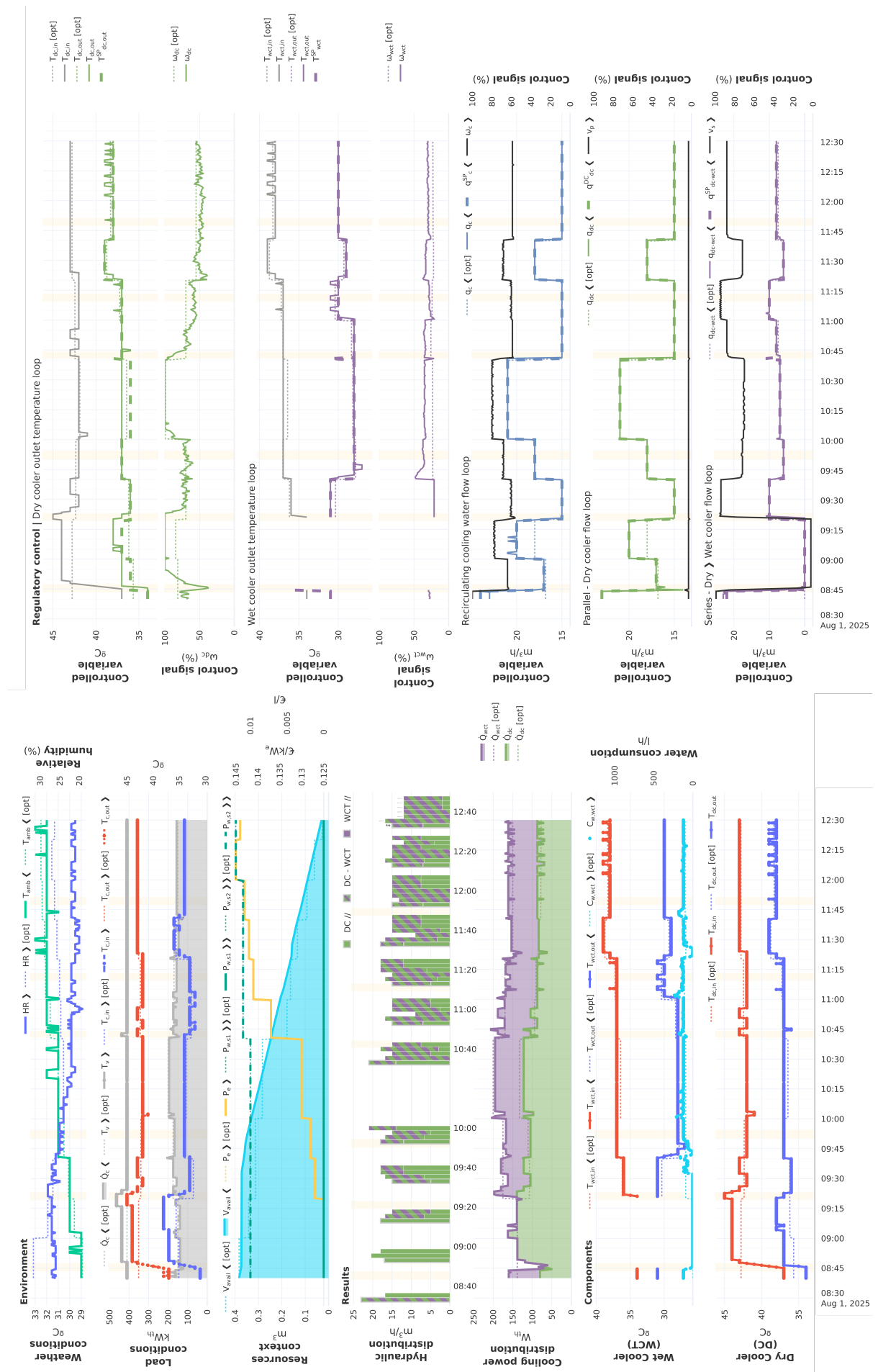
In Figure 8.12 – *Hydraulic Distribution*, several sequentially added bars are shown. The first bar corresponds to the experimental value, while the remaining bars represent the predicted hydraulic distributions from successive optimization evaluations: the second bar comes from the first evaluation, the third from the second, and so on.

From the results, a few observations can be made:

- ▶ Overall a very good agreement between the optimization layer predicted operation and the experimental values can be observed. It can be seen that as long as the environment does not change, the generated operation strategy is valid for hours. Particularly, the initial evaluation at XX:XX. In another test (not shown) where the thermal load does not change throughout the day the initial optimization held valid until the end of operation. But as mentioned, in this particular test a planned change in the thermal load profile is introduced at 10:30, which is then taken into account in the optimization layer re-evaluation at 10:40, and thus a new adapted operation strategy to the new scenario is generated and successfully applied.
- ▶ The dry system is very sensitive to the ambient temperature when operating in its limits. Less than half-degree prediction error in the ambient temperature (0.4 °C between 09:04 and 09:17) translates in a 15% difference between the expected and the actual fan speed.
- ▶ When both systems are operating, if the dry cooler falls short in its cooling allocation, the wet cooler can compensate for the dry cooler shortcoming on its cooling allocation. However, as can be seen at the beginning of the test (09:04 – 09:17), when only the dry cooler is used and does so

in its limits (Figure 8.12 - DC outlet temperature loop - Control signal) it can happen that the load is undercooled resulting in a higher condenser pressure (in terms of temperature, +1-2 °C can be observed, which would translate in a penalty in the power produced by the turbine). A low-level supervisory controller should be set in place to prevent this.

- ▶ To avoid using the alternative more expensive alternative water source, the optimization prioritized the use of the dry cooling (as far as being dry-only as long as the ambient temperature and demanded thermal load allowed it, up until 09:20) to conserve water until the end of operation. After the operation plan change, the lower expected load gives more room for adjustment and the optimization increases the load through the wet system from 0-40% to about 50% (Figure 8.12 - Hydraulic distribution and Cooling power distribution).
- ▶ The restricted availability of the water resource, means that the optimization strategy always prioritizes water savings either by dry-only operation, or combined operation using a series configuration, at no point the parallel configuration is used despite progressively increased electricity cost (*Resources context – P_e*).
- ▶ The good agreement between upper and lower layer, means that the upper layer predicted controlled variables values could be used by the low-level control, for example, in a static feed-forward action.
- ▶ From the initial optimization evaluation, the low-level control layer has available an operation strategy for the whole horizon. This makes the strategy robust in the case the optimization is not evaluated again, or not evaluated on time.



Annual analysis: Andasol-II CSP plant

TL;DR

This chapter presents an analysis of the annual performance of different cooling alternatives applied to a commercial 50 MW_e CSP plant, Andasol-II, located in southern Spain. Three cooling systems are compared: the actual cooling system of the plant, a WCT, the proposed combined cooling system (CC) with two different capacities for the dry cooler, 75% and 100% of the nominal thermal load of the WCT system. For each alternative the operation is optimized in a water-scarce scenario using the proposed multi-stage optimization framework, adapted to the particular case study.

Results show that integrating the CC can reduce specific cooling costs by up to 80% and annual water consumption by about 48%, with 38% savings during the driest months. These benefits arise from reduced dependence on costly alternative water sources. The CC alternatives also provide more stable, cost-effective operation across the year compared to the WCT, which is highly sensitive to water scarcity. Overall, the study demonstrates that optimized combined cooling can significantly enhance both economic and water-use efficiency in CSP plants.

Introduction

A modeling framework has been developed to simulate and optimize the operation of various cooling systems, with a particular focus on the proposed combined cooling system. This methodology has been validated using data from a pilot plant. In this chapter, the objective is to apply the framework to a specific case study: a commercial 50 MW_e Concentrated Solar Power (CSP) plant.

As previously mentioned, CSP plants are among the most water-intensive power generation technologies, a concern that is especially relevant in the arid regions where they are typically located. To assess the performance —water use and operational costs— of different cooling systems, the proposed methodology is applied to a real-world case study through an annual simulation. The case study examined is the Andasol-II CSP plant.

In the south-east of Spain, near Guadix and next to the Sierra Nevada mountain range (see Figure 9.1), thanks to the region high altitude (1100 m) and the semi-arid climate, the site has exceptionally high annual direct insolation (2260 W/m²) and thus is ideal for solar projects. This is why the first parabolic trough power plant in Europe, Andasol-I, was built there in 2008. One year later Andasol-II followed, located in the immediate neighbourhood and with almost identical construction. It has a rated output of 50 MW with 7.5 hours¹ of thermal storage, providing electricity for up to 200,000 people. According to the developer, Andasol-II vaporizes 870 000 m³/year, or in specific units 5 l/kWh. More specifications are available in Table 9.1.

9.1 Environment definition	90
9.1.1 Water context	90
9.1.2 Thermal load	90
9.1.3 Prices context	91
9.2 Alternatives comparison	91



Figure 9.1: Andasol I, II and III aerial view. Andasol-II is the one at .

Source: https://en.wikipedia.org/wiki/File:Andasol_5.jpg

1: This means that if fully charged, it can produce the nominal rated power of the turbine for that duration

Table 9.1: Andasol-II plant main characteristics

Technology	Parabolic Trough
Solar Resource	2260 W/m ²
Nominal Capacity	50 MW
Status	Operational
Start Year	2009
Expected Generation	158 GWh/year
Total Land Area	2 km ²
LCOE (2020)	0.27 €/kWh
TF Inlet Temperature	293°C
TF Outlet Temperature	393°C
Power Cycle	Steam Rankine
Turbine Efficiency	38.1%
Cooling Type	Wet
Storage Type	Molten salts
Storage Capacity	75 Hours – 1 GWh

Source: Institute for Advanced Sustainability Studies (IASS) and others, 2022; data by Lilliestam@IASS, Thonig@IASS, Zang@CAS, Gilmanova@CAS and others. Licensed under a Creative Commons Attribution 4.0 International License.

9.1 Environment definition

9.1.1 Water context

Obtaining accurate water availability data is challenging. Unlike resources such as electricity —where demand, supply, and prices are readily available— water availability data is often lacking. Water prices are not standardized; they vary from region to region, and even within the same region, depending on the source and the specific agreements in place.

2: See Section 7.1 (Environment description)

[130]: AG (), Meteonorm V8.2.0.24079

3: This is not an exogenous idea; the Villena CSP plant, for example, uses wastewater from a nearby prison to partially meet its water needs

For the simulation scenario, two sources of water are considered². The first source is rainwater collected in a reservoir, which is assumed to be available at a constant price. To create a representative dataset, water availability is modeled as a function of precipitation data, which can be obtained from hourly Typical Meteorological Year (TPY) data [130]. A linear model is fitted to relate maximum precipitation to maximum available water, and when there is no precipitation, water availability is set to zero. The data is then resampled every 15 days, and the daily volume of available water is calculated by dividing the resampled fortnightly volume by 15. This approach accounts for the presence of water reservoirs and some degree of management capacity.

The alternative regenerated water source³ is not limited in volume.

9.1.2 Thermal load

Traditionally, thermal power plants were designed and operated to generate electricity only when solar energy was available. This approach remained common until the rapid rise in competitiveness of PV plants, which offer significantly lower generation costs. In response, concentrated solar power plants began integrating thermal energy storage systems to enable dispatchable power generation. Today, 21 out of 51 CSP plants in Spain—approximately 42%—have thermal storage capacities exceeding two hours [75, 91, 92]. This enables them to produce electricity even when solar input is unavailable.

[75]: Lilliestam et al. (2021), “The Near- to Mid-Term Outlook for Concentrating Solar Power: Mostly Cloudy, Chance of Sun”

[91]: Thonig et al. (2023), CSP.Guru 2023-07-01

[92]: Bonilla et al. (2024), “CSP Data: A Data Discovery Web Application of Commercial CSP Plants”

4: The storage is primarily used to extend generation past sunset.

5: This trend is already observable in Spain during the summer months; see Figure ??

[131]: Ortega Delgado (2016), “Theoretical analysis of high efficient multi-effect distillation processes and their integration into concentrating solar power plants”

However, many of these plants still follow traditional operating patterns, generating most of their electricity during peak solar hours⁴. This strategy is increasingly seen as suboptimal and is likely to be phased out as the electric grid becomes saturated with PV generation⁵.

In this work, a different operational strategy is adopted: the plant is configured to generate electricity during off-peak solar hours, typically in the evening when electricity demand is at its highest. This is achieved by shifting the plant’s production to align with these peak demand periods.

A model of the Andasol-II plant, developed by Bartolomé et al. [131], was configured to follow this production strategy and simulated over an entire year. The resulting thermal load profile represents the demand to be met by the cooling system. The simulation used the same weather dataset as that employed for modeling the cooling system.

9.1.3 Prices context

Electricity. The spanish grid operator Red Eléctrica de España (REE) provides an API [128] to access the electricity market prices. A python script was developed to systematically download monthly data⁶ for each month in the desired year. The data is fetched in hourly intervals and saved in JSON format, then every file is read and joined into a single dataset resulting in prices for the whole year.

Water. Rainwater has a constant lower price of $P_{w,s1} = 0.03 \text{ €/m}^3$. This price was obtained considering that the plan has access to the same water than the irrigation community of the area. The alternative source, *i.e.* regenerated water, is considerably more expensive, and its price is linked to the electricity price, specifically by a factor of 80: $P_{w,s2} = 80 \times P_e = 8 \pm 5 \text{ €/m}^3$.

Simulation data and parameters information

- ▶ **Weather data.** Hourly weather data from TPY of Guadix (Spain) for the year. Data from [130].
- ▶ **Thermal load.** Hourly thermal load data from the power block of Andasol-II CSP plant from a simulation model [131].
- ▶ **Electricity price.** Spanish electricity pool market for 2022 [128].
- ▶ **Maximum available water.** 2 m³/day, modeled as a function of precipitation data.
- ▶ **Alternative water source factor.** $P_{w,s2} = 80 \times P_e$

9.2 Cooling alternatives comparison

The results presented in Figure 9.2 highlight the potential benefits of integrating the proposed combined cooler into the Andasol-II power plant, particularly under water-scarcity conditions. The comparison between the WCT baseline and the CC alternatives shows a remarkable reduction in the specific cooling cost: the CC achieves reductions of around 80% compared to the WCT reference case.

This cost improvement is mainly explained by the reduced reliance on the alternative water source, which dominates the cooling cost in the WCT configuration. By introducing the combined cooler, annual water consumption is reduced by 48% on average, and by 38% during the most critical driest and hottest months (see Figure 9.3). This demonstrates the ability of the CC to alleviate water stress without compromising cooling performance.

The figure also emphasizes the importance of comparing cooling system alternatives under representative annual operating conditions and not just analyzing annual averages. The WCT option exhibits much higher sensitivity to water availability, with sustained high associated costs through most of the year and negligible on periods of water abundance. The CC options (both at 75% and 100% DC capacity) provide stable and cost-effective operation across most of the year, only penalized in the most challenging (June - September) period and to a much lower degree compared to the WCT.

These findings confirm the need for optimization strategies in hybrid or combined cooling systems, where the optimized operation schedule can further improve both cost efficiency and water savings. The proposed multi-stage optimization framework can be adapted to other plant configurations and extended to different boundary conditions and resource availability scenarios, enabling informed decision-making for sustainable power plant operation.

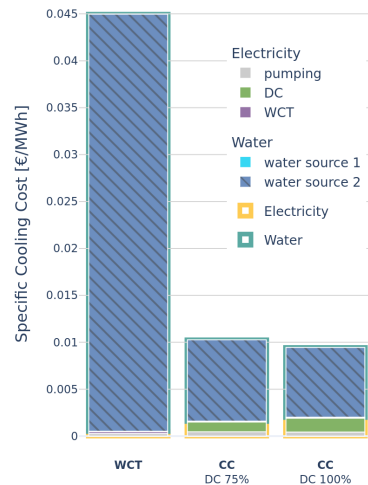


Figure 9.2: Composite specific cooling costs comparison.



One caveat that no optimization strategy can fully overcome is the natural mismatch between water availability and cooling needs: in most locations, ambient temperatures are lowest (favoring dry cooling) when water is most available, whereas in the hot-dry summer season, water scarcity coincides with the highest cooling demand (see Figure 9.3). Nevertheless, as shown, there remains significant margin for improved water management through system optimization with integrated dry and wet cooling. Moreover, CSP systems could consider not operating during the hottest hours of summer days—when water is scarce and other renewable generation is plentiful—and instead prioritize production during off-peak hours, when cooling is more efficient and renewable supply is lower.

Finally, it is clear from the results that water can be the dominant cost driver, and thus the most limiting resource depending on the location and chosen cooling solution. For the analyzed case study this is true even when assuming a conservative alternative water source cost of $\approx 0.08 \text{ €/l}$. Much higher values could be expected: in discussions with the Villena CSP plant O&M team, they indicated figures above 1 €/l for such alternative sources can be expected, which would further strengthen the case for water-efficient cooling strategies.

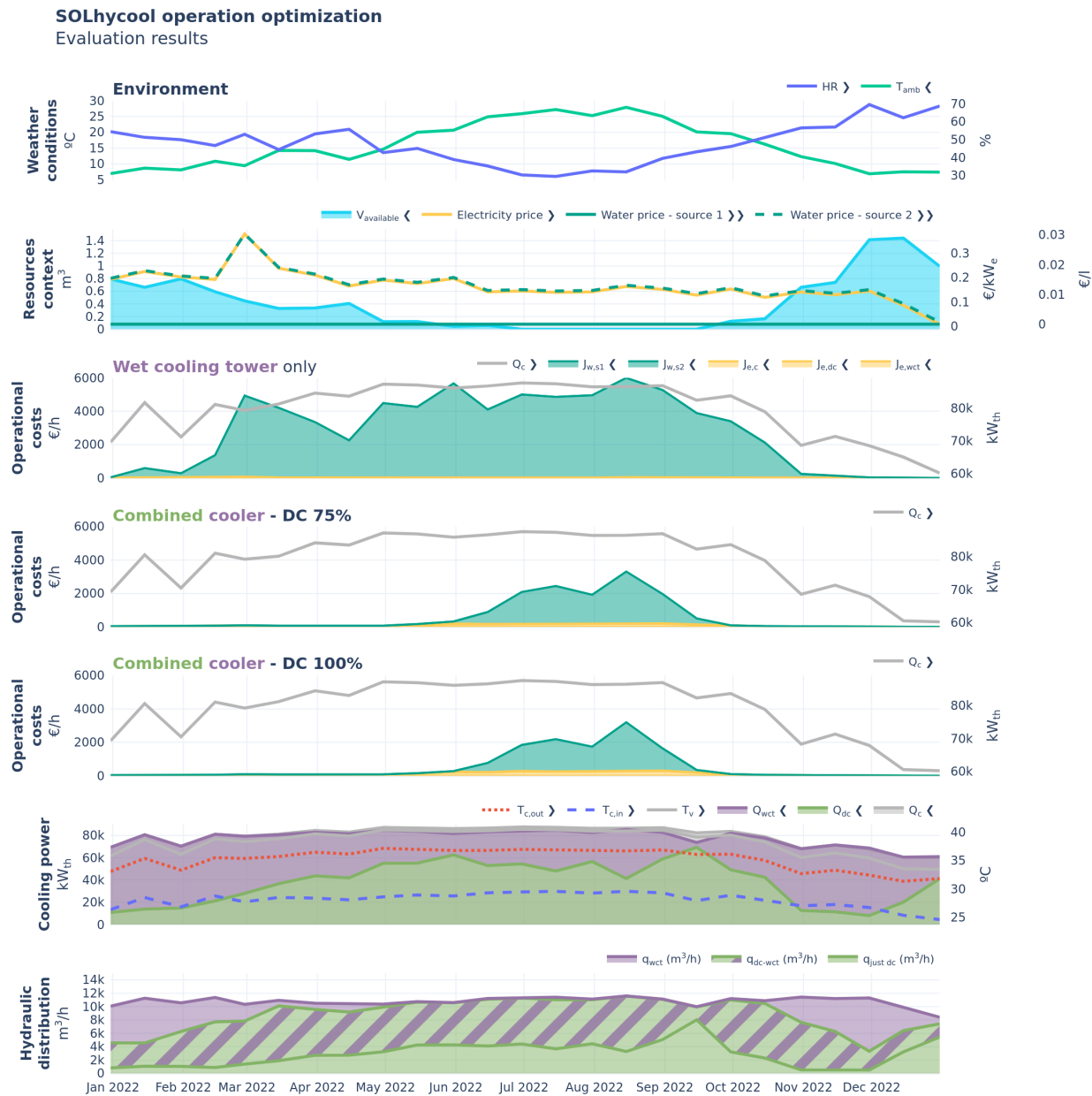


Figure 9.3: Annual simulation results for the different studied alternatives optimized with the proposed horizon optimization. Results are resampled every 15 days using their mean values.



Such arbitrariness had its origins in the example of the Catalan sage, for whom wisdom was not worthwhile if it could not be used to invent a new way of preparing chickpeas //

Tanta arbitrariedad tenía origen en el ejemplo del sabio catalán, para quien la sabiduría no valía la pena si no era posible servirse de ella para inventar una manera nueva de preparar los garbanzos

Gabriel García Márquez, One Hundred Years of Solitude // Cien años de soledad

Part II

ENERGY MANAGEMENT IN MULTI-EFFECT DISTILLATION (MED) PROCESSES DRIVEN BY VARIABLE ENERGY SOURCES

Such arbitrariness had its origins in the example of the Catalan sage, for whom wisdom was not worthwhile if it could not be used to invent a new way of preparing chickpeas //

Tanta arbitrariedad tenía origen en el ejemplo del sabio catalán, para quien la sabiduría no valía la pena si no era posible servirse de ella para inventar una manera nueva de preparar los garbanzos

Gabriel García Márquez, One Hundred Years of Solitude // Cien años de soledad

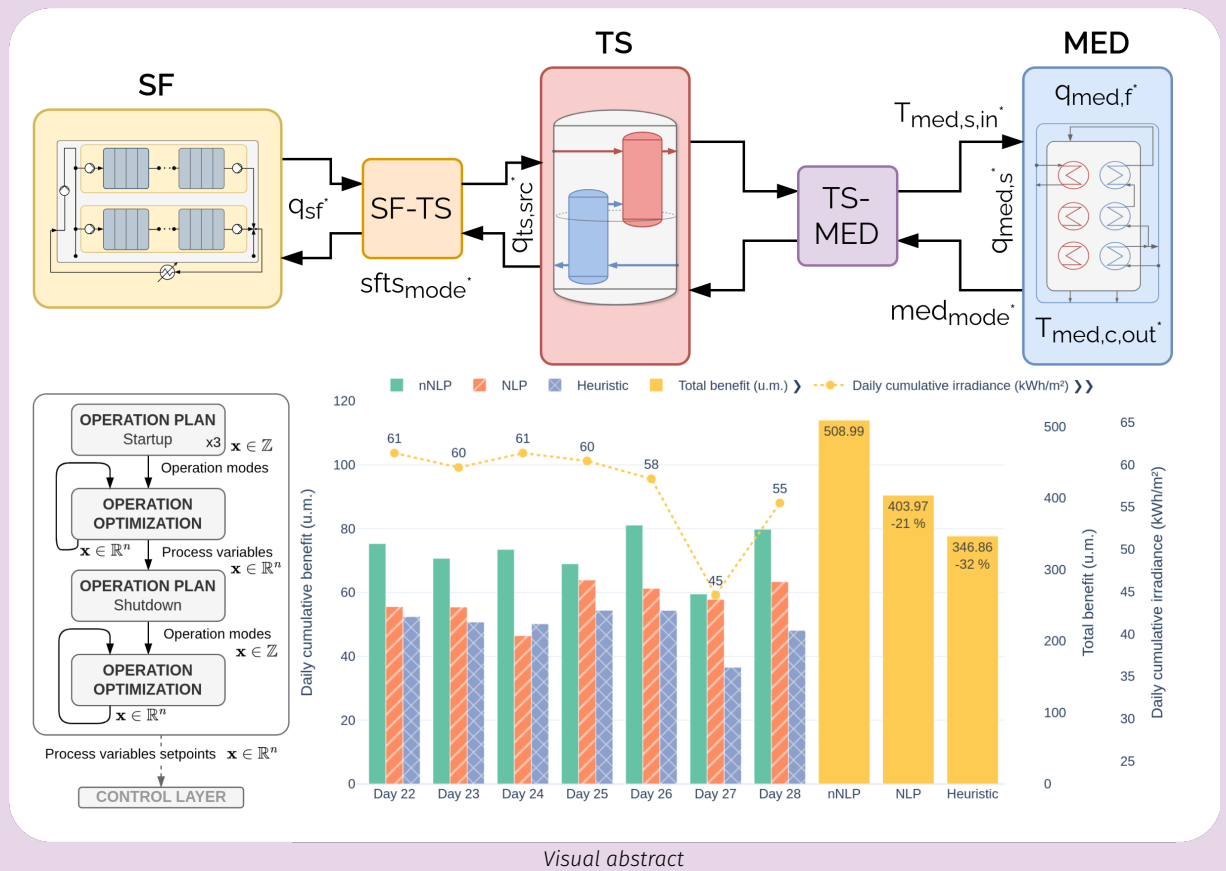
TL;DR

This work advances the integration, evaluation, and optimal operation of low-temperature Multi-Effect Distillation (MED) systems powered by variable energy sources such as thermal energy. As desalination becomes increasingly important to address global freshwater scarcity, modern thermal systems—particularly low-temperature MED—offer a robust and complementary pathway for brine concentration and resource recovery, especially when coupled with waste-heat or renewable sources.

A standardized methodology is developed to evaluate MED performance under realistic and highly variable operating conditions. The approach defines instrumentation requirements, key performance indicators, and uncertainty quantification procedures, complemented by an automated steady-state detection algorithm that enhances the robustness of experimental assessments. Tests at elevated top-brine temperatures confirm the feasibility of high-temperature operation without significant scale formation, although design changes are required to unlock further gains in concentration and thermal efficiency.

To reproduce system behavior, a complete hybrid model of the solar-driven MED installation at Plataforma Solar de Almería (PSA) is formulated. This includes physics-based and data-driven dynamic models for heat generation, storage, and desalination subsystems, combined with discrete supervisory finite-state machines that encode operational logic. The resulting model captures multi-hour system dynamics with mean absolute percentage errors below 15 %, ensuring both fidelity and computational tractability for optimization and control tasks.

The core contribution of the work is a novel hierarchical optimization strategy that governs the autonomous operation of the coupled solar-MED system. The upper-level controller solves a mixed-integer nonlinear economic problem that determines subsystem activation, startup, shutdown, and regulation while exploiting solar availability and storage flexibility. When compared over a full week of operation, the strategy outperforms both a heuristic rule-based baseline and a continuous-only optimization approach by 32 % and 21 %, respectively. These gains stem from the ability to maximize useful temperature differences and align MED operation with the temporal value of heat. This performance levels are achieved with a similar operation strategy of a waste-heat driven system.



Part structure

This part is structured as follows: first in Chapter 10 (Thermal desalination) a context of thermal desalination technologies is provided and their applicability to new applications such as brine-mining, specifically for the case of MED. Then, the experimental solar-driven MED pilot at PSA is presented in Chapter 11. A standard methodology for the experimental assessment of MED systems under variable operating conditions is detailed in Chapter 13, and its application to the experimental plant is shown in Chapter 13 in a high-TBT experimental campaign. The methodology for modelling and optimizing the operation of the system are described in Chapter 12 and Chapter 14, respectively.

TL;DR

Desalination is often seen as a solution to mitigate freshwater scarcity in the face of climate change and population growth [132, 133]. It already plays a fundamental role in many regions [134], but, as more frequent droughts and water shortages are expected, the demand for desalinated water is likely to increase.

However, desalination also faces several challenges, the most important being the intense energy required to separate salts from seawater, which makes it an expensive process compared to other methods to obtain fresh water.

Low-temperature Multi-Effect Distillation (MED) systems constitute a mature, robust, and technically sound solution for brine concentration and resource recovery, especially when driven by waste or renewable heat sources. Rather than being seen as outdated compared to mechanical desalination, MED technology can play a complementary role in integrated water-energy systems aimed at sustainability and minimum-liquid discharge.

10.1 Water crisis

One of the many bad consequences of climate change is the rapid desertification of the planet. According to World Resources Institute projections [87] (see Figure 10.1), 51 countries will suffer from high water stress by 2050. Many regions, including the Arabian Peninsula, Iran, India, and North Africa, are expected to consume at least 80 % of their water supply. The issue is not confined to emerging economies, as Southern European countries like Spain, Italy, and Portugal are also significantly affected with projections of extremely high water scarcity.

Desalination is often seen as a solution to mitigate freshwater scarcity in the face of climate change and population growth [132, 133]. It already plays a fundamental role in many regions [134], but, as more frequent droughts and water shortages are expected, the demand for desalinated water is likely to increase [135]. However, desalination also faces several challenges, the most important being the intense energy required to separate salts from seawater, which makes it an expensive process compared to other methods to obtain fresh water.

In a water scarcity scenario, the priority should always be to reduce the water demand in the first place [136]. Secondly, to recycle as much water as possible so that it can be reused [137]. However, for many parts of the world, these are only palliative measures. Simply put, there will not be enough water available to satisfy its needs, and thus the energy intense process of desalination is the only viable alternative.

Great efforts are being made to reduce the energy consumption of desalination and use renewable energies to increase its sustainability [138–140]. Another path to follow is to generate added value from the separation process.

10.1	Water crisis	99
10.2	Brine concentration and mining	100
10.3	Overview of Desalination Technologies	101
10.3.1	Mechanical Technologies	101
10.3.2	Thermal Technologies	101
10.3.3	Thermal desalination timeline and comparison with Reverse Osmosis (RO)	102
10.4	(Variable) Energy sources for thermal separation processes	104
10.4.1	Solar thermal	104
10.4.2	Waste heat	105

[87]: Kuzma et al. (2023), “Aqueduct 4.0”

[132]: Pltonykova et al. (2020), “The United Nations World Water Development Report 2020: Water and Climate Change.”

[133]: Jones et al. (2019), “The State of Desalination and Brine Production”

[134]: Eke et al. (2020), “The Global Status of Desalination”

[135]: Mekonnen et al. (2016), “Four Billion People Facing Severe Water Scarcity”

[136]: Semiat (2008), “Energy Issues in Desalination Processes”

[137]: Howe et al. (2012), *Principles of Water Treatment*

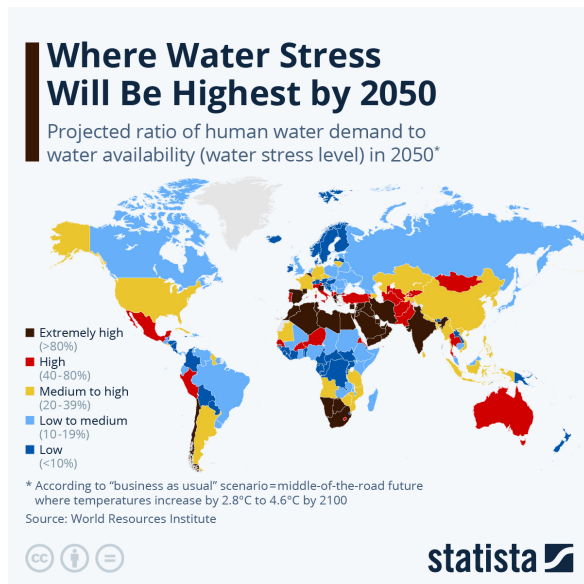
[138]: Shekarchi et al. (2019), “A Comprehensive Review of Solar-Driven Desalination Technologies for off-Grid Greenhouses”

[139]: Allouhi et al. (2024), “Towards Green Desalination”

[140]: Schär et al. (2023), “Optimization of Sustainable Seawater Desalination”

Figure 10.1: Global water stress map.

Source: Statista.



10.2 Brine concentration and mining

[141]: Panagopoulos (2022), "Study and Evaluation of the Characteristics of Saline Wastewater (Brine) Produced by Desalination and Industrial Plants"

[142]: Panagopoulos et al. (2020), "Environmental Impacts of Desalination and Brine Treatment - Challenges and Mitigation Measures"

Brine, a byproduct of the desalination process, typically exhibits salinities 1.6–2.1 times higher than seawater, along with residual process chemicals such as coagulants, antiscalants, and disinfectants [141]. Its conventional disposal methods—such as marine discharge, deep-well injection, evaporation ponds, and land application—are often unsustainable, leading to marine ecosystem stress, soil salinization, and groundwater contamination [142]. High-salinity plumes can cause osmotic shock in marine organisms, disrupt seagrass and coral communities, and alter local biogeochemical conditions. These impacts are particularly pronounced in semi-enclosed basins such as the Mediterranean or Red Sea, where dilution capacity is limited.

At the same time, desalination brine represents a largely untapped resource. Brines are rich in sodium, chloride, magnesium, calcium, and potassium, as well as trace valuable metals like lithium, rubidium, and celsium, which have high commercial value [142]. This recognition has led to growing interest in brine management and valorization, an approach that aligns with the principles of a circular water economy. Through Minimum Liquid Discharge (MLD) and MLD systems, it is possible to recover up to 95–100 % of freshwater and extract valuable salts and minerals, turning waste into a secondary source of raw materials [142]. This strategy not only reduces environmental impacts but also offers potential economic benefits, offsetting part of the desalination cost.

However, technical and economic barriers still limit large-scale implementation of brine mining. Challenges include high energy demand, low extraction efficiencies for trace elements, and the immaturity of integrated hybrid systems combining membrane, thermal, and chemical processes. Moreover, the dominance of sodium chloride—by far the most abundant constituent—means that saturation processes generate vast quantities of common salt, creating logistical and market challenges for its reuse. Recent studies are exploring new applications for desalination brines, such as using them as sources of chloride and nitrate ions in hydrometallurgical leaching or as inputs for industrial chemical production [143].

[143]: Hernández et al. (2020), "Use of Seawater/Brine and Caliche's Salts as Clean and Environmentally Friendly Sources of Chloride and Nitrate Ions for Chalcopyrite Concentrate Leaching"

10.3 Overview of Desalination Technologies

Desalination refers to the set of processes that remove dissolved salts and impurities from saline water to produce freshwater suitable for drinking, irrigation, or industrial use. These technologies can be broadly divided into thermal and mechanical-based processes, depending on the dominant physical mechanism of salt separation [144].

[144]: El-Dessouky et al. (2002), *Fundamentals of Salt Water Desalination*

10.3.1 Mechanical Technologies

Membrane processes rely on selective transport through semipermeable membranes, driven by pressure, concentration, or electrical potential differences, without phase change. They have become dominant in global desalination capacity because of lower energy requirements and modular scalability. The main categories are:

- ▶ Reverse Osmosis (RO). The most widely adopted method, where high-pressure pumps (50-80 bar for seawater) force water through semipermeable membranes, rejecting dissolved salts. RO systems achieve high recovery and energy efficiency, particularly when coupled with modern energy recovery devices, but require careful pretreatment to prevent fouling and scaling.
- ▶ Nanofiltration (NF) and Forward Osmosis (FO). Emerging variants designed for partial desalination, pretreatment, or hybrid systems that improve overall process efficiency.

10.3.2 Thermal Technologies

Thermal desalination processes are based on phase change, involving the evaporation of saline water and condensation of vapor as pure distillate. They were the first large-scale desalination methods to be commercialized and remain widely used, particularly in areas with access to low-cost fuel or waste heat. The main thermal processes are:

- ▶ Multi-Stage Flash (MSF). In MSF, seawater is heated and then flashed into vapor in a series of chambers operating at successively lower pressures. The vapor is condensed to produce distilled water, and the released heat is recovered to preheat the feed. MSF systems are robust and well-proven for large capacities but have high thermal and electrical energy requirements.
- ▶ Multi-Effect Distillation (MED). MED involves a sequence of evaporation-condensation stages (or “effects”) at decreasing pressures. Vapor produced in one effect serves as the heating medium for the next, significantly improving thermal efficiency. MED systems typically operate at 60–70 °C to minimize scaling but can reach up to 120 °C when properly pretreated. They are highly reliable and well-suited to integration with waste heat or solar thermal sources.
- ▶ Vapor Compression (VC). In Vapor Compression, the vapor generated from the feed is compressed either mechanically (MVC) or thermally (TVC) to raise its temperature and pressure so it can serve as the heat source for further evaporation. MVC systems are compact and efficient for small to medium capacities, while TVC is often combined with MED to improve energy recovery.
- ▶ Membrane Distillation (MD). Membrane Distillation bridges the gap between thermal and membrane technologies. It operates on the principle of vapor-phase transport through a hydrophobic, microporous membrane. The driving force is a vapor pressure difference generated by a temperature gradient across the membrane, rather than hydraulic pressure. The

[145]: Milow et al. (1997), “Advanced MED Solar Desalination Plants. Configurations, Costs, Future — Seven Years of Experience at the Plataforma Solar de Almeria (Spain)”

[146]: Alarcón-Padilla et al. (2007), “Application of Absorption Heat Pumps to Multi-Effect Distillation”

1: A variety of metrics can be used to measure the energy efficiency of a desalination plant, each with different purposes and conveying different information. GOR is a metric that measures the heat provided to the system per unit of distillate produced. Also relates to the number of times latent heat is reused in the system.

A detailed description of all metrics can be found in Chapter 13 (Performance evaluation in MED processes)

[147]: Khawaji et al. (2008), “Advances in Seawater Desalination Technologies”

2: Primary energy consumption is the metric most closely tied to fuel consumption and, ultimately, to operating costs. This metric provides the fairest comparison between desalination technologies [148]

[148]: Bouma et al. (2020), “Metrics Matter”

hot saline feed partially evaporates at the membrane surface, and the vapor diffuses through the membrane pores to condense on the cooler permeate side. MD can utilize low-grade or waste heat ($< 80^{\circ}\text{C}$), tolerate very high salinity feeds (even near saturation), and achieve high rejection rates (>99.9 %). Common configurations include Direct Contact MD (DCMD), Air-Gap MD (AGMD), Vacuum MD (VMD), and Sweeping-Gas MD (SGMD). Although still emerging at industrial scale, MD is particularly promising for brine concentration, MLD systems, and solar-driven desalination.

10.3.3 Thermal desalination timeline and comparison with RO

Thermal desalination technologies, such as MED, MSF, and newer hybrid configurations, have evolved through several decades of incremental improvements focused primarily on maximizing thermal efficiency and reducing specific energy consumption. Early developments emphasized heat recovery, exemplified by the integration of Thermal Vapor Compression (TVC) [145] and absorption heat pumps (DEAHP) [146], both designed to increase the Gain Output Ratio (GOR)¹ by reusing latent heat more effectively. Research throughout the 1980s and 1990s concentrated on optimizing heat exchanger design, corrosion resistance, and system modularity, leading to steady improvements in performance and reliability [147]. However, despite these advances, the fundamental thermodynamic limits of phase-change separation and the high capital cost of metallic heat exchangers have constrained further cost reductions and scalability.

By the late 1990s and early 2000s, it became increasingly clear that mechanically driven separation —particularly reverse osmosis (RO)— offered superior performance from both energetic and economic perspectives. RO’s rise was enabled by major advances in polymer science, leading to thin-film composite membranes with high salt rejection and flux, as well as by the widespread deployment of energy recovery devices that dramatically lowered specific energy consumption.

Under any accurately defined metric in use today, RO outperforms MED on the basis of primary energy consumption². RO’s efficiency and economic advantage results from the “conductivity” and cost advantages of membranes over heat exchangers. Significant improvements in heat exchanger costs or heat transfer coefficients would be needed to make thermal desalination technologies such as MED competitive in this respect [148].

If we extend the comparison to primary energy consumption —which correlates directly with fuel usage— while MED uses approximately three times the exergy of an RO system at the desalination system inlet, it requires less than twice the primary energy (11.3 % compared to 20.6 % in terms of second law efficiency) [148]. The smaller gap arises because of the thermodynamic penalty associated with converting primary energy into electricity rather than into steam. Thus, while RO remains more efficient overall, the difference narrows when considering primary energy or co-generation scenarios, where electricity and water are produced together. In such cases, overall second-law efficiencies can approach 70 %, with only about a 1 % difference between RO and thermal technologies [148].

In terms of costs, desalination plants are designed to minimize the Levelized Cost of Water (LCOW), which depends not only on energy consumption but also on capital costs, material properties, and maintenance requirements. For example, while the cost of energy is comparable in co-production systems, RO benefits from the lower material and fabrication costs of polymer membranes compared to the metallic heat exchangers used in thermal systems. Furthermore, membranes exhibit much higher effective conductance than heat exchangers, contributing to their overall economic and energetic advantage.

Finally, in terms of environmental impact, RO membranes are only partially recyclable. There are established reuse/recycling routes (direct reuse, conversion to other applications (*e.g.* NF), mechanical valorisation, thermal/chemical recovery). Recycling is technically feasible and can bring large environmental benefits versus landfilling or incineration, but practical recycling rates are limited today by mixed-material construction, fouling/contamination, cost of separation/transport/pretreatment, and economics of scaling recycling streams [149]. Thermal desalination technologies, on the other hand, primarily use metals and alloys that are widely recyclable.

In summary, RO technology is the most prevalent, with 74 % —See Figure 10.2— of the world's installed capacity using this technology in 2019, while another 21 % and 3 % remained in the use of thermal technologies (namely, MED and MSF) [142]. However, there has been a renewed research focus on low-temperature, small-scale thermal desalination. This resurgence is driven by the increasing availability of low-grade or waste heat, the desire for robust, low-maintenance systems in off-grid or remote regions, and the need for brine concentration and minimum-liquid discharge applications where RO performance declines sharply. The development of membrane distillation (MD) —a hybrid thermal-membrane process—is an example of this shift.

The Case for Multi-Effect Distillation

In light of the comparative analysis between thermal and membrane desalination technologies, Multi-Effect Distillation stands out as a resilient and adaptable option—particularly for brine concentration and MLD applications [150]. While RO dominates conventional seawater desalination due to its lower specific energy consumption, thermal systems offer unique advantages in scenarios where high salinity, waste heat availability, or stringent water quality requirements become critical factors.

Recent studies reinforce the viability of modern MED configurations. Panagopoulos [151] developed a comprehensive techno-economic model for a MED-thermal vapor compression (MED-TVC) system designed to treat high-salinity brines. The analysis demonstrated that a four-effect MED-TVC unit operating with steam at 120 °C achieved a freshwater production cost ($\approx 3.0 \text{ USD}_{2020} \cdot \text{m}^{-3}$) under conventional heat supply. When integrated with industrial waste heat, the cost decreased substantially to $\approx 1.7 \text{ USD}_{2020} \cdot \text{m}^{-3}$, with a payback period below two years. These results confirm that waste-heat-driven MED represents an economically viable pathway for sustainable brine management and resource recovery.

From a thermodynamic perspective, MED processes are capable of concentrating brines up to MLD conditions, particularly when constructed with advanced corrosion-resistant alloys (*e.g.*, super-duplex or hyper-duplex stainless steels) that withstand chloride concentrations above 18,000 mg/L. Exergy analyses from Panagopoulos [151] show that the largest irreversibilities occur in the thermal vapor compressor (TVC) and evaporation stages (effects); nonetheless, the overall exergy efficiency remains competitive for low-temperature thermal systems coupled with a better compatibility with low-grade heat sources.

Also, hybrid desalination systems that combine both membrane (RO) and thermal (MED) processes are also seen as a promising path for combined desalination and brine concentration applications [152, 153].

In conclusion, while RO remains the benchmark technology for large-scale seawater desalination, thermal and hybrid systems—particularly Low Temperature (LT)-MED and MED-TVC—play an indispensable complementary role. They enable the efficient use of low-grade heat, ensure superior product water quality, and provide a sustainable route for brine minimization and resource recovery.

[149]: Lejarazu-Larrañaga et al. (2022), "Thin Film Composite Polyamide Reverse Osmosis Membrane Technology towards a Circular Economy"

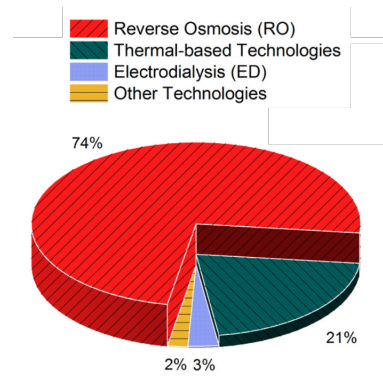


Figure 10.2: Desalination technologies used at plants worldwide in 2019

Source: Panagopoulos et al. [142]

[150]: Zaragoza et al. (2022), "Coupling of Nanofiltration with Multi-Effect Distillation for Solar-Powered Seawater Desalination towards Brine Mining and Water Production for Agriculture"

[151]: Panagopoulos (2020), "Process Simulation and Techno-Economic Assessment of a Zero Liquid Discharge/Multi-Effect Desalination/Thermal Vapor Compression (ZLD/MED/TVC) System"

[152]: Nassrullah et al. (2020), "Energy for Desalination"

[153]: Feria-Díaz et al. (2021), "Commercial Thermal Technologies for Desalination of Water from Renewable Energies"

10.4 (Variable) Energy sources for thermal separation processes

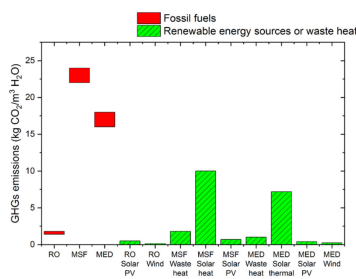


Figure 10.3: Greenhouse Gas (GHG)s emissions per cubic meter of freshwater produced
Source: Panagopoulos et al. [142].

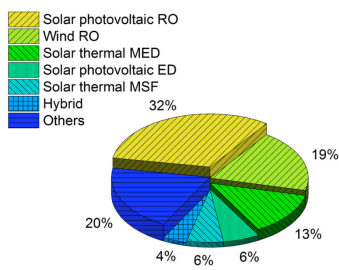


Figure 10.4: Desalination technologies coupled with renewable energy sources at plants worldwide.
Source: Panagopoulos et al. [142]

[93]: Palenzuela et al. (2015), *Concentrating Solar Power and Desalination Plants*

Coupling desalination plants with renewable energy sources —such as solar, geothermal, wind, tidal energy, or alternative sources like industrial waste heat—has become an increasingly attractive strategy. Unlike fossil fuels, renewables are abundant and more sustainable. This advantage is reflected in Figure 10.3 (green bars), which presents the GHG emissions per m³ of freshwater produced by major desalination technologies when powered by renewable energy or waste heat. As shown, the associated GHG emissions are significantly lower compared to conventional fossil-fuel-based operation.

Furthermore, Figure 10.4 illustrates the global distribution of renewable-driven desalination plants. In contrast to Figure 10.2, this distribution highlights a larger share of thermal desalination technologies when supplied by renewable energy sources or waste heat.

10.4.1 Solar thermal

There are two ways in which solar thermal energy can be coupled with thermal desalination processes. Either a solar field can be purposely built to drive the desalination process (standalone or partially with other heat source), or using a co-generation scheme of energy and water in a Concentrated Solar Power + Desalination (CSP+D) configuration. This integration offers significant advantages, including reduced costs for co-producing electricity and freshwater, improved cost-effectiveness through shared infrastructure and economies of scale, and additional savings in greenhouse gas emissions. One critical synergy arises from the fact that during high solar irradiance periods, when solar plants generate maximum (even excess) power coincides with water scarcity periods, making solar-driven desalination particularly effective. The choice between Concentrated Solar Power (CSP)+MED and CSP+RO is highly dependent on regional conditions [93]:

- ▶ In regions with low seawater salinity and lower ambient temperatures (like the Mediterranean), CSP+RO is generally more favorable. The penalty on power production from integrating MED is often higher than the electricity consumption of RO in these conditions.
- ▶ In regions with high seawater salinity and temperature (like the Arabian Gulf), CSP+MED becomes more attractive. The high salinity increases RO's electricity consumption, making the thermal route more efficient and cost-effective, especially when dry cooling is used for the power cycle.

To mitigate the risks of fully replacing the power plant's condenser with a desalination unit (which makes power production dependent on the desalination plant), hybrid configurations like LT-MED-TVC have been developed. This concept uses a combination of exhaust steam and extracted steam to drive the desalination, offering a good balance of efficiency and operational flexibility. In some cases, especially with dry cooling, it can outperform CSP+RO.

One example of a CSP+D system is Sundrop Farms in Port Augusta, South Australia, representing the world's first commercial application using concentrated solar thermal power to co-generate electricity, freshwater, and heating for horticulture [154]. Its central solar tower, targeted by 23,000 mirrors, produces steam to generate electricity, heat and cool greenhouses, and power a desalination plant. The system annually yields 1,700 MWh of electricity, 250,000 m³ of desalinated water from the saline Spencer Gulf, and 20,000 MWh of thermal energy. The freshwater is used in the greenhouses and then recycled, while the resulting brine is managed by sending it to existing power station outflows, with ongoing research into mineral recovery.

[154]: Palenzuela et al. (2019), "Concentrating Solar Power and Desalination Plants"

10.4.2 Waste heat

A significant portion of the world's primary energy consumption³ is ultimately released as waste heat from industrial processes and power generation facilities [155, 156]. This thermal energy, often regarded as a byproduct or liability, represents an immense and largely untapped resource. Instead of being vented to the environment, it can be harnessed either directly or through conversion systems to supply energy for various desalination technologies, thereby lowering operational costs and reducing the environmental footprint of freshwater production.

Broadly speaking, two main recovery pathways exist. The first involves direct heat-to-heat recovery, typically implemented through heat exchangers or heat pumps. This route is highly efficient and is particularly well suited to thermally driven desalination processes, such MED, MSF and MD. The second approach converts waste heat into mechanical work or electricity, most commonly using an Organic Rankine cycle systems or other thermodynamic engines. The generated power can then drive electricity-based desalination units.

Waste heat has therefore emerged as one of the most promising sustainable heat sources for low-temperature thermal desalination systems. Its integration into desalination processes can take several forms. In hybrid configurations, waste heat can be combined with other renewable sources, such as solar thermal energy, to increase the overall temperature level or availability of heat supplied to the thermal separator [157]. Alternatively, depending on the quantity and temperature of the available waste stream, it can operate standalone, driving thermally based desalination units without external fuel input.

The temperature grade of waste heat⁴ plays a decisive role in determining its recovery potential and the appropriate desalination technology [156]. This classification is crucial because it dictates not only the technical feasibility but also the economic viability of energy recovery.

In any case, effective utilization of waste heat not only enhances overall energy efficiency but also contributes to decarbonization efforts in the water and energy sectors. However, challenges remain in terms of temporal availability, temperature matching, and economic competitiveness.

Solar energy and waste heat are free – so why care about efficiency?

Is it not solar energy free? Yes and no. This has been a recurring topic of debate in the literature. Although the fuel, the Sun, is indeed free and practically inexhaustible, converting that energy into a useful form (whether electrical, thermal, or otherwise) requires a transformation process that entails costs.

In the case of solar fields, whether photovoltaic or solar-thermal, the more energy you need, the larger the field area required, and consequently, the higher the investment cost. Therefore, renewable sources do not provide free energy. A similar argument applies to waste heat: to obtain usable heat for a thermal separator, a transformation process is often required, typically involving costly heat exchangers.

In summary, generating heat solely to power a thermal separation process (renewable or not) is generally inefficient and capital-intensive.

A separate question –explored in Chapter 13 (Performance evaluation in MED processes)– is what we actually mean by efficiency, and how it should be defined according to the energy source.

3: Estimated between 20 and 50 %

[155]: Elsaïd et al. (2020), "Recent Progress on the Utilization of Waste Heat for Desalination"

[156]: Brückner et al. (2015), "Industrial Waste Heat Recovery Technologies"

[157]: Christ et al. (2015), "Boosted Multi-Effect Distillation for Sensible Low-Grade Heat Sources"

4: Generally categorized into low (<100 °C), medium (100–400 °C), and high (>400 °C)

TL;DR

The Multi-Effect Distillation (MED) pilot plant at Plataforma Solar de Almería (PSA) is one of the first demonstration plants of solar-powered thermal desalination in the world and one of the first facilities at PSA. Over the years, it has operated with different configurations: MED-Thermal Vapor Compression (TVC) (with steam ejectors), coupled with a Double-Effect Absorption Heat Pumps (DEAHPs) and Low Temperature (LT)-MED, which is the current one. It is coupled with a flat-plate collector solar field and a two-tank thermal storage system, with water as the heat transfer fluid. This chapter describes the main components of the facility, focusing on the MED plant, its particularities, instrumentation, and specifications.

At the end of the 1980s, CIEMAT (Centro de Investigaciones Energéticas, Medioambientales y Tecnológicas, Spain) and DLR (German Aerospace Center, Germany) joined efforts to develop an advanced desalination system powered by solar thermal energy and coupled to a TVC. This initiative, known as the Solar Thermal Desalination (STD) Project (1987–1994) [158], sought to demonstrate the feasibility of coupling large-scale seawater desalination with solar energy. During the first phase, a pilot plant was built at the PSA, combining a MED unit with a parabolic-trough solar field and thermal oil storage. The system operated with synthetic oil heated to drive a steam generator, reaching promising efficiencies and demonstrating high reliability. However, the setup was complex and operated at relatively high temperatures, requiring precise control and maintenance [145].

In the second phase of the STD Project [145], researchers focused on improving energy efficiency and reducing consumption through system integration. A DEAHP ($\text{LiBr}-\text{H}_2\text{O}$) was coupled to the MED unit, significantly lowering thermal demand and increasing performance. While these advancements confirmed the technical potential of solar-powered desalination, they also highlighted the challenges of operating high-temperature systems. This realization guided subsequent efforts toward simpler and more robust configurations.

A decade later, the AQUASOL I project [146, 159] built upon this experience by shifting to lower-temperature and more practical designs. The parabolic-trough field was replaced with a 500 m² stationary compound parabolic collector (CPC) field using liquid water as the heat transfer fluid and with a direct connection to the MED unit. It included two small tanks to attenuate fluctuations in thermal energy availability. The system could operate in solar, fossil, or hybrid modes, offering greater flexibility and easier operation. This transition marked a decisive move from complex, high-temperature solar technologies toward simpler, water-based systems, better suited for reliable and cost-effective desalination under real-world conditions.

In its current configuration, result of the AQUASOL-II project [32, 160], the Solar-driven Multi-Effect Distillation (SolarMED) system consists of an MED plant powered by a flat-plate solar collector field coupled to a two-tank thermal energy storage system (larger than previously). The main components are interconnected as illustrated in Figure 11.1: a flat-plate collector solar field serving as the heat source, a pressurized hot-water two-tank storage system, and an MED unit that utilizes this thermal energy to separate seawater into freshwater and brine. The solar field and the storage circuit are thermally coupled through a heat exchanger. Two subsystems can be distinguished: the

11.1 Solar field	108
11.2 Thermal storage	108
11.3 Multi-Effect Distillation	109

[158]: Gregorzewski et al. (1991), “The Solar Thermal Desalination Research Project at the Plataforma Solar de Almeria”

[145]: Milow et al. (1997), “Advanced MED Solar Desalination Plants. Configurations, Costs, Future — Seven Years of Experience at the Plataforma Solar de Almeria (Spain)”

[146]: Alarcón-Padilla et al. (2007), “Application of Absorption Heat Pumps to Multi-Effect Distillation”

[159]: Blanco et al. (2011), “The AQUASOL System”

[32]: Chorak et al. (2017), “Experimental Characterization of a Multi-Effect Distillation System Coupled to a Flat Plate Solar Collector Field”

[160]: Ampuño et al. (2018), “Modeling and Simulation of a Solar Field Based on Flat-Plate Collectors”

Solar Field and Thermal Storage subsystem (**sfts**), responsible for collecting and storing solar energy, and the thermal load, which in this case corresponds to the MED plant performing the separation process (separation subsystem).

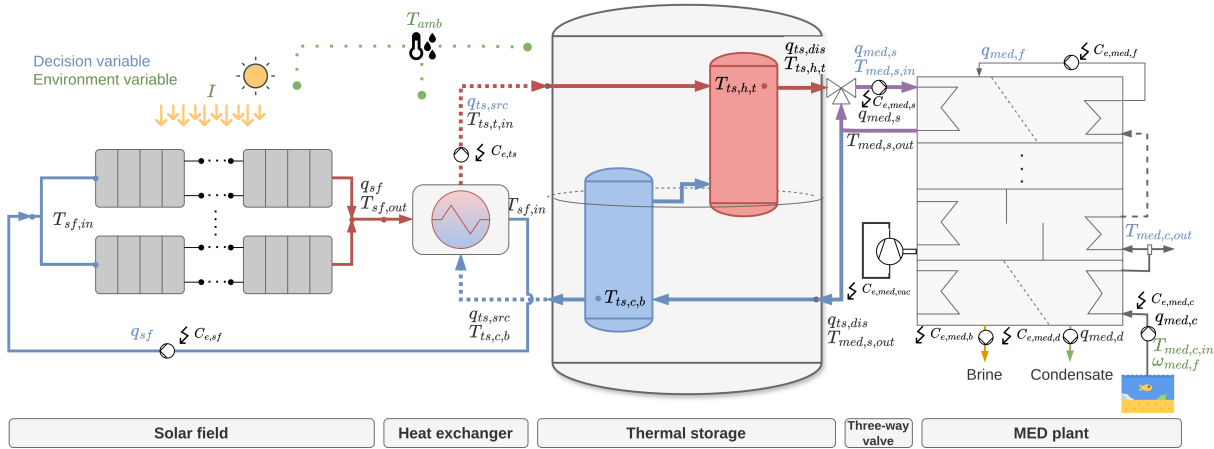


Figure 11.1: SolarMED process diagram

11.1 Solar field

1: See Figure 11.1 - Solar field

2: Depicted in Figure 11.2 (a)

[161]: Roca et al. (2024), "Modelo de parámetros concentrados para captadores solares planos con reflectores"

3: These boosters were implemented recently and have not been considered in this research work

The AQUASOL-II solar field¹ consists of 60 static collector modules (Wagner LBM 10HTF model) with a total aperture area of 606 m²². The solar field is arranged in a small loop (Loop 1) with 4 collector modules connected in parallel, and four larger loops (Loops 2–5), each composed of 14 collector modules (each loop consists of two rows connected in series, and each row is formed by 7 collector modules in parallel). All flat-plate collectors are oriented south and tilted 35° with respect to the horizontal plane [161].

Each collector module is composed of five individual collectors through which water circulates as the heat transfer fluid via a zigzag-shaped absorber tube. As water moves across the tube, it absorbs solar radiation, increasing its temperature before exiting the collector. Recently, the solar field has been equipped with movable –booster– flat mirrors installed south of each collector row. These mirrors automatically track the Sun and reflect direct solar radiation onto the collectors, thereby increasing the solar irradiance incident on them³. The design of the solar field allows independent operation of each loop through its own valves and pumping system. Each loop is connected to an individual heat exchanger, providing flexibility to couple different loads according to experimental requirements.

11.2 Thermal storage

4: See Figure 11.1 - Thermal storage

[162]: Duffie et al. (2013), "Energy Storage"

The thermal storage system⁴ consists on a two-tank connected system. It has a total capacity of 40 m³ (depicted in Figure 11.2 (b)). The system is based on the design principles outlined by Duffie and Beckman [162], and consists of two thermally insulated tanks: a hot tank (the red tank in Figure 11.1) operating at a higher temperature and a cold tank (blue tank in Figure 11.1) ensuring thermal stratification. The tanks are connected from top of the cold tank to the bottom of the hot tank, allowing for recirculation of the fluid between the two tanks. In normal operation, heat is extracted from the bottom of the cold tank, and after being heated, it is injected into the top of the hot tank. The load extracts



Figure 11.2: Heat generation and storage subsystem facilities

heat from the top of the hot tank, and returns it to the bottom of the cold tank, completing the cycle.

11.3 Multi-Effect Distillation

To understand the Multi-Effect Distillation (MED) process, it is useful to first describe the operation of the single-effect distillation unit depicted in Figure 11.4. Such a system mainly consists of an evaporator and a condenser. In the evaporator, an external heat source (typically hot water or steam from a boiler or power plant) transfers energy to seawater sprayed over a tube bundle, forming a thin film that partially evaporates. The generated vapor passes through a demister, which prevents salt droplets from being carried over, and then condenses in the condenser by transferring its latent heat to the seawater flowing inside the tubes. This process yields two products: the distillate (condensed vapor) and the brine (concentrated saline water).

The condenser's cooling water removes the excess heat not used for evaporation, and this water is discharged back to the sea. Since a single-effect unit has low efficiency, multiple stages are connected in series in an MED plant. In this configuration, the vapor produced in one stage serves as the heat source for the next, operating at progressively lower temperatures and pressures. Thus, evaporation and condensation occur simultaneously in each effect, requiring only one external heat source. The vapor condensed within all stages contributes to the total distillate production, while the final stage's condenser preheats the incoming seawater. Finally, the concentrated brine is discharged [93].

The experimental MED plant at PSA is a 14 effect, vertically stacked, forward-feed plant initially built to use low-pressure saturated steam as heat source (70 °C, 0.31 bar) for the first effect and, as mentioned, later replaced to use hot water. An image of the facility in its current state can be seen in Figure 11.3. It has been operated in different experimental campaigns and configurations robustly for more than three decades. A summary of its main specifications is shown at Table 11.1.

The first campaign from 2009 to 2012 is a comprehensive campaign covering the operating range of the plant and described in Palenzuela et al. [163]. Within the research work presented in this thesis, a second experimental campaign took place between 2021 and 2025, in order to validate a standardization methodology



Figure 11.3: MED plant at PSA with open effects for maintenance

[93]: Palenzuela et al. (2015), *Concentrating Solar Power and Desalination Plants*

[163]: Palenzuela et al. (2016), "Experimental Parametric Analysis of a Solar Pilot-Scale Multi-Effect Distillation Plant"

5: Each experimental campaign requires a significant number of test days due to the large number of target operating points. Achieving a valid steady state takes approximately 20–30 minutes—not including the transition time between operating points. On a good day, 3–4 stable operating points can be reached. This makes the experimental campaigns complex and extensive, making it highly suitable for extensive automation

proposal and experimentally characterize the behavior of the system at higher temperatures (see Section 13.5). It is not as extensive as the first one but extends the operation range of the heat source temperature. In total, the experimental data spans 6 years of operation and make available 549 operation points with the range per variable shown in Table 11.2⁵.

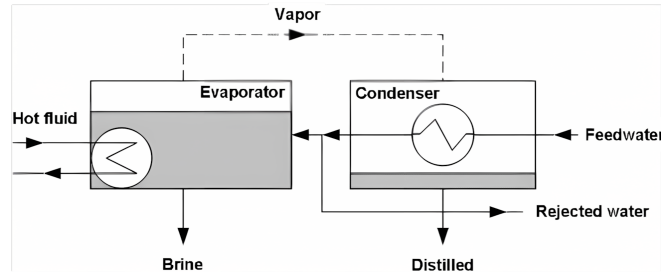


Figure 11.4: Single effect distillation unit schematic diagram

Table 11.1: MED plant at PSA specifications and nominal operating conditions

Parameter	Value
Capacity	72 m ³ /day
Number of effects	14
Feed type	Forward feed
Physical arrangement	Vertically stacked
Heat exchanger configuration	90/10 Cu-Ni HTE
Heat source type	Hot water
Vacuum system	Hydro-ejectors
Heat source flow rate	12 L/s
Feed water flow rate	8 m ³ /h
Brine rejection	5 m ³ /h
Distillate production	3 m ³ /h
Cooling flow rate at condenser	8–20 m ³ /h (10–25 °C)
Thermal power consumption	190 kW
Top Brine Temperature (TBT)	70 °C
Condenser temperature	35 °C

Table 11.2: MED plant available experimental data range.

Variable	\bar{x}	\bar{x}	Unit
q_s	10.50	44.35	m ³ /h
$T_{s,in}$	52.01	80.98	°C
q_f	4.98	8.27	m ³ /h
$T_{c,in}$	12.14	33.64	°C
$T_{c,out}$	19.36	39.89	°C
q_d	1.61	3.08	m ³ /h
$T_{s,out}$	50.05	77.31	°C
q_c	8.03	23.13	m ³ /h

Some particularities of this system are explained hereinafter:

- ▶ As an energy efficiency measure, the plant is equipped with 13 preheaters, which using a fraction of the vapor generated in the effects, preheat the feedwater before entering the first effect. The fourteenth “preheater” would be the condenser.
- ▶ As mentioned, the external heat source driving the process, is hot water from a thermal storage system. Water is drawn from one of the tanks and mixed with the water at the outlet of the first effect through a three-way valve (See Figure 11.1 - Three-way valve), allowing independent regulation of flow and temperature.
- ▶ The inland location of this experimental plant is another particularity of the system. A fixed amount of seawater (30 m³), stored in a reservoir, is available to be used in the process and replenished as needed. The effluents from the plant are mixed in a different reservoir (5 m³), and returned to the feed in a close loop operation. Because water exits the process at a higher temperature than when it enters, this type of operation implies an ever-increasing heat sink temperature. A wet cooling tower, installed between the two reservoirs, is used to mitigate this effect.
- ▶ The previous particularity leads to a significant variation in the inlet water temperature from day to day and also within the same day depending on the operation conditions. To ensure the stability of the condenser (i.e. a constant vapor pressure and outlet cooling water temperature), the cooling flow rate is regulated. This allows to have a stable system representative of a real plant operating under normal conditions. However, this can lead to variable electrical consumption of the cooling pump.
- ▶ The vacuum system of the plant is based on two hydro-ejectors and a pump. The pump is operated always at fixed speed and its electrical consumption has been characterized with measurements under various conditions as being near-constant and independent of the operation conditions. Its associated nominal power is 5 kW_e.
- ▶ The salinity of the feedwater is checked before every test measuring its conductivity with a conductivity meter (see Table 11.3).

The experimental facility is a complex system of considerable size for a pilot plant. It includes over 100 variables, between inputs and monitored outputs. Its instrumentation is shown in Table 11.3 and the placement in the system can be seen in Figure 11.5. PT100 sensors are used to measure all liquid temperatures (TT01..TT05), while a PT1000 sensor is used to measure the ambient temperature (TT06). The pressure inside the first effect and condenser (PT01 and PT02, respectively) is measured by two different pressure transducers which fundamentally differ in their measurement range. To monitor the power consumption of the system, various subsystems have been individually instrumented using

Table 11.3: Characteristics of the instrumentation installed at MED-PSA unit (^a value of the measured temperature in °C, ^b of reading, ^c full scale).

Measured variable	Instrument	Model	Range	Measurement uncertainty
Water temperature, TT01...TT0N	PT100 Class A	SEDEM OF112871	0 - 100°C	± 0.15 + 0.002·T ^a
Distillate flow rate, FT03	Vortex flow meter	ABB TRIO-WIRL VT4	1.6 - 18 m ³ /h	± 0.75% o.r. ^b
Hot water flow rate, FT01	Electromagnetic	Endress+Hauser Proline Promag 50P	2.42 - 78.33 L/s	± 0.5% o.r.
Feedwater flow rate, FT02	Electromagnetic	Endress+Hauser Proline Promag P 300	2.1 - 66 m ³ /h	± 0.5% o.r.
Ambient temperature, TT05	PT1000	-	-40 - 60 °C	± 0.15 + 0.002·T
Pressure, PT01	Pressure capacitive	Endress+Hauser Cerabar T-PMC131	0 - 1 bar	± 0.5% FS ^c
Pressure, PT02	Piezoresistive sensor	WIKI S-10	0 - 0.6 bar	± 0.5% FS
Level, LT01, LT02	Magnetic level gauge	IGEMA NA7-50	0-750 mm	± 5 mm
Power, JT01...JT04	Power meter Class 1 IEC 62053-21	Circutor CM31	0-7 kW	±1% o.r.
Conductivity, CT01...CT02	Conductivity meter	Prominent Portamess 911	0.1 μS/cm - 1000 mS/cm	± 0.5% o.r. < 500 mS/cm ± 1% o.r. ≥ 500 mS/cm

a power meter (JT01..JT04). Conductivity is measured using a portable conductivity meter (CT01, CT02), to which a calibration is periodically performed to convert conductivity to salinity. Flow rates (FT01..FT04) are measured using different types of flowmeters depending on the characteristics of the fluid being evaluated. Electromagnetic flowmeters are used for conductive fluids, while vortex flowmeters are used for non-conductive fluids. All sensors transmit a 4-20 mA analog signal that is converted to digital by Analog-to-Digital Converter (ADC) converters. Variable Frequency Drives (VFDs) are used to control all flow rates in the system: heat source, cooling, feed, brine and distillate.

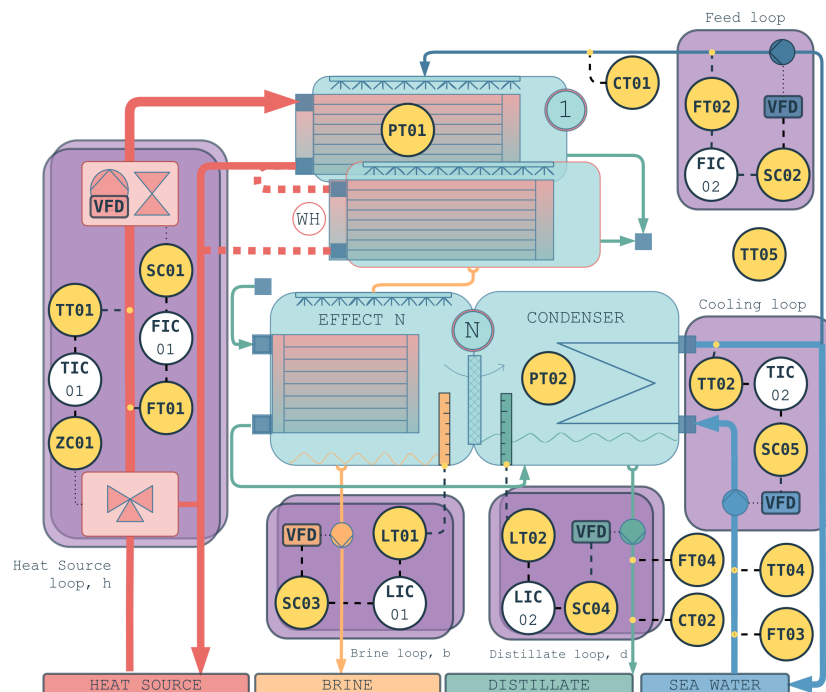


Figure 11.5: Piping and Instrumentation Diagram (P&ID) representative of the MED-PSA plant with the installed instrumentation, Key Process Variables (KPVs), and implemented control loops (ANSI/ISA 5.1-2022).

Hybrid modelling of a solar driven MED system

TL;DR

This chapter presents the discrete and complete dynamic modelling of the Solar-driven Multi-Effect Distillation (SolarMED) system. First, dynamic physics-based models are developed for the solar field, heat exchanger, thermal storage, three-way valve, and a data-driven static model for the Multi-Effect Distillation (MED) plant.

These models are then combined with the discrete behavior of the installation. This is represented by means of two supervisory Finite-State Machines (FSMs) that define the operation states of the Solar Field and Thermal Storage subsystem (**sfts**) and the Separation subsystem (**med**). Each FSM determines subsystem activation and transitions based on system inputs, internal rules, and configurable parameters such as cooldown or startup durations. The integrated hybrid model is evaluated under realistic operation conditions with different prediction horizons, showing good agreement with experimental data. Results demonstrate that the model accurately reproduces the coupled dynamics of the system, maintaining Mean Absolute Percentage Error (MAPE) below 15% for multi-hour predictions while preserving computational efficiency.

12.1	Introduction	113
12.2	Dynamic modelling	113
12.2.1	Solar field	113
12.2.2	Thermal storage	118
12.2.3	Heat exchanger	122
12.2.4	MED	124
12.3	Discrete modelling	129
12.3.1	Heat generation and storage subsystem (sfts)	129
12.3.2	Separation subsystem (med)	129
12.3.3	Validation	131
12.4	Complete system model	132
12.4.1	Validation	133

12.1 Introduction

The behavior of the SolarMED process can be abstracted into two components, a continuous and a discrete one. Each component is described and validated in the respective Section 12.2 (Dynamic modelling. Process variables) and Section 12.3 (Discrete modelling. Operation state). Then, they are combined to create a complete model of the SolarMED process in Section 12.4 (Complete system model).

12.2 Dynamic modelling. Process variables

The dynamic behavior of the SolarMED governs the evolution of the continuous process variables. It is represented by a set of models, one for each system component. A discrete representation¹ is used: process variables are sampled at a fixed interval, T_s , and system dynamics are expressed through difference equations.

In most cases, this representation captures the transient behavior of the system. However, some models described in the following sections are steady-state approximations. While this can introduce discrepancies during transient events, the impact is minor. The model is intended primarily for optimization, with sampling times on the order of minutes. Moreover, inputs to slower components –like the MED– are adjusted infrequently (typically at intervals of 30 minutes or more) allowing sufficient time for the system to reach steady state².

12.2.1 Solar field

The (flat-plate collector) solar field can be seen as a converter of electrical to thermal energy, subject to irradiance availability. The main outputs, in terms of

1: Not to be confused with the discrete model, see Section 3.1.3

2: Further discussed in Section 3.1 (Modelling and simulation)

In all models, it has been assumed that model parameters like heat transfer coefficient (U) or heat loss coefficients (H) are constant, and not a function of temperature.

operation of the solar field, are the thermal power obtained, \dot{Q}_{sf} (kW_{th}), at what temperature that heat is obtained, $T_{sf,out}$ (°C), and the electricity needed to do so, $C_{e,sf}$ (kW_e).

3: i.e., a balanced flow distribution with similar collectors, which is the case in the experimental facility for the considered loops 2 to 5 [160]: Ampuño et al. (2018), "Modeling and Simulation of a Solar Field Based on Flat-Plate Collectors"

[161] Also called model (2019) "A model for dynamic parameters, respectively Flat Plate Solar Field Model Designed for Control Purposes"

5: Transport delays are a common feature in dynamic systems, where the response of the system to an input is not instantaneous, but rather delayed by a certain amount of time. This delay can be caused by various factors. In this particular system, is due to the time it takes for the water to flow through the solar field and reach the temperature sensors. The apparent delay is the result of adding up the individual –different delays of each collector cell

[165]: Normey-Rico et al. (1998), "A Robust Adaptive Dead-Time Compensator with Application to A Solar Collector Field"

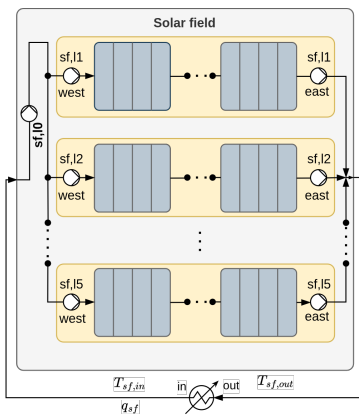


Figure 12.1: Solar field process diagram.

The diagram in Figure 12.1 illustrates the individual loops that make up the field. In the model, it is assumed that all loops have equal flow rates and temperatures³. As a result, the system can be simplified to a single loop with a collector area equal to the sum of the collector areas of the individual rows of collector loops.

A first-principles model —see Model 12.1— based on the one presented in Ampuño et al. [160] is used to model the solar field. The model has two types of parameters: dynamic and constant⁴. The dynamic parameters are the thermal loss coefficient, H_{sf} ($\frac{J}{s \cdot C}$), which relates thermal losses to the environment and the gain coefficient, β (m), encompassing the collector transmissivity and absorstance, and determines the amount of irradiance that is transferred to the working fluid. These two dynamic parameters are calibrated using experimental data, and their values, together with the constant parameters, are presented in Table 12.4.

The main difference of the model developed in this research work with respect to the model presented in [160] is how the apparent transport delay is modelled [164]⁵. In this implementation, the transport delay is simplified to a single steady state parameter based on the work presented in Normey-Rico et al. [165] since delays vary less than 30 % from the nominal value.

Model 12.1: Solar field

$$\begin{aligned}
 T_{out}(k) &= sf \text{ model}\left(T_{out,k-1}, T_{in,k:n:k}, q_{k:n:k}, I_k, T_{amb,k}; \beta, H_{sf}, \theta\right) \\
 L_{pipe,eq} &= \frac{T_s}{A_{pipe,eq}} \sum_{k=0}^n q_{sf}[k] && \text{Equivalent pipe length [m]} \\
 L_{eq} &= n_{c-s} \cdot L_{tb} && \text{Eq. collector tube length [m]} \\
 c_f &= n_{c-loop} \cdot n_{tb-c} && \text{Conversion factor [-]} \\
 K_1 &= \beta / (\rho \cdot c_p \cdot A_{cs}) && [K \cdot m^2/J] \\
 K_2 &= H / (L_{pipe,eq} \cdot A_{cs} \cdot \rho \cdot c_p) && [1/s] \\
 K_3 &= 1 / (L_{pipe,eq} \cdot A_{cs} \cdot c_f) \cdot (1/3600) && [h/(3600 \cdot m^3 \cdot s)] \\
 T_{out}(k) &= T_{out}(k-1) + \left(\begin{array}{l} + K_1 \cdot I \\ - K_2 \cdot (\bar{T} - T_{amb}) \\ - K_3 \cdot q_{k-n_d} (T_{out,k-1} - T_{in,k-n_d}) \end{array} \right) \cdot T_s && \begin{array}{l} \text{Solar contribution [K/s]} \\ \text{Environment losses [K/s]} \\ \text{Heat absorbed [K/s]} \end{array}
 \end{aligned}$$

The number of delay samples (n_d) depends on the model sample time and a system parameter called the equivalent length. The following procedure was followed to estimate it:

1. Using a reference test with a fixed sample time, T_s , the number of delay samples (n_d) was manually fitted to the data, by visually inspecting the response of the system to a step change in the input flow.

2. Estimate the equivalent length of the solar field by taking the average flow rate (\bar{q}_{sf}) across the delay samples span⁶, and divide it by a fixed parameter- the solar field pipe equivalent cross-sectional area, $A_{pipe,eq}$.

6: In reverse order, from newest to oldest

$$\bar{q}_{sf} = \sum_{k=-n_d}^{k=0} q(k)/n_d$$

$$L_{pipe,eq} = \frac{\bar{q}_{sf} \times T_s \times n_d}{A_{pipe,eq}}$$

3. With this equivalent length ($L_{pipe,eq}$), the number of delay samples can be estimated for any sample time T_s and flows vector \mathbf{q}_{sf} by iteratively adding the distance that flow travels at each sample time until the equivalent length is reached.

Electrical consumption

Definition 12.2.1 Step train test. Variations in the Variable Frequency Drive (VFD) pump speed from a minimum to a maximum value, with fixed increments.

The AQUASOL-II solar field consists of a set of pumps that recirculate water through the system. The pumps are controlled by VFDs that allow to vary the flow rate through the solar field. A main recirculation pump (P_{l0}) is responsible for the primary flow, while additional pumps (P_{l1}, P_{l2} , etc.) are used in the individual loops to either increase the total flow rate or to operate with the isolated loop. This redundancy means that the same flow rate can be achieved with different pump configurations.

The electrical consumption of the solar field is characterized by determining the relationship between flow rate and power consumption for each configuration. This allows for the identification of the configuration that minimizes electrical consumption across the range of operating flow rates. Once this characterization is established, the overall electrical consumption of the solar field can then be modelled.

A series of tests were performed as can be seen in Figure 12.2. The tests were carried out in two different dates since they have to be performed early, before the solar field is irradiated by the sun and the field heats up⁷. In the first day, step trains are applied to the main loop and individual isolated loops⁸. On the second day, different speeds levels were set for the main recirculation pump (10% - 100%, 10% increments) while step trains were applied to the individual loops (40% - 100%, 20% increments)⁹.

7: Observe the trend in Figure 12.2 - Temperatures. The flow needs to be purposely regulated to maintain safe solar field temperatures
8: 20240925 07:15 – 08:30

9: In Figure 12.2, from 20240927 07:35 to 08:20

Figure 12.3 shows the relationship between flow rate and power consumptions for different configurations and pump speeds. Up to 91.9 l/min the best configuration is to just use the main recirculation pump. Above this flow rate, the main pump is used in combination with the individual loop pumps. First, a combination of main pump from 85 to 100% and individual loops fixed at their 40% minimum speed up until 105 l/min, then the main pump fixed at 100% and individual loops at increasing values from 40 to 100% until a maximum flow rate of 148 l/min is achieved.

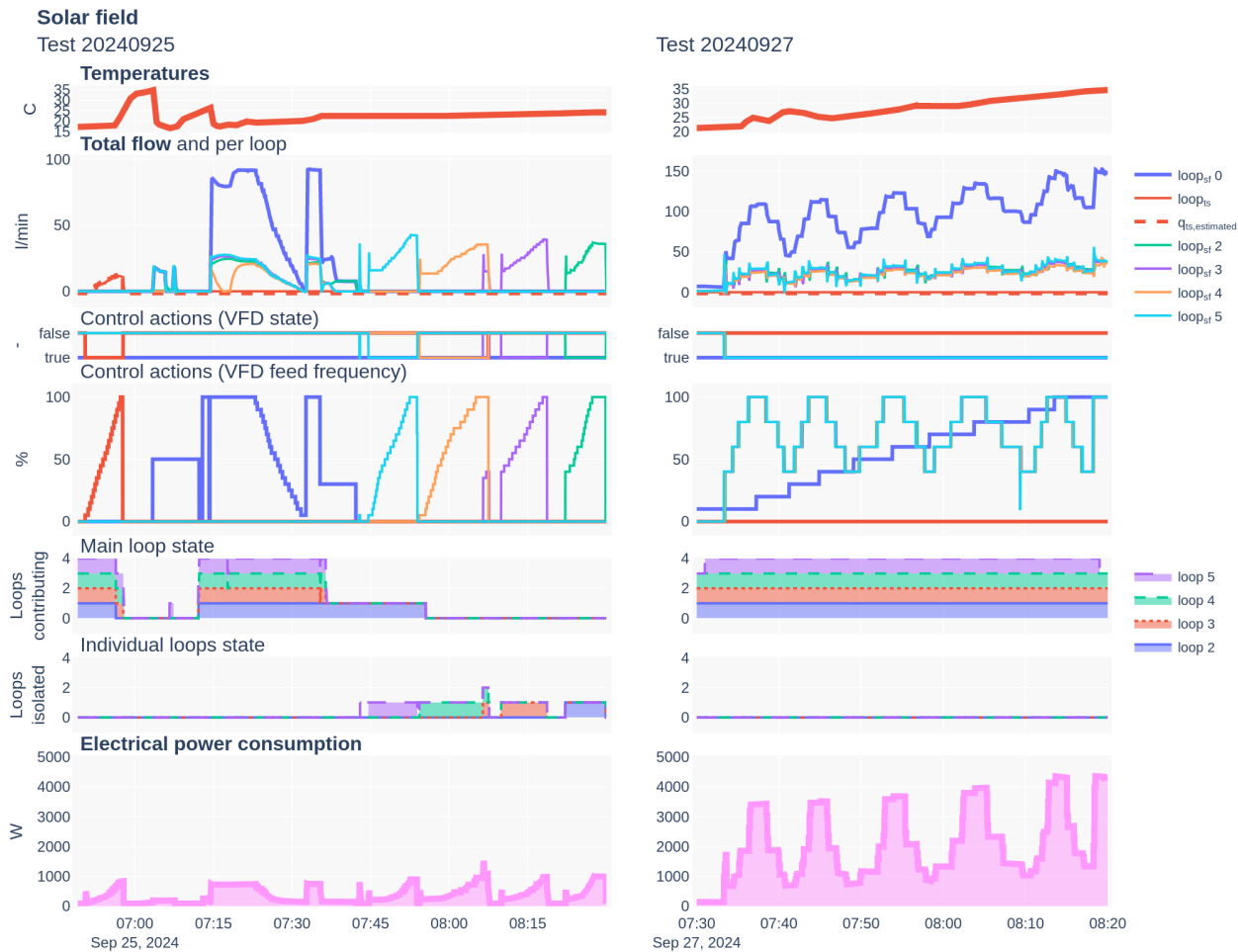
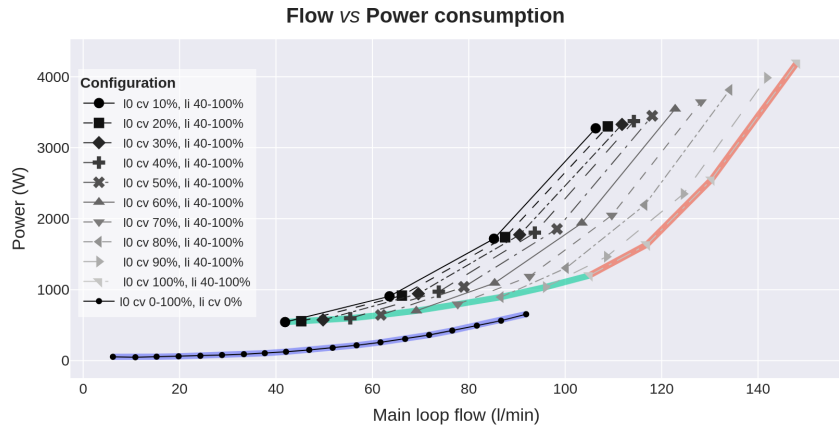


Figure 12.2: Solar field and thermal storage electrical characterization tests.



Figure 12.3: Solar field flow rate for different pump configurations and their associated power consumption.



$$\text{Optimal configuration}(q_{sf}) = \begin{cases} l_{0,cv} \in [0, 100] \% \wedge l_{i,cv} = 0\%, & 6.2 < q_{sf} \leq 91.9 \text{ (l/min)} \\ l_{0,cv} \in [0, 100] \% \wedge l_{i,cv} = 40, & 91.9 < q_{sf} \leq 105 \\ l_{0,cv} = 100 \% \wedge l_{i,cv} \in [40, 100], & 105 < q_{sf} \leq 148 \end{cases} \quad (12.1)$$

With this optimal selection, a third-order polynomial regression is fitted to the data, with a coefficient of determination of $R^2 = 0.99$.

Model 12.2: Solar field electrical consumption

$$C_{e,sf} [\text{kW}_e] = \text{sf electrical consumption}(q_{sf} [\text{m}^3/\text{h}])$$

$$C_{e,sf} = 1.3 \cdot 10^{-5} \cdot q_{sf}^3 + -8.72 \cdot 10^{-4} \cdot q_{sf}^2 + 2.29 \cdot 10^{-2} \cdot q_{sf} + -8.48 \cdot 10^{-2}$$

Summarizing, the electrical consumption of the solar field is modelled as a function of the flow rate through the solar field from a minimum value of $3.7 \text{ m}^3/\text{h}$ (50 W) to a maximum value of $88.84 \text{ m}^3/\text{h}$ (4.2 kW). This is achieved as the result of different combinations of the main recirculation pump and the individual loops depending on the working flow range.

Validation

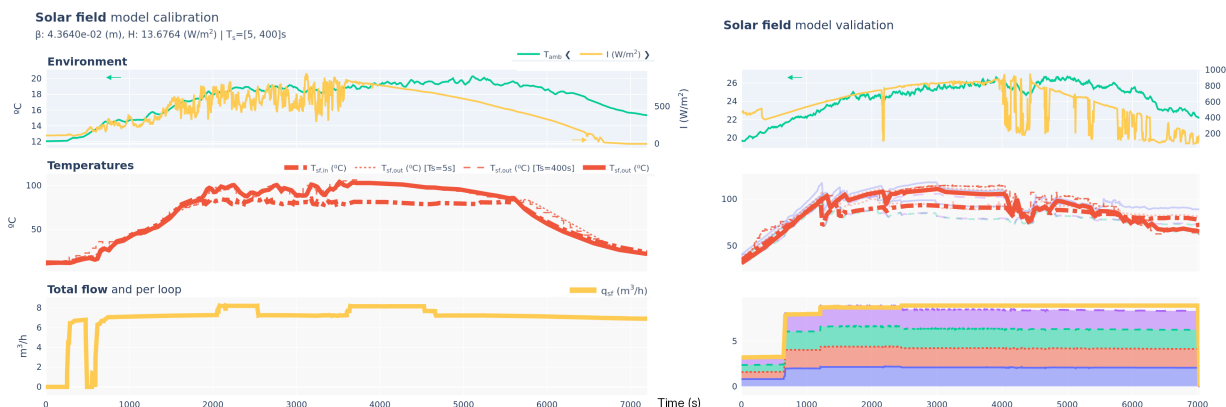


Figure 12.4: Solar field model calibration and validation tests. The colors in the validation plot represent the different loops (not available in the calibration data)

In order to calibrate the model parameters (β and H), one representative experimental test is used¹⁰ where the parameters are fitted. The values can be found in Table 12.4. Compared to the results presented in Ampuño *et al.* [160], double the gain coefficient is obtained while higher losses are found. This could be explained by the fact that the calibration was performed including the warm-up and cooldown periods of the solar field.

10: See Figure 12.4– left

Table 12.1: Summary table of the prediction results obtained with the solar field model for different test days and sample times.

Predicted variable	Sample time (s)	Test date	Performance metric						Time (s)	
			R ² (-)		MAE (s.u.)		MAPE (%)			
			Test	Avg.	Test	Avg.	Test	Avg.	Test	Avg.
$T_{sf,out}$ (°C)	5	20231030	0.97	4.41	9.17	1.48				
		20231106	0.97	2.97	6.25	1.40				
		20230630	0.81	9.77	17.95	1.70				
		20230703	0.92	5.07	6.05	1.60				
		20230508	0.89	5.59	7.86	1.42				
	400	20230628	0.90	4.93	2.50	9.37	1.61	1.43		
		20230511	0.87	5.02	6.30	1.43				
		20230629	0.85	7.22	11.61	1.58				
		20230505	0.76	10.13	13.74	1.52				
		20231031	0.96	2.50	9.37	1.43				

s.u. stands for same units as the predicted variable

As can be seen in the figure, most of the error is accumulated during the cooldown of the field. In Figure 12.4– right the dynamic behavior of the model is validated with another test. The dynamic response obtained is very similar to the one experimentally measured for most of the test, similar to the calibration test despite the cloudy conditions. A higher error is observed between calibration and the particular validation test shown: $R^2=0.97$ compared to 0.87, but this can be explained because during the latter part of the experiment the irradiance was very intermittent while a high flow was kept which even manages to invert outlet and inlet temperature. Nonetheless, in relative terms very similar errors are obtained¹¹.

11: 6.25 compared to 6.3 in terms of MAPE

Several more tests (10) are evaluated, and the performance obtained is shown in Table 12.1. Here it can be seen than for many tests performance close to the calibration tests are obtained. There is a notable difference in the performance of the model depending on the sample rate used. R^2 goes from 0.96 to 0.93, and Mean Absolute Error (MAE) from 2.50 to 2.84 °C, when moving from a fast sample rate ($T_s = 5$ s) to a slow one ($T_s = 400$ s). This is expected since the model loses performance in transient periods which are a constant in cloudy days. However, the average error is still accurate enough for the intended use of the model while having a significant reduction in computational time, from 1.43 s to 0.02 s, 71 times faster.

In general, good metrics are obtained for most tests, with maximum percentage errors below 10 % MAPE, and in those who do not, the error is usually accumulated while the solar field is heating up or cooling down, that is, when no heat is being delivered to the load.

12.2.2 Thermal storage

A first-principles model of a two-tank thermal storage system is developed to capture the key thermodynamic and fluid dynamic phenomena governing energy

transfer and stratification based on the methodology developed by Duffie et al. [162].

[162]: Duffie et al. (2013), "Energy Storage"

The governing model equations and boundary conditions to simulate the transient thermal behavior of the storage system, including mass and energy balances, heat transfer mechanisms, and the stratification dynamics are shown in Model 12.3.

Model 12.3: Thermal storage

$T_h(k)$, $T_c(k)$ = thermal storage model($T_h(k-1)$, $T_c(k-1)$, $T_{src}(k)$,

$T_{dis}(k)$, $\dot{m}_{src}(k)$, $\dot{m}_{dis}(k)$, $T_{amb}(k)$; θ_h , θ_c)

if $\dot{m}_{dis}(k) > \dot{m}_{src}(k)$: *(cold to hot recirculation)*

$T_c(k)$ = single tank model($T_c(k-1)$, $T_T=0$, $T_B=T_{dis}(k)$, $T_{amb}(k)$,
 $\dot{m}_{in,T}=0$, $\dot{m}_{in,B}=\dot{m}_{dis}(k)$, $\dot{m}_{out,T}=\dot{m}_{dis}(k)-\dot{m}_{src}(k)$, $\dot{m}_{out,B}=\dot{m}_{src}(k)$; θ_c)

$T_h(k)$ = single tank model($T_h(k-1)$, $T_T=T_{src}(k)$, $T_B=T_c^{out}(k)$, $T_{amb}(k)$,
 $\dot{m}_{in,T}=\dot{m}_{src}(k)$, $\dot{m}_{in,B}=\dot{m}_{dis}(k)-\dot{m}_{src}(k)$, $\dot{m}_{out,T}=\dot{m}_{dis}(k)$, $\dot{m}_{out,B}=0$; θ_h)

else: *(hot to cold recirculation)*

$T_h(k)$ = single tank model($T_h(k-1)$, $T_T=T_{src}(k)$, $T_B=0$, $T_{amb}(k)$,
 $\dot{m}_{in,T}=\dot{m}_{src}(k)$, $\dot{m}_{in,B}=0$, $\dot{m}_{out,T}=\dot{m}_{dis}(k)$, $\dot{m}_{out,B}=\dot{m}_{src}(k)-\dot{m}_{dis}(k)$; θ_h)

$T_c(k)$ = single tank model($T_c(k-1)$, $T_T=T_h^{out}(k)$, $T_B=T_{dis}(k)$, $T_{amb}(k)$,
 $\dot{m}_{in,T}=\dot{m}_{src}(k)-\dot{m}_{dis}(k)$, $\dot{m}_{in,B}=\dot{m}_{dis}(k)$, $\dot{m}_{out,T}=0$, $\dot{m}_{out,B}=\dot{m}_{src}(k)$; θ_c)

where:

$T(k)$ = single tank model($T(k-1)$, $T_{T,in}(k)$, $T_{B,in}(k)$, $\dot{m}_{in,T}(k)$, $\dot{m}_{in,B}(k)$,
 $\dot{m}_{out,T}(k)$, $\dot{m}_{out,B}(k)$, $T_{amb}(k)$; θ)

► Top volume

$$\begin{aligned} -\rho \cdot V_T \cdot c_p \cdot \frac{T_{T,k} - T_{T,k-1}}{T_s} + \dot{m}_{src} \cdot T_{T,in} \cdot c_p - \dot{m}_{dis} \cdot T_{T,k} \cdot c_p \\ - \dot{m}_{src} \cdot T_{T,k} \cdot c_p + \dot{m}_{dis} \cdot T_{T,k} \cdot c_p - H_T \cdot (T_{T,k} - T_{amb}) = 0 \end{aligned}$$

► Bottom volume

$$\begin{aligned} -\rho \cdot V_B \cdot c_p \cdot \frac{T_{B,k} - T_{B,k-1}}{T_s} + \dot{m}_{src} \cdot T_{i-1,k} \cdot c_p + \dot{m}_{dis} \cdot T_{B,in} \cdot c_p \\ - \dot{m}_{src} \cdot T_{B,k} \cdot c_p - \dot{m}_{dis} \cdot T_{B,k} \cdot c_p - H_N \cdot (T_{B,k} - T_{amb}) = 0 \end{aligned}$$

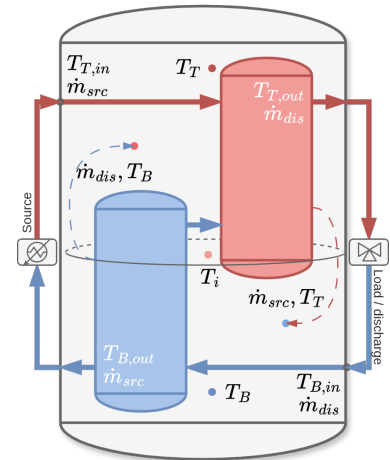


Figure 12.5: Thermal storage process diagram.

► Inner volume

$$\begin{aligned} & -\rho \cdot V_i \cdot c_p \cdot \frac{T_{i,k} - T_{i,k-1}}{T_s} + \dot{m}_{src} \cdot T_{i-1,k} \cdot c_p - \dot{m}_{dis} \cdot T_{i,k} \cdot c_p \\ & - \dot{m}_{src} \cdot T_{i,k} \cdot c_p + \dot{m}_{dis} \cdot T_{i+1,k} \cdot c_p - H_i \cdot (T_{i,k} - T_{amb}) = 0 \end{aligned}$$

Three types of volumes are defined: the inner volume, the top volume and the bottom volume:

- Top volume (V_T): can receive external heat, and have heat extracted from it. It interacts with the inner volume that it interfaces with.
- Bottom volume (V_B): can also have external interactions, and exchanges with the inner volume above it.
- Inner volume (V_i): is any volume that is not the top or bottom, that is, is surrounded by other volumes with which it exchanges heat and mass by inner recirculation.

Similar to the solar field model, it has two parameters that need to be calibrated using experimental data. These dynamic parameters are the thermal loss coefficient (H_i ($\frac{1}{s \cdot C}$)) which relates heat losses to the environment and the volume of each of the considered control volumes (V_i). Three temperature sensors are available in the experimental facility, so three volume divisions are used to model the thermal storage. With two tanks, this results in a total of 12 parameters to be calibrated.

Electrical consumption

The first step train given in Figure 12.2 – 20250925 from 06:50 to 07:15 is used to characterize the electrical consumption of recirculating water ($q_{ts,src}$) in the thermal storage circuit. The electrical consumption is modelled as a function of the flow rate through the thermal storage from a minimum value of $1.4 \text{ m}^3/\text{h} - 0.05 \text{ kW}_e$ to a maximum value of $8.4 \text{ m}^3/\text{h} - 0.75 \text{ kW}_e$ with a second-order polynomial regression, with a coefficient of determination of $R^2 = 0.99$.

Model 12.4: Thermal storage electrical consumption

$$\begin{aligned} C_{e,ts} [\text{kW}_e] &= \text{ts electrical consumption} (q_{ts,src} [\text{m}^3/\text{h}]) \\ C_{e,ts} &= 4.88 \cdot 10^{-1} \cdot q_{ts,src}^2 + -6.95 \cdot 10^{-3} \cdot q_{ts,src} + 0.01 \end{aligned}$$

Validation

In order to calibrate the model parameters (H_i and V_i), data from the system was recorded during four consecutive days under different operating conditions (see Figure 12.6 - left). The first and last days included both charge and discharge cycles, while the middle two days were dedicated to charging-only operations. In between these days, the system was left idle to observe the natural thermal losses. The model parameters were fitted¹² to minimize a combined metric averaging the three temperature measurements available per tank, obtaining a low thermal loss coefficient in the order of 10^{-2} to 10^{-4} (W/K). On the other hand, adding the volumes of the three control volumes totals around the 15 m^3 of the actual tank volume, which is a good indication that the model is capturing the

12: See their values in Table 12.4

thermal behavior of the system well. However, they are not distributed evenly; for both tanks the bottom volumes are significantly smaller than the upper ones. This can be explained by the fact that the temperature transmitters are not spaced evenly, and the bottom transmitter is located near the tank's bottom.

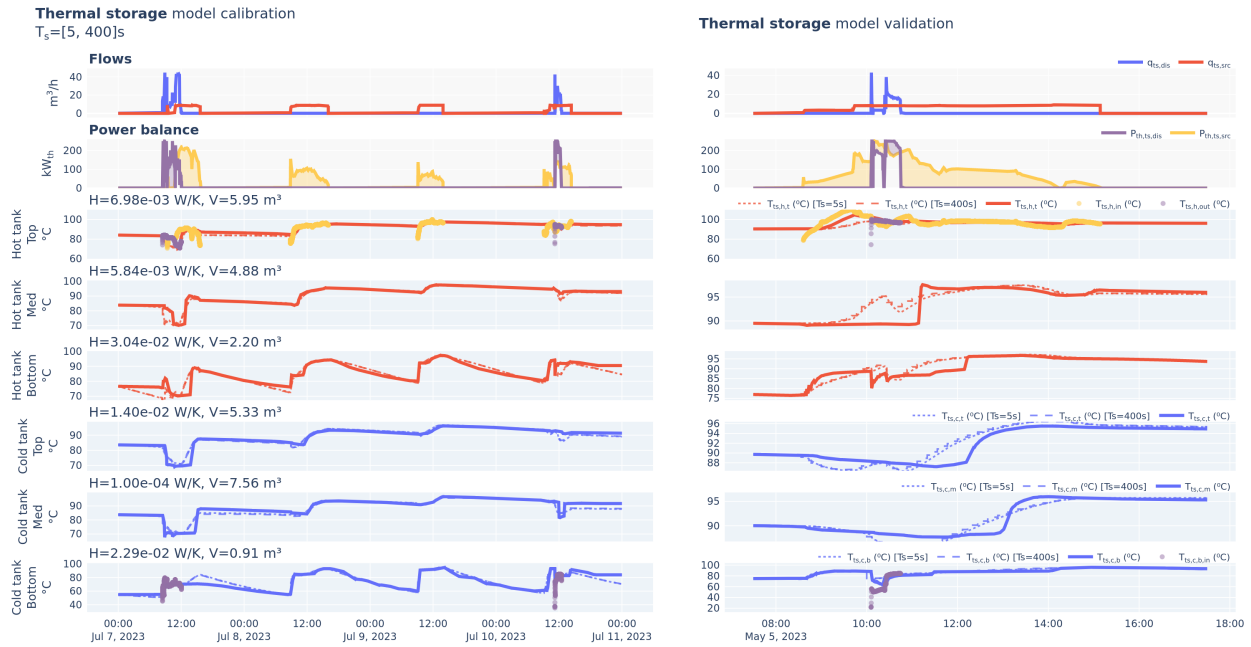


Figure 12.6: Thermal storage model calibration and validation tests.



In Figure 12.6 – right, the model is validated with a different test. It can be observed that the error between calibration and validation is similar, 1.11°C (MAE) compared to 1.14°C ¹³. The model seems to have a slower dynamic response to changes in the load-discharge balance than the actual system, which strangely stays impassive despite the changes in the load until some point where it reacts more aggressively. This could be explained by the interconnection between tanks. While the model assumes instantaneous and continuous flow recirculation between tanks, in reality it seems that the flow is discontinuous, only starting to flow when a certain pressure difference is reached. Nonetheless, both model and experimental data converge to similar values for all three measurements once the system stabilizes. Furthermore, the two most important measurements, the top of the hot tank and the bottom of the cold tank, which are the ones that interface with the rest of the system, have a very low error throughout the test.

Finally, several more tests (7) are evaluated, and the performance obtained is shown in Table 12.2. It should be noted that this model only receives feedback from the process initially, and then outputs are forecasted based on the inputs and the model own previously forecasted states. This means that any error in the prediction will be accumulated over time. This makes metrics like R^2 not representative of the model performance, as a small offset in the prediction will make R^2 drop significantly. For this reason, more emphasis is put on the MAE and MAPE metrics. In general, almost identical performance is obtained with the fast ($T_s = 5\text{s}$) and slow ($T_s = 400\text{s}$) sample rates, while the computational time is significantly reduced, from 5.45 s to 0.07 s, almost 80 times faster. This

13: See Table 12.2 – $T_{ts,h}$ – Sample time 5 seconds. Similar value for the 400 seconds sample time. Higher differences are observed for the cold tank, with even a better value obtained in validation compared to calibration (3.15 v.s. 1.78)

Table 12.2: Summary table of the prediction results obtained with the thermal storage model for different test days and sample times.

Predicted variable	Sample time (s)	Test date	Performance metric						Time (s)	
			R ² (-)		MAE (s.u.)		MAPE (%)			
			Test	Avg.	Test	Avg.	Test	Avg.	Test	Avg.
$T_{ts,h}$ (°C)	5	20230630	0.13		0.99		1.03		5.91	
		20230508	0.79		1.47		1.58		5.36	
		20230707	0.88		1.11		1.27		55.49	
		20230628	0.76	0.51	1.02	1.14	1.16	1.15	5.89	
		20230511	0.22		2.26		2.52		5.28	
		20230629	0.98		0.34		0.36		5.84	
		20230505	0.51		1.14		1.15		5.35	
		20230630	0.52		2.11		2.56		5.91	5.35
		20230508	0.83		1.05		1.37		5.36	
		20230707	0.87		3.15		4.35		55.49	
$T_{ts,c}$ (°C)	400	20230628	0.68	0.88	2.86	1.78	3.78	2.14	5.89	
		20230511	0.96		1.75		2.17		5.28	
		20230629	0.88		2.02		2.52		5.84	
		20230505	0.88		1.78		2.14		5.35	
		20230630	0.18		1.07		1.11		0.09	
		20230508	0.79		1.47		1.58		0.08	
		20230707	0.88		1.10		1.26		0.63	
		20230628	0.76	0.54	1.03	1.14	1.18	1.14	0.07	
		20230511	0.21		2.33		2.59		0.07	
		20230629	0.98		0.36		0.38		0.07	
$T_{ts,c}$ (°C)	400	20230505	0.54		1.14		1.14		0.07	0.07
		20230630	0.41		2.22		2.69		0.09	
		20230508	0.74		1.25		1.60		0.08	
		20230707	0.87		3.09		4.26		0.63	
		20230628	0.68	0.84	2.81	2.05	3.73	2.44	0.07	
		20230511	0.94		1.89		2.40		0.07	
		20230629	0.88		1.97		2.47		0.07	
		20230505	0.84		2.05		2.44		0.07	

s.u. stands for same units as the predicted variable. Alias: $T_{ts,h} == T_{ts,h,t}$ and $T_{ts,c} == T_{ts,c,b}$

is explained because the model on each iteration needs to solve a system of equations, so it has associated a higher time per iteration, making potential savings in the number of iterations more significant. On the other hand, less accuracy is lost when reducing the sample rate compared to the solar field since the dynamics of this system are naturally slower due to the high thermal inertia of the tanks, thus making it more insensitive to the sampling.

Analyzing the performance in terms of the point of measurement, the top of the hot tank has the lowest error, with a MAE of 1.14 °C, while the bottom of the cold tank has a slight higher error, with 1.78 °C. Overall good agreement between model and experimental data is observed with maximum errors below 3 % MAPE. This means than the state of the thermal storage can be predicted with a reasonable accuracy for hours ahead.

12.2.3 Heat exchanger

The solar field and thermal storage are interfaced by a Heat Exchanger (hex) or hx , particularly a water-to-water counter-flow heat exchanger. The component is modelled using a first-principles steady state model based on the effectiveness-NTU method [166, 167]. The following assumptions are considered [166]:

- ▶ It has been assumed that the rate of change for the temperature of both fluids is proportional to the temperature difference; this assumption is

[166]: Çengel et al. (2015), *Heat and Mass Transfer*

[167]: Kays et al. (1958), *Compact Heat Exchangers*

valid for fluids with a constant specific heat, which is a good description of fluids changing temperature over a relatively small range. However, if the specific heat changes, the Logarithmic Mean Temperature Difference (LMTD) approach will no longer be accurate.

- It has also been assumed that the heat transfer coefficient (U) is constant, and not a function of temperature.
- No phase change during heat transfer.
- Changes in kinetic energy and potential energy are neglected.

The model is described in Model 12.5. It returns the outlet temperatures from both primary circuit (solar field side), p , and secondary circuit s , the thermal storage side. As shown in Model 12.5, first the heat capacity C is determined in order to calculate the effectiveness (ϵ) of the heat exchanger. Finally, after determining the maximum heat transfer rate (\dot{Q}_{max}), the outlet temperatures can be obtained.

Validation

In order to calibrate the only parameter of this model (UA_{hx}), one representative experimental test is used where the parameters are fitted in order to obtain the *least-squares error* between the model and the experimental data. A heat transfer conductance value of 13 547 W/K is obtained. In Figure 12.8 the dynamic behavior of the model is validated with another test. It can be seen than the model performs fairly well even in transient conditions, with a MAE of $T_{hx,p,out} = 1.38^\circ\text{C}$, $T_{hx,s,out} = 1.39^\circ\text{C}$ and a coefficient of determination $R^2 = 99\%$ for both outputs¹⁴.

14: With fast sample rate –10 seconds

Model 12.5: Heat exchanger

$$\begin{aligned}
 T_{hx,p,out}, T_{hx,s,out} &= \text{hx model}(T_{hx,p,in}, T_{hx,s,in}, \dot{m}_p, \dot{m}_s, T_{amb}; (UA)_{hx}) \\
 C_{hx,p} &= \dot{m}_{hx,p} \cdot c_{p,Tp,in} && \text{Primary side heat cap. [J/Ks]} \\
 C_{hx,s} &= \dot{m}_{hx,s} \cdot c_{p,Ts,in} && \text{Secondary side heat cap. [J/Ks]} \\
 C_{min} &= \min(C_{hx,p}, C_{hx,s}) \\
 C_{max} &= \max(C_{hx,p}, C_{hx,s}) \\
 C &= \frac{C_{min}}{C_{max}} \\
 \dot{Q}_{max} &= C_{min} \cdot (T_{hx,p,in} - T_{hx,s,in}) \\
 NTU &= UA/C_{min} \\
 \epsilon &= \frac{1 - e^{(-NTU \cdot (1-C))}}{1 - C \cdot e^{-NTU \cdot (1-C)}} && \text{Effectiveness [-]} \\
 T_{hx,p,out} &= T_{hx,p,in} - (\dot{Q}_{max} \cdot \epsilon) / (C_{hx,p}) \\
 T_{hx,s,out} &= T_{hx,s,in} + (\dot{Q}_{max} \cdot \epsilon) / (C_{hx,s})
 \end{aligned}$$

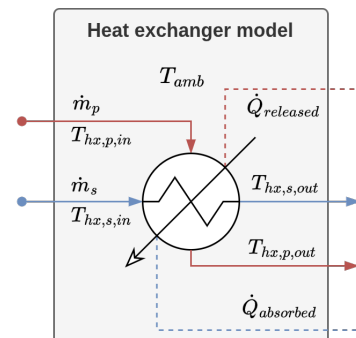


Figure 12.7: Heat exchanger process diagram.

Several more tests (11) are evaluated, and the performance obtained is shown in Table 12.3. In general, almost identical performance is obtained with the fast ($T_s = 5$ s) and slow ($T_s = 400$ s) sample rates, but as in the previous models, the computational time is significantly reduced, from 0.45 s to 0.01 s, an order of magnitude faster. In terms of accuracy, there seems to be a systematic higher error in the outlet of the secondary circuit with respect to the primary side, with

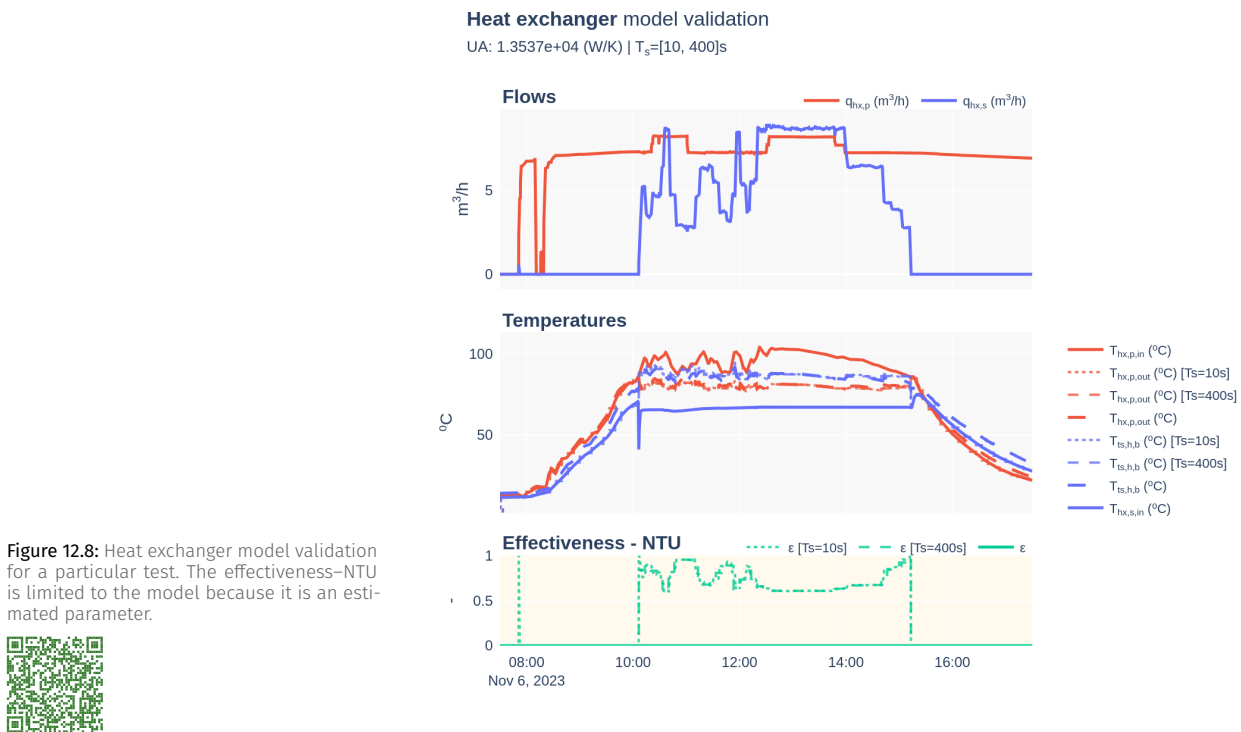


Figure 12.8: Heat exchanger model validation for a particular test. The effectiveness-NTU is limited to the model because it is an estimated parameter.



double the error (MAE: 1.08 compared to 2.16 °C). In general, good agreement between model and experimental data is observed with maximum errors below 8 % MAPE.

12.2.4 MED

The MED is modelled statically, considering changes in the system operating conditions happen at a slow enough rate that the dynamic behavior between stable states can be neglected, and thus, only those stable states are considered. Two models are developed for the MED: a data-driven model based on experimental data from the pilot plant, and a first-principles model based on thermodynamic equations. The data-driven model is the one integrated in the overall plant model used in optimization applications (See Chapter 14), while the first-principles model is used for comparison purposes and to gain insight into the operation of the MED (See Chapter 13).

Data-driven model

A Gaussian-Process Regression (GPR) model is calibrated using data from the two experimental campaigns described in Section 11.3.

Table 12.3: Summary table of the prediction results obtained with the heat exchanger model for different test days and sample times.

Predicted variable	Sample time (s)	Test date	Performance metric					
			R ² (-)		MAE (s.u.)		MAPE (%)	
			Test	Avg.	Test	Avg.	Test	Avg.
$T_{hx,p,out}$ (°C)	5	20231030	0.99	0.99	0.86	1.70	0.48	
		20231106	0.99		1.38	3.14		0.49
		20230630	0.99		0.68	1.11		0.56
		20230703	0.99		0.53	0.67		0.60
		20230508	0.99		1.24	1.76		0.58
		20230707	0.99	0.99	1.64	1.08	5.15	3.58
		20230628	0.99		0.73	0.93		0.58
		20230511	0.98		1.40	1.92		0.54
		20230629	0.99		0.58	0.80		0.59
		20230505	0.99		1.22	1.67		0.54
	400	20231031	0.99		1.08	3.58	0.45	0.45
		20231030	0.98		2.58	5.54	0.48	
		20231106	0.97		3.19	6.88	0.49	
		20230630	0.98		2.71	4.63	0.56	
		20230703	0.98		1.72	2.47	0.60	
$T_{hx,s,out}$ (°C)	5	20230508	0.96		2.57	3.70		0.58
		20230707	0.98	0.96	2.90	2.16	7.24	7.55
		20230628	0.95		2.78	3.96		0.58
		20230511	0.95		2.88	3.95		0.54
		20230629	0.98		2.46	4.05		0.59
		20230505	0.97		2.93	4.31		0.54
		20231031	0.96		2.16	7.55		0.45
		20231030	0.99		0.87	1.74		0.01
		20231106	0.99		1.39	3.17		0.01
		20230630	0.99		0.70	1.16		0.01
$T_{hx,p,out}$ (°C)	400	20230703	0.99		0.55	0.70		0.01
		20230508	0.99		1.26	1.82		0.01
		20230707	0.99	0.99	1.63	1.08	5.14	3.60
		20230628	0.99		0.71	0.93		0.01
		20230511	0.98		1.45	2.01		0.01
		20230629	0.99		0.58	0.81		0.01
		20230505	0.99		1.23	1.71		0.01
		20231031	0.99		1.08	3.60	0.01	0.01
		20231030	0.98		2.60	5.64	0.01	
		20231106	0.98		3.19	6.93	0.01	
$T_{hx,s,out}$ (°C)	5	20230630	0.98		2.69	4.65		
		20230703	0.98		1.77	2.60		
		20230508	0.96		2.61	3.79		
		20230707	0.98	0.96	2.92	2.13	7.26	7.46
		20230628	0.95		2.77	3.98		0.01
		20230511	0.95		2.84	3.90		0.01
		20230629	0.98		2.52	4.19		0.01
		20230505	0.97		2.92	4.34		0.01
		20231031	0.96		2.13	7.46		0.01

s.u. stands for same units as the predicted variable

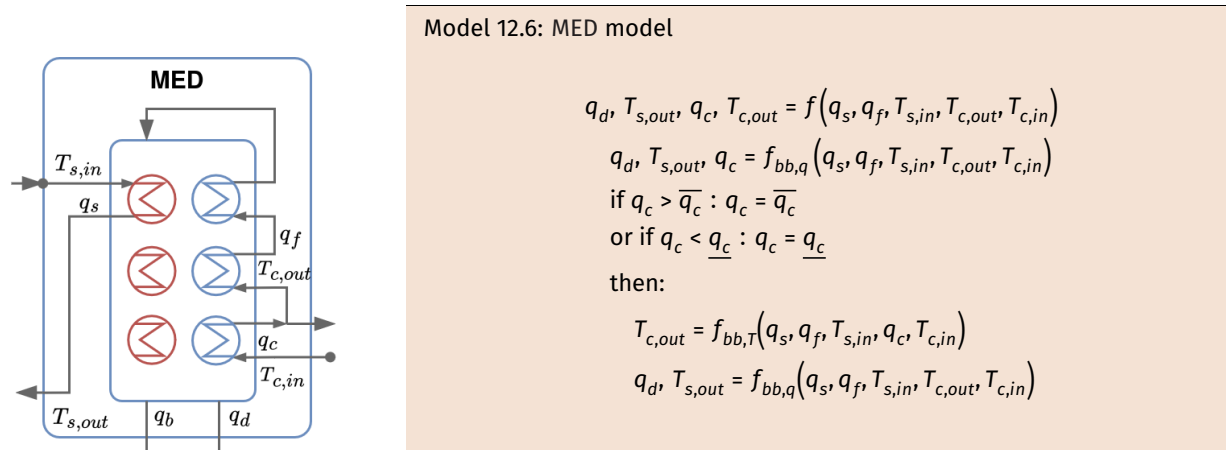


Figure 12.9: MED process diagram.

As observed in Model 12.6, the model has five inputs: the heat source flow rate (q_s), the feedwater flow rate (q_f), the inlet temperature of the heat source ($T_{s,in}$), the inlet temperature of the cooling water ($T_{c,in}$) and the outlet temperature of the cooling water ($T_{c,out}$). The model returns three main outputs: the distillate flow rate (q_d), the outlet temperature of the heat source ($T_{s,out}$) and the cooling water flow rate (q_c). An additional output is included with a validated value for the condenser outlet temperature ($T_{c,out}$), in cases where an unfeasible temperature is given as input. In Model 12.6, the functions $f_{bb,q}$ and $f_{bb,T}$ represent the black-box GPR models for the model with the main outputs and the auxiliary output, respectively.

First-principles model

The first-principles model is based on thermodynamic equations and mass and energy balances. A detailed description of the model can be found in the Appendix, Chapter B (MED First-Principles Model).

Electrical consumption

A similar procedure to the one for the solar field and thermal storage was followed, with some particular considerations:

The extraction pumps need to be evaluated under vacuum conditions, since this is how the system operates under normal conditions. This has a direct influence on the intake conditions (lower head pressure). The brine pump is evaluated with a step train test while the plant is inactive (no thermal input), in vacuum conditions and with feedwater being pumped. The water will naturally fall by gravity to the final effect¹⁵. The power consumption is measured using the VFD integrated power meter. For the distillate pump, water does not reach the final condenser unless vapor is generated, so the pump is evaluated with the plant active in operating conditions that produce distillate at the midrange working conditions of the VFD, around 35 Hz. The step train is then performed by alternating high and low values¹⁶ and making sure the level stays within the operating range.

For the rest of the system pumps: heat source, feedwater and cooling water, a simple step train test is performed. The vacuum system has three levels: high when generating vacuum, low when maintaining vacuum, and inactive. Each with an associated constant consumption. Finally, the obtained electrical model is shown in Model 12.7.

15: Given the plant vertically-stacked configuration

16: For example, 35 → 40 → 30 → 45 → 25 → 50 → 20 Hz

Validation

As explained, two GPR models are used, so two models need to be calibrated, one for the aforementioned desired system outputs (q_d , $T_{s,out}$ and q_c) and an additional one for the condenser outlet temperature. An 80/20 training/validation split is used. The training is performed using an Radial Basis Function (RBF) kernel. The regression model is defined with the GPy library, which includes a Gaussian likelihood with a noise term by default. The kernel hyperparameters (variance, lengthscale, and noise variance) are optimized by maximizing the log-marginal likelihood using GPy's [168] built-in L-BFGS local optimizer. The regression results for the main outputs are shown in Figure 12.10. As can be seen, the model performs very well for all outputs, with R^2 values above 0.90 in all cases.

[168]: GPy (), GPy: A Gaussian Process Framework in Python

Model 12.7: MED electrical consumption

$$\begin{aligned} C_{e,med} &= \text{med electrical consumption}(q_{med,s}, q_{med,f}, q_{med,c}, q_{med,d}, q_{med,b}) \\ C_{e,med,s} &= 0.0104 - 0.025 q_{med,s} + 0.0339 q_{med,s}^2 \quad \text{m}^3/\text{h} \rightarrow \text{kW}_e \\ C_{e,med,f} &= 0.704 - 0.0947 q_{med,f} + 0.0191 q_{med,f}^2 \quad \text{m}^3/\text{h} \rightarrow \text{kW}_e \\ C_{e,med,c} &= 5.218 - 0.924 q_{med,c} + 0.0567 q_{med,c}^2 \quad \text{m}^3/\text{h} \rightarrow \text{kW}_e \\ C_{e,med,d} &= 4.150 - 3.657 q_{med,d} + 0.948 q_{med,d}^2 \quad \text{m}^3/\text{h} \rightarrow \text{kW}_e \\ C_{e,med,b} &= 0.031 - 0.019 q_{med,b} + 1.33 \times 10^{-3} q_{med,b}^2 \quad \text{m}^3/\text{h} \rightarrow \text{kW}_e \\ C_{e,med,vac} &= \begin{cases} 5, & \text{if } \text{med}_{vac} = 2 \\ 1, & \text{if } \text{med}_{vac} = 1 \\ 0, & \text{if } \text{med}_{vac} = 0 \end{cases} \\ C_{e,med} &= C_{e,med,s} + C_{e,med,f} + C_{e,med,c} + C_{e,med,d} + C_{e,med,b} + C_{e,med,vac} \end{aligned}$$

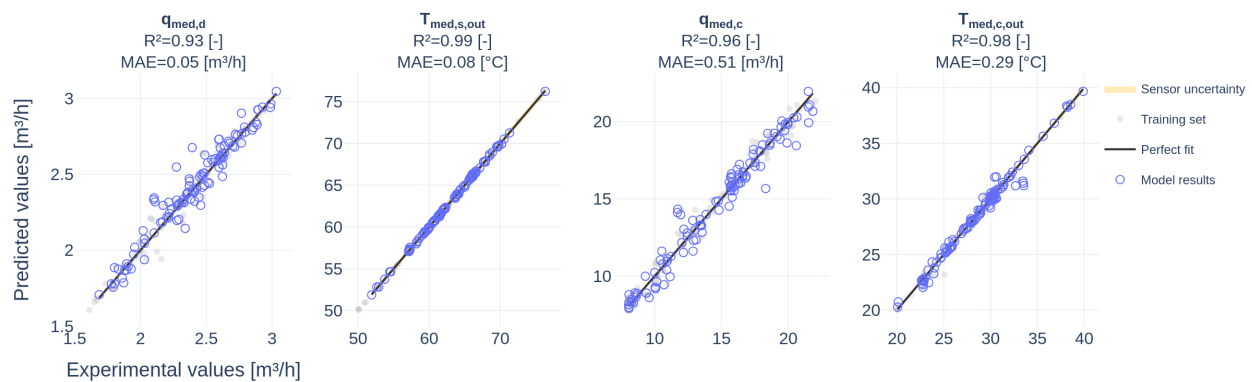


Figure 12.10: MED GPR model regression for different outputs. Dataset includes data spanning 6 years of operation.



Figure 12.11 shows the model validation for two particular tests. Several observations can be drawn. First, the model shows high accuracy in predicting both distillate production and the heat source outlet temperature, even during

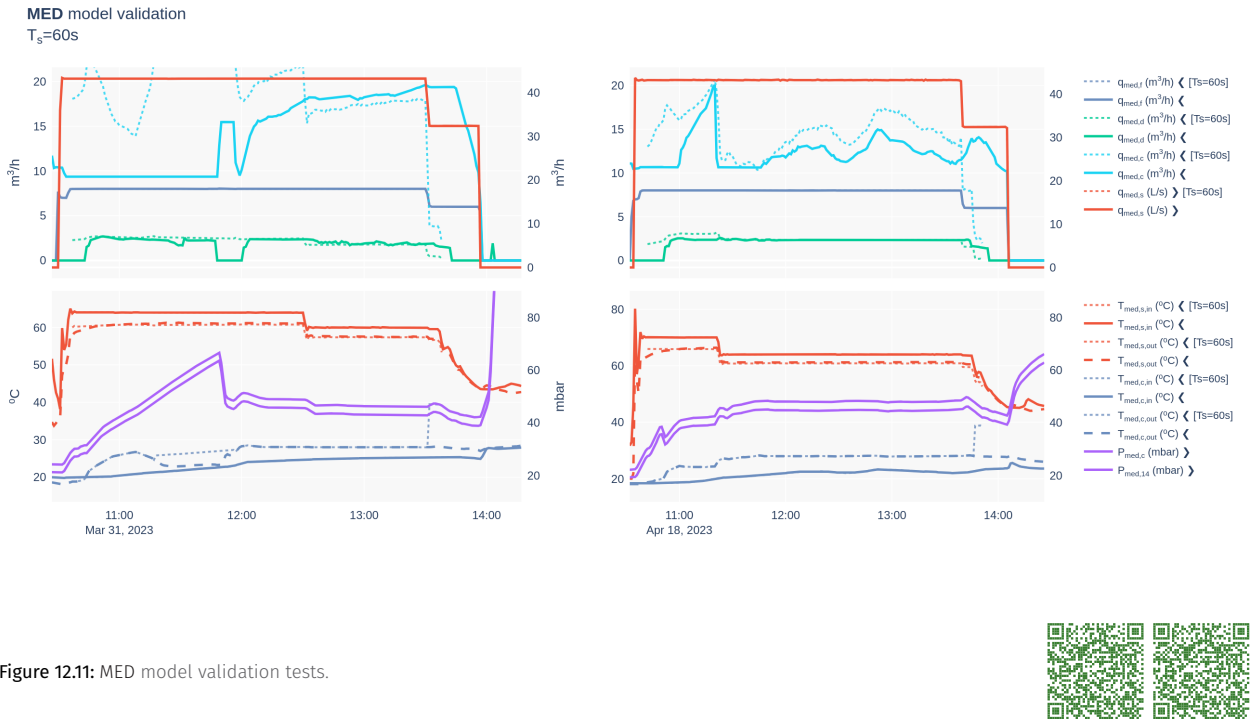


Figure 12.11: MED model validation tests.



transient phases such as those observed in the early part of the 31032023 test (Figure 12.11, left).

In contrast, the cooling water predictions are less reliable during these transitions. As vapor gradually accumulates—visible as a pressure ramp in the condenser between 10:30 and 12:30 in the 202303031 test—it becomes difficult to predict how much vapor ultimately reaches the final condenser. Once stable conditions are established, however, the model can accurately estimate the cooling water demand required to maintain equilibrium at a given operating point, even under varying inlet water temperatures ($T_{c,in}$). This is evident in the later phase of the 202303031 test and throughout most of the 20230418 test.

A further observation is the system's strong sensitivity to the cooling water inlet temperature. In the pilot plant, which operates in a closed loop, these inlet conditions are constantly shifting. Despite this, the static model is able to capture the condenser's overall behavior once the system stabilizes and the inlet temperature becomes the primary changing variable.

Subsystem	Parameter	Description	Value	Units
Model parameters				
Solar field	β	Gain coefficient	4.36×10^{-2}	m
	H	Heat loss coefficient	13.67	W/m ²
	V_p	Volume of control volume	[5.94, 4.87, 2.19]	m ³
Thermal storage	H_n	Heat loss coefficient	$[6.98, 5.84, 30.41] \times 10^{-3}$	W/K
	V_c	Volume of control volume	[5.33, 7.56, 0.9]	m ³
Heat exchanger	H_c	Heat loss coefficient	$[0.013.96, 0.1, 0.022] \times 10^{-3}$	W/K
	UA	Heat transfer conductance	1.35×10^4	W/K
Fixed model parameters				
Solar field	A_{cs}	Collector tube cross-section area	7.85×10^{-5}	m ²
	n_{tb-c}	Number of parallel tubes per collector	1	-
	n_{c-loop}	Number of parallel collectors per loop	7×5	-
	L_{tb}	Individual collector tube length	23	m
	n_{c-s}	Number of collector row's in series	2	-
	T_{max}	Maximum working temperature	120	°C

Table 12.4: Models parameters

12.3 Discrete modelling. Operation state

In the previous section, the dynamic and static models of each component were explained. This section focuses on the discrete behavior, its *operation state*. This component is modelled by means of FSMS. In order to determine its state, the Finite-State Machine (FSM) uses information from its inputs, internal state and the configured parameters.

The complete system is divided into two subsystems: the heat generation and storage subsystem (**sfts**) and the separation subsystem (**med**).

12.3.1 Heat generation and storage subsystem (**sfts**)

This subsystem encompasses the Solar Field (**sf**) and the Thermal Storage (**ts**). The subsystem can be modelled with a simple FSM. The FSM has two inputs, the recirculation flow rate on each circuit (q_{sf} and $q_{ts,src}$), and the FSM states are computed based on whether water is being recirculated on each. Four states are defined as shown in Table 12.5 and the possible transitions are visualized in Figure 12.12 (a). The states involve:

- ▶ **Off** (0). The system is off, no water is being recirculated in either circuit.
- ▶ **Warming up solar field** (1). Water is being recirculated in the solar field circuit but not in the thermal storage circuit. The solar field is being heated up.
- ▶ **Recirculating thermal storage** (2). Water is being recirculated in the thermal storage circuit but not in the solar field circuit. The thermal storage is being mixed.
- ▶ **Solar field heating up thermal storage** (3). Water is being recirculated in both circuits. The solar field is heating up the thermal storage.

Additionally, some conditions are configured with the following parameters¹⁷:

- ▶ **Enable recirculating thermal storage** (false). Allow to recirculate water in the thermal storage circuit while no water is being heated in the solar field. This would be used to mix the hot and cold tanks.
- ▶ **Active cooldown time** (10 minutes). Time to wait before activating the system again after stopping it.

12.3.2 Separation subsystem (**med**)

Two inputs are used in this machine, one logical which indicates the active state the system when all of the required pumps for operation are enabled. The other is an integer variable that regulates the vacuum state (med_{vac}). This latter variable has three possible values: 0 when the vacuum pump is off, 1

Reminder: FSMS

A finite state machine is a model of behavior composed of a finite number of *states* and *transitions* between those states. Within each state and transition some *action* can be performed^a.

^a See Section 3.1.3 (Discrete modelling by means of FSMS) for a more detailed description.

Table 12.5: **sfts** FSM states definitions. \wedge represents the logical AND operator.

State	Name	Condition
0 (00)	Off	$q_{sf} \wedge q_{ts,src} == 0$
1 (01)	Warming up Solar Field (sf)	$q_{sf} > 0 \wedge q_{ts,src} == 0$
2 (10)	Recirculating Thermal Storage (ts)	$q_{sf} == 0 \wedge q_{ts,src} > 0$
3 (11)	sf heating up ts	$q_{sf} \wedge q_{ts,src} > 0$

17: In parentheses the value used

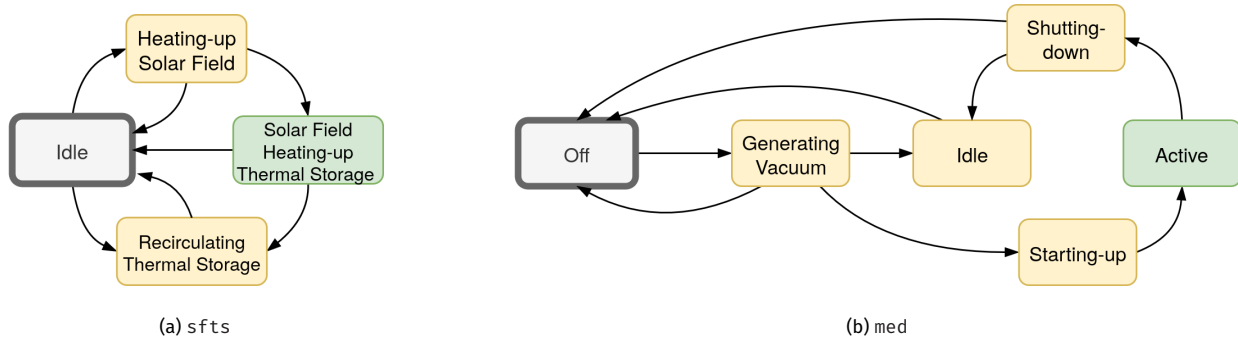


Figure 12.12: Finite-state machines for the different subsystems

when the vacuum pump operates at low speed (maintaining vacuum) and 2 when the vacuum pump operates at high speed (generating vacuum). The FSM states are computed based on these two inputs and the conditions shown in Table 12.6. The possible transitions are visualized in Figure 12.12 (b). The states are described in the following:

- ▶ **Off** (0). The system is off, no pumps are operating and no vacuum is being generated.
- ▶ **Generating vacuum** (1). The system is off, no pumps are operating but vacuum is being generated.
- ▶ **Idle** (2). The system is off, no pumps are operating but vacuum is maintained.
- ▶ **Starting-up** (3). The system is starting up, all pumps start operation following the procedure outlined in Section 13.5. No distillate is produced at this stage and the temperatures and pressures progressively ramp up until reaching equilibrium for the given inputs.
- ▶ **Shutting down** (4). The system is being shut down, distillate production has stopped and the system is cooled-down progressively. Extraction pumps start cycles of operation to empty the system. Vacuum may be maintained at this stage.
- ▶ **Active** (5). The system is active, all pumps are operating and distillate is being produced. Vacuum is maintained.

As in the previous machine, the machine has additional FSM parameters that regulate its behavior, specifically:

- ▶ **Vacuum duration time** (30 minutes). Time to generate vacuum in the MED system.
- ▶ **Brine emptying time** (60 minutes). Time to extract brine from MED plant.
- ▶ **Startup duration time** (20 minutes). Time to start up the MED plant, once vacuum is generated.
- ▶ **Off cooldown time** (12 hours). Time to wait before activating the MED plant again after shutting it off.
- ▶ **Active cooldown time** (2 hours). Time to wait before activating the MED plant again after shutting it off or suspending it.

Finally, the machine has internal states that are updated during the machine evaluation in order to keep track of the progress of the different timed actions and whether they have been completed or not. These are for example the vacuum elapsed samples, the startup elapsed samples or the brine emptying elapsed samples. The associated logical states would be whether vacuum has been generated, whether the startup procedure has been completed or whether the brine emptying has been completed.

State	Name	Condition
0	Off	$\forall q == 0$
1	Generating vacuum	$med_{vac} == 2$
2	Idle	$\forall q == 0 \wedge med_{vac} == 1$
3	Starting-up	$\forall q > \underline{q} \wedge med_{vac} \geq 1$
4	Shutting down	$\exists q < \underline{q}$
5	Active	$\forall q > \underline{q} \wedge med_{vac} \geq 1$

Table 12.6: med FSM states definitions. \wedge represents the logical AND operator, \exists represents that at least one meets the condition, and \forall represents that all meet the condition.

12.3.3 Validation

Figure 12.13 shows the evolution of the states of both FSMs during a test. It can be seen how both machines evolve in parallel in the bottom plot, while the upper one shows the cumulative input values¹⁸. The sfts first starts with the heating up of the solar field state triggered by the activation of the solar field pump (**sf_active**), and once the temperature is high enough after few samples the thermal storage starts recirculating (**ts_active**). This continues until the end of the tests when the temperature decreases so it gets deactivated (at sample 80 in Figure 12.13).

For the med, there is no measurement for the vacuum state of the system so it is assumed that it is set at a high-level from the beginning and kept until the end of the test. The system starts in the off state, and once vacuum is generated the start-up procedure gets triggered at sample 12-13. The system then stays active producing separation until it is shut-off at sample 56 for two samples, equivalent to over 10 minutes.

18: All variables are shown as integers and aliases are created to group the logical active conditions e.g. $med_active = \forall q > \underline{q}$

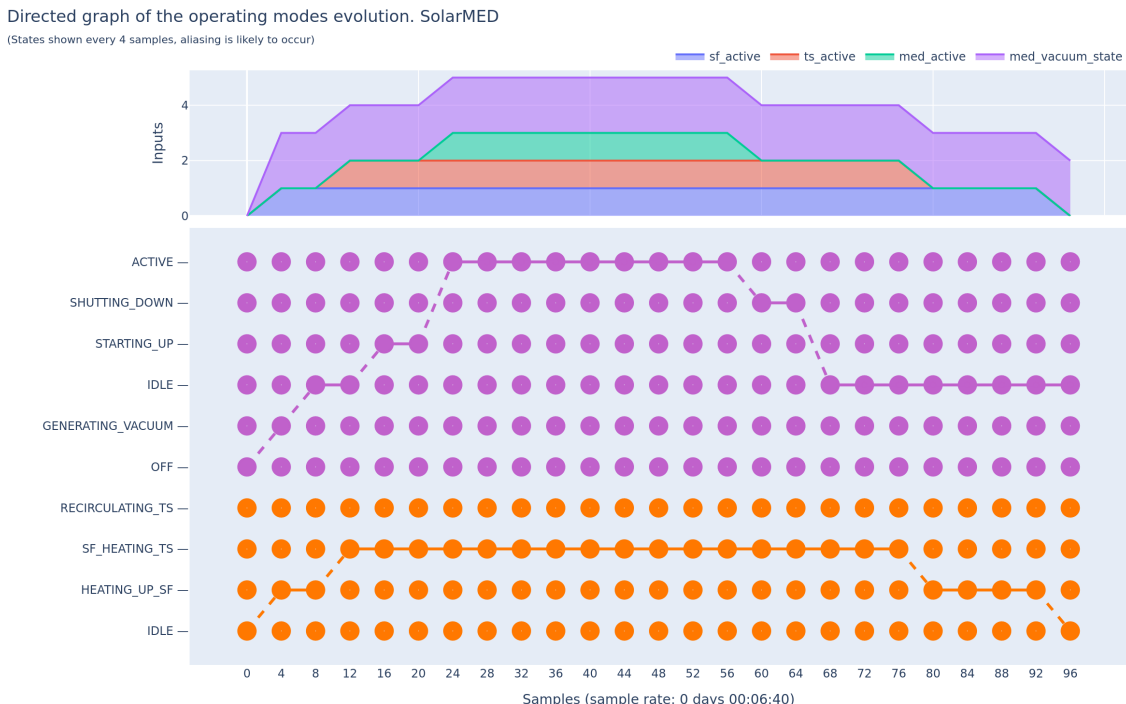


Figure 12.13: SolarMED FSM states evolution during a test on 20230703. Purple represents the med state and orange the sfts.
NOTE: $med\ active$ is equivalent to the condition $\forall q_{med,i} > \underline{q}_{med,i}$

12.4 Complete system model

19: To clearly distinguish that a variable belongs to a subsystem, the subsystem acronym is added as a subscript e.g. $q_s \rightarrow q_{med,s}$

20: Specifically as a Python class

21: For example, if the MED subsystem is in the shutting down process, no thermal load is extracted from the thermal storage, and only the electrical consumption of the extraction pumps is considered (and of the vacuum if kept active)

Finally, all the individual components described above (continuous and discrete) are combined to form the complete system model¹⁹. The complete model is a hybrid model that orchestrates physics models for the solar field, heat exchanger, thermal storage, three-way valve and data-driven for the MED, plus two supervisory finite state machines. The continuous states are the outputs of the different subsystems, while the discrete states are the states of the two FSMs.

The model –defined in Model 12.8– is implemented following an object-oriented approach²⁰. Once it is initialized by being provided with the initial discrete states (e.g. vacuum generated, brine emptied from final effect, etc) and system parameters (e.g. thermal storage volumes, heat exchanger transfer conductance, med timings, etc). It also needs to be initialized with the initial solar field and thermal storage temperatures.

Each step takes environment inputs (irradiance I , ambient temperature T_{amb} , seawater temperature $T_{med,c,in}$) and operation decisions (e.g., q_{sf}^* , $q_{ts,src}^*$, $q_{med,s}^*$, $q_{med,f}^*$, $T_{med,s,in}^*$, $T_{med,c,out}^*$). Setpoints reflect operator/optimizer intent, the model then validates and turns them into realized outputs. Each step advances the plant one sampling interval. Physically, the model treats the installation as three hydraulic/thermal loops that exchange energy, all embedded in ambient conditions and subject to equipment limits.

The supervisory logic (*i.e.*, FSMs) first decides which subsystems are allowed to act (solar field circulating, storage charging/discharging, MED producing). That logic turns setpoints into admissible operating points: a requested flow or temperature may be permitted as is, clipped to a limit, or forced to zero if a component is inactive, or set to a predefined value²¹. Once the discrete state of the system is fixed for the current step, the physics is evaluated in a sequence that mirrors causality and heat flow. This set of dependencies between the different subsystems is visualized in Figure 12.14.

The MED is solved first because it defines the thermal demand that the rest of the system must support. With the MED demand known, the three-way valve determines how much hot water must be extracted from storage and how to mix it to meet the MED hot-side inlet target. Physically, it blends water drawn from the top of the hot tank with the MED return, choosing a mix ratio and discharge flow that close the MED's energy balance. That fixes the storage discharge flow and the thermal duty the storage must deliver in this step.

Next, the heat supply side is computed. When the solar field is circulating and storage is being recharged, the solar field, heat exchanger, and tanks are thermally coupled: the solar outlet temperature, the heat exchanger primary/secondary outlet temperatures, and the evolving tank stratification all depend on each other. In that coupled case, a small nonlinear subproblem is solved so that energy balances are simultaneously satisfied across generation, transfer, and load (storage), considering the previous tank states. When the solar field and storage are not simultaneously active (for example, idle storage or solar field, or storage discharging), the supply side decouples: the solar field is first evaluated alone, producing a primary-side outlet temperature ; then the tanks update their stratified temperatures by applying the computed inlet/outlet temperatures and the discharge flows.

Once temperatures and flows are settled, the model computes electrical powers using the actuators fitted curves. Finally, time-dependent states are rolled forward: solar loop histories are shifted to carry the new inlet/outlet values into the next step, and the tank stratification produced this step becomes the initial condition for the next.

Model 12.8: SolarMED model

$$q_{med,d}, C_e = f(q_{med,s}, q_{med,f}, T_{med,s,in}, T_{med,c,out}, q_{ts,src}, q_{sf}, med_{vac,st}, T_{med,c,in}, T_{amb}, I; \theta_{sf}, \theta_{hx}, \theta_{med}, \theta_{sfts}^{fsm}, \theta_{med}^{fsm}, \theta_{\infty})$$

$$st_{sfts} = sfts \text{ fsm model}(q_{sf}, q_{ts,src}; \theta_{sfts}^{fsm})$$

$$st_{med} = med \text{ fsm model}(q_{med,s}, q_{med,f}, T_{med,c}; \theta_{med}^{fsm})$$

$$T_{sf,out} = sf \text{ model}(T_{sf,out,k-1}, T_{sf,in,k-n:k}, q_{sf,k-n:k}, I, T_{amb}; \theta_{sf})$$

$$T_{ts,h}, T_{ts,c} = ts \text{ model}($$

$$T_{ts,h}(k-1), T_{ts,c}(k-1), T_{hx,s,out},$$

$$T_{med,s,out}, q_{ts,src}, q_{ts,dis}, T_{amb}; \theta_{ts}$$

)

$$T_{sf,in}, T_{hx,s,out} = hx \text{ model}(T_{sf,out}, T_{ts,c,b}, q_{sf}, q_{ts,src}, T_{amb}; \theta_{hx})$$

$$q_{ts,dis} = 3wv \text{ model}(q_{med,s}, T_{med,s,in}, T_{med,s,out})$$

$$q_{med,d}, T_{med,s,out}, q_{med,c}, T_{med,c,out} = med \text{ model}($$

$$q_{med,s}, q_{med,f}, T_{med,s,in}, T_{med,c,out}, T_{med,c,in}$$

)

$$C_{e,sf} = sf \text{ electrical consumption}(q_{sf})$$

$$C_{e,ts} = ts \text{ electrical consumption}(q_{ts,src})$$

$$C_{e,med} = med \text{ electrical cons.}(q_{med,s}, q_{med,f}, q_{med,c}, q_{med,d}, q_{med,b})$$

$$C_e = C_{e,sf} + C_{e,ts} + C_{e,med}$$

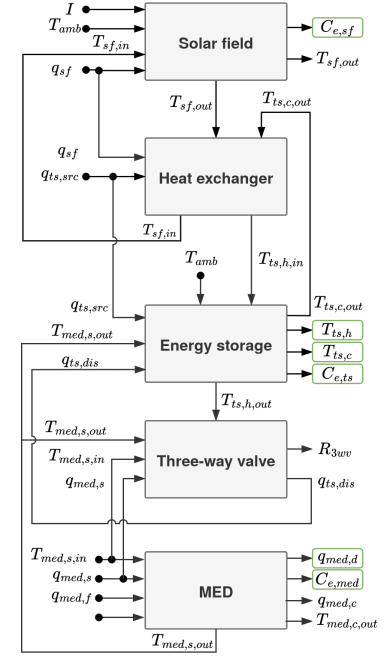


Figure 12.14: Complete SolarMED model architecture.

12.4.1 Validation

Figure 12.15 and Table 12.7 show the results obtained for some days when evaluating the complete model. The model is evaluated with a sample time of 400 s but four different prediction horizons. In Figure 12.15 two of them are shown, 1 hour and 8 hours. This means, e.g., that for a horizon of 1 hour, the model is evaluated for 1 hour with no feedback from measured data. Then the model is updated with the actual measured state at that time and the process is repeated for the rest of the test. Finally, the error is computed between the model output and the actual measurement.

In Figure 12.15, while all subsystems are active, it can be seen a good agreement between the model prediction and the actual measurements for both horizons. A higher error is observed during startup and shutdown for the solar field²² (which propagates to the heat exchanger).

The MED, since it is a static model, is not affected by the horizon time (as long as the hot tank top temperature is above the operating temperature), while the solar field, and specially the thermal storage, show a higher error that accumulates

22: Figure 12.15 – Solar field from 06:00 to 10:00 and from 15:00 to 17:45

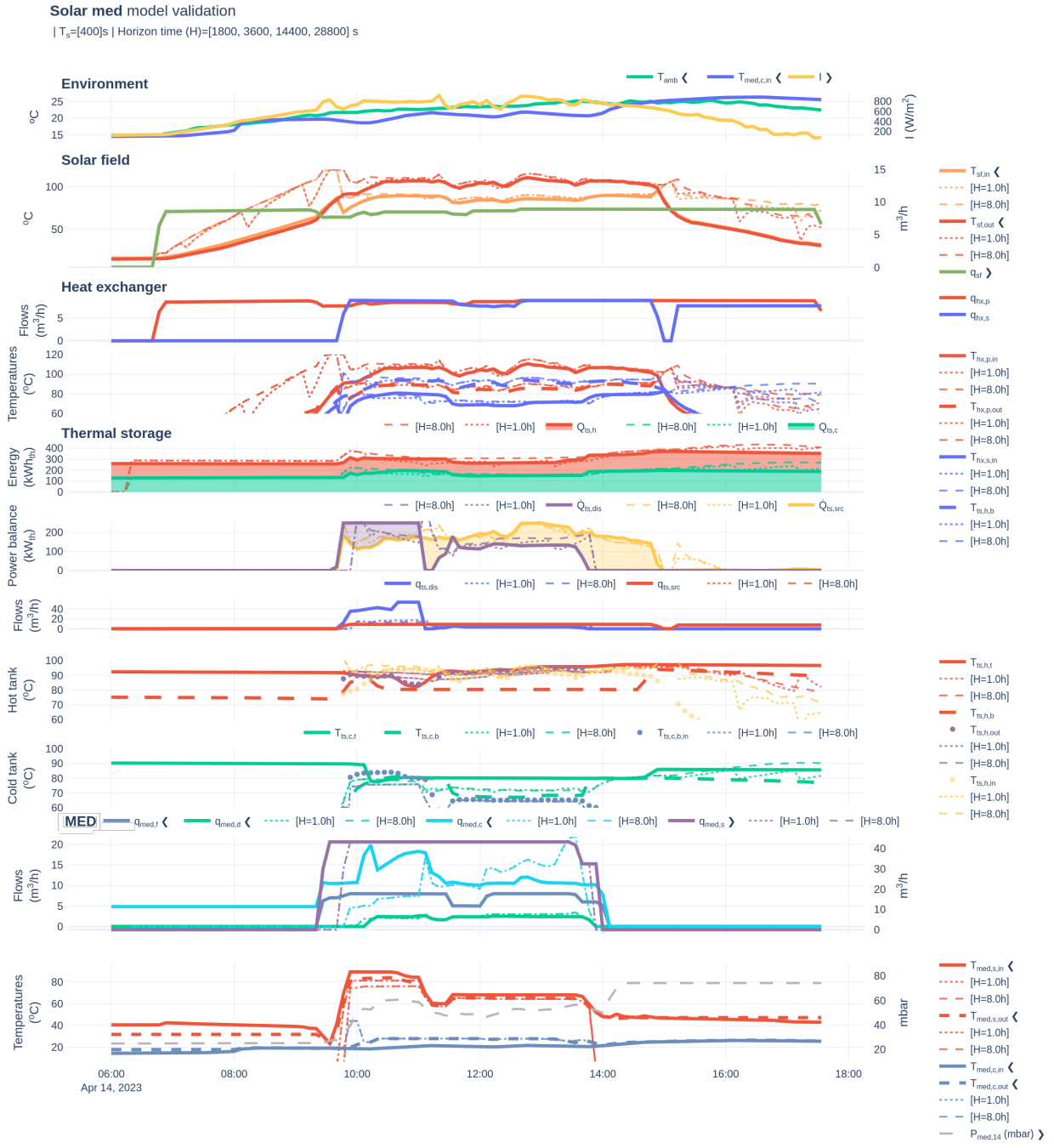


Figure 12.15: SolarMED model validation



23: At the end of operation (15:00), for the 8-hour horizon: $T_{ts,h,t} = 96.98^\circ\text{C}$ vs 95.69 and $T_{ts,c,b} = 80.2^\circ\text{C}$ vs 81.7 . In terms of energy stored: $Q_{ts,c} = 194.45 \text{ kWh}_{th}$ vs 211.36 and $Q_{ts,c} = 170.24 \text{ kWh}_{th}$ vs 173.52

over time. As expected, the 8-hour horizon shows a higher error than the 1-hour horizon, since the model is not updated with actual measurements for the whole duration of the test. Nonetheless, the final state of the thermal storage temperature profiles is not too far from the actual measurements²³, showing that the model is able to capture the overall behavior of the system. This is

confirmed by the good agreement observed in the energy stored throughout the test²⁴.

For the MED, as commented in the component section, the output with the highest error is the cooling water flow rate, showing higher errors at the beginning where there is a heat source temperature mismatch (the actual temperature is higher than the upper limit of the data-driven model so it is clipped). In the second part of the test, the inlet cooling water temperature increases significantly, and since the flow was kept constant in the test, the condenser is not stable anymore²⁵.

Table 12.7 shows the results obtained for different metrics (MAE, MAPE) for two different test days. This time two additional horizons are included, 30 minutes and 4 hours. The table also shows the computation time required to evaluate the model for each prediction horizon.

As mentioned, static variables such as the distillate production show no variation with the prediction horizon (e.g. MAE: $q_{med,d} = 0.15 \text{ m}^3/\text{h}$ for all horizon times in test 20230414), while dynamic variables such as the thermal storage hot tank top temperature show a clear increase in error with longer horizons (e.g. MAE $T_{ts,h} = 2.36^\circ\text{C}$ for a 30-minute horizon and $T_{ts,h} = 3.59^\circ\text{C}$ for a 4-hour horizon in test 20230414).

When judging the performance metrics, it is important to keep in mind that for the complete model, feedback from the real system is only available at the beginning of the day. From that point on, most subsystem inputs depend on states from other subsystems. For example, the solar field inlet temperature depends on the heat exchanger output, which in turn depends on the thermal storage state, which itself depends on the MED plant operation and, ultimately, on the solar field. Consequently, errors can propagate and accumulate over time.

Therefore, achieving consistent accuracy for multi-hour horizons in a fully coupled system is challenging. For standalone component models, MAPE values above 5–10 % would typically be considered poor; however, for the complete integrated system, maintaining MAPE values below roughly 15 % across several hours is a commendable result. This is particularly the case for thermal state variables such as $T_{ts,h}$ and $T_{ts,c}$, where the model captures the general dynamic behavior well even at long horizons. The computation times shown in the last column remain reasonable, with the 8-hours horizon evaluation taking around 5 s.

24: Figure 12.15 – Thermal storage – Energy

25: Observe the trend in Figure 12.15 – MED – Temperatures (right) – $P_{v,14}$

Extended validation results

A visualization of all evaluated tests for every model validation are available in the thesis repository as a compressed folder



Table 12.7: Summary table of the prediction results obtained with the SolarMED model for different test days, sample time set to 400s and different prediction horizons.

Predicted variable	Test date	Horizon time (s)	Performance metric		
			MAE (s.u.)	MAPE (%)	Time (s)
$q_{med,d}$ (m^3/h)	20230414	1800	0.15	16.80	13.42
		3600	0.15	16.80	22.13
		14400	0.15	16.80	8.15
		28800	0.15	16.80	5.86
	20230418	1800	0.07	9.99	7.83
		3600	0.07	9.99	4.52
		14400	0.07	9.99	2.64
		28800	0.07	9.99	2.52
$T_{ts,h}$ ($^\circ C$)	20230414	1800	2.36	2.50	13.42
		3600	3.15	3.32	22.13
		14400	3.59	3.78	8.15
		28800	3.18	3.37	5.86
	20230418	1800	0.48	0.52	7.83
		3600	1.09	1.18	4.52
		14400	3.95	4.29	2.64
		28800	5.87	6.38	2.52
$T_{ts,c}$ ($^\circ C$)	20230414	1800	2.66	3.76	13.42
		3600	3.03	4.27	22.13
		14400	4.20	5.93	8.15
		28800	4.31	6.20	5.86
	20230418	1800	2.76	3.94	7.83
		3600	3.19	4.52	4.52
		14400	5.37	7.59	2.64
		28800	6.85	9.74	2.52
$\dot{Q}_{ts,src}$ (kW_{th})	20230414	1800	14.12	16.85	13.42
		3600	13.37	16.18	22.13
		14400	13.71	15.79	8.15
		28800	13.80	15.92	5.86
	20230418	1800	15.93	43.31	7.83
		3600	18.35	47.19	4.52
		14400	13.04	33.59	2.64
		28800	12.85	30.99	2.52
$\dot{Q}_{ts,dis}$ (kW_{th})	20230414	1800	25.02	30.60	13.42
		3600	23.59	30.07	22.13
		14400	26.78	37.01	8.15
		28800	25.81	36.43	5.86
	20230418	1800	13.02	45.83	7.83
		3600	12.69	44.46	4.52
		14400	19.82	78.38	2.64
		28800	26.58	97.08	2.52
$Q_{ts,h}$ (kWh_{th})	20230414	1800	20.57	15.29	13.42
		3600	17.02	12.65	22.13
		14400	14.90	11.34	8.15
		28800	19.23	15.01	5.86
	20230418	1800	8.73	6.23	7.83
		3600	8.71	6.23	4.52
		14400	16.92	11.64	2.64
		28800	21.01	14.35	2.52
$Q_{ts,c}$ (kWh_{th})	20230414	1800	11.82	6.87	13.42
		3600	14.58	8.17	22.13
		14400	26.15	14.61	8.15
		28800	22.15	12.37	5.86
	20230418	1800	9.30	4.64	7.83
		3600	10.37	5.12	4.52
		14400	21.75	10.76	2.64
		28800	30.39	15.11	2.52

s.u. stands for same units as the predicted variable

Performance evaluation in MED processes: standard methodology proposal and high TBT experimental campaign

13

TL;DR

This chapter presents a standardized method for evaluating the performance of Multi-Effect Distillation (MED) processes, which can also be extended to other thermal separation technologies. The method addresses key aspects such as instrumentation requirements, process control, and the suitability of performance metrics, including the uncertainties associated with their determination. Additionally, an algorithm has been developed for the automatic detection of steady-state operation, enhancing the reliability and robustness of evaluations under variable conditions. Experimental results confirm that the proposed method is both robust and reliable, enabling fair comparisons of MED processes across different operating scenarios.

The experimentation includes the evaluation of the process at high Top Brine Temperatures (TBTs). The results are analyzed using different performance metrics and the scale formation risk is estimated by the Ryznar Stability Index (RSI). The results show that the MED process can be operated at high TBTs without significant scale formation and achieve higher concentrations, but without significant improvements in thermal performance and limited concentration capacity if no changes to its design are made.

Introduction

The future of MED in desalination and brine concentration applications depends on the technical development of the process and its integration with other technologies [25, 26]. The performance of this technology and how it is evaluated plays an important role in this development.

Although efforts have been made to propose performance metrics to evaluate the multi-effect evaporation process, there is neither consensus in which metrics are the most suitable [27] nor standards on how to evaluate the experimental process. The only standard existing in MED is not related to performance evaluation, but to cost structures and determinants [28].

For the performance evaluation of MED processes, originally, the index Gain Output Ratio (GOR) was used for plants operating with steam as external energy source. In order not to be limited to steam-driven systems and to take into account sensible heat sources, a new performance index was defined: the Performance Ratio (PR) [144, 169], which is currently the most widely adopted for MED performance evaluation although it is constrained by using a reference enthalpy of 2326 kJ equivalent to 1000 BTU. In [170], a variation of this metric called the Waste Heat Performance Ratio (PR_{WH}) was suggested to account for the potential of low-grade waste heat sources. Another widespread thermal performance metric that has been used in MED is the Specific Thermal Energy Consumption (STEC) and its electrical equivalent, the Specific Electrical Energy Consumption (SEEC). However, there are certain limitations in the aforementioned metrics that challenge making a fair comparison between desalination systems that use different energy sources *i.e.* electrical and thermal¹. Furthermore, the ability of thermal energy to perform work changes with its temperature, so it is essential to consider the quality of the thermal energy used in desalination processes. This limitation of traditional energetic metrics was showcased in Bouma *et al.* [148] where they compared four different configurations of MED plants: a

13.1	Process analysis	140
13.2	Performance metrics	141
13.2.1	Separation metrics	141
13.2.2	Energetic metrics	142
13.2.3	Exergetic metrics	144
13.3	Instrumentation	145
13.3.1	Key Process Variables (KPVs)	145
13.3.2	Instrumentation requirements	146
13.3.3	Uncertainty determination .	148
13.4	Monitoring and process control	148
13.4.1	Monitoring: steady-state identification	148
13.4.2	Control system	150
13.5	Methodology validation and high TBT results	152

[25]: Ghenai et al. (2021), "Performance Analysis and Optimization of Hybrid Multi-Effect Distillation Adsorption Desalination System Powered with Solar Thermal Energy for High Salinity Sea Water"

[26]: Son et al. (2020), "Pilot Studies on Synergistic Impacts of Energy Utilization in Hybrid Desalination System"

[27]: Burgess et al. (2000), "Solar Thermal Powered Desalination: Membrane versus Distillation Technologies"

[28]: Pinto et al. (2017), "Desalination Projects Economic Feasibility"

[144]: El-Dessouky et al. (2002), *Fundamentals of Salt Water Desalination*

[169]: Mistry et al. (2011), "Entropy Generation Analysis of Desalination Technologies"

[170]: Christ et al. (2014), "Thermodynamic Optimisation of Multi Effect Distillation Driven by Sensible Heat Sources"

1: the value of 1 kWh electric differs from that of 1 kWh thermal in terms of their ability to produce work, as the latter is constrained by the Carnot efficiency [171]

[148]: Bouma et al. (2020), "Metrics Matter"

low temperature MED configuration (Low Temperature (LT)-MED), a MED unit incorporating Thermal Vapor Compression (MED-Thermal Vapor Compression (TVC)), a MED unit using nanofiltration (Nanofiltration (NF)-LT-MED) for feedwater pretreatment, and a combination of TVC and nanofiltration. Although the Specific Thermal Energy Consumption (STEC) values favored the use of TVC, a more rigorous —exergetic— analysis revealed that the most efficient systems were those that used lower temperature heat sources (LT-MED and NF-LT-MED).

[172]: Darwish et al. (2006), “Multi-Effect Boiling Systems from an Energy Viewpoint”

[173]: Shahzad et al. (2019), “A Standard Primary Energy Approach for Comparing Desalination Processes”

[171]: Lienhard et al. (2017), “Thermodynamics, Exergy, and Energy Efficiency in Desalination Systems”

[174]: Brogioli et al. (2018), “Thermodynamic Analysis and Energy Efficiency of Thermal Desalination Processes”

[175]: Spiegler et al. (2001), “El-Sayed, Y.M.”

[176]: Sharqawy et al. (2011), “On Exergy Calculations of Seawater with Applications in Desalination Systems”

[177]: Sharqawy et al. (2010), “Formulation of Seawater Flow Exergy Using Accurate Thermo-dynamic Data”

[178]: Mistry et al. (2012), “Effect of Nonideal Solution Behavior on Desalination of a Sodium Chloride (NaCl) Solution and Comparison to Seawater”

[179]: Mistry et al. (2013), “Generalized Least Energy of Separation for Desalination and Other Chemical Separation Processes”

[180]: Thiel et al. (2015), “Energy Consumption in Desalinating Produced Water from Shale Oil and Gas Extraction”

[181]: Valenzuela et al. (2014), “Optical and Thermal Performance of Large-Size Parabolic-Trough Solar Collectors from Outdoor Experiments”

[182]: Prahl et al. (2018), *Protocol for Characterization of Complete Solar Concentrators Using Photogrammetry or Deflectometry*

[183]: Bayón et al. (2019), “Development of a New Methodology for Validating Thermal Storage Media”

Some authors have carried out exergy analysis to overcome the limitations aforementioned of energy performance metrics. Darwish et al. [172] proposed two new metrics: Specific Fuel Energy and Equivalent Specific Work. The first compares the energy used for the desalination process that could otherwise be used for energy generation in a turbine for which it was assumed a value for the efficiency of the power plant. The second sets the work potential of the extracted steam as a baseline, considering the desalination plant separation efficiency and adding the energy consumption for pumping. The problem of this study is that it is limited to cogeneration schemes (joint electricity and water production) and would not be useful in the case of desalination with LT sources. Shahzad et al. [173] developed an approach based on the second law of thermodynamics, which is also useful only for cogeneration schemes. They proposed a common metric called the Standard Universal Performance Ratio to compare desalination processes using different kinds of energy, which is based on conversion of different types and grades of energies to standard primary energy. In this case, conversion factors were proposed to convert the derived energy input to the standard primary energy. Other authors have performed exergy analyses for stand-alone desalination processes, as is the case of Lienhard et al. [171] and Brogioli et al. [174], who considered desalination processes as a black box and the ideal work or the thermodynamic limit for the separation of dissolved salts in seawater as the Carnot work.

The problem with the exergy analyses is that they are more complex [175] due to the need to consider several aspects not present in simple energetic metrics: definition of dead state and control volume [176], chemical exergy modeling of seawater [177, 178] and minimum energy reference (least and minimum work of separation) [179, 180]. Probably because of their complexity, they have not been widespread in the performance evaluation of practical setups. Also, none of the works published so far in the scientific literature addresses specifically the exergetic evaluation when using non-conventional energy sources such as waste heat.

Two important requirements for an accurate and reliable performance assessment are the steady state identification and the uncertainty of both the direct measurement and that associated with the performance metric determination. With respect to the former, it is highly recommended to use automatic procedures that increase the reliability of the measurements. The steady state evaluation carried out manually so far by qualified operators [181–183], leads to high time consumption and full dependence on the operators’ attention, leading to potential unreliable identifications. With respect to the latter, it allows for a more comprehensive and nuanced approach to performance evaluation, since it increases the robustness of the evaluation while providing information on the reliability of the results. Neither of these two aspects have yet been addressed in the performance assessment of thermal desalination plants. There is a gap in the establishment of standard methodologies that include all the necessary requirements for the reliable assessment of the performance of thermal desalination processes. This chapter aims to address this gap by proposing a method with potential for a broader application in other thermal desalination processes. The method is applied and validated in the MED-Plataforma Solar de Almería (PSA) plant as part of a high TBT experimental campaign.

Evaluation at high Top Brine Temperature

The performance of a thermal process, such as MED, is dictated by the Carnot cycle [174], which sets the theoretical maximum efficiency for any heat engine. The efficiency of the Carnot cycle is limited by the temperature difference between the hot and cold sinks, which determine the amount of thermal energy that can be converted into useful (separation) work.

An approach to bring the MED closer to its thermodynamic limit can be achieved by raising the Top Brine Temperature (TBT) (from 70 to 80–90°C), which allows to increase the number of effects [184] while maintaining an optimal temperature drop across them (*pinch*)². This leads to an improvement in the thermal performance of traditional desalination applications and an increase in the concentration factors achievable [150].

High TBT does not mean high heat source temperature

MED-TVC plants even when operating at low TBT require motive steam at *high* temperatures (120–150°C) [93]. However, the extension of the MED process to higher TBT values in the range of 80–90°C still requires relatively low temperature heat (<100°C), so it can still be considered low-temperature and compatible with low-grade waste heat sources.

In practice, the TBT in the MED system is limited to 70°C, since higher TBTs increase the risk of precipitation of divalent ions, which tend to form incrustations on the heat exchange surfaces. These deposits reduce heat transfer efficiency, as extensively analyzed by Glade *et al.* [185, 186].

Ryznar Stability Index (RSI)

The Ryznar Stability Index (RSI) is an empirical indicator used in water chemistry to predict the tendency of water to form scale (calcium carbonate deposits) or to cause corrosion. It is based on the Langelier Saturation Index (LSI) but is formulated to better correlate with observed scaling and corrosion behavior [187]. It is defined as:

$$RSI = 2pH_s - pH,$$

where pH is the measured pH of the water sample and pH_s is the pH at which the water is saturated with calcium carbonate (CaCO_3).

Figure 13.1 shows the RSI of seawater at different temperatures and concentrations, where the background surface color represents the RSI. For un-treated feedwater this risk of precipitation is present at almost any temperature due to its composition (RSI below 4, see Table 13.1). This situation can be attenuated either by the use of an anti-scalant, or by treating the feedwater to remove the divalent ions. One promising option to achieve the latter is to use selective nanofiltration membranes [188]. A nanofiltration pretreatment can be used to selectively remove the divalent ions while leaving relatively unaffected the components to be separated in the MED process, *i.e.* NaCl. This allows the operation of MED processes at higher TBTs or higher feed concentrations.

This second feature potentially enables hybrid systems combining two separation phases *e.g.*: an initial Reverse Osmosis (RO) stage for traditional seawater desalination followed by a MED brine concentrator that tolerates higher feed concentrations.

The chapter is structured as follows. First, in Section 13.1, a process analysis focused on performance evaluation is presented to clearly define the eval-

[174]: Brogioli *et al.* (2018), “Thermodynamic Analysis and Energy Efficiency of Thermal Desalination Processes”

2: With limitations, as in each effect a considerable amount of exergy is destroyed and a minimum pinch is required

[150]: Zaragoza *et al.* (2022), “Coupling of Nanofiltration with Multi-Effect Distillation for Solar-Powered Seawater Desalination towards Brine Mining and Water Production for Agriculture”

[185]: Glade *et al.* (2010), “Scale Formation of Mixed Salts in Multiple-Effect Distillers”

[186]: Krömer *et al.* (2015), “Scale Formation and Mitigation of Mixed Salts in Horizontal Tube Falling Film Evaporators for Seawater Desalination”

[188]: Schafer *et al.* (2021), *Nanofiltration: Principles, Applications, and New Materials*

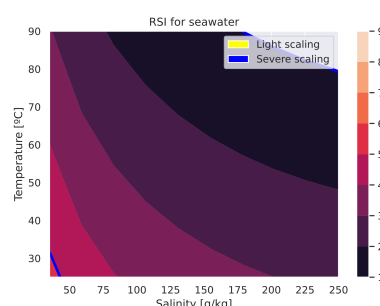


Figure 13.1: RSI of seawater at different temperatures and concentrations

Table 13.1: Ryznar Stability Index (RSI) values and their interpretation in terms of scaling and corrosion risk [187].

RSI > 9	Severe corrosion
7.5 < RSI < 9	Heavy corrosion
7 < RSI < 7.5	Significant corrosion
6 < RSI < 7	Stable water
5 < RSI < 6	Moderate to light scaling
4 < RSI < 5	Severe scaling

3: e.g. a design metric would be the specific area [144]

[148]: Bouma et al. (2020), "Metrics Matter"

4: The use of electrical energy will always be desired to be minimized, so the distinction is not needed.

5: e.g. a less efficient system will require a larger heat exchanger area to extract more energy from the waste heat source, leading to increased system costs

[189]: Mistry et al. (2013), "An Economics-Based Second Law Efficiency"

[190]: Christ et al. (2017), "Techno-Economic Analysis of Geothermal Desalination Using Hot Sedimentary Aquifers"

[157]: Christ et al. (2015), "Boosted Multi-Effect Distillation for Sensible Low-Grade Heat Sources"

[170]: Christ et al. (2014), "Thermodynamic Optimisation of Multi Effect Distillation Driven by Sensible Heat Sources"

[191]: Christ et al. (2015), "Application of the Boosted MED Process for Low-Grade Heat Sources – A Pilot Plant"

ation scope as well as the process inputs and outputs. Then, in Section 13.2, the performance metrics are introduced, including separation, energetic, and exergetic criteria. Section 13.3 describes the system instrumentation, covering Key Process Variables (KPVs), instrumentation requirements, and the uncertainty determination for both direct measurements and derived metrics. Section 13.4 presents the proposed steady-state identification algorithm for stable operation monitoring, together with the control strategies to be implemented. Finally, in Section 13.5, the proposed methodology is applied to a case study—an experimental campaign at the MED-PSA plant—to experimentally characterize the system under high TBTs. The results of this high-TBT operation are also analyzed in this section.

13.1 Process analysis

Metrics are defined based on some criteria, and this criteria is of paramount importance because resources and efforts are invested in optimizing the process in its direction. In order to adequately define these criteria, it is important to have an overall perspective of the process: defining its inputs and useful outputs—from a qualitative point of view—as well as a clear delineation of the scope of the evaluation.

Metrics can be related either to the operation or to the design of the system³. In terms of scope, they can span from primary energy sources [148] or the isolated MED process. This chapter focuses on the **operation** of an **isolated** MED system. Additionally, for the determination of the performance metrics, the following aspects are considered:

Application. Two applications are distinguished:

- ▶ **Seawater desalination.** The objective is to obtain fresh water. The level of separation achieved is a secondary (not useful) output.
- ▶ **Brine concentration.** The objective is to extract resources from the brine in order to valorize it. Here, the level of separation is a crucial factor to consider.

External heat source type. Two types of external heat sources are distinguished⁴:

- ▶ **Process heat.** Process heat is the heat utilized by a system and its associated costs are related to the amount of energy consumed.
- ▶ **Waste heat.** Waste heat is the heat utilized by a system that would otherwise be lost to the environment. It has no associated costs to the amount of heat used, though there are other costs associated with its use⁵ [189, 190]. Here the goal is to maximize the amount of product by maximizing the utilization of the waste source [157, 170, 191].

Process heat vs waste heat take on efficiency

In a process heat driven system, between two plants that produce the same amount of useful product, the most efficient one is the one that uses the least external heat to do so, whereas in a waste heat driven system, the two plants would be considered as efficient since the unused heat would be wasted to the environment. A more intuitive definition would be:

Given two plants that consume the same waste heat, the most efficient one is the one that produces the most product with that available heat.

Based on the above considerations, Figure 13.2 shows the control volume of the MED process with the inputs and outputs used for the definition of the

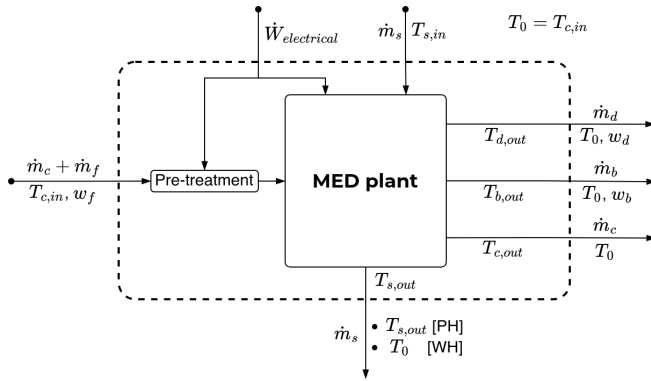


Figure 13.2: Inputs and outputs variables in an MED process. The dash line delimits the control volume

performance metrics. From left to right, seawater (including cooling water, c , and feed, f) enters the control volume at the seawater intake conditions ($T_{c,in}$). The cooling water is rejected at $T_{c,out}$. On the right side, the distillate and the brine are discharged from the MED system at temperatures $T_{d,out}$ and $T_{b,out}$ and mass fractions w_d and w_b , respectively. The temperatures of all these outlet streams, from a qualitative (*i.e.* exergetic) point of view, are useless and thus considered to be at T_0 when leaving the control volume⁶.

From top to bottom, the energy sources for the system are depicted. Electrical work is depicted as $\dot{W}_{electrical}$ and includes pumping, vacuum system, and feed water pretreatment, among others. The heat source is represented by the subscript (s) and as shown in the figure, it enters the MED plant at $T_{s,in}$ and leaves it at $T_{s,out}$ after releasing part of its energy. When leaving the control volume, $T_{s,out}$ value depends on the type of heat source:

- ▶ Process heat (PH). The value of $T_{s,out}$ does not change. In case steam is used as heat source, the primary energy driver is the latent heat of phase change and $T_{s,out}$ is usually similar to or equal to $T_{s,in}$. In case a sensible heat source is used, the driving force is the temperature difference and $T_{s,out}$ is between $T_{s,in}$ and T_0 .
- ▶ Waste heat source (WH). In this case, $T_{s,out}$ is considered to leave at the sink conditions (T_0) since this heat is not reused but lost to the environment.

6: It is heat that is lost to the environment, and thus no additional work can be feasibly extracted from these streams

13.2 Performance metrics

A performance metric is a quantitative measure used to evaluate the effectiveness or efficiency of a system. It provides objective information that can be used to monitor progress, identify areas for improvement, and inform decision making. A metrics division in three categories is proposed: separation, energetic, and exergetic metrics. A detailed description of each of them within each category is presented below.

13.2.1 Separation metrics

Recovery Ratio. The Recovery Ratio (RR) represents the flow ratio of unit of distillate produced per unit of feed and is very useful in seawater brine concentration applications [133]. It is related to electricity consumption, since the lower the Recovery Ratio (RR) the higher the feed pumping needs are for the same distillate production [93]. It is determined as follows:

[133]: Jones et al. (2019), "The State of Desalination and Brine Production"

[93]: Palenzuela et al. (2015), *Concentrating Solar Power and Desalination Plants*

$$RR = \frac{\dot{m}_d}{\dot{m}_f} \times 100 [\%], \quad (13.1)$$

where \dot{m}_d is the mass flow rate of distillate and \dot{m}_f is the feedwater mass flow rate, both in kg/s.

Concentration Factor. An equivalent metric is the concentration factor, which accounts for how many times the brine is concentrated with respect to the feed concentration:

$$CF = \frac{w_b}{w_f} = \frac{\dot{m}_f}{\dot{m}_f - \dot{m}_d} [-], \quad (13.2)$$

where w_b is the brine concentration and w_f is the feedwater concentration, both in g/kg.

Reconcentration Index. Apart from the already known previous metrics, a new one is proposed in this work that can be useful for seawater brine concentration applications. This metric is called Reconcentration Index (RI), and it allows to determine how close the separation achieved (RR) is to the theoretical maximum recovery ratio (RR_{max}). It is defined as:

$$RI = RR/RR_{max} [-], \quad (13.3)$$

[180]: Thiel et al. (2015), "Energy Consumption in Desalinating Produced Water from Shale Oil and Gas Extraction"

7: sodium chloride is the only solute considered, as it sets the concentration limit being the solute in seawater with the highest concentration and the greatest solubility [180]

8: Limited to steam or 1000 BTU as arbitrary conversion factor

[192]: Lienhard V et al. (2012), "SOLAR DESALINATION"

$$RR_{max} = w_{w,f} \left(1 - \frac{b_{NaCl,f}}{b_{NaCl,sat}} \right) \times 100 [\%], \quad (13.4)$$

where $w_{w,f}$ is the water mass fraction in the feed (which is $1 - w_{sol,f}$, where $w_{sol,f}$ is the mass fraction of the solutes in the feed) and $b_{NaCl,f}$ is the molality of sodium chloride in the feed, in mol_{NaCl}/kg_w (both can be obtained from a feedwater chemical analysis). On the other hand, $b_{NaCl,sat}$ is the molality of sodium chloride at saturation conditions⁷ (see Section A.3 (Separation metrics calculation) for more details of its estimation).

13.2.2 Energetic metrics

The energetic metrics are metrics that consider only the first law of thermodynamics (*i.e.* quantity). They are: Gain Output Ratio (GOR), Specific Thermal Energy Consumption (STEC), and Specific Electrical Energy Consumption (SEEC) and are described in the following.

Gain Output Ratio. Regarding the Gain Output Ratio (GOR), a universal definition of this metric that avoids the limitations of some of the commonly used definitions mentioned⁸ is the ratio between the energy in the form of latent heat required to vaporize all the distillate produced and the external thermal energy contributed to the system (Equation 13.5) [192].

$$GOR = \frac{\dot{m}_d \cdot \Delta h_{avg}}{\dot{Q}_{in}} \quad (13.5)$$

where Δh_{avg} is the latent heat of vaporization at the average vapor temperature between the first effect and the last effect, in kJ/kg, and \dot{Q}_{in} is the external

thermal energy consumption required to drive the process, in kW. In case process heat is used, it is determined by \dot{m}_s (mass flow rate of the external energy source supplied in the first effect, in kg/s) and Δh_s , which can be calculated as $h_{s,in} - h_{s,out}$ (in case of sensible heat) or as $h_{s,sat,vap} - h_{s,sat,liq}$ (in case of latent heat of phase change at saturation conditions from vapor to liquid at temperature $T_{s,in}$).

In case waste heat is used as external thermal energy source for the MED system, \dot{Q}_{in} is determined with \dot{m}_s and Δh but referred to the lowest temperature of the system ($T_{c,in}$).

Specific Thermal Energy Consumption. Another performance index widely used in thermal desalination is the Specific Thermal Energy Consumption (STEC). For desalination applications, it is defined as the input heat to the system per unit of product (distillate). If process heat is used, this index has units of energy per fraction of volume and its expression is shown in Equation 13.6.

$$STEC = \frac{\dot{m}_s \cdot (h_{s,in} - h_{s,out})}{\dot{m}_d} \cdot \rho_d \cdot \frac{1 \text{ kWh}}{3600 \text{ kJ}} \left[\frac{\text{kWh}_{th}}{\text{m}^3} \right]. \quad (13.6)$$

For brine concentration applications, it is named as $STEC_{bc}$ and it is determined as the energy required (in kJ) per unit of feed (in kg) (i.e. \dot{m}_f in the denominator) [193].

Both STEC and GOR are equivalent and are related via Equation 13.7.

[193]: Chen et al. (2021), "A Zero Liquid Discharge System Integrating Multi-Effect Distillation and Evaporative Crystallization for Desalination Brine Treatment"

$$STEC = \frac{2326 \text{ kJ/kg}}{GOR} \cdot \rho_d \cdot \frac{1 \text{ kWh}}{3600 \text{ kJ}}, \quad (13.7)$$

where ρ_d is the density of the distillate in kg/m^3 .

For the cases in which waste heat source is used as energy source, a variation of the STEC is proposed: the waste heat STEC ($STEC_{wh}$). For desalination applications, it is determined as follows:

$$STEC_{wh} = \frac{\dot{m}_s \cdot (h_{s,in} - h_{c,in})}{\dot{m}_d} \cdot \rho_d \cdot \frac{1 \text{ kWh}}{3600 \text{ kJ}} \left[\frac{\text{kWh}_{th}}{\text{m}^3} \right]. \quad (13.8)$$

As before, for brine concentration applications, \dot{m}_d would be replaced by \dot{m}_f in the denominator.

Specific Electrical Energy Consumption. Another important index in desalination is the Specific Electrical Energy Consumption (SEEC), which represents the total electrical consumption of the plant per unit of distillate water produced. These are the subsystems that should be considered:

- ▶ J_s . External heat source pumping (if any)
- ▶ J_f . Feed pumping
- ▶ J_c . Cooling
- ▶ J_d, J_b . Discharge extractions
- ▶ J_{vacuum} . Vacuum system
- ▶ J_{aux} . Auxiliary consumptions. Represents any additional power that the system may require to function (e.g., electrical consumption for feedwater pretreatment such as nanofiltration)

For desalination applications, the following equation is used for the calculation of this metric:

$$SEEC = \frac{\sum_{i=1}^N (J_i)}{\dot{m}_d} \left[\frac{\text{kWh}_e}{\text{m}^3} \right], \quad (13.9)$$

where J_i is the electrical consumption of the i_{th} subsystem. In the case of brine concentration applications, the index is called $SEEC_{bc}$ and the denominator would be replaced by \dot{m}_f .

13.2.3 Exergetic metrics

Exergy is the maximum amount of work achievable when a system is brought into equilibrium from its initial state to a reference state (known as the dead state and represented by the subscript "0") [176, 194]. This reference state is usually established for desalination applications as the seawater intake temperature ($T_{c,in}$). In contrast to the energetic metrics, it considers not only the first law of thermodynamics (quantity), but also the second law (quality).

Second law efficiency. The most widespread exergetic metric is the second law efficiency (η_{II}) [171], which accounts for irreversible losses within a system. It is calculated as the ratio of the useful exergy output of a system ($\dot{Ex}_{out,useful}$) to the exergy input given to the system (\dot{Ex}_{in}) (a further explanation of how to determine the different exergy flows can be found in Section A.2 (Exergy calculations)):

$$\eta_{II} = \frac{\dot{Ex}_{out,useful}}{\dot{Ex}_{in}} \times 100 [\%]. \quad (13.10)$$

Considering exergy losses, which are the sum of the exergy destroyed in each individual component ($\dot{Ex}_{destroyed}$) and exergy losses due to discharge streams in disequilibrium to the environment ($\dot{Ex}_{streams}$), the previous equation can be written as follows:

$$\eta_{II} = 1 - \frac{\dot{Ex}_{destroyed} + \dot{Ex}_{streams}}{\dot{Ex}_{in}} \times 100 [\%]. \quad (13.11)$$

Specific Exergy Consumption. Another useful metric is the Specific Exergy Consumption (SEXC), which was firstly referenced as specific consumed available energy in [172]. Similarly to Specific Electrical Energy Consumption (SEEC) and STEC, it accounts for the exergy input to the system per unit of distillate produced (Equation 13.12) and it is determined as follows [148]:

$$SEXC = \frac{\dot{Ex}_{in}}{\dot{m}_d} \left[\frac{\text{kWh}_{ex}}{\text{m}^3} \right]. \quad (13.12)$$

It is important to note that the terms $\dot{Ex}_{out,useful}$ and \dot{Ex}_{in} from the previous exergetic metrics are determined depending on what is considered as useful exergy leaving the process and what is deemed as exergy input to the system⁹:

- ▶ **Useful exergy output.** The useful exergy output of the system ($\dot{Ex}_{out,useful}$) depends on what is considered the valuable product generated by the process. In a separator in which the objective is to separate water and brine, the useful exergy is the chemical exergy of separation. As discussed in [171], for seawater desalination applications, where the valuable product

[172]: Darwish et al. (2006), "Multi-Effect Boiling Systems from an Energy Viewpoint"

[148]: Bouma et al. (2020), "Metrics Matter"

9: It mirrors the qualitative analysis presented in Section 13.1

[171]: Lienhard et al. (2017), "Thermodynamics, Exergy, and Energy Efficiency in Desalination Systems"

is fresh / pure water, the chemical exergy of separation corresponds to that of a reference ideal separator that achieves the *minimum separation work* ($\dot{W}_{\text{least}}^{\min} = \dot{W}_{\text{least}}|_{RR \rightarrow 0}$). The objective is to minimize the required energy consumption to produce fresh / pure water, regardless of how much separation takes place ($RR \rightarrow 0$), so $\dot{Ex}_{\text{out,useful}} = \dot{W}_{\text{least}}^{\min}$.

On the other hand, in brine concentration applications, since the objective is to maximize the separation achieved, the separator takes into account the amount of separation achieved ($\dot{W}_{\text{least}}|_{RR}$), and $\dot{Ex}_{\text{out,useful}} = \dot{W}_{\text{least}}$ ^[180].

The definition and determination of the least and minimum least work of separation can be found in Section A.2.

[180]: Thiel et al. (2015), "Energy Consumption in Desalinating Produced Water from Shale Oil and Gas Extraction"

- **Exergy input.** The exergy input (\dot{Ex}_{in}) is determined according to the type of external heat source. In case process heat is used, the exergy input is determined as:

$$\dot{Ex}_{in} = \dot{Ex}_{s,in} - \dot{Ex}_{s,out} + \sum_i \dot{E}_i, \quad (13.13)$$

where $\dot{Ex}_{s,in}$ and $\dot{Ex}_{s,out}$ are the exergy flows associated with the thermal energy source at the inlet and outlet, respectively.

When using waste heat sources, the exergy input is determined as:

$$\dot{Ex}_{in} = \dot{Ex}_{s,in} - \dot{Ex}_{s,out}^{wh} + \sum_i \dot{E}_i, \quad (13.14)$$

where $\dot{Ex}_{s,out}^{wh}$ is the outlet heat source exergy flow, which is evaluated at temperature T_0 (dead state).

Thus, for brine concentration applications or in case waste heat is used, the metric should include the subscript *bc* or *wh*, respectively, to distinguish between the application and external energy source types.

13.3 Instrumentation

13.3.1 Key Process Variables (KPVs)

The KPVs are those variables that uniquely define an operating point, which is obtained by averaging all monitored variables when stable operation is achieved. In other words, any change in the key variables is associated with a different operating point, since the plant outputs are affected accordingly. The following selected variables apply to any MED plant with any configuration in terms of seawater flow direction, tube arrangement in tube bundles, or effect layout [93]. They are represented in Figure 13.3 and described hereinafter:

[93]: Palenzuela et al. (2015), *Concentrating Solar Power and Desalination Plants*

- **Heat source flow rate** (\dot{m}_s - FT01), inlet temperature and pressure ($T_{s,in}$ and $P_{s,in}$ - TT01 and PT03) for sensible heat sources, and just **FT01** and **TT01** if saturated steam is used (otherwise steam quality needs to be estimated). They determine the hot side conditions, which usually take place in the first effect that is at the highest temperature and pressure. If multiple effects receive external heat sources, each one has to be monitored.
- **Feed water flow rate** (\dot{m}_f - FT02), which affect the overall plant operation conditions. A precise and stable input feed flow rate ensures consistent heat transfer rates, residence times, and separation efficiencies.

- ▶ **Distillate flow rate (\dot{m}_d - FT03).** It is a basic variable that gives information about the production of the system. As long as this output variable is stable, it can be assumed that the sum of it plus the brine flow rate is equal to the feed flow rate.
- ▶ **Condenser pressure / temperature ($P_{v,c}$ - PT02 / $T_{v,c}$)** or condenser outlet temperature ($T_{c,out}$ - TT02). The stability of any of these variables, together with that of the distillate production, establish a stable heat sink.
- ▶ **Effect pressure / temperature ($P_{v,1}$ - PT01 / $T_{v,1}$)** or heat source outlet temperature ($T_{s,out}$ - TT05), which is always required in case that sensible heat source is considered as the external energy source. The stability of this output variable determines a stable hot side. In case other effects, apart from the first one, receive external heat sources, each one has to be monitored.
- ▶ **Feed water salinity (w_f - CT01).** It affects the overall plant operation conditions since any stream with different salinity would have different thermodynamic properties (i.e. boiling point elevation) and therefore, different energy requirements are needed to perform the separation.
- ▶ **Condensate salinity (w_d - CT02).** This variable together with the distillate flow rate gives information on the achieved levels of salt separation.
- ▶ **Ambient temperature (T_{amb} - TT06).** The ambient conditions determine the losses to the environment which can change the results for the –otherwise— same operating conditions.
- ▶ **Seawater temperature** or condenser inlet temperature ($T_{c,in}$ - TT04). It is another environment variable that sets the minimum achievable temperature in the system.
- ▶ **Last effect (L_b - LT01)** and condenser (L_d - LT02) levels. In the case of the final condenser, it is a vessel in which the vapor coming from the final effect condenses, producing distillate that is continuously extracted from the system. The stability in this vessel is achieved when the extraction rate is equal to the condensate production rate. A higher extraction rate would eventually lead to unstable production, while a lower extraction rate would cause an increase in the vapor pressure, which would lead to induced lower production caused by misoperation. A stable level throughout the operation can ensure that the extraction and production rates (\dot{m}_d) are in balance. In the case of the last effect, it is important to keep the level as low as possible in order to avoid brine contamination in the distillate. variables are not relevant to the operating point, but are relevant to the plant operation.

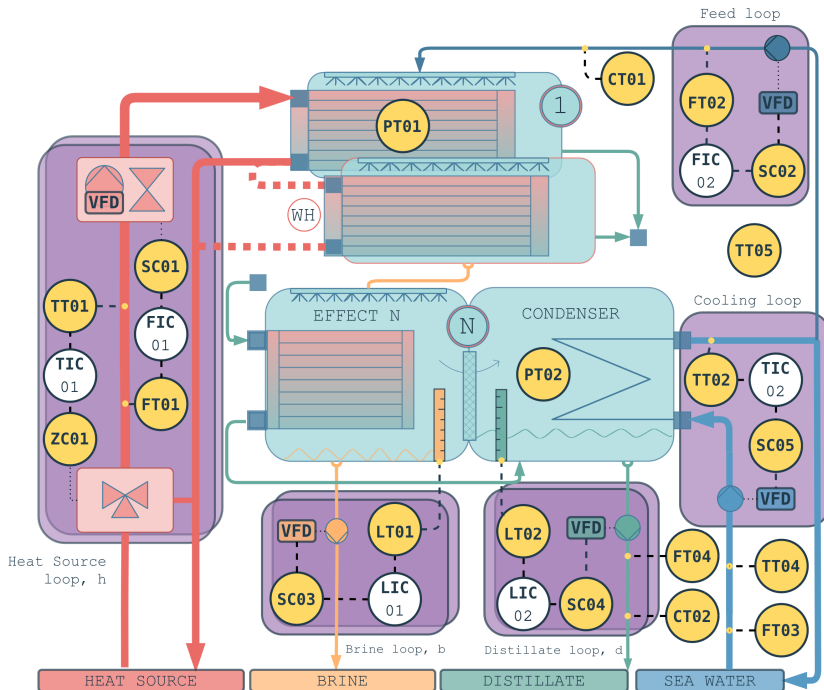
13.3.2 Instrumentation requirements

The installed instrumentation must measure magnitudes such as flow rate (mass or volumetric), temperature, pressure, water conductivity, level, and power. First, it is important to account for the influence of the quality of each measured variable on the reliability of the performance metrics, which is determined by a sensitivity analysis.

Reminder: How to interpret Sensitivity Analysis (SA) results

The results include different sensitivity indices, namely first-order, second-order, and total-order indices. The first-order index measures the direct effect of an input variable on the output, excluding interactions with other variables. The second-order index quantifies the interaction effects between pairs of variables. Finally, the total-order index represents the overall contribution of an input variable, including both its direct and interaction effects.^a

^a More details are shown in Section 3.1 (Modelling and simulation)



All KPVs must be monitored regardless of their influence on the performance metric being evaluated because, as mentioned above, the average values of these variables at steady state conditions define an operating point.

Figure 13.3: Piping and Instrumentation Diagram (P&ID) with the required instrumentation, KPVs, and basic control loops (ANSI/ISA 5.1-2022) required in an MED plant

Figure 13.4 shows the results obtained from the sensitivity analysis in terms of total-order Sensitivity Index (SI). The closer the SI is to 1, the greater the influence of the variable (shown on the left axis) on the reliability of the performance metric (shown on the top). In other words, the quality of the variable measurement should be higher for variables with a higher SI. The cases where no sensitivity index is obtained indicate that the variable has no effect on the metric.

In general, monitoring of these variables must be performed online for each operating point evaluated. However, some of the variables rarely change and can be measured periodically or offline. This is the case of environment variables such as w_f , w_d , T_{amb} .

Another aspect that deserves careful consideration is the measurement of the temperature of the heat source. To determine the thermal efficiency of the system when a sensible heat source is utilized, it is crucial to accurately measure the temperature difference between the inlet and outlet of this energy source (ΔT_s). Using temperature transmitters with high accuracy rates (*i.e.* Platinum temperature transducer, 100 ohms at 0 °C (PT100)), uncertainties of about 0.5 °C or below 1 % for the absolute temperature can be expected at temperatures exceeding 60 °C. However, when considering the small temperature differences between the inlet and outlet, which can be as low as 2 °C, the resulting relative uncertainty could be up to 25 %. To address this problem, it is recommended that both temperature transmitters are identical and calibrated simultaneously, using the same calibration pattern, which translates into observed values for the uncertainty of the temperature difference in the range of 0.1 °C or 5 %.

On the other hand, the total electrical energy consumption (represented as $JT01$ in Figure 13.3) can be monitored as global system consumption, or independently per subsystem ($J_s, J_c, J_f, J_d, J_b, J_{vacuum}, J_{aux}$).

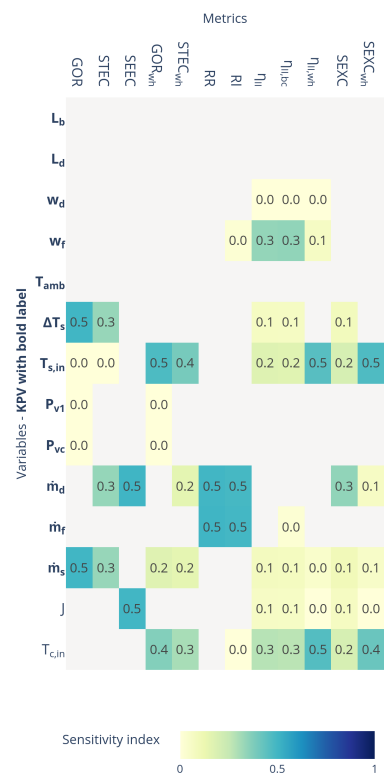


Figure 13.4: Sensitivity index results for different variables. Useful to assess the impact of the different measured variables uncertainty on the performance metrics. KPVs are shown in bold notation

13.3.3 Uncertainty determination

[195]: BIPM (2008), JCGM 100:2008. GUM 1995 with Minor Corrections. Evaluation of Measurement Data — Guide to the Expression of Uncertainty in Measurement

Uncertainty determination is particularly valuable in assessing the reliability and validity of predictions, forecasts, or results evaluation. The framework on which the uncertainty assessment of this proposed methodology is based is the **JCGM 100:2008** [195].

In an uncertainty analysis, the uncertainties of direct measurements must be firstly determined. The uncertainty of each direct measure (ΔX_i) consists of the sum of two components, as indicated below:

$$\Delta X_i = \Delta X_{\text{sensor}} + \Delta X_{\text{control}}$$

where:

- ▶ ΔX_{sensor} is the contribution of the sensor, which depends on its accuracy, calibration and conversion errors, and should be available from the instrument datasheet.
- ▶ $\Delta X_{\text{control}}$ is the uncertainty attributed to the quality of the control and is estimated using the standard deviation of the measurement throughout the period considered as stable.

[196]: Smith (2013), Uncertainty Quantification

On the other hand, when working with derived variables, *i.e.* quantities that are calculated based on other measured or known quantities, the uncertainty is determined through uncertainty propagation. There are several analytical and numerical methods to propagate uncertainty [196]. One simple approach is the use of first-order Taylor series approximation, obtained calculating the partial derivative of the different direct measurements ($X_i = 1..N$) that take part in the calculation of an output (Y):

$$Y = f(X_1, \dots, X_N),$$

$$\Delta Y = \left(\sum_{i=1}^N \left(\left| \frac{\partial Y}{\partial X_i} \right| \Delta X_i \right) \right)^{1/2},$$

[197]: NIST (), “NIST Guidelines for Evaluating and Expressing the Uncertainty of NIST Measurement Results Cover”

where ΔY can be expressed in terms of absolute uncertainty, relative, or standard uncertainty [197]. This alternative provides a simple mathematical expression to directly estimate uncertainty. Expressions for the uncertainty estimation of energetic and separation metrics of MED processes with this approach are available in Section A.1. However, first-order Taylor series approximation has certain limitations, being the main one that it is not adequate for highly non-linear models, where a higher order Taylor expansion is required, or when uncertainties are far from the mean. Also, when working with complex models, as in the case of exergetic metrics, its expression can not be practically obtainable. For these cases, the recommended approach are numerical methods, specifically the Monte Carlo method [198], which despite its higher computational requirements does not have the aforementioned limitations [199].

[198]: BIPM (2008), JCGM101:2008. Evaluation of Measurement Data — Supplement 1 to the “Guide to the Expression of Uncertainty in Measurement” — Propagation of Distributions Using a Monte Carlo Method

[199]: Wolff (2007), “Monte Carlo Errors with Less Errors”

13.4 Monitoring and process control

13.4.1 Monitoring: steady-state identification

The evaluation of the system performance must be carried out when the plant is at steady state conditions, that is, when the mass and energy balances are in equilibrium and thus do not change with time; otherwise, erroneous results can be obtained. Steady-state conditions can be identified by observation

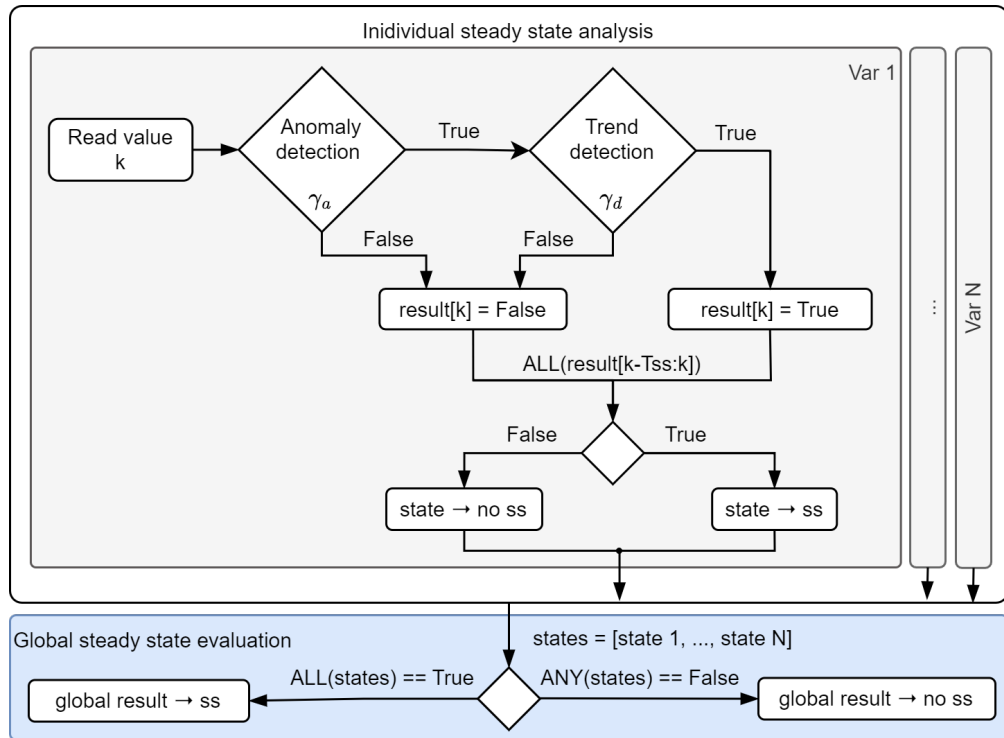


Figure 13.5: Diagram of the steady-state identification procedure

by qualified and experienced plant operators. However, the use of automatic detection algorithms is recommended for experimental facilities where a wide range of operating conditions are involved. In this work, an automatic detection algorithm has been purposely developed and implemented to identify the steady state of the process.

The methodology is based on the idea presented by M. Korbel *et al.* [200] and consists of combining an algorithm to detect anomalies, such as the wavelet transform [201, 202] (which allows detecting abrupt signal changes and distinguishing between high-frequency noise, transient states and steady states), with a trend detection method to identify smooth ramps as non-steady states. Whereas M. Korbel [200] *et al* propose a statistical trend detection approach, in this paper the derivative of the signal is used due to its simplicity since in this case, a threshold is the only parameter that has to be established. A diagram of the steady-state detection procedure is shown in Figure 13.5, where three parameters are mainly required: wavelet transform threshold (γ_a), derivative threshold (γ_d) and time window duration (T_{ss}).

[200]: Korbel et al. (2014), "Steady State Identification for On-Line Data Reconciliation Based on Wavelet Transform and Filtering"

[201]: Jiang et al. (2003), "Application of Steady-State Detection Method Based on Wavelet Transform"

[202]: Jiang et al. (2000), "Industrial Application of Wavelet Transform to the On-Line Prediction of Side Draw Qualities of Crude Unit"

[200]: Korbel et al. (2014), "Steady State Identification for On-Line Data Reconciliation Based on Wavelet Transform and Filtering"

At each sampling time k , a new value is read, and the *Anomaly Detection* algorithm (in this case, the wavelet transform) is applied. If the output is positive (true, meaning no anomaly is detected), the next step is *Trend Detection*. The variable is considered to be under steady-state (ss) conditions only if all elements in the results vector are positive over the period T_{ss} . Finally, the *Global Steady-State Evaluation* identifies a steady-state period when all N variables involved have been classified as steady-state.

13.4.2 Control system

Figure 13.3 shows the control loops to be implemented in an MED unit, whose subsystems and their control are described below:

- ▶ **Heat source** (*Heat Source loop* in Figure 13.3). Both the inlet temperature (TT01) / pressure (PT03) and the flow rate of the heat source (FT01) must be controlled. It can be done either by direct control over the source heat generating heat under the required operating conditions (flow and temperature/pressure), or by performing a transformation. Depending on the heat source characteristics, this transformation involves:
For sensible heat sources, independent variation of temperature and flow rate can be achieved by means of: 1) a mixing three-way valve that mixes part of the return fluid, at temperature TT05, with the inlet fluid, at TT01 by acting over the control signal for temperature regulation ZC01 and; 2) flow (FT01) regulation by acting over the control signal SC01, which can be a Variable Frequency Drive (VFD) or valve. This decoupled regulation is shown in Figure 13.3. The flow rate regulation (FT01) is achieved by acting on the selected actuator (SC01), which can be a VFD or a valve¹⁰.
For latent heat sources (steam), the pressure-flow-independent regulation is not possible since they are intrinsically coupled variables. In this case, a pressure regulator valve (ZC01) can be used to control either the flow rate (FT01) or the pressure (PT03).
- ▶ **Cooling** (*Cooling Loop* in Figure 13.3). The pressure inside the condenser (PT02) or the condenser outlet temperature (TT02) can be controlled by regulating the cooling flow rate (FT03), being the cooling water inlet temperature (TT04) a disturbance. This control loop (TIC02) consists in turn in two control loops (cascade control [203]), where an outer loop sets a reference flow rate value to achieve the desired condenser outlet temperature (or pressure), and an inner loop (not shown in Figure 13.3) acts on SC05 (VFD's frequency) to achieve the desired flow rate. Direct regulation of condenser outlet temperature using the VFD is also valid in case the measurement of the cooling flow rate is not available.
- ▶ **Brine extraction** (*Brine loop* in Figure 13.3). The brine level in the last effect (LT01), or in all effects if a parallel feed configuration is used, is controlled by the brine flow rate –see control loop LIC01 in Figure 13.3. In this case, the controller can act directly on the VFD frequency (SC03) to avoid the need for an additional flow meter.
- ▶ **Distillate extraction** (*Distillate loop* in Figure 13.3). As in the previous case, the distillate level (LT02) is controlled by acting on the control variable (SC04).
- ▶ **Feedwater** (*Feed loop* in Figure 13.3). The feed water flow rate is regulated by the FIC02 control loop, using a VFD (SC02) and a flow meter (FT02).

Startup and shutdown procedures

On MED systems with discontinuous operation, such as experimental plants, or plants driven by intermittent energy sources (e.g. solar energy), the startup and shutdown procedures are critical for ensuring safe and efficient operation. It is a repetitive and sufficiently complex process that requires an experienced operator. Manual management of the a process leads to errors that cause setbacks or, in the worst cases, premature failures in the facility: contamination of the condenser with brine due to erratic draining of the last effect, accumulation of scale on the surfaces of heat exchangers due to rapid cooling after shutdown, pumps cavitating because they are not stopped when the water flow at the intake ceases, etc. Thus this procedure should be automated.

10: It should be noted that this decoupling comes at the cost of an inefficient energy mixing process.

[203]: Åström et al. (1995), *PID Controllers: Theory, Design, and Tuning*

This can be achieved through the implementation of two finite state machines that manage the startup and shutdown of the facility, respectively. These have been designed to perform a sequence of operations that take the plant from an initial state to a final state following proper operating practices. A diagram of the process is shown in Figure 13.6.

The machines are responsible for managing the activation and deactivation of devices as well as controllers. Additionally, they set reference values for these based on a previously established configuration and evaluate whether the reference has been reached before proceeding to the next step. They also adjust certain parameters of the control system (level control) and restore the initial values once the task is completed.

The startup procedure follows an activation sequence of the different subsystems: extractions → cooling → feedwater and heat source. Then the system is left to stabilize and the startup sequence is complete.

Regarding the shutdown procedure, the two most delicate processes are the progressive cooldown of the first effect¹¹ and the complete draining of the last effect and condenser. For the gradual temperature decrease of the first effect, after the plant shutdown signal, the hot water temperature is reduced in 5-minute steps starting from the last recorded value until a final temperature of 50°C is reached (and then left to cooldown to ambient temperature). To drain the levels, a reference value well below the normal operating level is set, and the controller parameters are changed to more aggressive ones. Additionally, the device is deactivated each time the reference is reached and is not reactivated until the level reaches a specified value. This activation and deactivation process continues while the feedwater finishes draining from the upper effects of the plant. Once the control system has been deactivated for longer than a preset time, the plant shutdown procedure is considered complete, and the level controller parameters are restored.

¹¹: which has the highest scaling potential if not handled properly

A standard method for performance evaluation of thermal separation processes

1. Define the Key Process Variables (Section 13.3.1)
2. Select the required performance metrics to be evaluated according to the application and type of energy source(s) (Section 13.1).
3. Define the required instrumentation of the KPVs and of any additional variables needed for the target performance metrics (Section 13.3.2).
4. Define the uncertainty associated with the measurement and that associated with the performance metric determination (Section 13.3.3)
5. Implement the required actuators and integrate them into a control system to ensure the stability of the plant operation (Section 13.4.2).
6. Identify a time window where stable operation is achieved (Section 13.4.1).

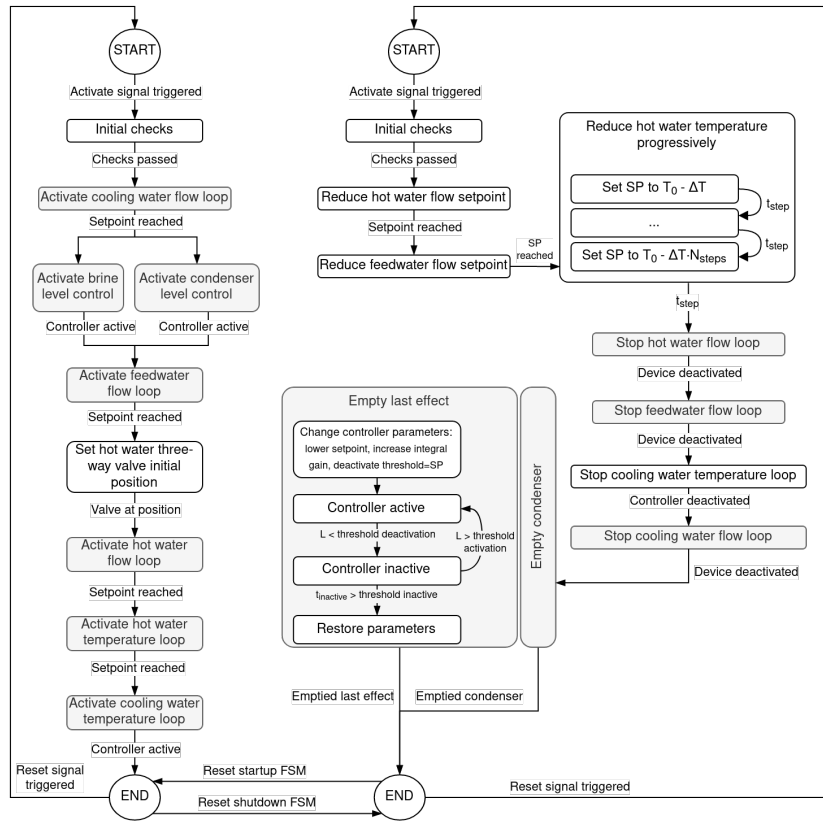


Figure 13.6: Flowchart of finite state machines for plant start-up (left) and shutdown (right)

13.5 Case study: methodology validation and results analysis in a high TBT experimental campaign at the MED-PSA plant

To showcase the application and usefulness of the proposed methodology, a case study consisting on the application of the methodology to an experimental campaign at the Solar-driven Multi-Effect Distillation (SolarMED) pilot plant is presented. The campaign was designed to evaluate the performance of the MED process under different operating conditions (see Table 13.2 and Figure 13.7), with the aim of improving its thermal performance and assessing the feasibility of using higher Top Brine Temperatures.

The following sections describe the implementation of the methodology, which is showcased in Figure 13.8 for one particular test and further discussed in the following.

Monitoring and control system implementation results

Finite state machines. In Figure 13.8 the activation sequence can be visualized at the beginning of the test (09:49–10:00): extractions → cooling → feedwater and heat source. The Flows are activated in about two minutes followed by another minute for the inlet temperature. Then the system is left to stabilize. At 09:52 the delay between activating the feedwater and it reaching the last effect is completed and the brine extraction pump starts operating. Pressures, temperatures and the distillate level in the system progressively evolve up to 10:00 when the conditions are changed for the first operation point for the day. The distillate level control action is delayed further until 10:04 when the first distillate is produced.

Table 13.2: Experimental campaign design specifications

Variable	Unit	Range
$T_{s,in}$	°C	60-89
q_s	l/s	7-14
$T_{c,out}$	°C	20-40
q_f	m ³ /h	5-9
w_f	g/kg	40

The shutdown procedure can be observed in Figure 13.8 starting from 13:07. After a decrease in flow rates, the first effect heat load is progressively decreased until 13:34. From this time, pumps are stopped and the extraction cycles begin as can be noted by the high oscillations in the *Electrical consumption – J_b* and *Levels*.

Steady state identification. The steady state identification algorithm has been implemented in the control system. It allows the automatic detection of stable operation points. This is done by monitoring the KPVs and applying the algorithm described in Section 13.4.1. In Figure 13.8, steady state periods are highlighted with a yellow background, which indicates that the algorithm has detected a stable operation point. Two are detected, the first one from 11:00 to 11:55 and the second one from 12:16 to 12:59.

Control. In terms of control, a Proportional-Integral-Derivative controller (PID) control has been implemented to effectively regulate and maintain the desired setpoints of the subsystems mentioned in Section 13.4.2. This approach enables the system to respond quickly to changes, minimize steady state errors, reject disturbances, and enhance overall performance and reliability. Figure 13.9 shows the development procedure for one of the main loops, the condenser outlet temperature control. To tune the controller, the system was excited with a Pseudo-Random Binary Sequence (PRBS) signal Figure 13.9 (a), obtaining an ARX model ($n_a = 20$, $n_b = 49$, $n_k = 5$, 96.38% fit) using the *System Identification Toolbox* from MATLAB. It allowed to extract an approximate first-order dynamic with which to tune the controller. Figure 13.9 (b) shows the controller performance for a particular test. Initially, the control signal (q_c) increases to compensate for the trend observed in the condenser inlet temperature. At 11:45, the setpoint is changed to 24 °C, to which the controller immediately adapts by decreasing its input, allowing the temperature to rise. The system progressively evolves toward the new setpoint, which is reached at 12:30. The controller then maintains the desired temperature, compensating for other disturbances (not shown in the figure). A similar behavior can be observed in the test shown in Figure 13.8 – *Temperatures and Flows*. For the first operating point (11:00 onwards), the continuously increasing inlet temperature ($T_{c,in}$) is compensated by the controller, which increases the cooling flow rate to maintain the condenser outlet temperature at the setpoint. For the second operating point (12:16), the simultaneous change of outlet temperature to a higher value, and the activation of the cooling tower –not shown in the figure— allows the inlet temperature to stabilize. This permits the controller to reduce the cooling flow rate and remain relatively unchanged from that point onwards.

Uncertainty propagation. The chosen uncertainty propagation method has been the Monte Carlo method, in which, given the time-series signals of the directly measured variables with their associated uncertainties, a normally distributed random signal is generated with a certain number of samples. The metric is then evaluated as many times as samples are available and thus a vector is obtained for the evaluated metric.

Reproducibility and the effect of the steady state duration

The operation points pairs 1–2 and 3–4 in Table 13.3 are the same test, *i.e.* the same operating conditions, but performed on different dates. Particularly for points 1–2, the duration of the steady state is significantly different (16 and 76 minutes, respectively). The obtained performance metrics are similar, with almost identical values for the energetic (GOR, STEC) and separation metrics (RR, RI). Minor differences, but still within the uncertainty margin are observed in metrics influenced by electrical consumption (η_{II} , SEXC, SEEC)—which varies between tests. The observed differences are mainly due to variations in the cooling water inlet temperature, which in turn affect the required cooling water

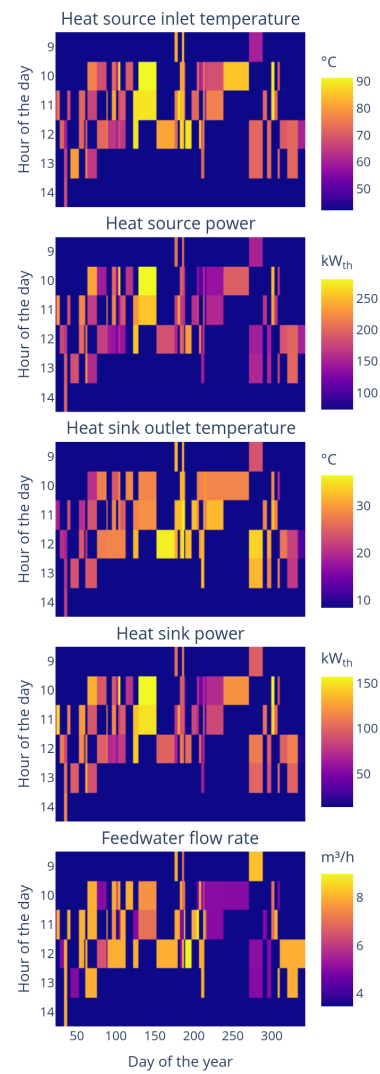


Figure 13.7: Visualization of the different process inputs values during the experimental campaign.



Parameters for both the control system and the steady-state identification algorithm can be found in the Appendix, Section A.4.

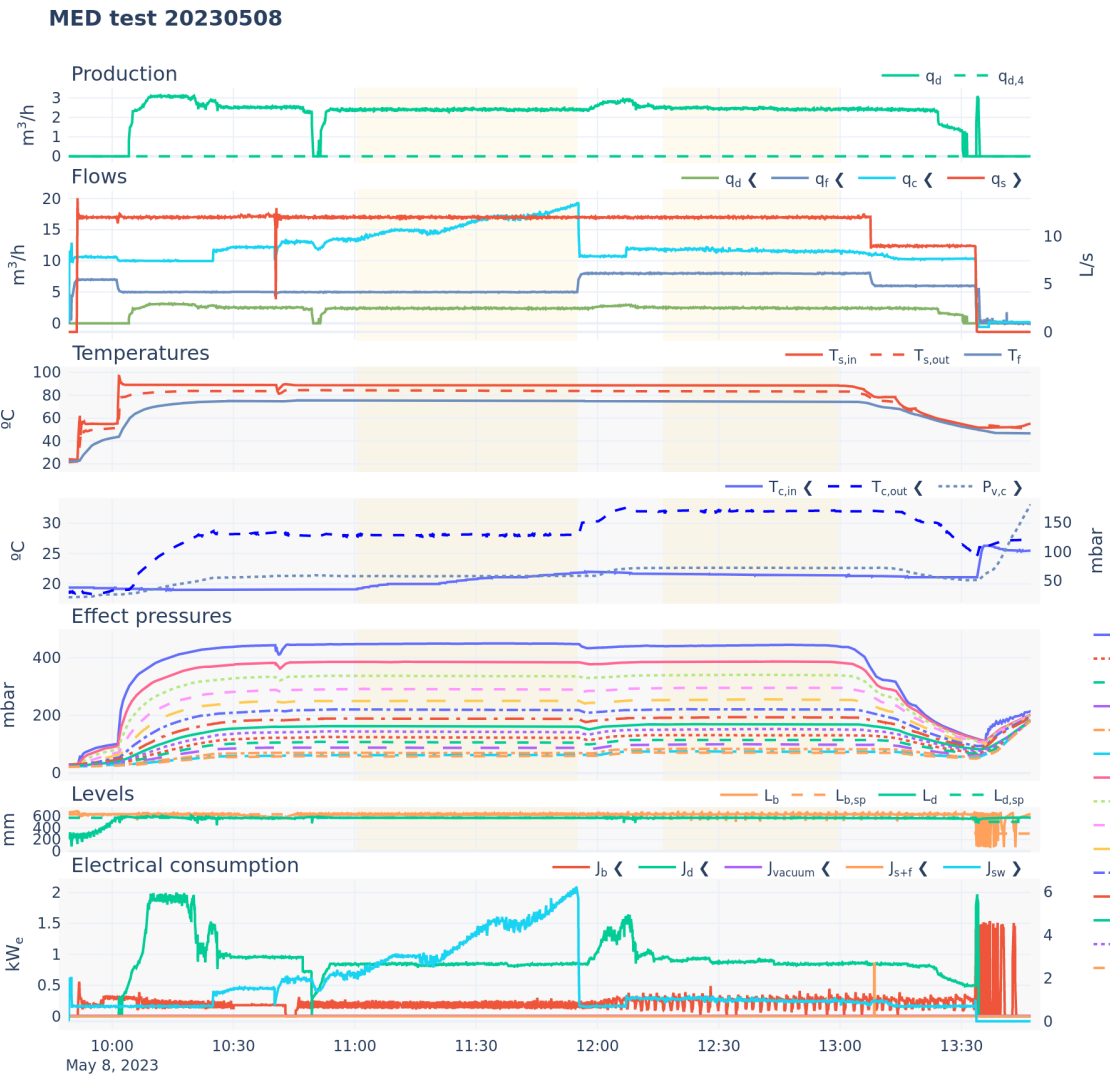


Figure 13.8: Test results. Several days available in interactive version



flow rate. For point 1, the inlet condenser temperature ($T_{c,in}$) is $24.5\text{ }^\circ\text{C}$, requiring a cooling water flow rate of $17 \text{ m}^3/\text{h}$ ($J=8.0\pm0.2 \text{ kW}_e$), whereas for point 2, $T_{c,in}$ is $23\text{ }^\circ\text{C}$, requiring $13 \text{ m}^3/\text{h}$ ($J=8.1\pm0.2 \text{ kW}_e$). These differences result in a 0.3% variation in the second-law efficiency and $0.1 \text{ kWh}_e/\text{m}^3$ in the SEEC. In contrast, for points 3 and 4, the inlet condenser temperatures are similar enough (22.6 and $21.4\text{ }^\circ\text{C}$, respectively), making the differences in all performance metrics negligible ($J=8.1\pm0.2 \text{ kW}_e$ for both points).

Thus, it can be stated that the proposed methodology provides reproducible results and that the quality of stable operation and the ability to correctly identify it are of greater importance than the specific duration of the steady state.

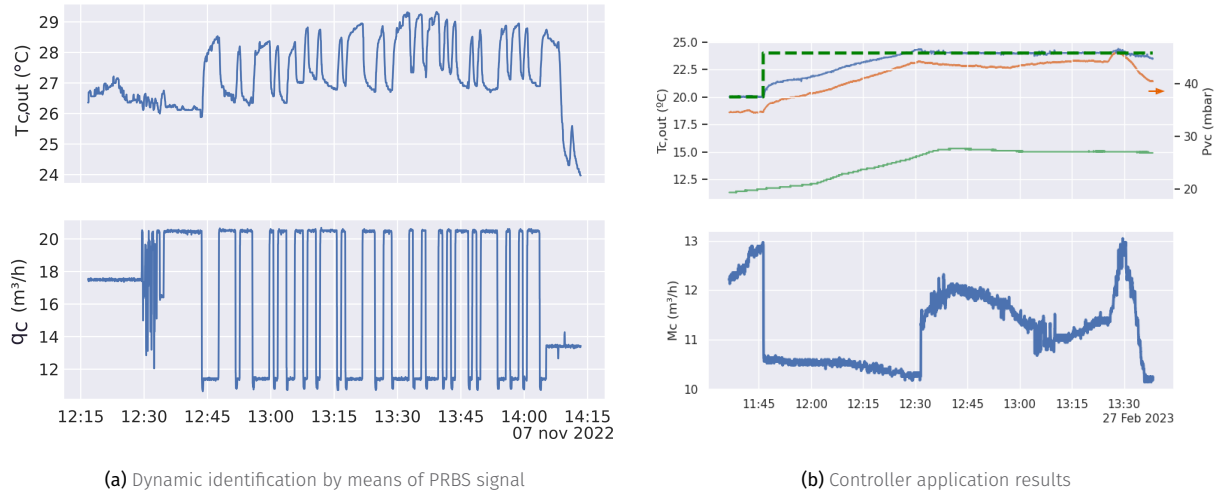


Figure 13.9: Condenser outlet temperature controller implementation. On (b) the perturbation (inlet temperature) is shown with a solid-green line, while the output (condenser outlet temperature) is shown with a solid-blue line. The reference is a thick dashed-green line.

Experimental evaluation at high Top Brine Temperatures

As mentioned in the introduction, in practice, the TBT in the MED system is typically limited to 70 °C or below to prevent scaling. This limitation can be assessed using the RSI, which requires knowledge of the water pH. To obtain this parameter, a laboratory analysis of the water composition was carried out for both the untreated seawater at the intake of the MED system and the pretreated water after the nanofiltration unit. The results of this analysis are presented in Figure 13.10 (center bar plot). Subsequently, the *PyEqulon* open-source library [35] was used to estimate the pH at various temperatures and concentration factors. For the latter, it was assumed that all ions scale uniformly, *i.e.*, that the concentration factor is identical for all species. Based on these values, the RSI was computed for different temperatures and concentrations.

For un-treated feedwater (Figure 13.10 - left) the risk of precipitation is present at almost any temperature due to its composition¹². A nanofiltration pretreatment¹³ is used to selectively remove the divalent ions while leaving relatively unaffected the monovalent ones, *i.e.* NaCl. After pretreatment, severe scaling –RSI values below 4— can only be observed above 80°C and ≈ 100 g/kg as shown in Figure 13.10 – right.

[35]: Marcellos et al. (2021), *PyEqulon*

12: Figure 13.10 – seawater in center bar plot

13: Figure 13.10 – pretreated water in center bar plot

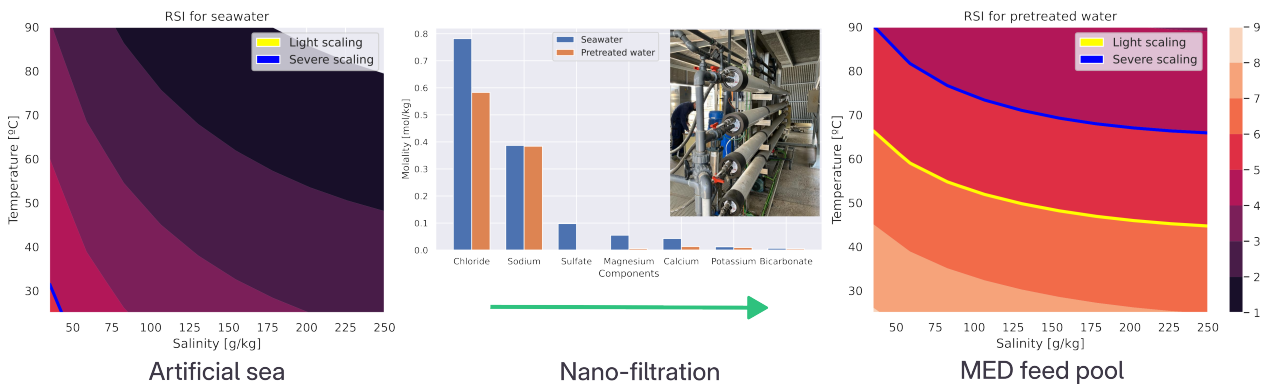


Figure 13.10: RSI values as a function of temperature and concentration before (left) and after (right) pretreatment using nanofiltration.

Using a physical model of the plant¹⁴, a better insight into the inner working of

14: A detailed description of the model can be found in the Appendix, Chapter B (MED First-Principles Model)

Table 13.3: Measured variables and performance metrics for some operation points of the experimental campaign. The values are expressed as mean \pm standard deviation with a coverage factor of 2 (95% confidence interval). D is the duration of the steady state period.

	Test date (UTC)	D (min)	Performance metrics						
			GOR (-)	STEC ($\text{KW}_{th}/\text{m}^3$)	SEEC (KW_e/m^3)	RR (-)	RI (-)	η_{II} (%)	SEXC ($\text{kWh}_{ex}/\text{m}^3$)
1	20230331 12:15	16	11 \pm 1	60 \pm 6	3.9 \pm 0.2	29 \pm 1	0.35 \pm 0.02	8.0 \pm 0.6	10.9 \pm 0.8
2	20230418 12:22	76	11 \pm 1	59 \pm 6	4.0 \pm 0.2	29 \pm 2	0.35 \pm 0.02	7.7 \pm 0.6	11.3 \pm 0.9
3	20230329 13:10	24	10.1 \pm 0.7	66 \pm 5	3.9 \pm 0.2	30 \pm 2	0.35 \pm 0.02	6.9 \pm 0.4	12.7 \pm 0.8
4	20230414 12:51	27	10.2 \pm 0.7	65 \pm 5	3.9 \pm 0.2	30 \pm 2	0.36 \pm 0.02	6.8 \pm 0.4	12.8 \pm 0.8
5	20230511 11:23	32	8.1 \pm 0.4	81 \pm 4	3.2 \pm 0.2	44 \pm 2	0.52 \pm 0.02	4.6 \pm 0.3	17.8 \pm 0.9
6	20230414 11:49	18	11 \pm 1	59 \pm 5	3.8 \pm 0.2	47 \pm 3	0.56 \pm 0.03	7.2 \pm 0.5	11.9 \pm 0.9
7	20230508 11:00	54	7.0 \pm 0.4	93 \pm 6	3.7 \pm 0.2	48 \pm 3	0.57 \pm 0.03	3.9 \pm 0.3	21 \pm 1

Measured variables											
	$T_{s,in}$ ($^{\circ}\text{C}$)	$T_{c,out}$ ($^{\circ}\text{C}$)	q_s (L s^{-1})	q_f ($\text{m}^3 \text{ h}^{-1}$)	q_d ($\text{m}^3 \text{ h}^{-1}$)	$T_{s,out}$ ($^{\circ}\text{C}$)	$T_{c,in}$ ($^{\circ}\text{C}$)	w_f (mS cm^{-1})	w_d ($\mu\text{S cm}^{-1}$)	q_c ($\text{m}^3 \text{ h}^{-1}$)	J (kW)
1	64.0 \pm 0.8	28.1 \pm 0.6	12.0 \pm 0.2	8.0 \pm 0.1	2.4 \pm 0.1	61.1 \pm 0.7	24.5 \pm 0.7	67.4 \pm 0.7	8.00 \pm 0.08	17 \pm 1	(8.0 \pm 0.2) $\times 10^3$
2	64.0 \pm 0.7	28.0 \pm 0.6	12.0 \pm 0.3	8.0 \pm 0.1	2.3 \pm 0.1	61.2 \pm 0.7	23 \pm 1	67.4 \pm 0.7	8.00 \pm 0.08	13 \pm 2	(8.1 \pm 0.2) $\times 10^3$
3	68.0 \pm 0.7	28.0 \pm 0.6	12.0 \pm 0.2	8.0 \pm 0.1	2.4 \pm 0.1	64.8 \pm 0.7	22.6 \pm 0.6	67.4 \pm 0.7	8.00 \pm 0.08	13.8 \pm 0.8	(8.1 \pm 0.2) $\times 10^3$
4	68.0 \pm 0.7	27.9 \pm 0.8	12.0 \pm 0.3	8.0 \pm 0.1	2.4 \pm 0.1	64.8 \pm 0.6	21.4 \pm 0.8	67.4 \pm 0.7	8.00 \pm 0.08	10.9 \pm 0.9	(8.1 \pm 0.2) $\times 10^3$
5	88.9 \pm 0.9	29 \pm 1	12.0 \pm 0.3	7.0 \pm 0.1	3.1 \pm 0.1	83.8 \pm 0.9	22 \pm 1	64.7 \pm 0.6	8.00 \pm 0.08	20.1 \pm 0.3	(7.9 \pm 0.3) $\times 10^3$
6	68.0 \pm 0.7	28.0 \pm 0.5	12.0 \pm 0.3	5.0 \pm 0.1	2.4 \pm 0.1	65.2 \pm 0.7	20.8 \pm 0.6	67.4 \pm 0.7	8.00 \pm 0.08	10.1 \pm 0.4	(7.9 \pm 0.3) $\times 10^3$
7	89.0 \pm 0.7	28.1 \pm 0.6	12.0 \pm 0.3	5.0 \pm 0.1	2.4 \pm 0.1	84.4 \pm 0.8	21 \pm 2	64.5 \pm 0.7	8.00 \pm 0.08	16 \pm 3	(7.8 \pm 0.3) $\times 10^3$

the plant can be obtained. The model is based on the energy and mass balances of the system, and it is used to estimate different outputs at the effect level, such as the temperature and pressure of the vapor, the distillate production, and the brine concentration.

Scaling assessment during high Top Brine Temperature operation

Using the aforementioned physical model of the plant, it is possible to analyze the temperature and concentration evolution and visualize them as shown in Figure 13.11 (a).

The figure shows the temperature and concentration evolution at each effect in the MED plant for several operation points: low-temperature operation points (4: 68–8, 6: 68–5) and high-temperature operation points (5: 89–8, 7: 89–5). According to the RSI, the high-temperature operation points (5, 7) enter the light scaling risk zone for the first seven effects —above the yellow line in Figure 13.11 (a)— while the low-temperature operation points (4, 6) remain within the stable water zone for all effects.

To assess whether scaling occurred during high-temperature operation, control tests were conducted both before the high-temperature tests and repeated after approximately 30 hours of high TBT operation. In Table 13.3, the same operation points used to validate reproducibility¹⁵, i.e., 1–2 and 3–4, can be used to draw conclusions. No significant differences can be observed for any of the performance indicators, with the values remaining consistent between tests. This suggests that the system operated efficiently, without significant fouling or scaling.

This is further confirmed by applying the physical model of the plant to estimate the heat transfer coefficients. Figure 13.11 (b) illustrates the comparison of heat transfer coefficients before and after the high-temperature campaign for both control tests. The results show only minor variations between the pre- and post-high-temperature operation. With measurements across all effects showing no systematic degradation trend. The consistency of the coefficients indicates that no measurable scaling occurred during the high TBT operation period.

15: Section 13.5 (Reproducibility and the effect of the steady state duration)

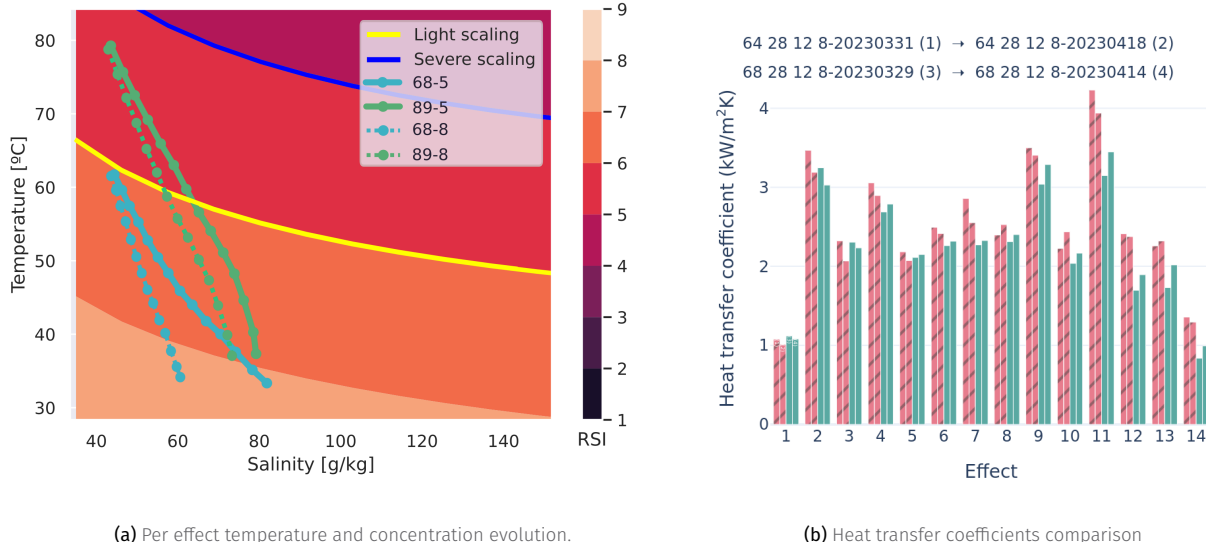


Figure 13.11: Scaling assessment during high TBT operation

Performance analysis at high Top Brine Temperature

In Table 13.3 operation points 4–5 and 6–7 compare low and high TBT operation. Two of them (4 and 6) receive heat at 68°C, while they differ in the feedwater flow rate (q_f), one (4) with a higher value (8 m³/h) and the other (6) at a lower one (5 m³/h). The other two operation points receive heat at 89°C and similar feedwater flow rate¹⁶. The first two operation points result in an approximate TBT of 61.5°C while the last two operation points have an approximate TBT of 79.2°C. This operation points selection is made to compare the performance of the plant at low and high TBT operation with otherwise equivalent conditions.

16: Equal between 4 and 5, slightly different but comparable between 6 and 7

The first key observation is that, contrary to the statement in the introduction, the plant's performance does not improve with higher heat source temperatures; rather, it deteriorates significantly. The GOR decreases by approximately 20% and 36% for the low (4–5) and high (6–7) q_f scenarios, respectively. The results are even more pronounced in terms of second-law efficiency, with reductions of 32% and 46%, respectively. This decline occurs because higher-quality exergy is being destroyed in the process. More energy —of superior quality— is being consumed to produce distillate less efficiently.

This behavior is expected and can be attributed to the fact that the increase in heat source temperature is not utilized to incorporate additional effects, which would be the driver enhancing system efficiency.

On the other hand, the concentration achieved does increase significantly for the high q_f scenario, with a 47% increase in the recovery ratio. This is not the case for the low q_f scenario, where the recovery ratio is similar to the low temperature operation point. A possible explanation is presented hereinafter.

A per effect comparison can also be made in terms of energy contribution for vapor generation. This is shown in Figure 13.12 in terms of energy contributions (a) and vapor generation mechanisms (b) for the low q_f (=5 m³/h) operation points. In Figure 13.12 (a) it can be seen how, in the first effect, the only contributor to vapor generation is the external heat source (red bar). For the following effects, most of the energy comes from the previous effect vapor (purple bar)

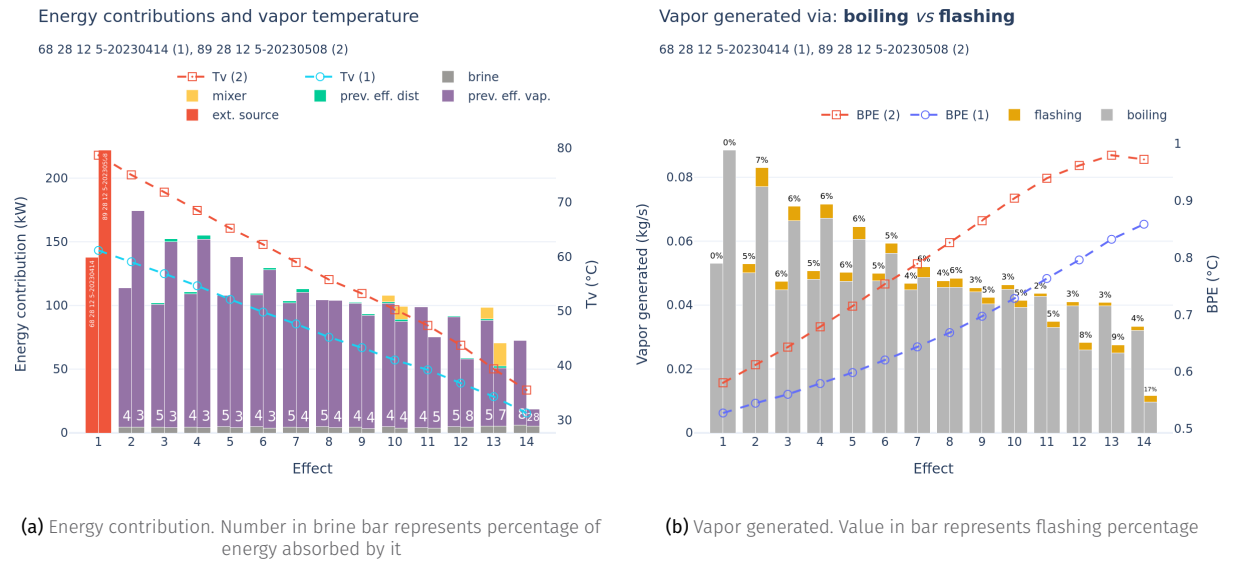


Figure 13.12: Per effect comparison between low and high TBT operation points

17: This is achieved by sacrificing the previous effects distillate (green bar) in some other effects

with some contribution at specific effects —10, 13— from distillate coming from previous effects (yellow bar, *mixer*)¹⁷. The only negative contributor (it absorbs heat instead of releasing it) is the brine (gray bar), which is warmed up. Also in the plot is shown the vapor temperature evolution.

Figure 13.12 (b) shows the vapor generation per effect deaggregated in terms of the different mechanisms: boiling (gray bars) and flashing (yellow bars). Additionally, the Boiling Point Elevation (BPE) of the brine is shown as dashed lines. In this plot, it can be seen how in general boiling is the main driver for vapor generation.

In the first effect a stark difference between low and high operation can be seen, with almost double the power released by the external source, producing almost double the vapor —Figure 13.12 (b). However this difference is not maintained in the following effects, but an opposite trend is observed. Effect 8 is the crossing point and from there on the low temperature operation point produces more vapor. Another interesting comparison is the *mixer* energy contribution, the higher temperature of the distillate produced in the first effects becomes a significant contributor in the later effects, with a greater impact compared to the low temperature operation. Thus, distillate distribution is more effective when total plant temperature differences are higher.

A possible explanation as to why vapor generation seems limited and thus the achieved concentration, can be that the BPE of the brine —Figure 13.12 (b)— is a function of temperature and concentration, increasing with the latter. This means that the temperature difference between the brine and the vapor is reduced, which in turn reduces the boiling driving force. In the visualized case, the final BPE value for the low-temperature operation is reached by effect 9 of the high temperature one. In an MED plant, the vapor generated in the previous effect is the driving force for the next effect —Figure 13.12 (a). Low vapor production on one effect means a diminished force for heat transfer in the next one, which in turn reduces the vapor production on that effect. It is an exponential decay process. That is why despite the larger energy availability

in the first effects, the better balanced effects of the low temperature operation turns out to ultimately produce similar levels of separation [204].

Also in this figure, it can be seen than flashing takes a more relevant role in vapor generation in the latter effects of the high temperature alternative, since it is not affected by BPE (8, 9 and 17% of the total vapor generated in effects 12, 13 and 14, respectively). This indicates that maybe flashing is a good alternative to increase the vapor production in the latter stages of a thermal brine concentrator plant.

[204]: Lienhard V (2019), "Energy Savings in Desalination Technologies"

Remark 13.5.1 A MED-MSF hybrid could be a good alternative to increase the brine concentration in the last effects, where the vapor production is limited by the BPE. Another option worth exploring is variable geometry effects, in order to increase temperature differences and mantain vapor production at higher concentrations.

TL;DR

This chapter describes a novel method to develop an operational strategy that enables the seamless integration of a solar-driven MED system in an autonomous and optimal manner. The strategy includes decisions on when to start or stop each subsystem and how to regulate them throughout operation. The method is based on a hierarchical control approach consisting of three layers, where the upper operation layer solves a Mixed Integer Non-Linear Programming (MINLP) economic problem.

Results from a week-long system simulation are compared against two alternative strategies: a baseline heuristic rule-based operation and an operation-only optimization (solving a Non-Linear Programming (NLP) problem). The results show that the proposed method can significantly improve system performance by 32 % and 21 %, respectively. This improvement is achieved by fully exploiting the flexibility offered by the thermal storage and the solar resource, maximizing temperature differences in a manner akin to a waste-heat-optimized process.

14.1 Introduction

Most of the literature on automatic control of MED processes focuses on low-level control strategies. These are typically based on simple control loops, using either PID controllers [29] or Model Predictive Control (MPC) [30], with the main objective of maintaining desired temperature setpoints —primarily the heat source inlet temperature. A number of works have also addressed optimization of the MED process in isolation. For example, Carballo et al. [31] optimized the steady-state MED process using genetic algorithms under different criteria (e.g., maximum production, highest performance ratio, minimum energy consumption, best second-law efficiency, and combinations thereof). However, their approach treated the inlet cooling/seawater flow as a decision variable, which is an uncontrolled input and thus invalidates the results. The condenser outlet temperature, which can be regulated through the cooling water flow, would have been the appropriate decision variable. Similarly, Chorak et al. [32] experimentally characterized the pilot plant described in Chapter 11 under a wide range of operating conditions. Their results highlighted how distillate production and thermal performance are highly sensitive to the chosen operating point: feedwater flow rate, condenser operating temperature, and heat source temperature have strong impacts, whereas the system is less sensitive to variations in heat source flow rate, owing to its sensible heat transfer nature.

There are inherent limitations in optimizing the MED process in isolation, without considering the complete system. As explained in Chapter 13, an MED plant (or any thermal separator) requires two forms of energy: heat and electricity. Electricity costs can be directly assigned using, for instance, market prices. For fossil-fuel-based thermal energy, it is straightforward to relate operating conditions to fuel consumption and thus cost. However, when thermal energy is provided by a variable source such as solar and/or waste heat, the situation becomes more complex. In the case of solar, its availability is intermittent, and both the operation and efficiency of the solar field depend strongly on how the MED load is managed. The two subsystems are intrinsically coupled. This complexity is further amplified by the presence of thermal storage, which

14.1	Introduction	161
14.2	Problem description	163
14.2.1	Implementation discussion	165
14.3	Proposed strategy	166
14.4	Operation plan layer description	167
14.4.1	Candidate problems generation	167
14.4.2	Update times generation	168
14.5	Operation optimization layer description	170
14.6	Alternative strategies. Heuristic approach	171
14.7	Optimization results	172
14.7.1	Candidate problems generation	172
14.7.2	Choosing an algorithm	172
14.7.3	Choosing a candidate problem	173
14.7.4	Simulation results	173
14.7.5	Operation and performance comparison between strategies	175

[29]: Roca et al. (2008), “Solar Field Control for Desalination Plants”

[30]: González et al. (2014), “Economic Optimal Control Applied to a Solar Seawater Desalination Plant”

[31]: Carballo et al. (2018), “Optimal Operating Conditions Analysis for a Multi-Effect Distillation Plant According to Energetic and Exergetic Criteria.”

[32]: Chorak et al. (2017), “Experimental Characterization of a Multi-Effect Distillation System Coupled to a Flat Plate Solar Collector Field”

enables time-shifting of solar energy use and adds another layer of operational decisions.

In short, the true cost of thermal energy in a solar-driven system is difficult to assess, and achieving optimal MED operation requires optimizing the entire coupled system.

Several studies have addressed this broader problem at varying levels of complexity. For instance, González *et al.* [30] proposed a receding-horizon optimal control strategy with economic objectives —maximizing water production while minimizing electricity costs. Their work relied on a simplified linear model, optimizing only the solar field flow while keeping the MED inlet temperature constant. Nevertheless, the most advanced optimization efforts reported in the literature have focused not on MED, but on Membrane Distillation (MD).

[205]: Porrazzo *et al.* (2013), “A Neural Network-Based Optimizing Control System for a Seawater-Desalination Solar-Powered Membrane Distillation Unit”

In Porrazzo *et al.* [205], the authors developed a neural network-based optimizing control system for a solar-powered seawater MD unit. Because solar energy is intermittent and variable, efficient operation requires advanced control strategies. A neural network model, trained on experimental data, was used to capture the relationships between solar radiation, feed flow rate, inlet water temperature, and distillate production. This model was then applied to identify optimal feed flow conditions that maximize distillate output under varying conditions. The proposed feedforward control strategy was validated through simulations and tested in a pilot plant, demonstrating improved efficiency.

[33]: Gil *et al.* (2019), “Hybrid NMPC Applied to a Solar-powered Membrane Distillation System”

Gil *et al.* [33] extended this approach by recognizing that a solar MD plant does not operate as a single continuous process but transitions through distinct operating modes (e.g., heating the solar field, charging the storage tank, or running the MD module) dictated by solar and thermal conditions. In their formulation, the switching logic is predefined: the solar field is started once irradiance exceeds a threshold, the tank is then charged, and the MD module only begins operation once its inlet temperature reaches a set value. In other words, the decision of when to start each subsystem is hardwired into the control rules. As a result, these operating modes are treated as part of the environment, not as free decision variables —representing a limitation of the work. To manage the predefined mode transitions, the authors modeled the facility as a hybrid system and developed a Hybrid Nonlinear Model Predictive Control (H-PNMPC) scheme. This framework optimizes flow rates while anticipating and coordinating the fixed transitions between modes. In doing so, it generalizes the earlier feedforward optimization into a predictive control framework that incorporates environmental constraints, enabling more robust operation. Simulation results showed that the H-PNMPC increased operating hours and slightly improved water production compared to rule-based control. Nevertheless, the choice of optimization parameters —operation time, operating temperature, and distillate production— together with the omission of electrical consumption, led to potentially inefficient outcomes. For instance, the system achieved an 11.31 % increase in operating time for only a 1.23 % gain in production, likely at the expense of higher auxiliary energy consumption.

From this analysis, it can be seen that existing literature on the optimization of MED plants presents significant limitations. Firstly, many studies on the optimization of MED plants either consider too few variables, rely on uncontrollable variables, or use overly simplified models. From the process analysis in Chapter 13, it was concluded that the key controllable variables that fully define the operating conditions of an MED plant are: the heat source flow rate ($q_{med,s}$), the heat source inlet temperature ($T_{med,s,in}$), the feedwater flow rate ($q_{med,f}$), and the condenser outlet temperature ($T_{med,c,out}$). These should therefore serve as the decision variables when optimizing plant operation.

Secondly, the objective in optimizing desalination processes is to maximize distillate production while minimizing the resources required. In solar-driven

processes, the solar resource itself has no direct cost. However, its use requires electricity to recirculate the working fluid through the solar field. Since the solar field essentially acts as a solar-to-heat converter, the only relevant consumption to be minimized in the optimization is the electricity demand of all system components.

A further consideration, often overlooked in the literature, concerns decisions on when to start and stop the operation of different subsystems in the presence of thermal storage. Thermal storage allows heat to be used independently of solar availability—with certain limits. Depending on its size, this makes the timing of subsystem operation—heat generation and thermal load¹—crucial for maximizing system performance both on the current day and over subsequent days. Relying on a fixed irradiance threshold to trigger the system startup sequence is therefore suboptimal, as it ignores the state of thermal storage and forecasts of solar availability that could enable longer or shorter operation of the heat source, or earlier or later startup and shutdown of the thermal load.

In this work, the operation of a solar-driven MED system is optimized with these aspects in mind. This is the first study to include explicit decisions on when to start and stop each subsystem, while also accounting for a two-day prediction horizon. This allows the optimization to consider not only immediate performance, but also the impact of present decisions on future production. The method relies on an experimentally validated system model that incorporates the electrical consumption of each component, combined with the most comprehensive data-driven MED model currently available in the literature².

This chapter is structured as follows: first, the optimization problem is described in Section 14.2, then the proposed optimization strategy to solve it is presented in Section 14.3. The strategy consists on two fundamental blocks which are detailed in Section 14.4 (Operation plan layer description) and Section 14.5 (Operation optimization layer description). Finally, the results of the proposed strategy are presented in Section 14.7.4 and its comparison against alternative strategies.

1: i.e. solar field and MED plant, respectively

2: Described in Chapter 12 (Hybrid modelling of a solar driven MED system)

14.2 Problem description

The behavior of the SolarMED process is controlled by acting on two components, a discrete (operation state) and a continuous one (process variables).

The goal is to design an operational strategy that enables the seamless integration of both subsystems in an autonomous and optimal manner, including decisions on when to start or stop each subsystem and how to regulate them during operation. Therefore, considering the whole system as a Mixed Integer Non-Linear Programming (MINLP) optimization problem³ that aims to maximize the water production while minimizing the (electrical) consumption of the system. Decisions on when to operate the system are weighted considering an optimization horizon, approximating the operation strategy of the system to the optimum. The problem is defined in Problem 14.1:

Problem 14.1: SolarMED

$$\min_{\mathbf{x}, \mathbf{e}; \theta} J = f(\mathbf{x}, \mathbf{e}; \theta) = \sum_{i=1}^{n_{steps}} (J_{e,i} - J_{w,i})$$

3: See Section 3.2.2 (MINLP problems)

In general q represents flow rates while T is used for temperatures. Figure 11.1 can be consulted for subscript reference.

$\forall i = 1 \dots n_{steps}$ is a notation to indicate that a condition must be held at every step i in the optimization horizon (n_{steps}).
Bold variables represent vectors.

with:

```
for i = 1 ... nsteps :
    Jw,i = qd,i · Pw,i if valid operation else 0
    Je,i = Ce,i · Pe,i
    qd,i, Ce,i, valid operation = solarmed model(xc,i, xp,i, ...)
```

► Decision variables

$$\mathbf{x} = [\text{med}_{\text{mode}}, \text{sfts}_{\text{mode}}, q_{\text{sf}}, q_{\text{ts,src}}, q_{\text{med,s}}, q_{\text{med,f}}, T_{\text{med,s,in}}, T_{\text{med,c,out}}]$$

$$\text{where } \mathbf{x}_{n_x \times \sum n_{\text{updates},x_i}} = [x_{1,i}, \dots, x_{1,n_{\text{updates},x_1}}, \dots, x_{n_x,n_{\text{updates},x_{n_x}}}]$$

► Environment variables

$$\mathbf{e} = [\mathbf{I}, T_{\text{amb}}, T_{\text{med,c,in}}, \mathbf{P}_e, \mathbf{P}_w]$$

$$\text{where } \mathbf{e} = [e_{1,1}, \dots, e_{1,n_{\text{steps}}}, \dots, e_{n_e,n_{\text{steps}}}]$$

subject to:

► Box-bounds

- $\text{med}_{\text{mode}} \in [0, 1] \subset \mathbb{Z}$
- $\text{sfts}_{\text{mode}} \in [0, 1] \subset \mathbb{Z}$
- $q_{\text{sf}} \in [q_{\text{sf}}, \overline{q_{\text{sf}}}] \subset \mathbb{R}$
- $q_{\text{ts,src}} \in [\underline{q}_{\text{ts,src}}, \overline{q}_{\text{ts,src}}] \subset \mathbb{R}$
- $q_{\text{med,s}} \in [\underline{q}_{\text{med,s}}, \overline{q}_{\text{med,s}}] \subset \mathbb{R}$
- $q_{\text{med,f}} \in [\underline{q}_{\text{med,f}}, \overline{q}_{\text{med,f}}] \subset \mathbb{R}$
- $T_{\text{med,s,in}} \in [\underline{T}_{\text{med,s,in}}, \overline{T}_{\text{med,s,in}}] \subset \mathbb{R}$
- $T_{\text{med,c,out}} \in [\underline{T}_{\text{med,c,out}}, \overline{T}_{\text{med,c,out}}] \subset \mathbb{R}$

valid operation conditions, $\forall i = 1 \dots n_{\text{steps}}$:

$$\blacktriangleright T_{\text{sf,out}} \leq \overline{T}_{\text{sf,out}}$$

Where the objective is to minimize the cumulative cost of operation (J). Fresh water ($q_{\text{med,d}}$) sold (J_w) at price P_w is the negative term while electrical consumptions (C_e) at price P_e make up the positive cost term (J_e). The benefit (B) of operation is simply the inverse of the cost of operation.

The environment is represented by the vector \mathbf{e} , which includes the global solar irradiance (\mathbf{I}), ambient temperature (T_{amb}), and the prices of water (\mathbf{P}_w) and electricity (\mathbf{P}_e).

The decision vector \mathbf{x} is composed of the decision variables for both the discrete and the continuous space. Two decision variables are defined to manipulate the discrete state of each subsystem defined in Section 12.3: med_{mode} and $\text{sfts}_{\text{mode}}$. These binary ($\subset \mathbb{Z}$) variables establish whether the particular subsystem is active ($x_i = 1$) or inactive ($x_i = 0$). This is directly related to the operation state of the particular subsystem⁴ and accounted for in the models by the integrated finite-state machines as explained in Section 12.3. For the continuous space, the decision variables include the ones that define the operating conditions (i.e. operation point) of the MED system, and the two recirculation flow rates that determine the conditions of the heat source ($q_{\text{sf}}, q_{\text{ts,src}}$).

4: As defined in Tables 12.5 and 12.6.
Once the values for these decision variables are provided, the low-level control layer is in charge of safely transitioning between operation states e.g.:
 $\text{med}_{\text{mode}} : 0 \rightarrow 1$
 $\text{med state: off} \rightarrow \text{generating vacuum} \rightarrow \text{starting-up} \rightarrow \text{active}$

14.2.1 Implementation discussion

On the constraint handling

The reader might notice that no constraints are explicitly defined in the problem definition. This is because the constraints are implicitly defined in the model equations, which are used to evaluate the objective function. This design decision is motivated to avoid the need for a constraint-handling capable optimization algorithm, limiting the choice for an already complex MINLP problem⁵. Specifically, two aspects demand further consideration:

1. The decision value for the MED outlet condenser temperature ($T_{med,c,out}$) is not a direct input to the system, but rather a setpoint to be followed by a low-level control loop by manipulating the cooling water flow rate ($q_{med,c}$). This input might saturate and thus not be able to achieve the desired setpoint. In this case, a new value for the decision variable is computed, which is the minimum value that can be achieved (with $\bar{q}_{med,c}$). In this case, the value used in the SolarMED and the output from the optimization to the low-level control layer would be the validated value for $T_{med,c,out}$. No additional actions are needed.
2. In the solar field, in order to not constantly interrupt the evaluation due to the solar field temperature going above $\bar{T}_{sf,out}$ (120 °C), the model saturates this temperature when going above and sets a flag. The limitation of this approach is that when there is low energy demand from the load, and likely because it favors energy transfer in the heat exchanger⁶, it has been observed that the optimizer tends to minimize the solar field flow, and systematically lets the solar field outlet temperature reach the limit. To avoid this situation, the positive term of the objective function is nullified in iterations where the constraint is not met.

Here, in order to ensure *valid operation* the fitness function is manipulated to de-incentivize decision variable values that lead to unfeasible operation.

⁵: See Section 3.2.3 (A discussion on constraint handling) for a more detailed discussion on the topic

⁶: greater temperature difference in primary side instead of greater mass flow rate with its associated increase in pumping power

On the prediction horizon

The problem is designed as an optimization problem with a shrinking horizon. The horizon size should be large enough so that decisions on how to operate the system are made with perspective, taking into account how they will affect the system in the future, but not so large that current decisions have no impact on the far future, and making the problem dimensionality become unmanageable.

For this case study, this parameter should be chosen based on the hours of capacity of the thermal storage to operate the MED system.

The thermal storage capacity allows the system to operate with no supply from the solar field for several hours. This means that depending on the charge state of the thermal storage, the system could start operation independently of the irradiance conditions, or operate at different levels of temperature. Considering this the optimization horizon, in time units, chosen was 36 hours. This means that if the optimization is evaluated at 5:00 on day 1, the fitness function is evaluated until 19:00 of day 2 i.e. including the end of operation for day 2.

Reminder: Shrinking horizon optimization

An optimization where the horizon end is fixed, and as time progresses, the start of the horizon moves forward.⁹

⁹: See Section 3.2 (Optimization)

On solving the optimization problem

Solving the optimization problem for this Mixed Integer Non-Linear Programming (MINLP) formulation presents significant challenges due to the combinatorial nature of the integer decision variables [206]. As shown in Figure 14.1, each combination of integer decisions, such as the operational modes of the separation

[206]: Grossmann (2021), Advanced Optimization for Process Systems Engineering

7: This will be referred to as: operation plan

8: For example:
 $n_{\text{updates},xi} = 6 \rightarrow n_{\text{problems}} = 64$,
 $n_{\text{updates},xi} = 24 \rightarrow n_{\text{problems}} = 16\,777\,216$

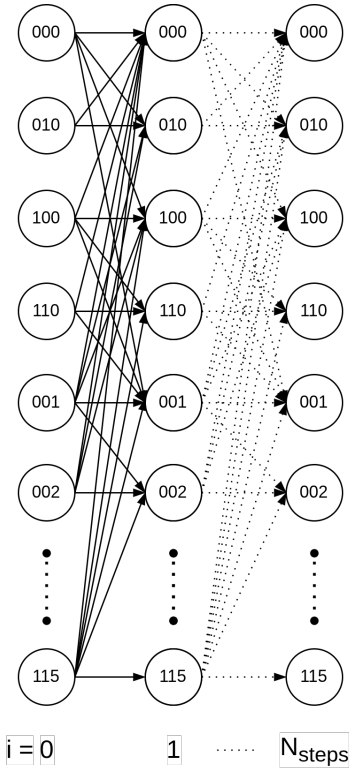


Figure 14.1: Decision tree resulting from the combinatorial nature of the integer part of the optimization problem. Text in nodes represents system states.

subsystem (med_{mode}) and the solar field thermal storage subsystem ($\text{sfts}_{\text{mode}}$), leads to a different system trajectory along the prediction horizon⁷.

The number of possible operation trajectories increases exponentially with both the number of integer variables (n_{xi}) and the number of decision updates ($n_{\text{updates},xi}$), following the expression:

$$n_{\text{problems}} = n_{xi}^{n_{\text{updates},xi}}. \quad (14.1)$$

This exponential growth makes the search space extremely large and complex⁸.

An important design consideration when solving the optimization problem is whether the sequence of integer decisions (*i.e.*, operational mode transitions over time) is predefined or whether the optimization algorithm is allowed to explore the decision tree freely and determine the optimal sequence. The latter case requires more computational effort but allows for potentially better-performing solutions by dynamically adjusting to system conditions.

On the decision variables update frequency

Apart from the integer decision variables, if a fixed update frequency is chosen for all continuous decision variables, the size of the decision vector can grow rapidly for long horizons, often with diminishing returns. To address this, a new design parameter is introduced: the number of updates ($n_{\text{updates},xi}$) assigned to each decision variable in the optimization problem.

Accordingly, the decision vector is constructed by repeating each decision variable as many times as the number of updates defined for it:

$$X_{n_x \times \sum n_{\text{updates},xi}} = [x_{1,1}, \dots, x_{1,n_{\text{updates},x_1}}, \dots, x_{n_x,n_{\text{updates},x_{n_x}}}]$$

The number of updates for each decision variable ($n_{\text{updates},xi} \in [1, n_{\text{steps}}]$) can be selected independently. More frequent updates are assigned to variables governing faster dynamics (*e.g.*, q_{sf} , $q_{ts,src}$). These updates are evenly distributed throughout the *active* period of the corresponding subsystem within the horizon. This design choice is important, since otherwise the limited number of updates could be wasted on inactive periods (*e.g.*, between the end of operation on day 1 and the start on day 2).

This approach also implies that the continuous portion of the decision vector can only be defined after the integer component is established, since the latter determines the subsystem activity periods. Once timestamps are assigned to each decision variable, their values are resampled to match the desired temporal resolution of the optimization problem. This resampling is performed by forward-filling the latest known value until the next update time [207].

14.3 Proposed optimization strategy

A hierarchical control approach (see Figure 14.2) was chosen consisting of three layers: operation plan, operation optimization, and control. This scheme was chosen for two main reasons. On the one hand, the time scales of the different aspects of the operation of the system (operation mode changes, process variables setpoint changes, regulatory control, respectively) can differ substantially. Secondly, it allows to abstract process complexity from the more computationally demanding upper layers by allocating it into the downstream layers. The

operation plan layer makes decisions for the *operation modes*, the operation optimization layer sets the setpoints given to the continuous *process variables* that are to be followed by the low-level regulatory control layer.

Both operation plan and operation optimization layers share the same underlying problem structure, the difference being that the operation plan layer evaluates a predefined library of n_{problems} combinations of the binary decision variables med_{mode} and $\text{sfts}_{\text{mode}}$ twice; once to decide the operation start, and another to end operation. The operation optimization layer periodically solves a single NLP problem with the selected values for these two variables fixed. They are further described in the following sections.

14.4 Operation plan layer description

This layer determines the integer decision variables of the MINLP problem, namely, the sequence of operation modes producing an operation plan. To make the problem computationally tractable, only a limited number of combinations, n_{problems} ⁹, are evaluated. This transforms the mixed-integer problem into a simpler form by moving the integer variables from the decision to the environment space. In effect, the original MINLP is decomposed into a library of NLP problems⁹ that are individually evaluated, n Non-Linear Programming problems (nNLP problems).

To improve robustness, the layer can be evaluated multiple times (n_{evals}) under different scenarios —typically reflecting variations in forecasted environmental conditions. The final operation plan is selected as the best compromise across these scenarios using a composite evaluation metric.

This composite score considers three aspects in the performance across different scenarios. Each alternative is assessed according to: its average performance, its consistency across scenarios, and its robustness in the worst-case situation. The average performance μ_i reflects the overall expected behavior of the alternative, while the standard deviation σ_i captures its sensitivity to scenario variability, penalizing options that exhibit large fluctuations in performance. Similarly, the worst-case performance W_i represents the most adverse outcome among all considered scenarios, ensuring that alternatives prone to extreme negative results are appropriately penalized. These three components are combined into a single composite score (S_i), where weighting factors control the influence of consistency and worst-case penalties relative to the mean performance. The alternative with the lowest composite score is selected as the most balanced and robust solution according to Equation 14.2.

$$S_i = \mu_i + w_{\text{std}} \sigma_i + w_{\text{wc}} W_i, \quad (14.2)$$

where w_{std} is the weight applied to the standard deviation penalty and w_{wc} is the weight applied to the worst-case penalty.

The time required to perform this layer's computation is denoted $\Delta t_{\text{eval,plan}}$.

14.4.1 Candidate problems generation

Given the available computational resources and the complexity of the objective function, it has been found feasible to evaluate in the order of $n_{\text{problems}} \sim 100$ candidate combinations. This constraint informs how many Degrees of Freedom (DoF) (i.e. number of updates available for the operation modes) can be defined by using Equation 14.1. The particular design choice for the number of updates

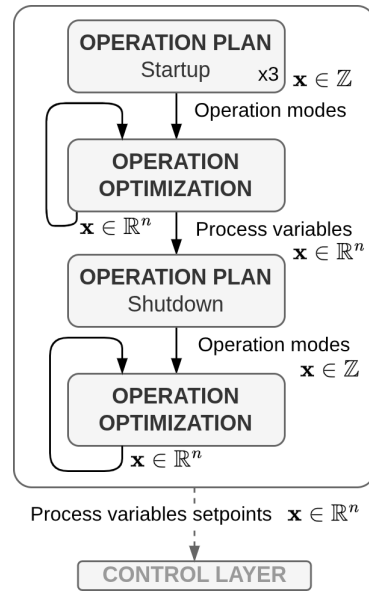


Figure 14.2: Proposed optimization strategy architecture

The number of updates available for each integer variable $n_{\text{updates},xi}$ will be interchangeably referred to as Degrees of Freedom (DoF).

9: MINLP → nNLP

10: Notice the total number does not match exactly Equation 14.1 since special cases are added like having inactive subsystems

Table 14.1: Operation plan layer. Degrees of freedom assignment for changes in the operation state for start-up (1) and shutdown (2) evaluations.

11: DoF=2 for start and stop in day 2

12: As with the continuous component of the decision vector, this is achieved by forward-filling the values until the next update time. This approach is also known as *Last Observation Carried Forward* [207]

per subsystem is shown in Table 14.1. In total, 101 distinct operation plans are generated for the start-up evaluation and 144 for the shutdown¹⁰.

Subsystem	Degrees of freedom				n_{problems}
	Day 1		Day 2		
	Start	Stop	Start	Stop	
Evaluation: Start-up (1)	sfts	3	3	1	1
	med	3	3	1	1
Evaluation: Shutdown (2)	sfts	-	3	2	2
	med	-	3	2	2
					144

In Table 14.1, it can be seen that the available DoF are assigned asymmetrically between the two days of the prediction horizon. More DoF (*i.e.* flexibility) are given to the actions closer in time to the evaluation. For example, the start and stop actions in day 1 for the start-up evaluation (1) have a more direct impact on the immediate operation of the system. Conversely, fewer DoF are allocated to day 2 actions, as these decisions are more speculative and have a less direct effect on the current operation. For the shutdown evaluation (2), no start actions are considered in day 1 since the system is already operational, and day 2 operation becomes more relevant when deciding when to stop operation in day 1, hence the allocation of more DoF to day 2 actions¹¹.

This allocation strategy balances the need for flexibility in near-term decisions with the computational constraints of evaluating a large number of operation plans.

14.4.2 Update times generation

Up to this stage, the operation plans generated consist merely of lists of ones and zeros for each subsystem, indicating whether the subsystem is active or inactive at each update. The next step is to assign these operation mode updates to specific time instants, which can then be resampled to match the desired sampling time of the optimization problem¹².

To maintain solutions close to the optimal one while keeping the number of decision variables manageable, updates are distributed throughout the prediction horizon at strategic time instants. Since the case study system is fundamentally solar-driven, its operation is highly dependent on irradiance availability, and thus changes in operation typically occur at the beginning and end of the solar day.

The temporal distribution of operation mode updates is shown in Figure 14.3, which depends on the number of available updates (DoF). These update times are determined based on the solar irradiance profile and are bounded by lower and upper thresholds. Depending on the type of operation (start-up or shutdown), these thresholds are referred to as early–late start or early–late stop thresholds, respectively.

In Figure 14.3, up to three DoF are illustrated. If only one update is available (1 DoF), it is placed at the midpoint between the early and late thresholds. When two DoF are available, they are located at the early threshold and the midpoint, and at the late threshold, respectively. With three DoF, the subsystem updates occur at the early, average, and late thresholds. For the MED subsystem, these updates can be delayed with respect to those of the Solar Field and Thermal Storage subsystem (sfts) subsystem as illustrated in Figure 14.3 – 2 DoF. If more DoF are available, additional thresholds can be introduced as needed.

The relative shift or delay between subsystems acts as an additional tuning parameter of the methodology. However, for simplicity, this offset has been set to zero, as the inherent differences in subsystem start-up times already provide a natural temporal offset. Combined with the varying number of DoF assigned

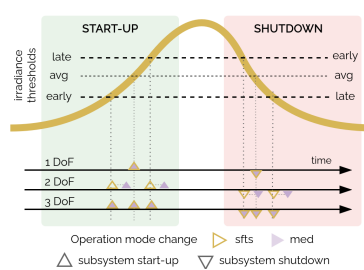


Figure 14.3: Operation mode updates time distribution. The thick-yellow line illustrates the irradiance.

to each subsystem, this configuration naturally results in staggered operation changes across the candidate problems.

Given a number of updates per subsystem and the update times assigned. The potential operation time change candidates are defined as:

$$t_{mode-change,candidates} = [t_0, t_1, \dots, t_{\max(n_{updates}, \forall x_i)}]$$

Ordered in ascending order, where t_0 is the earliest potential operation change time and $t_{\max(n_{updates}, \forall x_i)}$ is the latest potential operation change time¹³.

13: Based on this definition, the earliest potential subsystem start-up would be at $t_{\uparrow,candidates}(0)$. Similarly, the earliest potential shutdown would be at $t_{\downarrow,candidates}(0)$.

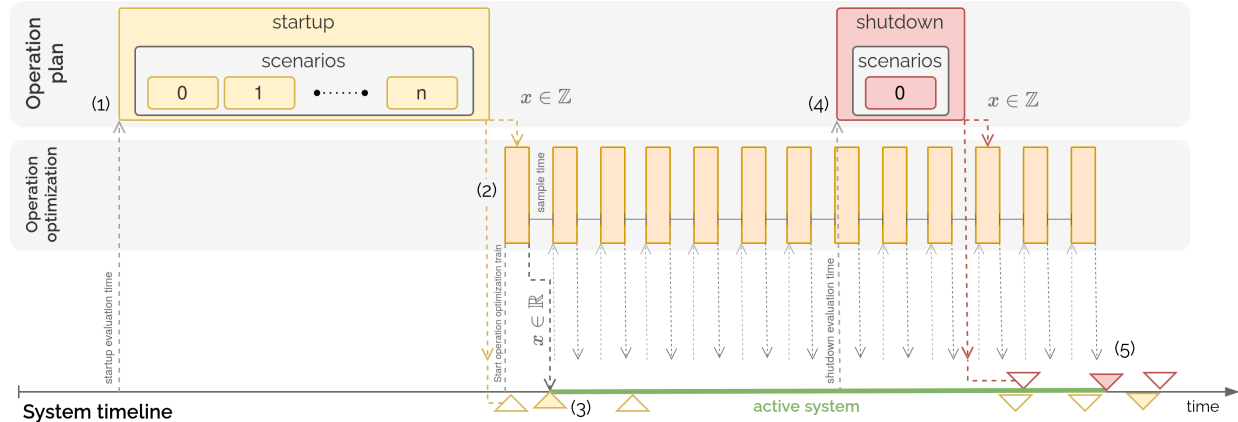


Figure 14.4: Proposed nNLP methodology computation timeline. (1) Operation plan start-up evaluation. (2) Start of operation optimization evaluation train. (3) System operation start. (4) Operation plan shutdown evaluation and (5) System operation end.

Start-up

This is the first evaluation of the proposed methodology as illustrated in Figure 14.4 (1). It is computed ahead of the first potential operation mode change ($t_{\uparrow,candidates}(0)$), with enough lead time to complete the evaluation before any potential change in operation mode¹⁴:

$$t = t_{\uparrow,candidates}(0) - (\Delta t_{eval,plan} \times n_{evals})$$

14: This is represented by the first yellow triangle group (▲) in Figure 14.4

The most important aspect of this evaluation is to find the right time to bring the subsystems online¹⁵, and a secondary objective is to provide a preliminary estimate for their shutdown timing¹⁶.

As the earliest evaluation, it considers the longest prediction horizon and therefore the highest uncertainty in the predicted variables. On the other hand, starting the evaluation early provides ample computation time—several hours in advance—to perform multiple assessments under different scenarios. In this work, three evaluations ($n_{evals} = 3$) are conducted using distinct solar irradiance estimates. Irradiance is selected as the uncertain variable because it has the strongest influence on system operation and performance. The three scenarios considered are: a nominal scenario based on the forecasted environmental conditions, a pessimistic scenario with a 20 % decrease in the expected solar irradiance, and an optimistic scenario with a 20 % increase in the expected solar irradiance.

15: Yellow upward-pointing triangles (▲) in Figure 14.4 (3)

16: Yellow downwards-pointing triangles (▼) in Figure 14.4 (5)

Shutdown

17: Represented in Figure 14.4 (5) as red downwards-pointing triangles (

18: See Table 14.1

19: Explained in the following section

A second evaluation is carried out later in the day, prior to system shutdown (see Figure 14.4 (4)). Its objective is to determine the most appropriate moment to stop operations based on the most up-to-date system state information¹⁷. This evaluation also includes DoF related to the operation schedule of the following day, enabling the shutdown decision for day 1 to account for its influence on the start and end times of day 2¹⁸.

Only a single scenario evaluation is required, since the uncertainty in the prediction horizon at this stage is considerably lower than during the start-up evaluation. It is executed in parallel with the operation optimization layer¹⁹ and triggered shortly before the earliest expected shutdown time of any subsystem estimated by the start-up evaluation, $t_{\downarrow, \text{candidates}}(0)$, while accounting for subsystem shutdown constraints:

$$t = t_{\downarrow, \text{candidates}}(0) - \Delta t_{\text{eval,plan}}$$

Once the evaluation is completed, the integer decisions are updated in the immediate posterior operation optimization layer. Faster computation is advantageous, as it allows the operation optimization layer to re-optimize the control trajectory for the actual shutdown time and adapt as soon as possible system operation accordingly.

Candidate problems evaluation

The candidate problems are evaluated by evolving each of them individually in a ranked evaluation. The concept involves keeping a collection of candidate problems that are evaluated in stages. First, a maximum number of objective function evaluations per problem and a number of stages is established. With this information, the number of iterations per stage can be computed. After each evaluation stage, the problems are ranked based on their performance, and a fraction of the worst-performing ones are removed from the collection. This process is repeated over time so that the library gradually focuses on the better-performing problems while discarding the less successful ones.

This strategy provides a trade-off between exploring a wide range of operation plans, initially, but gradually concentrating computational resources on the most promising candidates. If too aggressive pruning is applied, there is a risk of discarding potentially good solutions early on. Conversely, if pruning is too lenient, computational resources may be wasted on poor-performing candidates.

14.5 Operation optimization layer description

As mentioned, this middle layer establishes the setpoints for the continuous process variables, *i.e.* the continuous part of the MINLP problem. It is depicted in Figure 14.4 – *Operation optimization* and starting its evaluation cycle at (2). The operation optimization layer evaluates periodically, with a sample time $T_{\text{eval,optim}}$, a NLP problem where the integer decision variables are fixed to the values provided by the operation plan layer²⁰. It uses the latest available state of the system and environment predictions to evaluate the objective function.

The layer computation time is named $\Delta t_{\text{eval,optim}}$.

One key feature to increase the computational efficiency of this layer, is to provide initial solutions for decision variables based on:

20: It is exactly equivalent to the operation plan layer problem, just making $n_{\text{problems}} = 1$

- ▶ this layer previous solution if available, or
- ▶ the best candidate problem solution from the operation plan layer evaluation.

This warm-starting strategy helps to speed up the convergence of the optimization algorithm by starting from a solution that is already close to optimal.

SolarMED nNLP problems optimization methodology

1. Generate operation mode change candidates based on the available updates per subsystem (DoF) and irradiance thresholds.
2. Before the first potential operation change and considering the evaluation time, $t = t_{\downarrow, candidates}(0) - (\Delta t_{eval,plan} \times n_{evals})$, evaluate the operation plan layer to establish the operation start of the subsystems and an estimation of when to stop.
3. Before the established startup and considering the layer evaluation time, $t = t_{\downarrow} - \Delta t_{eval,optim}$, start evaluating the operation optimization layer periodically ($T_{eval,optim}$) to establish the setpoints for the continuous process variables.
4. Before the earliest subsystem projected shutdown and considering the operation optimization layer evaluation time, $t = t_{\downarrow, candidates}(0) - \Delta t_{eval,plan}$, evaluate the operation plan layer, in parallel to the operation optimization layer, to establish the shutdown time of the subsystems.
5. Continue evaluating the operation optimization layer periodically ($T_{eval,optim}$) until the last subsystem is shutdown.

14.6 Alternative strategies. Heuristic approach

This alternative makes use of a rule-based approach to decide when to start and stop the subsystems based on threshold values of the solar irradiance and the thermal storage state of charge. The rules are defined as follows:

- ▶ Start solar field operation when the solar irradiance exceeds a predefined threshold ($I_{\uparrow} = 500 \text{ W/m}^2$). Stop operation when it falls below a lower threshold ($I_{\downarrow} = 400 \text{ W/m}^2$).
- ▶ Start thermal storage charging when the solar field outlet temperature exceeds the one of the (top) hot tank: $T_{sf,out} > T_{ts,h,t}$. Stop charging when the solar field outlet temperature falls below the hot tank temperature: $T_{sf,out} < T_{ts,h,t}$.
- ▶ Start MED operation when the thermal storage is above 76 °C. Stop operation when it falls below 65 °C.

As for the continuous decision variables:

- ▶ The MED operates fixed setpoints at nominal conditions: $T_{med,s,in} = 74 \text{ }^{\circ}\text{C}$, $q_{med,f} = 8 \text{ m}^3/\text{h}$, $q_{med,s} = 12 \text{ l/s}$, $T_{med,c,out} = 28 \text{ }^{\circ}\text{C}$.
- ▶ The solar field recirculation flow rate is set to maintain the solar field outlet temperature at 90 °C.
- ▶ The thermal storage recirculation flow rate is set to maximize the heat transfer from the solar field while keeping the inlet hot tank temperature above its current value to avoid colder water mixing.

$$\max_{q_{ts,src} \in \Theta} \dot{Q}_{ts,src}$$

subject to: $T_{ts,h,in} > \min(T_{ts,h,t}, 90 \text{ }^{\circ}\text{C})$

14.7 Optimization results

14.7.1 Candidate problems generation

Figure 14.5 shows the initial evaluation of the operation plan layer – startup. In Figure 14.5 (a) it is shown how the available degrees of freedom are distributed for Days 23 and 26. Three DoF are available for the initial startup, two for the shutdown, and none for the second day in the horizon. From this selection the operation plans are generated as shown in Figure 14.5 (b) – Day 23, where the dashed-gray (– –) vertical lines are equivalent to the arrows in (a) and the horizontal lines represent the active operation span. For this particular day the optimization favors the shortest operation time and most delayed start (Problem 29 in Figure 14.5 (b)).

Another thing to notice, is how despite the unstable irradiance in Day 26, the smoothed prediction (1 hour samples) results in overall similar update times—only being slightly delayed.

14.7.2 Choosing an algorithm

Once the optimization problem(s) are defined, an algorithm must be selected to explore the solution space and identify a decision vector that minimizes the objective function.

The solution space has proven to be non-convex, exhibiting numerous local minima—poor results were obtained when using gradient-based local search algorithms. The size of the decision vector depends on the duration of the active periods, typically around 120 elements. Moreover, simulating two days of operation (even when inactive periods are skipped) requires approximately 5–10 seconds of computation time. Algorithm-level parallelization is not advantageous in this context, since many candidate problems are already evaluated concurrently. The objective, therefore, is to identify a global large-scale optimization algorithm capable of finding near-optimal solutions within 200 to 300 objective function evaluations, corresponding to a total computation time of roughly 2–4 hours.

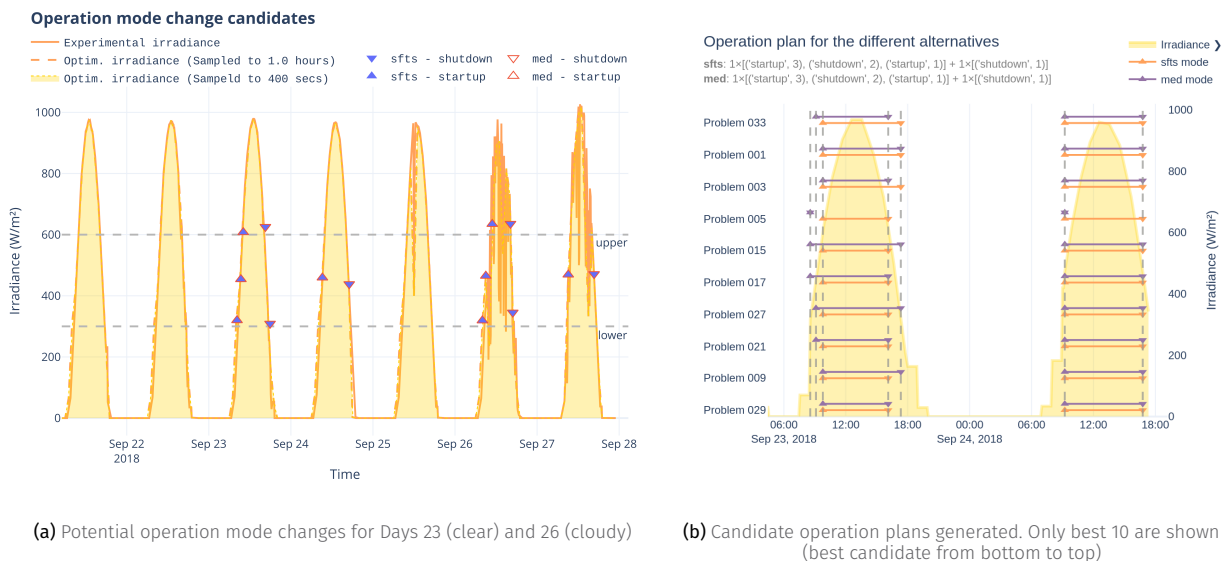


Figure 14.5: Operation plan layer (start-up) candidate problem generation results for specific dates

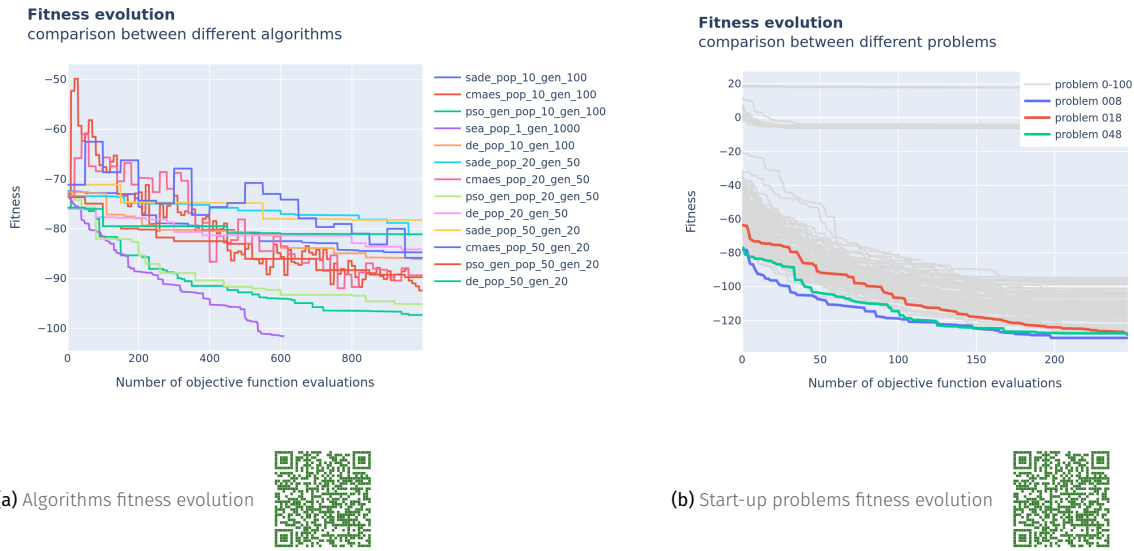


Figure 14.6: Fitness evolution comparison for a representative start-up problem.

To select the most suitable algorithm, one candidate problem was arbitrarily chosen, and a library of global evolutionary algorithms from the open-source PyGMO Python package was tested²¹. The algorithms considered include: Differential Evolution algorithm (DE), Self-adaptive Differential Evolution (SADE), (N+1)-ES Simple Evolutionary algorithm (SEA), Covariance Matrix Adaptation Evolution Strategy (CMA-ES), and Particle Swarm Optimization algorithm (PSO)²². The evolution results are shown in Figure 14.6 (a), indicating that, for this particular problem, the best-performing algorithm is the (N+1)-ES Simple Evolutionary Algorithm²³.

21: See Section 2.4 (Implementation software tools)

22: All of these algorithms are described in Section 3.2.5 (Optimization algorithms)

23: sea_pop_1_gen_1000 in Figure 14.6 (a)

14.7.3 Choosing a candidate problem

Once the algorithm is selected, all n_{problems} can be evaluated, where the algorithm is required only to determine values for the continuous process variables. The results of this evaluation are presented in Figure 14.6 (b), showing the fitness evolution as a function of the number of objective function evaluations for all 101 problems. Problems 8, 18, and 48 yielded the best fitness values after the evolution process. Notably, Problem 18 was not among the top candidates during the initial half of the evaluation, but it eventually surpassed the others to achieve the second-best fitness. This highlights the importance of setting correct parameters for the candidate problems ranked evaluation in order not to early drop potential best-performing candidates.

14.7.4 Simulation results

Figure 14.7 shows the time-series results for one episode composed of seven consecutive days of operation applying the proposed nNLP methodology. As seen in Figure 14.7 – *Environment*, the solar irradiance remains stable under clear-sky conditions during the first five days, while the last two are cloudy. The weather corresponds to typical end-of-summer conditions for Almería (southeast Spain). The seawater inlet temperature remains nearly constant at the characteristic temperature of the Mediterranean Sea (22.1 °C on average for

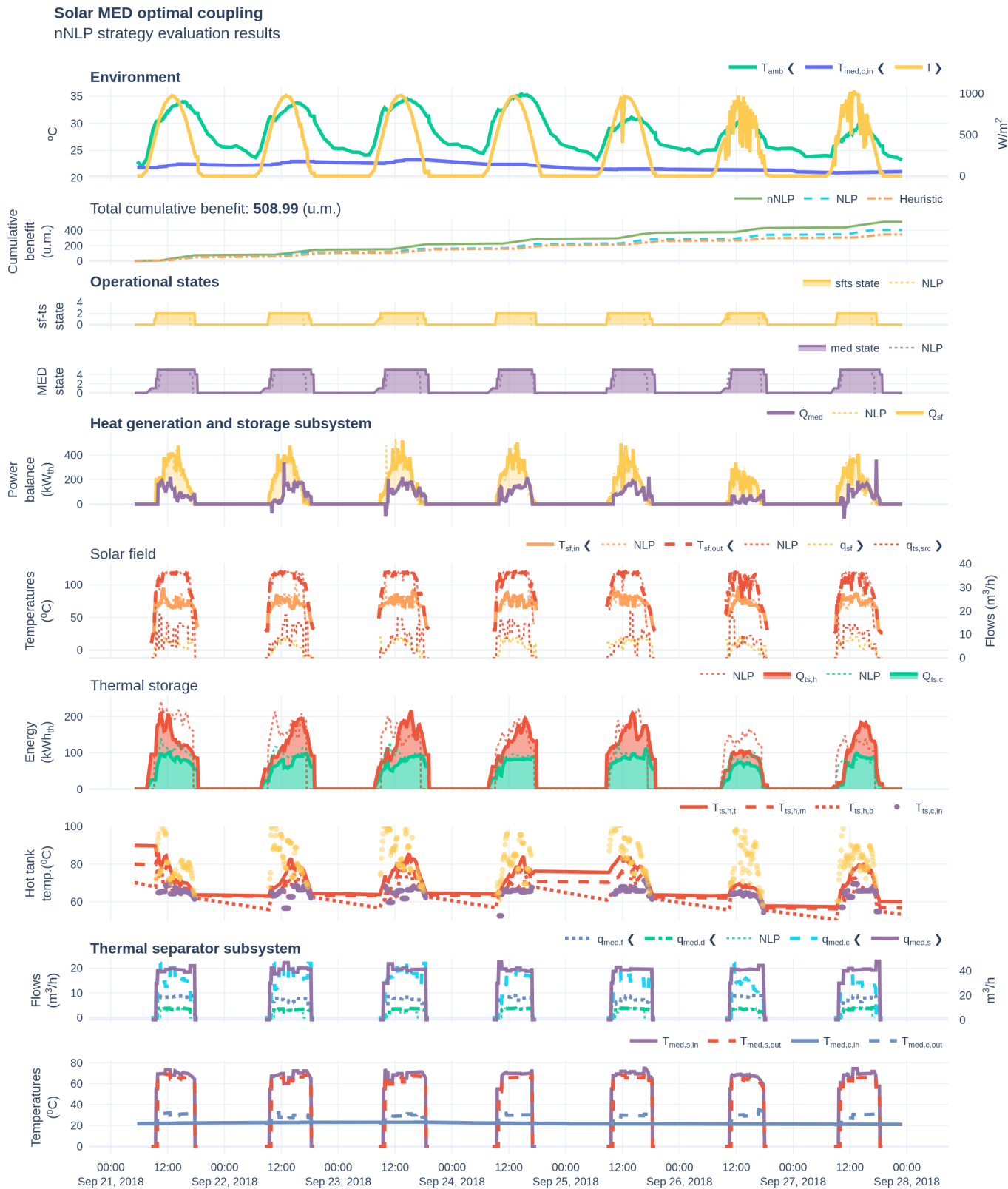


Figure 14.7: SolarMED nNLP optimization strategy results



the episode), obtained from the *Copernicus Marine Programme* [208]. The figure also displays the results for the alternative operation strategies across selected variables; however, a detailed comparison of these strategies is presented in the next section.

In Figure 14.7 – *Solar Field*, it can be observed that both strategies optimize the solar field operation almost identically, maximizing the outlet temperature (around 120 °C) and achieving large temperature differences (averaging more than 33 °C over the episode). This operation pattern is consistent with the objective of maximizing energy transfer, which can be achieved either by increasing the temperature gain in the solar field or by raising the mass flow rate—the latter incurring additional pumping costs.

Regarding energy management, Figure 14.7 – *Thermal Storage* shows that during the first day the system starts with highly charged tanks (significant stored energy) and gradually depletes them. From the second day onward, most days follow a similar charge–discharge cycle: initial charging during the first part of the active period, followed by discharge toward the end, with varying final storage levels and temperatures. A clear increasing trend is seen from Days 22 to 24, culminating in a marked rise on Day 25 (particularly in temperature). This behavior is likely a preparation for the drop in irradiance observed at the beginning of Day 25 (see Figure 14.7 – *Environment*). For the remaining two days, the algorithm prioritizes production on Day 26 while reducing operating time and heat-source temperatures—especially on Days 26 and 27. The dotted lines represent the alternative NLP strategy, which maintains a higher amount of stored energy at the end of each day, resulting in a more balanced storage level throughout the episode.

14.7.5 Operation and performance comparison between strategies

To better understand how each alternative operates the system and how this affects overall performance, different visualizations are presented in Figures 14.8, 14.9, and 14.10. Each operation strategy is compared on a day-by-day basis²⁴.

Figure 14.8 (a) displays the initial and final temperatures of the upper (hot) tank, while Figure 14.8 (b) presents the average MED hot-side inlet and outlet temperatures.

Figure 14.9 shows the daily operation schedule of each subsystem. Yellow bars correspond to the heat generation and storage subsystem (*sfts*), while purple bars represent the MED desalination subsystem. The start and end of each bar indicate subsystem start-up and shutdown times, respectively, with the bar length representing the active period duration²⁵.

Finally, Figure 14.10 compares the cumulative daily benefit (left bars) and the total benefit obtained at the end of the episode (rightmost yellow bars).

Results discussion. As expected, the Heuristic alternative fully depletes thermal storage at the end of each operation day (see Figure 14.8 (a), Heuristic). This means that each cycle starts and ends at the same storage level. While this strategy delivers regular daily benefits under clear conditions (see Figure 14.10, Heuristic), it is strongly penalized during unstable conditions (e.g., Day 27), where the benefit drops to nearly half of the other alternatives. This occurs because the Heuristic MED operation (see Figure 14.8 (b)) consistently targets higher hot-side inlet temperatures than the optimized approaches. As a result, the MED operates for significantly shorter periods (e.g., 6.9 hours on Day 27, compared to over 9 hours on average for other days; see Figure 14.9 – MED – Heuristic).

The comparison also highlights the differences between the NLP and nNLP alternatives. The nNLP strategy consistently operates the MED at lower temperatures

[208]: CNR (2024), *Mediterranean Sea Surface Temperature Time Series and Trend from Observations Reprocessing*

24: In Figures 14.8 and 14.10, the cumulative daily irradiance is shown in the background as a reference of the available solar energy, which is the primary determinant of system operation.

25: Also displayed numerically next to each bar, and the mean value summarized in the legend

Reminder: Strategies nomenclature

Heuristic: Rule-based approach.
NLP: Optimized alternative with fixed subsystem start-up and shutdown based on rules.
nNLP: Optimized approach where the operation schedule is part of the decision variables.

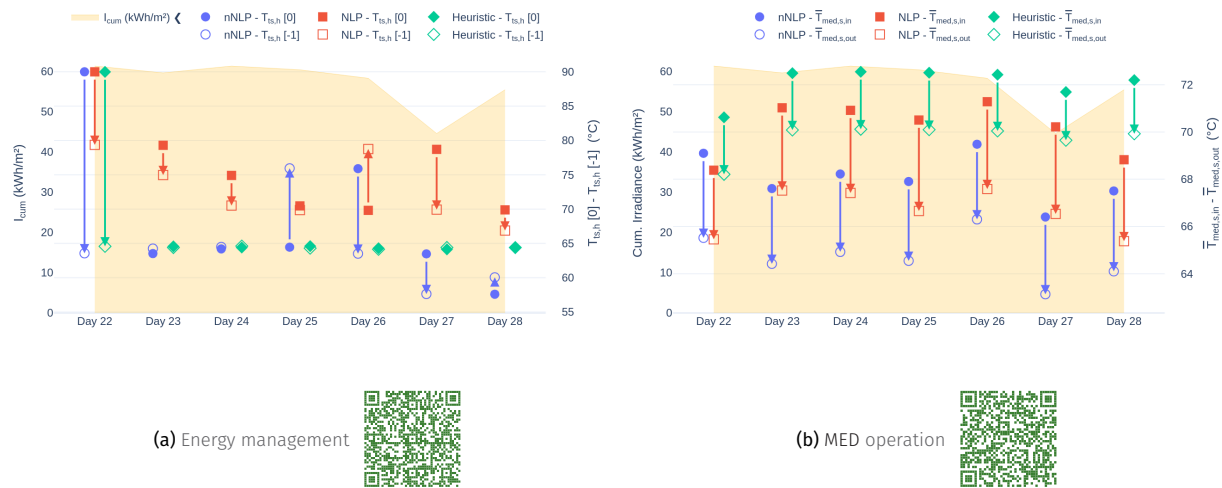


Figure 14.8: Daily key variables differences comparison

and for longer durations (9.8 h vs. 8.1 h, see Figure 14.9). This is particularly evident on the cloudy Day 27, where the nNLP maintains operation at the lowest temperature ($T_{med,s,in} = 66.4^\circ\text{C}$).

Overall, the Heuristic approach tends to delay MED start-up relative to the other strategies, while keeping it active later into the evening. Although it operates the MED longer than the NLP, this does not translate into higher benefits (see Figure 14.10, Heuristic vs. NLP).

Another interesting observation is the difference in MED heat source temperature span between the Heuristic and optimized strategies²⁶. 2.34 K for the Heuristic versus 3.51 K (NLP) and 3.32 K (nNLP). This indicates that maximizing SolarMED system performance is achieved by operating for longer periods at lower temperatures and with high temperature differences— in both the solar field and MED sides— thereby maximizing the utilization of sensible heat.

A key distinction between the NLP and nNLP strategies appears during cloudy conditions (Day 27). The nNLP strategy depletes storage on the previous day—Day 26, see Figure 14.8 (a)— and adapts the following day by delaying start-up more significantly than on other days—Day 27 in Figure 14.9— while operating at a lower temperature—Day 27 in Figure 14.8 (b). In contrast, the NLP strategy reserves energy, allowing it to operate in a more consistent manner across the episode.

As shown in Figures 14.9 and 14.10, the NLP strategy generally stops subsystem operation earlier than the nNLP alternative. Adjusting the shutdown threshold to match the average stop time of the nNLP strategy could potentially improve NLP performance. Still, as observed in Figure 14.9, there is notable variability in start and shutdown times, particularly on cloudy days (Days 27 and 28). This adaptability to changing conditions is something the fixed NLP alternative can only approximate through heuristic rules (e.g., advancing or delaying operation based on predicted irradiance availability). Overall, the NLP strategy manages stored energy and MED operation in a consistent but moderately adaptive manner.

By far, the best-performing strategy (see Figure 14.10) is the nNLP alternative, achieving a total benefit of 508.99 u.m., followed by the NLP (403.97 u.m.) and Heuristic (346.86 u.m.) alternatives. As mentioned earlier, some performance gap could be reduced by incorporating smarter rule-based logic into the NLP

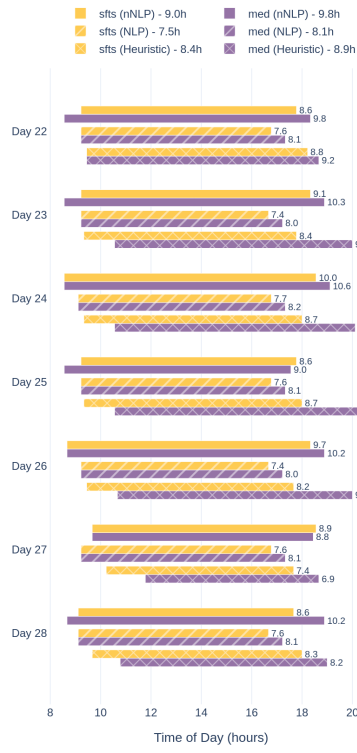


Figure 14.9: Operation schedule comparison between optimization strategies

26: See Figure 14.9

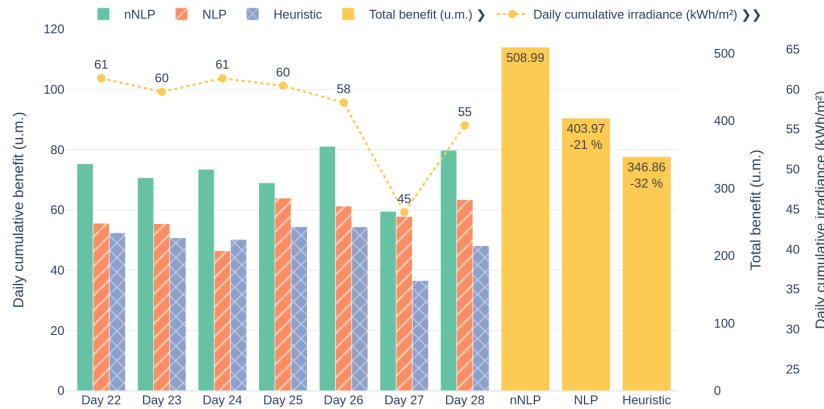


Figure 14.10: Daily and total cumulative benefits comparison. *u.m.* represents arbitrary monetary units.

27: The results presented here can serve as useful guidance for defining such rules.

and Heuristic strategies²⁷, but they would still remain suboptimal compared to the nNLP approach. Since the NLP is effectively a subset of the nNLP, it cannot consistently outperform it.

Conclusions. The nNLP alternative outperforms the NLP and Heuristic strategies by 21 % and 32 %, respectively. These results correspond to a seven-day episode characterized mainly by clear-sky conditions, with cloudy days occurring only toward the end of the period. It is expected that evaluating performance over an entire year—with its substantially higher environmental variability—would further accentuate the advantages of the nNLP strategy proposed in this chapter.

This study demonstrated that sensible-driven thermal separation processes are optimally operated when temperature differences are maximized. This finding contrasts with conventional operation strategies for thermal (latent-driven) desalination systems, which typically consider the process in isolation and aim to minimize energy consumption. When the entire system is evaluated from the perspective of primary energy utilization, the optimal operation of a solar-driven MED unit more closely resembles that of a waste-heat-driven process.

Furthermore, it was shown that achieving optimal performance in a thermally driven separation process powered by variable energy sources requires a combination of factors: a sufficiently long optimization horizon, careful selection of decision variables, flexible scheduling of subsystem operation, and a fitness function that accurately reflects performance relative to primary energy input. Together, these elements enable a truly optimized and resilient operation of solar-thermal separation systems.

Open source is like academia is meant to
be. You're paid a salary but your research
contributions are distributed to the public,
freely.
//

El código abierto es como el mundo
académico debería de ser. Se te paga un
salario, pero el fruto de tu investigación es
distribuido a la sociedad, de manera libre.

CONCLUSIONS AND OUTLOOK

Open source is like academia is meant to be. You're paid a salary but your research contributions are distributed to the public, freely.
//

El código abierto es como el mundo académico debería de ser. Se te paga un salario, pero el fruto de tu investigación es distribuido a la sociedad, de manera libre.

Conclusions

Optimal water and electricity management in a combined cooling system

This work has addressed the challenge of reducing water consumption in Concentrated Solar Power (CSP) plants through the development and assessment of a hybrid combined cooling concept that integrates dry and wet technologies. Starting from the broader context of concentrated solar thermal power and its dependence on water resources, the thesis has motivated the need for more water-efficient cooling solutions, particularly in water-scarce regions where CSP deployment is most attractive.

A detailed steady-state modelling framework was developed for the main components of the combined cooler. Two complementary modelling strategies were employed: (i) physics-based, first-principles models with broad applicability, and (ii) several data-driven, black-box approaches, including artificial neural networks, Random Forest, Gradient Boosting, and Gaussian-Process Regression (GPR).

To reconcile the accuracy and generality of physical models with the computational efficiency of data-driven surrogates, Gaussian Process Regression models were trained on synthetic data generated by the first-principles models. This hybrid strategy yields fast, on-demand surrogate models that can be adapted to different plant scales while preserving high predictive accuracy. Validation against 24 experimental tests covering a wide operating envelope demonstrated mean absolute errors below 0.97 °C for key temperatures and 19.4 l/h for water consumption, confirming that the integrated model can reliably reproduce the behavior of the combined cooling system under diverse operating and ambient conditions. Given the obtained accuracy, the significant reductions in computational time and experimental data requirements—the same amount as the physical model—this approach has proven to be a robust and practical alternative to purely physics-based simulations.

Building on this modelling framework, a two-stage multi-objective optimization strategy was proposed to minimize the daily cost of cooling—comprising both electricity and water costs—under limited water availability, while guaranteeing the required cooling duty. At each time step of a prediction horizon, a multi-objective optimization problem is solved to obtain a Pareto front between cost and water use. A second-stage global optimization problem then selects an optimal path through the sequence of Pareto fronts, effectively planning an operation schedule over the horizon. This is the first time that an advanced optimization framework has been applied to the operation of combined cooling systems in concentrated solar power plants.

Experimental tests confirmed that the optimized operation strategy consistently match the measured behavior of the pilot plant, demonstrating its effectiveness in managing cooling resources under realistic operating conditions. The results demonstrated that:

- ▶ The dry cooler becomes highly sensitive to ambient temperature when operating near its limits, whereas the wet cooler reliably compensates in such cases when operating in the often used series configuration.
- ▶ The optimization framework also showed a clear tendency to prioritize water savings, favoring dry-only operation or series operation of the coolers whenever feasible.
- ▶ Importantly, the optimized strategies remained valid over extended periods, even through planned changes in thermal load, and could therefore support robust operation.

- ▶ The close agreement between predicted and measured variables further indicates that upper-layer forecasts can be safely exploited in low-level control (e.g. in feedforward actions).

Finally, the methodology was applied to a case study of a commercial 50 MW_e CSP plant with 8 h of storage (Andasol-II, southern Spain). Three cooling configurations were compared under a water-scarcity scenario using annual simulations: the existing wet-only Wet Cooling Tower (WCT) system, and the proposed Combined Cooler (CC) concept with two dry-cooler capacities (75 % and 100 % of the nominal wet-system load). For each configuration, operation was optimized using the proposed multi-stage framework. The combined cooler alternatives reduced specific cooling costs by up to 80 % and decreased annual water consumption by about 48 %, with 38 % savings during the driest and hottest months. These improvements were mainly due to the fact that optimal solutions are less reliant on costly alternative water sources, which can dominate cooling costs. The CC options also exhibited much more stable and predictable costs throughout the year compared to the wet-only reference, which proved highly sensitive to water availability.

Overall, the analysis underscores the importance of evaluating cooling concepts over representative annual conditions rather than relying on aggregated averages, and confirms that water availability can become the dominant constraint and cost driver, especially where alternative water sources are costly. Although no optimization strategy can fully resolve the intrinsic mismatch between peak cooling demand and water scarcity in hot-dry seasons, the results demonstrate significant remaining potential for improved water management through optimized operation of hybrid cooling systems. The proposed modelling and optimization framework is generic and can be adapted to other plant designs, locations, and resource scenarios, thereby supporting informed design and operational decisions for more sustainable CSP power plants.

Energy management in MED processes driven by variable energy sources

The second part of this thesis concerns the integration, evaluation, and optimal operation of low-temperature MED systems powered by variable energy sources, with a particular focus on solar-thermal driven systems. As desalination becomes increasingly important to address global freshwater scarcity, thermal systems — and especially low-temperature MED — offer a robust and complementary pathway for brine concentration and resource recovery, particularly when coupled with waste-heat or renewable energy sources.

A standardized methodology was firstly developed to evaluate MED performance under realistic and supporting highly variable operating conditions. The method defines instrumentation requirements, key performance indicators, and uncertainty quantification procedures, and is complemented by an automated steady-state detection algorithm that enhances the robustness of experimental assessments. Application of the methodology showed that reproducible performance metrics can be obtained even when the duration of steady-state episodes differs significantly, provided that stable operation is correctly identified. Tests at elevated top-brine temperatures confirmed the feasibility of high-temperature operation without significant scale formation, as corroborated with control tests and stable heat transfer coefficients estimated from a physical model. The results further showed that, while higher top-brine temperatures enable higher brine concentrations, they do not necessarily improve thermal performance in the absence of design changes (e.g. additional effects or modified geometry), due to increased exergy destruction in unbalanced heat exchangers and limitations imposed by boiling point elevation.

To reproduce system behavior under realistic solar-driven conditions, a complete hybrid dynamic model of the SolarMED installation at PSA was formulated. The model combines continuous physics-based and data-driven sub-models for the solar field, heat exchanger, thermal storage, three-way valve, and MED plant with discrete supervisory Finite-State Machines (FSMs) that model the operational logic of both the *sfts* and the Separation subsystem (*med*). Each FSM governs subsystem activation, startup, shutdown, and transitions based on system inputs, internal rules, and configurable parameters such as cooldown or startup durations.

The integrated hybrid model was evaluated under realistic operation conditions—experimental data from the pilot-plant—with different prediction horizons and showed good agreement with experimental data. For multi-hour predictions, the model maintained Mean Absolute Percentage Error (MAPE) values below 15 %, which is a commendable result given the strong coupling between subsystems and the absence of feedback within the prediction horizon. Static variables, such as distillate production, were accurately captured and showed little sensitivity to the prediction horizon, while dynamic variables associated with thermal storage and solar field temperatures exhibited increasing errors with longer horizons, as expected. Nevertheless, the final thermal states and stored energy at the end of operation remained close to the measured values, demonstrating that the model captures the essential dynamic behavior of the coupled system with reasonable computational time—in the order of single-digit seconds for multi-day simulations.

With the model of the SolarMED system, a novel hierarchical optimization strategy was proposed to enable its autonomous and economically optimal operation. The strategy is structured into three layers, with the upper operation layer solving a MINLP economic problem that decides when to start or stop each subsystem and how to regulate them throughout operation, while exploiting solar availability and thermal storage flexibility.

The proposed method was benchmarked over a week-long system simulation against two alternative strategies: a baseline heuristic rule-based operation and a fixed-schedule operation-only optimization solving a continuous NLP problem. The results showed that the hierarchical MINLP-based strategy improves the economic system performance by approximately 32 % relative to the heuristic baseline and by 21 % relative to the fixed-schedule NLP strategy. These gains arise from the ability to fully exploit the temporal flexibility provided by the thermal storage and the solar resource, maximizing useful temperature differences. The resulting near-optimal operation closely resembles that of a waste-heat-driven process—focusing on maximizing energy utilization—highlighting that, when evaluated from the perspective of primary energy utilization, the optimal strategy for a solar-driven MED unit differs markedly from conventional fossil-driven approaches that focus solely on minimizing process energy consumption.

The analysis showed that achieving near-optimal performance in thermally driven separation processes powered by variable energy sources requires the combination of a sufficiently long optimization horizon, carefully selected decision variables, flexible scheduling of subsystem operation, and an objective function that accurately reflects performance relative to primary energy input. When these elements are jointly considered, solar-thermal separator systems can be operated in a truly optimized and autonomous manner. This can be accomplished with the proposed optimization framework, which brings notable improvements to the economic and energetic performance of state-of-the-art solar-driven MED systems.

Together with the combined cooling contributions, these results provide a coherent set of tools and insights for the design and operation of water- and

energy-efficient solar-thermal systems.

Outlook and future work

Water and electricity management in a combined cooling system

Improved Pareto front computation. In the current optimization implementation, the Pareto front for each step in the optimization horizon is constructed using a grid search over the decision space. This approach can become computationally expensive, especially as the grid resolution increases. Additionally, the Pareto front must be recalculated from scratch at every step, even though the sequential steps are often very similar; cost parameters remain constant, and only the thermal load and weather conditions change, typically with small variations. A more efficient solution would be to use a multi-objective optimization algorithm, which can transfer evolved populations between successive evaluations, significantly reducing redundant computations.

Low-level control. Enhance the robustness of the operation strategy by ensuring that cooling demand is satisfied even under unexpected disturbances, such as rapid changes in thermal load. This can be achieved by incorporating a supervisory low-level controller that monitors the condenser pressure and, whenever the target value is not met, increases the cooling recirculation flow rate until the pressure returns to its setpoint. At the higher flow rate, the cooling components naturally attempt to maintain their outlet temperatures, thereby increasing the available cooling capacity.

Better water management In the current implementation, the primary water source is distributed evenly each day, so the optimization process uses up the entire supply daily. However, a more intelligent daily distribution—essentially, a new optimization problem—could improve water management by allocating different amounts on different days, based on expected weather conditions and predicted generation. This approach would likely be incorporated as a new upper layer in the hierarchical control structure.²⁸ At the higher level a simpler and more abstract model would be considered to predict the long term behavior of the system and to optimize it over a long time horizon, probably considering the availability and capacity of a water reservoir.

Analyze different combined coolers configurations and within each configuration, different component sizes. The cooler analyzed has a combined dry and wet coolers which can either satisfy the nominal cooling load. Different ratios could be analyzed and one would probably be a better fit for the particular case study. Furthermore, the Air-Cooled Heat Exchanger (ACHE) is used for the Dry Cooler (DC), but other options could be considered and added to the comparison, such as an Air-Cooled Condenser (ACC) in parallel with a surface condenser together with a WCT or a deluged condenser.

This in itself is a design optimization problem that is not addressed in this thesis. However, it is important to integrate a method like the proposed optimization and include it in the design process to evaluate the performance of different configurations and sizes. In the end, the decision of the configuration and size of the cooling system should be based on a techno-economic analysis.

Techno-economic analysis. The presented cooling alternatives comparative in this thesis focus on the operation cost of the system, but to get a better picture of the alternatives performance, a techno-economic analysis that includes the capital cost of the system and the expected lifetime of the components should be performed *i.e.* considering all costs associated with the system the plant's lifetime. This is currently being worked on as part of SOLhycool²⁹, where the

28: The resulting structure would be: 1. Water allocation, 2. CC operation optimization, 3. CC regulatory control.

29: <https://solhycool.psa.es/>

methodology presented here in terms of operation costs will be integrated in a techno-economic analysis for different case studies.

Energy management in MED processes driven by variable energy sources

Analysis in simulation of a high-TBT case study. As mentioned in Chapter 13, increasing the number of effects and/or modifying the geometry of the heat exchangers could improve the performance of high-TBT MED systems. This is not practical to test in the experimental facility but it could be analyzed in simulation.

Analysis and optimization in simulation of a waste-heat-driven MED case study. It would be interesting to analyze the performance of the proposed hierarchical optimization strategy in a waste-heat-driven MED from its integration with an industrial process. This would allow to evaluate the performance of the strategy in a scenario with less variability than the solar-driven case, but with different constraints and objectives, such as minimizing the impact on the industrial process or maximizing the use of waste heat.

Alternative configurations for an MED brine concentrator. Several non-standard MED configurations could be considered for brine concentration applications. Examples include variable-effect geometry (increasing the temperature difference in effects as brine concentration rises to maintain balanced vapor production), the use of external heat sources in effects beyond the first (see Figure 14.11 – *MED – alternative B*), and hybridization with Multi-Stage Flash (MSF) in later effects where BPE significantly limits the driving force. Depending on the application and heat-source availability, these configurations may offer enhanced performance or reduced cost.

Alternative configurations for solar and/or waste heat driven MED processes. The current layout of the experimental SolarMED facility at PSA was designed with priorities on reliability, flexibility, and reduced operation and maintenance costs, rather than strict thermodynamic optimization. This approach led to the separation of the solar field and thermal storage into two independent circuits, minimizing the volume of antifreeze additives (used only in the solar field) and increasing operational flexibility by enabling independent pumping per solar field loop. This arrangement also allows external loads to be connected to the solar field when the MED unit is offline.

However, the overall efficiency and cost-competitiveness of the system could be improved if some of these design choices were revisited with the goal of maximizing the performance of solar- and waste-heat-driven MED processes, in light of the findings of this research (see Figure 14.11). Potential improvements include:

- ▶ **SF.** By adding a small number of three-way control valves, the solar field could operate in both parallel and series configurations, improving its ability to adapt to variable solar input and enhancing outlet temperature control. This is particularly beneficial at the beginning and end of the solar day, when a series configuration would enable earlier and more sustained useful heating of the thermal storage.
- ▶ **SF-TS.** Direct coupling of the solar field and thermal storage could eliminate the energy transfer losses associated with the intermediate heat exchanger.
- ▶ **TS.** Allowing charge and discharge at different levels of the thermal storage tank would take advantage of thermal stratification while avoiding fluid mixing.

- ▶ **TS-MED.** Directly connecting the thermal storage to the MED unit would reduce regulation capability but eliminate mixing losses in the three-way valve.
- ▶ **MED.** As noted above, alternative MED configurations (e.g., variable geometry, multiple external heat sources at different effects, or heat-source recirculation) could further improve performance for brine concentration and enable better integration with solar and waste-heat sources.

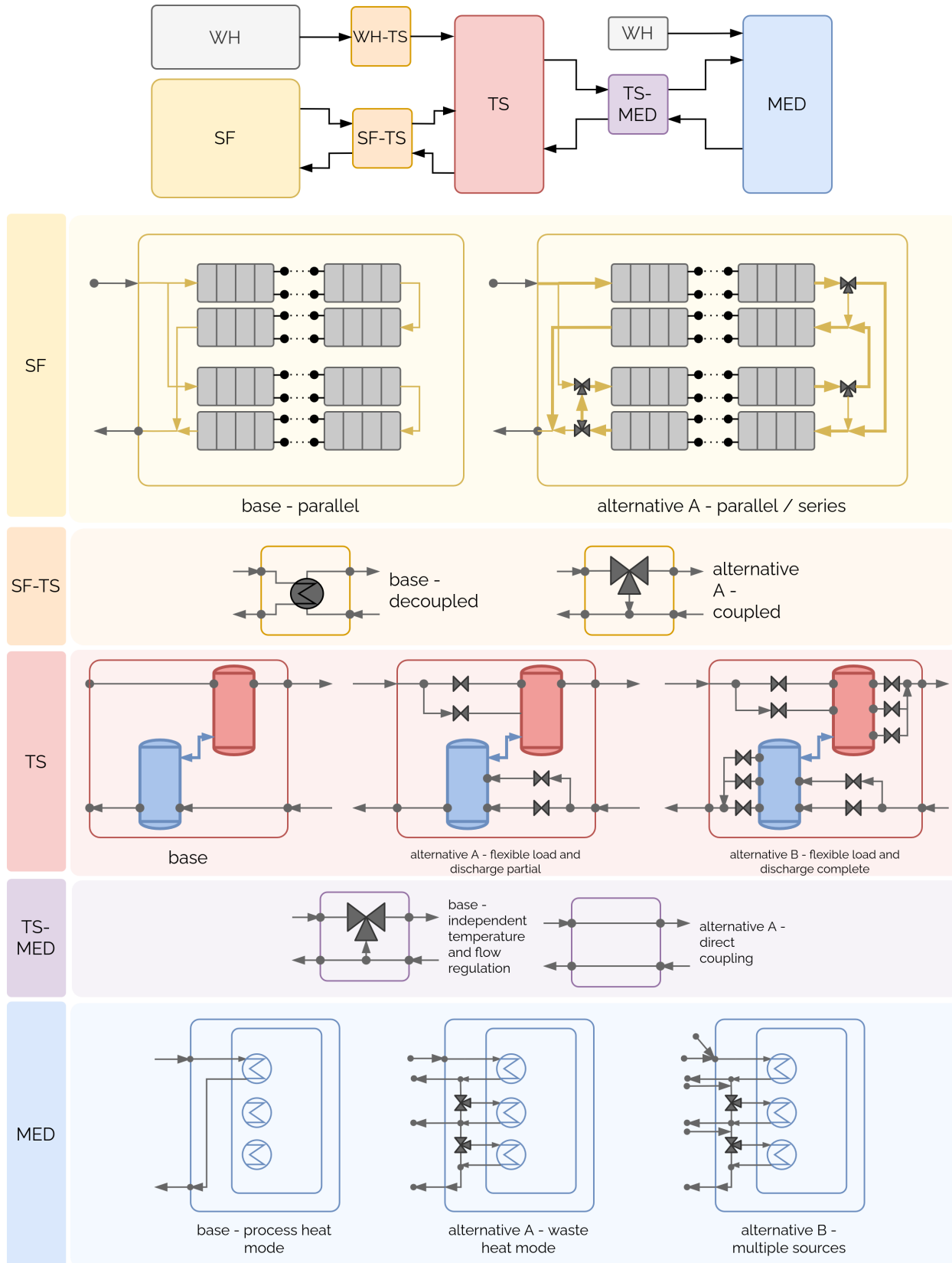


Figure 14.11: Alternative configurations for variable energy source(s) driven MED processes.

Derived scientific contributions

The author has published or submitted for publication several journal articles, contributed to conferences (national and international) and colloquiums:

Journal publications

- ▶ J. M. Serrano, P. Navarro, J. Ruiz, P. Palenzuela, M. Lucas, and L. Roca. "Wet Cooling Tower Performance Prediction in CSP Plants: A Comparison between Artificial Neural Networks and Poppe's Model." *Energy*, May 29, 2024, 131844.
DOI: <https://doi.org/10.1016/j.energy.2024.131844>.
- ▶ P. Navarro, J. M. Serrano, L. Roca, P. Palenzuela, M. Lucas, and J. Ruiz. "A Comparative Study on Predicting Wet Cooling Tower Performance in Combined Cooling Systems for Heat Rejection in CSP Plants." *Applied Thermal Engineering*, June 21, 2024, 123718.
DOI: <https://doi.org/10.1016/j.aplthermaleng.2024.123718>.
- ▶ J. M. Serrano, P. Palenzuela, J. Ruiz, P. Navarro, J. Muñoz, B. Ortega, L. Roca. "Combined cooling for CSP plants: Modeling, experimental validation and optimization analysis" *Energy Conversion and Management* 348 (January 2026): 120752.
DOI: <https://doi.org/10.1016/j.enconman.2025.120752>.

Contribution to conferences

- ▶ J. M. Serrano, J. D. Gil, J. Bonilla, P. Palenzuela, and L. Roca, "Optimal operation of a combined cooling system" in 4th IFAC International Conference on Advances in Proportional-Integral-Derivative Control, Almería, Spain, 2024-06-12/2024-06-14.
- ▶ J. M. Serrano, J. D. Gil Vergel, J. Bonilla, P. Palenzuela, and L. Roca, "Operación óptima de un sistema de refrigeración combinada," in XLIV Jornadas de Automática, Universidad de Zaragoza, 6, 7 y 8 de septiembre de 2023, Zaragoza, 2023rd ed., Aug. 2023, pp. 477-482.
DOI: <10.17979/spudc.9788497498609.477>.
- ▶ P. Navarro, J. M. Serrano, J. Ruiz, M. Lucas, L. Roca, and P. Palenzuela. "Comparison Between an Artificial Neural Network and Poppe's Model for Wet Cooling Tower Performance Prediction in CSP Plants." Efficiency, Cost, Optimization, Simulation and Environmental Impact of Energy Systems. International Conference., ECOS 2023, June 25, 2023, 1609-20.
DOI: <10.52202/069564-0146>.
- ▶ L. Roca, J. M. Serrano, J.D. Gil, G. Zaragoza, M. Beschi, and A. Visioli. "Modelo de parámetros concentrados para captadores solares planos con reflectores." Jornadas de Automática, no. 45 (July 2024): 45.
DOI: <10.17979/ja-cea.2024.45.10930>

Participation in conferences and colloquiums

- ▶ J.M. Serrano, L. Roca, P. Palenzuela. "Yearly Simulation of a Combined Cooling System Integrated into a Concentrating Solar Power Plant". SolarPACES. Almería, Spain (September 2025).
- ▶ J.M. Serrano, P. Palenzuela and L. Roca. "Methodology for the implementation of a steady state simulation model in a multi-effect distillation plant. Case study: PSA MED pilot plant". Desalination for the Environment, Clean Water and Energy (EDS). Las Palmas de Gran Canaria, Spain (2022).
- ▶ J.M. Serrano, P. Palenzuela and L. Roca. Experimental evaluation of

MED at high top brine temperatures with no divalent ions in feed water. Desalination for the Environment, Clean Water and Energy (EDS). Limassol, Chipre (2023).

► 3rd SFERA-III Doctoral Colloquiums:

1. Technological developments for solar multi-effect distillation processes. Almería, Spain (2021).
2. Modelling and automation of a multi-effect distillation plant for the optimal coupling with solar energy. ETH Zurich, Switzerland (2022).
3. Towards the optimal coupling of multi-effect distillation with solar energy. DLR. Cologne, Germany (2023).

As a result of the work developed in the present research work, several repositories containing experimental datasets and open-source code have been made publicly available. Particularly, each of the parts of the thesis has an associated repository with the implementation of the presented results, in order to facilitate transparency, reproducibility, and reusability of the developed methods. Additionally, this thesis manuscript itself is also made available together with all its associated media:

Open datasets

- P. Palenzuela, L. Roca, J.M. Serrano (CIEMAT-PSA). "Steady-State Operation Dataset of an Experimental Wet Cooling Tower Pilot Plant Located at Plataforma Solar de Almería." Version 1.0.0. Zenodo, June 21, 2024. DOI: [10.5281/zenodo.10806201](https://doi.org/10.5281/zenodo.10806201).
- P. Palenzuela, L. Roca, J.M. Serrano (CIEMAT-PSA). "Steady-State Operation Dataset of an Experimental Air-Cooled Heat Exchanger Located at Plataforma Solar de Almería." Version 1.0.0. Zenodo, December? , 2025. DOI: [10.5281/zenodo.17312369](https://doi.org/10.5281/zenodo.17312369) (To be published).
- P. Palenzuela, L. Roca, J.M. Serrano (CIEMAT-PSA). "Steady-State Operation Dataset of an Experimental Surface Condenser Located at Plataforma Solar de Almería." Version 1.0.0. Zenodo, December? , 2025. DOI: [10.5281/zenodo.17312530](https://doi.org/10.5281/zenodo.17312530) (To be published).
- P. Palenzuela, L. Roca, J.M. Serrano (CIEMAT-PSA). "Steady-State Operation Dataset of an Experimental Combined Cooling System Located at Plataforma Solar de Almería." Version 1.0.0. Zenodo, December? , 2025. DOI: [10.5281/zenodo.17312546](https://doi.org/10.5281/zenodo.17312546) (To be published).

Open-source implementation

- J.M. Serrano, L. Roca. "Repository with the implementation source code for modeling, optimization and simulation of a combined cooling system (wet cooling tower, dry cooler and surface condenser) at Plataforma Solar de Almería as part of the SOLhycool research project". DOI: <https://doi.org/10.5281/zenodo.CHANGEME>
- J.M. Serrano, "Repository with the implementation and results of the modeling and optimization of a solar-driven multi-effect distillation system at Plataforma Solar de Almería". DOI: <https://doi.org/10.5281/zenodo.CHANGEME>
- J.M. Serrano, Repository with the source code for the PhD thesis manuscript: "Towards optimal resource management in solar thermal applications: CSP and desalination". DOI: [10.1596/XXX](https://doi.org/10.1596/XXX)

APPENDIX

Open source is like academia is meant to be. You're paid a salary but your research contributions are distributed to the public, freely.
//

El código abierto es como el mundo académico debería de ser. Se te paga un salario, pero el fruto de tu investigación es distribuido a la sociedad, de manera libre.

A

MED Performance Evaluation

A.1 Uncertainty estimation through first-order Taylor series approximation

In this appendix, expressions for the uncertainty estimation of energetic and separation metrics are shown.

A.1.1 Specific Thermal Energy Consumption (STEC)

$$\Delta STEC = \left(\left(\left| \frac{\delta STEC}{\delta \dot{m}_d} \right| \Delta \dot{m}_d \right)^2 + \left(\left| \frac{\delta STEC}{\delta \dot{m}_s} \right| \Delta \dot{m}_s \right)^2 + \left(\left| \frac{\delta STEC}{\delta T_s} \right| \Delta T_s \right)^2 \right)^{1/2} \quad (\text{A.1})$$

Calculating the partial derivatives, the expression is obtained:

where: $T_s = T_{s,in} - T_{s,out} \rightarrow \Delta T_s = \Delta(T_{s,in} - T_{s,out})$.
If they are the same sensor and were calibrated at the same time using the same calibration standard

$$STEC \pm \Delta STEC \left[\frac{\text{kWh}_{\text{th}}}{\text{m}^3} \right] = \frac{\dot{m}_s c_p T_s}{\dot{m}_d} \pm \frac{c_p}{\dot{m}_d} \times \left[(T_s \Delta \dot{m}_s)^2 + (\dot{m}_s \Delta T_s)^2 + (\dot{m}_s T_s \dot{m}_d^{-1} \Delta \dot{m}_d)^2 \right]^{1/2} \quad (\text{A.2})$$

A.1.2 Specific Electrical Energy Consumption (SEEC)

$$SEEC \pm \Delta SEEC \left[\frac{\text{kWh}_e}{\text{m}^3} \right] = \frac{\sum_{i=1}^N E_i}{\dot{m}_d} \pm \left[\left(\frac{\sum_{i=1}^N \Delta E_i}{\dot{m}_d} \right)^2 + \left(\frac{\sum_{i=1}^N E_i}{\dot{m}_d^2} \Delta \dot{m}_d \right)^2 \right]^{1/2} \quad (\text{A.3})$$

A.1.3 Performance Ratio

$$PR \pm \Delta PR = \frac{\dot{m}_d \Delta h_{ref}}{\dot{m}_s \Delta h_s} \pm \frac{\Delta h_{ref}}{\dot{m}_s \Delta h_s} \left[(\Delta \dot{m}_d)^2 + \dot{m}_d^2 \left(\left(\frac{\Delta \dot{m}_s}{\dot{m}_s} \right)^2 + \left(\frac{\Delta(\Delta h_s)}{\Delta h_s} \right)^2 \right) \right]^{1/2} \quad (\text{A.4})$$

A.1.4 Waste heat performance ratio

$$PR_{WH} \pm \Delta PR_{WH} = \frac{\dot{m}_d}{\dot{m}_s T} \frac{\Delta h_{ref}}{c_p} \pm \frac{\Delta h_{ref}}{c_p} \frac{1}{\dot{m}_s T} \\ \times \left[(\Delta \dot{m}_d)^2 + \dot{m}_d^2 \left(\frac{\Delta \dot{m}_s}{\dot{m}_s} + \frac{\Delta T}{T} \right)^2 \right]^{1/2} \quad (A.5)$$

where: $T = T_{s,in} - T_{c,in} \rightarrow \Delta T = \Delta T_{s,in} + \Delta T_{c,in}$

A.1.5 Recovery ratio

$$RR \pm \Delta RR = \frac{\dot{m}_d}{\dot{m}_f} \pm \left(\left(\frac{1}{\dot{m}_f} \Delta \dot{m}_d \right)^2 + \left(\frac{\dot{m}_d}{\dot{m}_f^2} \Delta \dot{m}_f \right)^2 \right)^{1/2} \quad (A.6)$$

A.1.6 Concentration factor

$$CF \pm \Delta CF = \frac{\dot{m}_f}{\dot{m}_b} \pm \frac{1}{\dot{m}_b} \left(\left(1 + \frac{\dot{m}_f}{\dot{m}_b} \right)^2 \cdot \Delta \dot{m}_f^2 + \left(\dot{m}_f \cdot \Delta \dot{m}_b \right)^2 \right)^{1/2} \quad (A.7)$$

where: $\dot{m}_b = \dot{m}_f - \dot{m}_d \rightarrow \Delta \dot{m}_b = \Delta \dot{m}_f + \Delta \dot{m}_d$

A.2 Exergy calculations

Exergy consists on two components: thermomechanical exergy and chemical exergy. When performing an exergetic analysis, the balances of the exergy flows of interest are calculated given the control volume presented in Fig. ???. Any external stream entering the control volume is considered an exergy input (\dot{Ex}_{in}), while any stream leaving it is considered an exergy output (\dot{Ex}_{out}). A general expression to determine the specific exergy flow (\dot{e}_x) of a stream is given in Equation A.8, where the first two summands represent the thermomechanical component and the last the chemical component.

$$\dot{e}_x = (h - h^*) - T_0(s - s^*) + \sum_{i=1}^n w_i(\mu_i^* - \mu_i^0). \quad (A.8)$$

In Equation A.8, the variables h , s , μ , and w represent the specific enthalpy, specific entropy, chemical potential, and mass fraction, respectively. The properties denoted with an asterisk in the equation are calculated at the restricted dead state conditions (when the temperature and pressure of the system change to match the temperature and pressure of the environment). On the other hand, properties labeled with a superscript of “0” are determined at the global dead state (when the concentration is also changed to match that of the environment). The subscript i represents a species (NaCl, H₂O and others if considered). Notice that the chemical exergy component in this work has been calculated by two approaches: empirical correlations (i) and modelling seawater as an electrolyte for a solution of NaCl with the same concentration as the feedwater salinity (ii). In the latter case, the required activity coefficients have been determined by Pitzer equations [209].

Finally, in order to calculate the specific exergy flows, libraries in MATLAB [210, 211] and Python [romera_jjgomera_2021a] are available. However, they are limited to 120 kg/kg of concentration. For higher values, the approach used is the modelling of seawater as an electrolyte and in this case the chemical exergy

[209]: Pitzer (1973), “Thermodynamics of Electrolytes. I. Theoretical Basis and General Equations”

[210]: Sharqawy et al. (2010), “Thermophysical Properties of Seawater: A Review of Existing Correlations and Data”

[211]: Nayar et al. (2016), “Thermophysical Properties of Seawater”

flows are determined by the activity coefficients using a free and open source tool [35].

Least and minimum least work of separation. To determine how efficient a desalination plant is at separating fresh water from seawater, it is compared to the thermodynamic minimum. This is the least work required to accomplish the separation and is only achievable with an ideal reversible separator (without entropy generation). It has been analyzed and presented in different ways in the literature [171, 175, 176, 180]. A general expression is shown in Equation A.9 in terms of the Gibbs free energy (g).

$$\dot{W}_{\text{least}} = \dot{m}_d \cdot g_d + \dot{m}_b \cdot g_b - \dot{m}_f \cdot g_f. \quad (\text{A.9})$$

If it is normalized to the distillate production and the flows expressed in terms of the recovery ratio according to Equation 13.1, the expression becomes:

$$\frac{\dot{W}_{\text{least}}}{\dot{m}_d} = g_d + \frac{1 - RR}{RR} \cdot g_b - \frac{1}{RR} \cdot g_f. \quad (\text{A.10})$$

As can be seen in Equation A.10, the least work of separation depends on how much pure water is extracted per unit of feed (RR), and as proven in [169], the higher the RR, the higher the least energy required to produce the separation. In this context, the minimum least work of separation (W_{least}^{\min}) is determined when $RR \rightarrow 0$.

A.3 Separation metrics calculation

The molality of sodium chloride at saturation (see Equation 13.4) is determined using the following correlation that was established by [212] in terms of mass fraction and it is valid for a temperature range between 25 and 80 °C:

$$w_{\text{NaCl,sat}} = a + b \cdot T + c \cdot T^2 + d \cdot T^3 \left[100 \text{g}_{\text{NaCl}} / \text{g}_w \right]$$

Likewise, the following conversion formula between mass fraction and molality can be used:

$$b_{\text{NaCl,sat}} = \frac{w_{\text{NaCl,sat}} / 100}{M_{\text{NaCl}} \left(1 - w_{\text{NaCl,sat}} / 100 \right)} \left[\text{mol}_{\text{NaCl}} / \text{g}_w \right]$$

Where M_{NaCl} is the molecular weight of NaCl in g/mol.

[35]: Marcellos et al. (2021), *PyEqulon*

[171]: Lienhard et al. (2017), "Thermodynamics, Exergy, and Energy Efficiency in Desalination Systems"

[175]: Spiegler et al. (2001), "El-Sayed, Y.M."

[176]: Sharqawy et al. (2011), "On Exergy Calculations of Seawater with Applications in Desalination Systems"

[180]: Thiel et al. (2015), "Energy Consumption in Desalinating Produced Water from Shale Oil and Gas Extraction"

[169]: Mistry et al. (2011), "Entropy Generation Analysis of Desalination Technologies"

[212]: Pinho et al. (2005), "Solubility of NaCl, NaBr, and KCl in Water, Methanol, Ethanol, and Their Mixed Solvents"

where:

- $a = 5.671 \cdot 10^1$
- $b = -2.713 \cdot 10^{-1}$
- $c = 7.598 \cdot 10^{-4}$
- $d = -6.373 \cdot 10^{-7}$

A.4 Control system and steady state identification parameters

This appendix section provides reference tables outlining parameters used in the algorithms discussed in this document. Table A.2 summarizes the parameter values for the PID-based process control, while Table A.1 details those for steady-state detection. For the first, K_p , K_i , and K_d are the proportional, integral, and derivative gains, respectively (see Section 3.3.1 (PID controllers)). In the latter, γ_a represents the wavelet transform threshold, γ_d the derivative threshold and finally T_{ss} the time window duration. The algorithm they are used in is described in Section 13.4.1 (Monitoring: steady-state identification). In both tables, T_s represents the sample time.

Parameter	Variable				
	$P_{v,c}$	$P_{v,1}$	\dot{m}_d	\dot{m}_s	\dot{m}_f
Y_0 [v.u.]	0.05	0.05	0.1	0.3	0.2
Y_d [v.u./s]	0.002	0.03	0.001	0.02	0.001
Ts [s]			1		
Tss [s]			600		

Table A.1: Parameters for the steady-state detection algorithm, where s.u. represents that the parameter has the same units to the related variable

Parameter	Subsystem					
	Brine level	Distillate level	Condenser outlet temperature	Heat source temperature	Heat source flow	Feedwater flow
Kp [i.u./o.u.]	-0.01	-0.05	-1.7526	1	5	4
Ki[i.u.](o.u.s)]	-0.02	-0.005	-0.0322	0.2	1	1
Kd [i.u.](o.u./s)]	0	0	0	0.5	0.8	0
Ts [s]	5	3	5	2	1	1
Configuration	Parallel configuration					

Table A.2: Parameters for the PID based process control, where i.u. represents the input variable units, and o.u. the output units.

B

MED First-Principles Model

TL;DR

A first-principles model of a MED plant is presented in this appendix. It is based on thermodynamic equations and mass and energy balances and can be used in two modes depending on the application.

This model simulates thermal and mass transfer processes in a MED plant, such as the one at PSA. The MED process consists of a series of effects (evaporators) and preheaters connected in sequence. In each effect, seawater partially evaporates under decreasing pressure and temperature conditions, while in the preheaters, the feed water is gradually warmed using the condensation heat from the vapor produced in the effects.

The model is based on several assumptions to simplify the calculations:

- ▶ Steady-state operation.
- ▶ Negligible heat losses to the environment.
- ▶ Isothermal physical properties have been considered for all cases.

And is based on several works found in the literature [184, 213, 214] but extends them by including more detailed calculations for the different heat transfer modes (boiling, flashing), considering not-constant Non-Equilibrium Allowance (NEA) and BPE effects, and considering the flashing process of the distillate. It works both at nominal and partial load conditions.

To solve the model, an iterative process is followed where the model proceeds effect by effect, starting from the first stage. For each effect, it uses nonlinear solvers to solve a system of non linear equations (see Figures ??–??) ensuring consistent heat exchange and energy balances. The preheaters are solved in a similar manner. Throughout the process, mass and energy conservation are verified. After completing a cell, the model updates the inlet conditions for the next effect taking into consideration the distillate vapor lost in the preheater-effect distribution line, temperature losses and more importantly, the plant's condensate distribution layout (see Figure B.8).

The model can be used in two modes depending on the application: *calibration mode* and *simulation mode*. Both modes share the same equations and structure, but differ in the inputs required and the parameters used.

[184]: Mistry et al. (2013), "An Improved Model for Multiple Effect Distillation"

[213]: Palenzuela et al. (2014), "Steady State Model for Multi-Effect Distillation Case Study"

[214]: El-Dessouky et al. (1998), "Steady-State Analysis of the Multiple Effect Evaporation Desalination Process"

B.1 Nomenclature

Nomenclature inconsistency

Flows (either mass or volumetric) are represented with a capital M , different to the rest of the manuscript where lowercase \dot{m} is used for mass flows or q for volumetric flows.

Plant parameters:

- ▶ Number of effects and preheaters (N_{ef} , N)

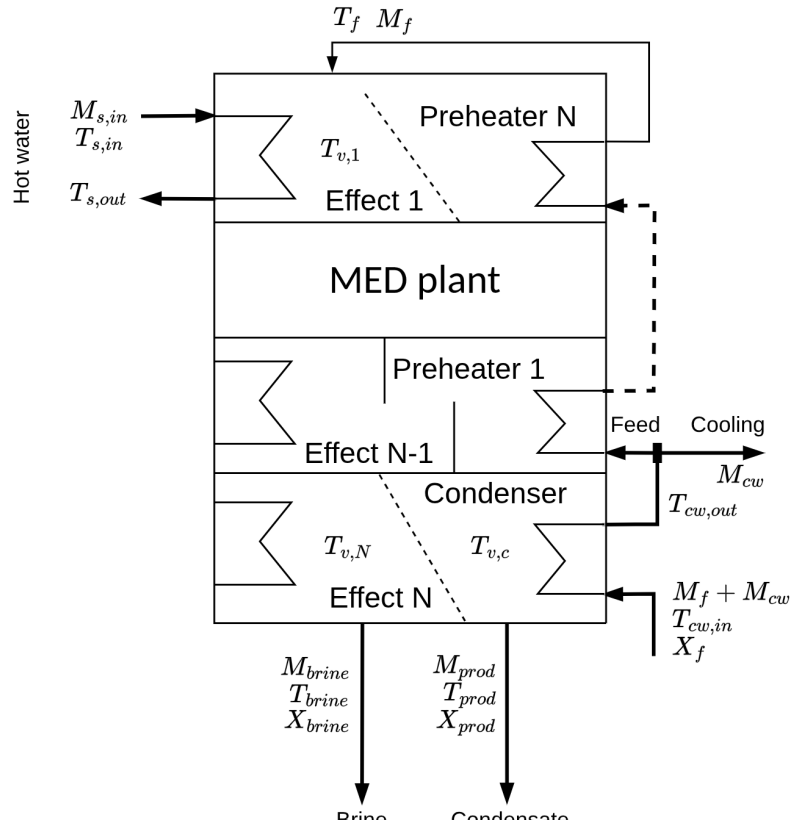


Figure B.1: Overall schematic of the MED model with inputs, outputs, main variables and components

- ▶ Mixer distribution ratios. ($\mathbf{Y} \in \mathbb{R}^3$)
- ▶ Effect and preheater areas ($\mathbf{A}_{ef} \in \mathbb{R}^N, \mathbf{A}_{ph} \in \mathbb{R}^N$) [m^2]
- ▶ Condenser area (\mathbf{A}_c) [m^2]
- ▶ m, m_2 : indices for effects without/with mixer distillate []

Model parameters:

- ▶ Overall effect heat transfer coefficients ($\mathbf{U}_{ef} \in \mathbb{R}^N$) [kW/m^2K]
- ▶ Overall preheater heat transfer coefficients ($\mathbf{U}_{ph} \in \mathbb{R}^N$) [kW/m^2K]
- ▶ Preheater-effect distribution line vapor-loss factor due to condensation ($\mathbf{M}_v \in \mathbb{R}^2$) []

Flows [kg/s]:

- ▶ M_s : Heat source
- ▶ M_{cw} : Cooling water
- ▶ M_f : Feedwater
- ▶ M_{prod} : total distillate production
- ▶ M_{brine} : total brine discharge
- ▶ $M_{v,in}, M_{v,out}$: vapor mass flow into / out of effect
- ▶ $M_{b,in}, M_{b,out}$: brine mass flow into / out of effect
- ▶ M_{gb}, M_{gf} : vapor generated by boiling / flashing
- ▶ M_{dest} : mixed distillates entering the effect ; $M_{dest,f}$: fraction that flashes
- ▶ $M_{d,in}$: distillate from previous effect
- ▶ M_{vh} : distillate from previous preheater
- ▶ $M_{d,out}$: distillate out of effect
- ▶ M_{da}, M_{db} : distillate split from mixer to effect / bypass

- $M_{mix,in}$: distillate in distribution line
- $M_{mix,out}$: out distillate from effect to distribution line
- M_{bb} : non-flashing brine

Temperatures [$^{\circ}\text{C}$] (some omitted when equivalent to flows):

- $T_{s,in}, T_{s,out}$: heat source in/out first effect
- $T_{cw,in}, T_{cw,out}$: cooling water in/out condenser
- T_f : preheated feedwater
- $T_{mix,in}, T_{mix,out}, T_{mixx}$: mixer in/out and after subcooling in effect
- T_{vv}, T_{dd} : preheater and previous-effect distillate temperatures after subcooling
- $T_{ph,in}, T_{ph,out}$: preheater in/out

Concentrations and pressures:

- $X_{b,in}, X_{b,out}, X_{bb}$: brine salinity in/out and non-flashing brine [g/kg]
- X_f : feedwater salinity [g/kg]
- P_s : source pressure at first effect [bar]

Heat contributions [W]:

- \dot{Q}_{vant} : from previous-effect vapor
- \dot{Q}_{phant} : from preheater distillate
- \dot{Q}_{efant} : from previous-effect distillate
- \dot{Q}_{mix} : from distribution-line mixer
- \dot{Q}_δ : from condensed vapor along path
- \dot{Q}_{dest} : total from distillate streams
- $\dot{Q}_{extsource}$: from external heat source

Auxiliary components and losses:

- Demister: v_{vap} vapor velocity [m/s]; h_{dem} height [m]; w_{dem} thickness [m]; l_{dem} length [m]; ρ_{dem} packing density [kg/m^3]; D_{dem} wire diameter [mm]
- Piping (preheater–effect): L_{tub} length [m]; D_{tub} internal diameter [mm]

B.1.1 Calibration mode

In the *calibration mode* (see Figure B.3), the model is used to obtain different detailed parameters/outputs of interest that cannot be measured directly, such as the heat transfer coefficients, the different heat transfer modes contribution (boiling, flashing, etc), per effect brine concentration, per effect distillate production, etc.. The computed parameters in this mode can then be used to generate models for these parameters. For this purpose, the model requires an extended set of inputs, including measured temperatures or pressures per effect and preheater¹.

To solve it, an initial guess of ΔM_v is provided, and then the model iteratively solves for the heat transfer coefficients (U_{ef} and U_{ph}) and outlet conditions until the final condenser. The total distillate produced is compared with the measured value, and ΔM_v is adjusted accordingly. This process continues until the calculated distillate matches the measured value within a specified tolerance.

This mode can be used to identify loss of performance, fouling and other issues. Evaluated over time, it can provide trends and be integrated into predictive maintenance strategies. It can also be used to generate data-driven models for the different parameters, which can then be used in the *simulation mode*. Also, it provides more detailed outputs that can be used for further analysis by the O&M team.

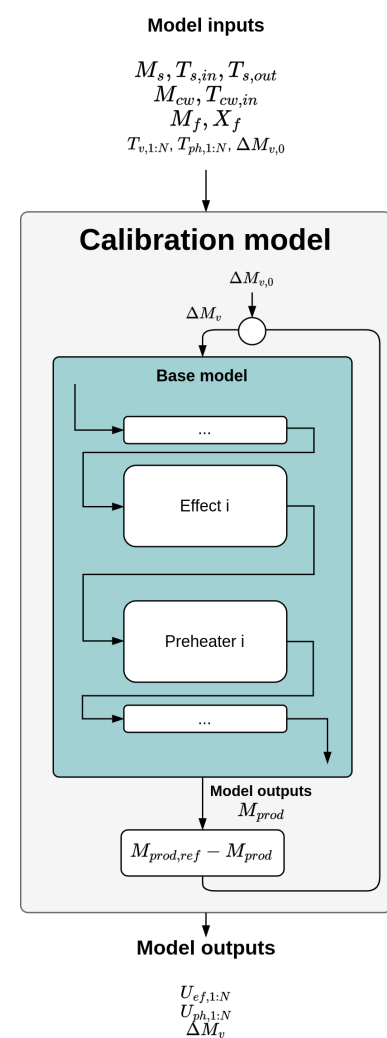


Figure B.2: MED model calibration mode diagram with inputs and outputs

1: Or a limited set of them, which the rest being estimated by interpolation or other methods

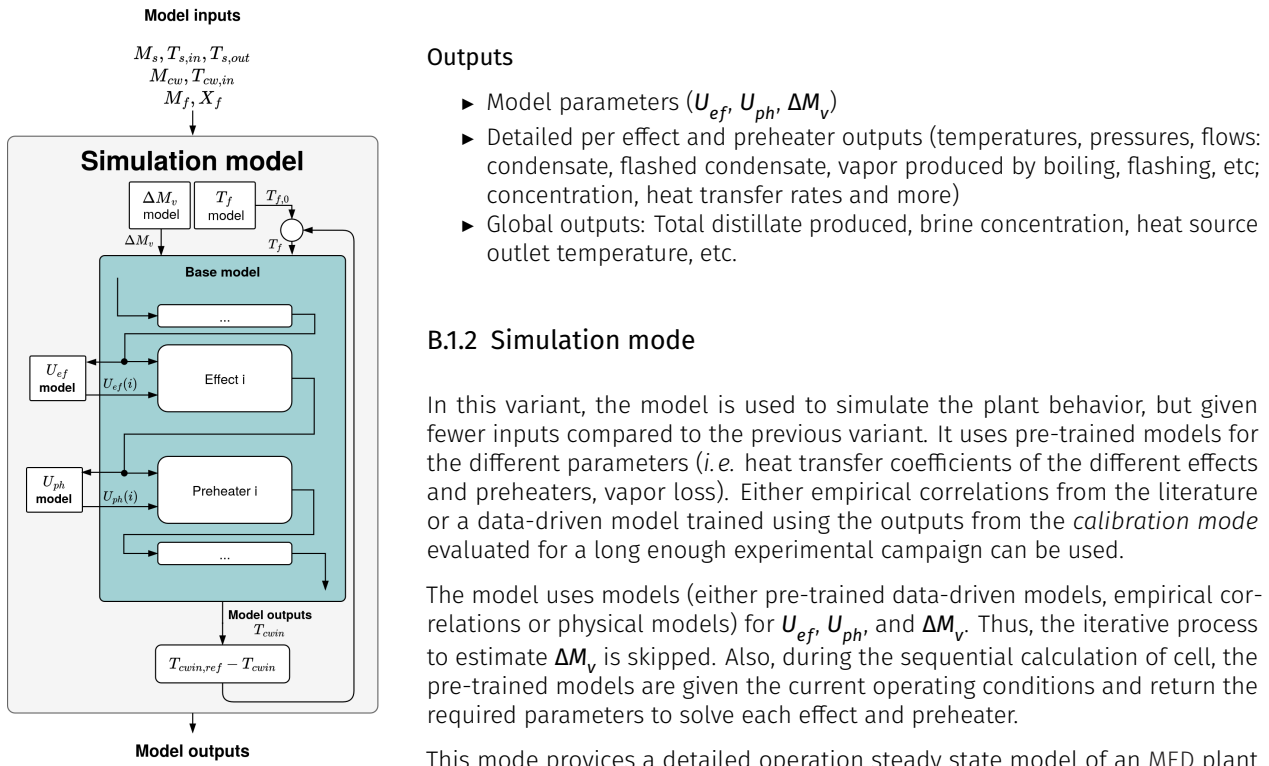


Figure B.3: MED model simulation mode diagram with inputs and outputs

B.1.2 Simulation mode

In this variant, the model is used to simulate the plant behavior, but given fewer inputs compared to the previous variant. It uses pre-trained models for the different parameters (*i.e.* heat transfer coefficients of the different effects and preheaters, vapor loss). Either empirical correlations from the literature or a data-driven model trained using the outputs from the *calibration mode* evaluated for a long enough experimental campaign can be used.

The model uses models (either pre-trained data-driven models, empirical correlations or physical models) for U_{ef} , U_{ph} , and ΔM_v . Thus, the iterative process to estimate ΔM_v is skipped. Also, during the sequential calculation of cell, the pre-trained models are given the current operating conditions and return the required parameters to solve each effect and preheater.

This mode provides a detailed operation steady state model of an MED plant with minimum assumptions and that does not require outputs of the plant as inputs.

B.2 Implementation

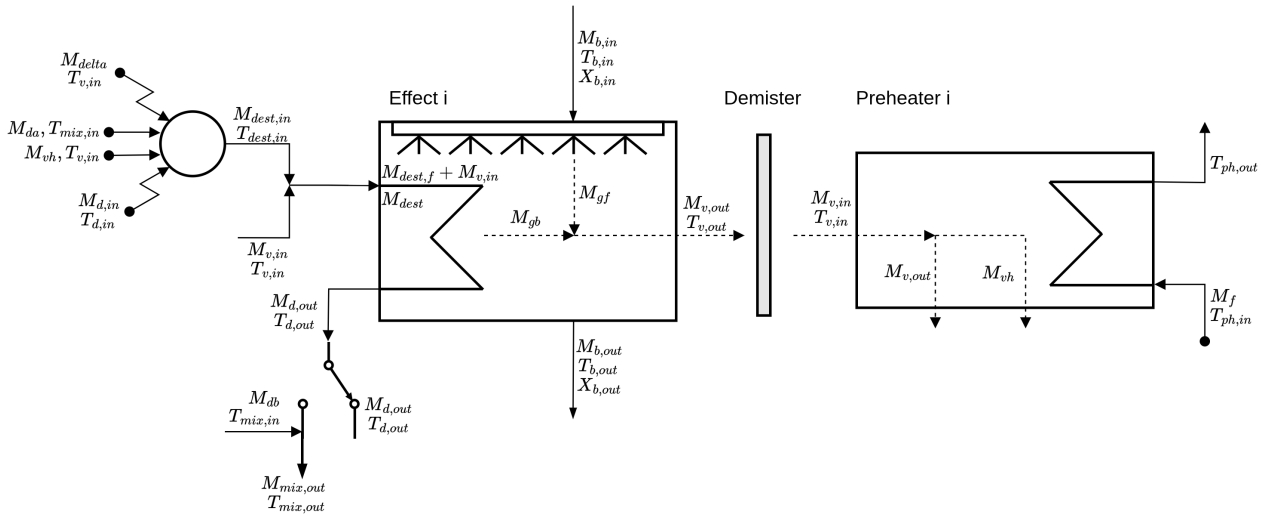


Figure B.4: Detailed schematic of a single cell in the MED containing the effect or evaporator (left) and the preheater (right)

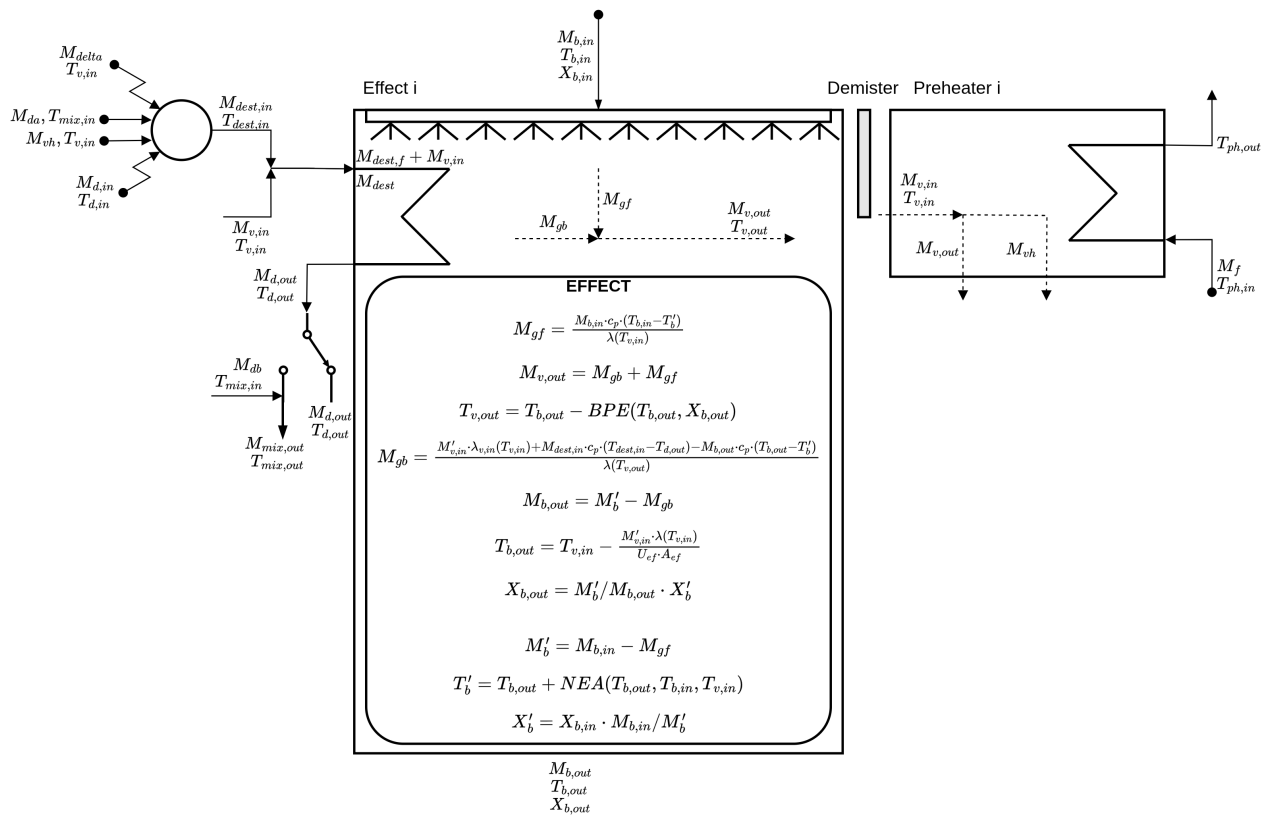


Figure B.5: Detailed schematic of a single cell in the MED with the effect's equations.

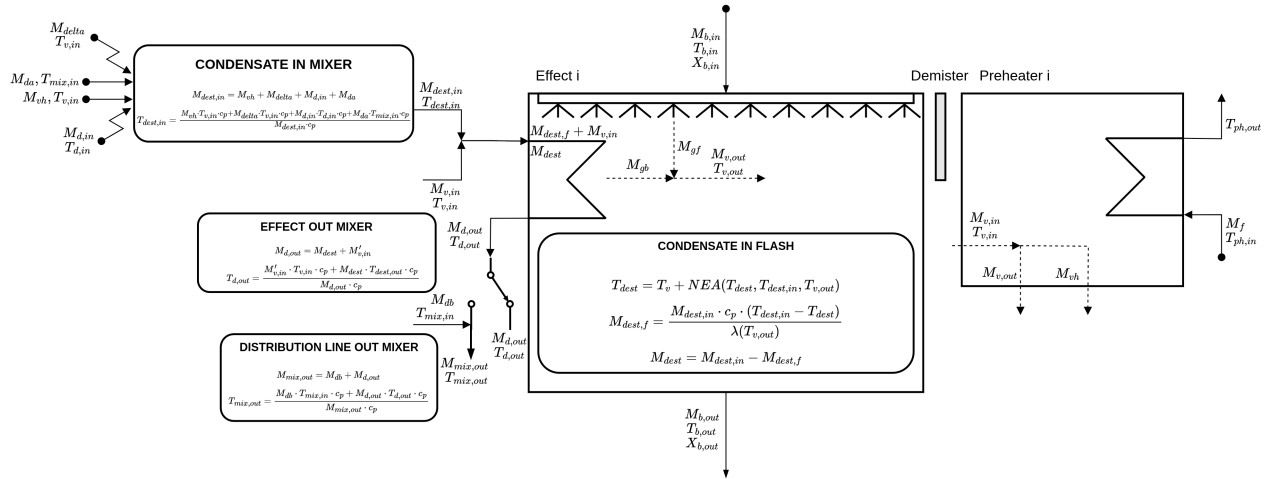


Figure B.6: Detailed schematic of a single cell in the MED with the energy source side equations and internal effect condensate flashing.

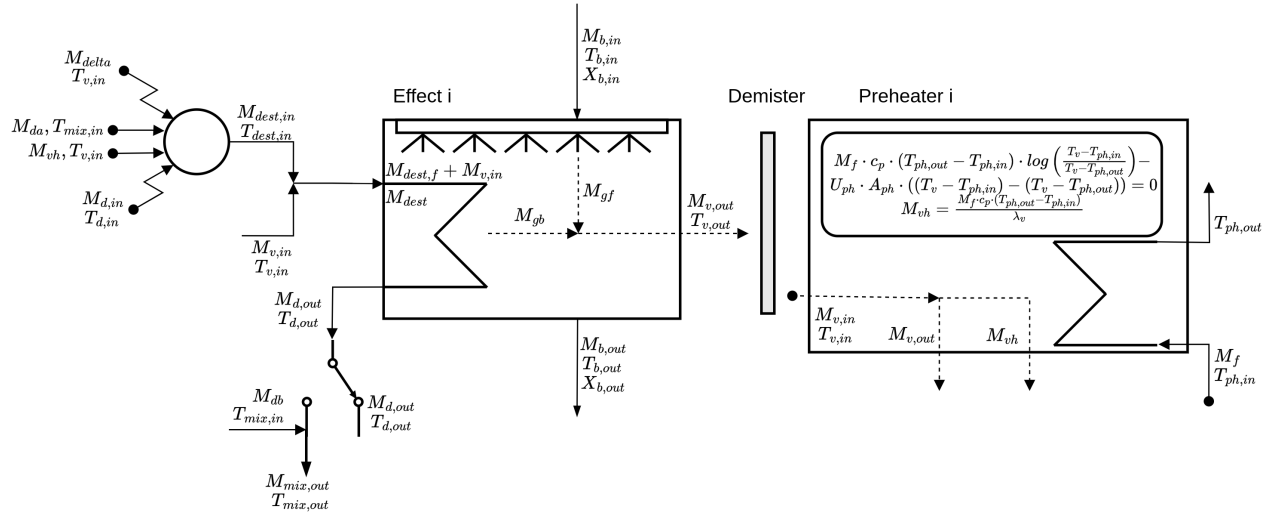


Figure B.7: Detailed schematic of a single cell in the MED with the preheater's equations.

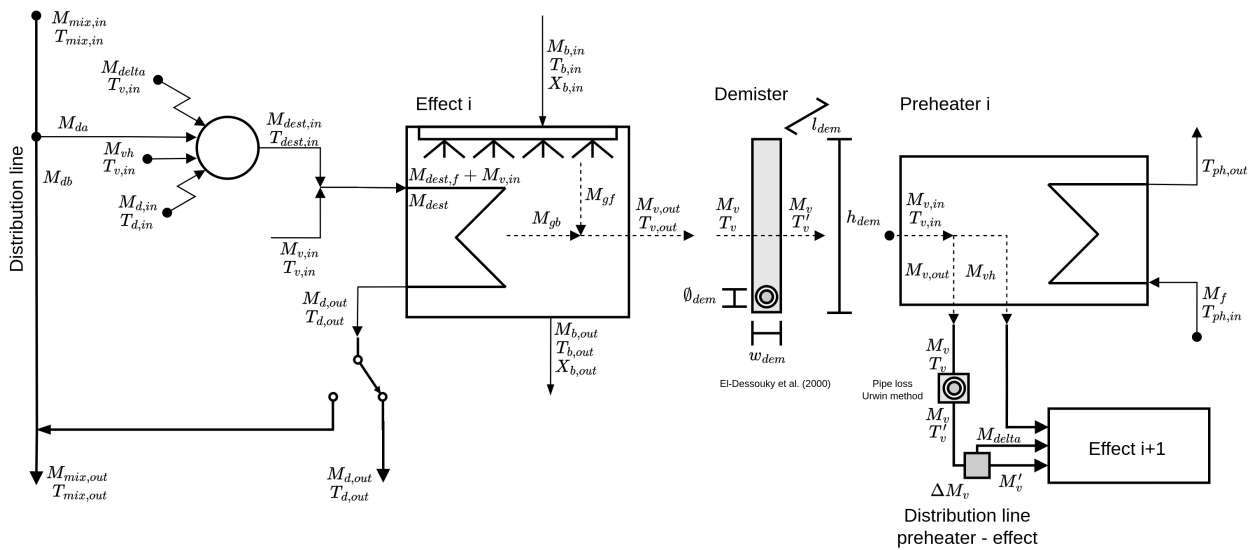


Figure B.8: Detailed schematic of a single cell in the MED with distribution lines for the energy source side and generated steam. Also, auxiliary elements like demister and preheater-effect distribution line geometry.

B.3 Validation

[163]: Palenzuela et al. (2016), “Experimental Parametric Analysis of a Solar Pilot-Scale Multi-Effect Distillation Plant”

Using the same dataset presented in Section 12.2.4 (MED) – Palenzuela et al. [163], the *calibration mode* of the model is evaluated, with the results shown in Figure B.10 (a). Then it was divided in training and validation set and the training set was used to generate data-driven models for the different parameters required in the *simulation mode*. The *simulation mode* was then evaluated using the validation set and the results are presented in Figure B.10 (b).

The results demonstrate that both variants of the model can accurately predict the output variables such as the plant’s distillate production. As expected, the calibration model performs better since it uses more detailed inputs, but the simulation model also shows good accuracy. Finally, a comparison of both modes

obtained heat transfer coefficients is shown in Figure B.9. They show similar trends except for part of the experimental dataset where higher discrepancies are observed for the latter effects (effects 11–14). This can probably be explained by the fact that the sequential calculation of the model coupled to its high non-linearity means that error is accumulated, where small deviations in the first effects can lead to larger errors in the latter ones. Nonetheless, both models overall provide similar results and trends.

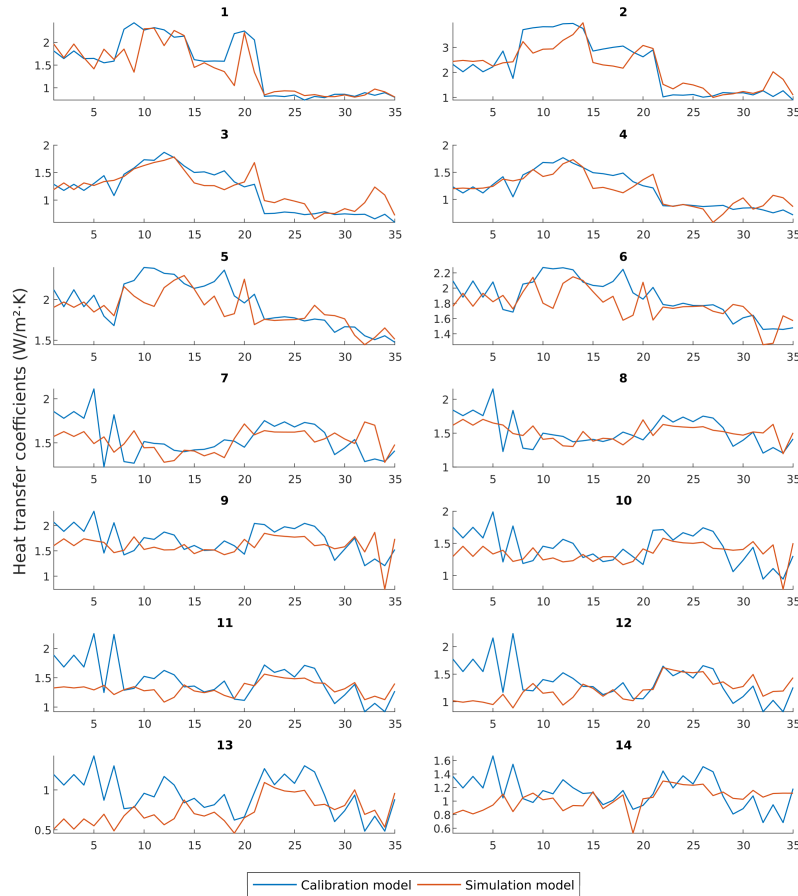
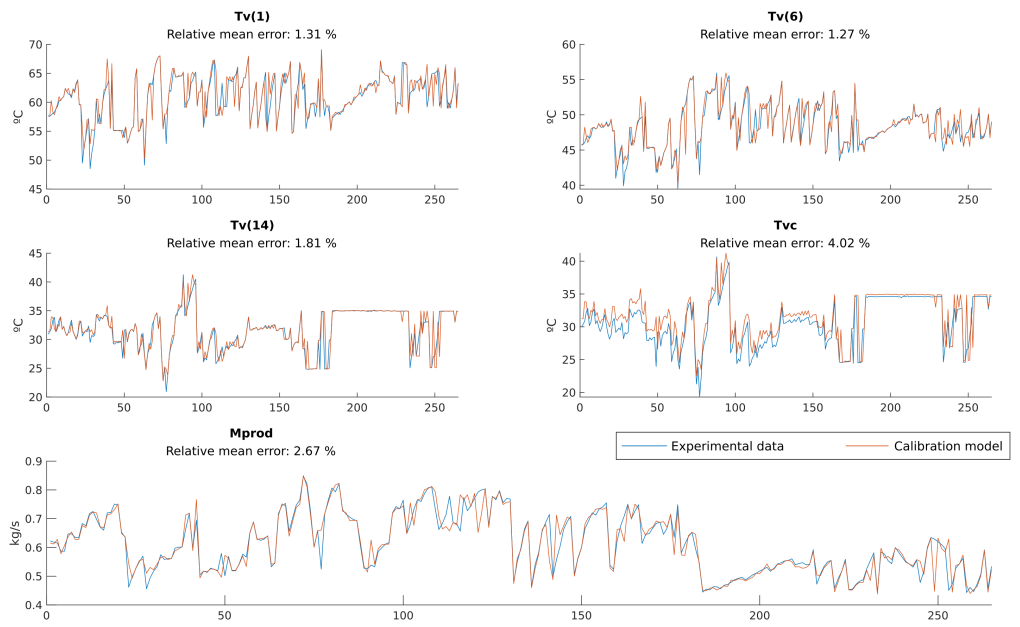
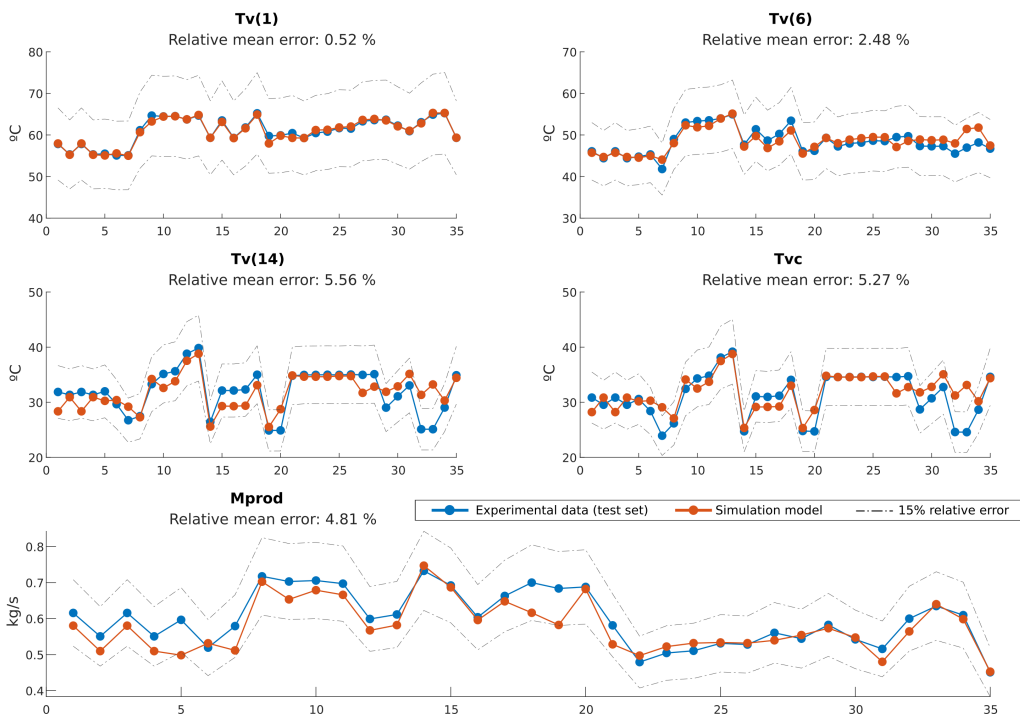


Figure B.9: Heat transfer coefficients comparison between *calibration mode* and *simulation mode* for the validation set



(a) Calibration mode



(b) Simulation mode

Figure B.10: MED first-principles model validation

Bibliography

Here are the references in citation order.

- [1] Andrew Sayer. *Why We Can't Afford the Rich*. 1st ed. Bristol University Press, 2016. (Visited on 06/27/2024) (cited on page 3).
- [2] José Esquinas Alcázar. *Rumbo al Ecocidio: Cómo frenar la amenaza a nuestra supervivencia*. Barcelona: Espasa, 2023. 256 pp. (cited on page 3).
- [3] World Meteorological Organization. *State of the Global Climate 2024*. Vol. 1368. Geneva: United Nations, 2025 (cited on pages 3, 4).
- [4] IEA. *Global Energy Review 2025*. Paris, Mar. 24, 2025 (cited on page 3).
- [5] Lucas Henneman et al. "Mortality Risk from United States Coal Electricity Generation." In: *Science* 382.6673 (Nov. 24, 2023), pp. 941–946. doi: [10.1126/science.adf4915](https://doi.org/10.1126/science.adf4915). (Visited on 10/14/2025) (cited on page 3).
- [6] Roland Geyer, Jenna R. Jambeck, and Kara Lavender Law. "Production, Use, and Fate of All Plastics Ever Made." In: *Science Advances* 3.7 (July 19, 2017), e1700782. doi: [10.1126/sciadv.1700782](https://doi.org/10.1126/sciadv.1700782). (Visited on 10/14/2025) (cited on page 3).
- [7] Robert McSweeney and Ayesha Tandon. *Mapped. How Climate Change Affects Extreme Weather around the World*. Carbon Brief. Nov. 18, 2024. URL: <https://interactive.carbonbrief.org/attribution-studies/> (visited on 10/14/2025) (cited on pages 3, 5).
- [8] IRENA. Press Release: *World Breaks Renewable Records but Must Move Faster to Hit 2030 Tripling Goal*. Oct. 14, 2025. URL: <https://web.archive.org/web/20251014182847/https://mailchi.mp/79ce55416f16/press-release-world-breaks-renewable-records-but-must-move-faster-to-hit-2030-tripling-goal?e=fdf79ae0c8> (visited on 10/14/2025) (cited on page 3).
- [9] Columbia Law School. *President Trump Prioritizes Fossil Fuel Development and Rolls Back Climate Action in Energy* | Sabin Center for Climate Change Law. Oct. 5, 2025. URL: <https://web.archive.org/web/20251005195227/https://climate.law.columbia.edu/content/president-trump-prioritizes-fossil-fuel-development-and-rolls-back-climate-action-energy> (visited on 10/15/2025) (cited on page 3).
- [10] elDiario.es. *La Confusión Sobre Las Causas Del Apagón Recrudece La Batalla Ideológica Entre Renovables y Nuclear*. 2025. URL: https://web.archive.org/web/20251014183542/https://www.eldiario.es/economia/confusion-causas-apagon-recrudece-batalla-ideologica-renovables-nuclear_1_12258635.html (visited on 10/14/2025) (cited on page 3).
- [11] BARREAU Marie-Sophie Amelie. "The Future of Climate Migration." In: (2025) (cited on page 4).
- [12] Diana Hicks et al. "Bibliometrics. The Leiden Manifesto for Research Metrics." In: *Nature* 520.7548 (Apr. 2015), pp. 429–431. doi: [10.1038/520429a](https://doi.org/10.1038/520429a). (Visited on 05/01/2025) (cited on page 5).
- [13] Mark D. Wilkinson et al. "The FAIR Guiding Principles for Scientific Data Management and Stewardship." In: *Scientific Data* 3.1 (1 Mar. 15, 2016), p. 160018. doi: [10.1038/sdata.2016.18](https://doi.org/10.1038/sdata.2016.18). (Visited on 06/16/2023) (cited on page 5).
- [14] Faisal Asfand et al. "Thermodynamic Performance and Water Consumption of Hybrid Cooling System Configurations for Concentrated Solar Power Plants." In: *Sustainability* 12.11 (2020). doi: [10.3390/su12114739](https://doi.org/10.3390/su12114739) (cited on pages 8, 59).
- [15] Ayman Mdallal et al. "Modelling and Optimization of Concentrated Solar Power Using Response Surface Methodology: A Comparative Study of Air, Water, and Hybrid Cooling Techniques." In: *Energy Conversion and Management* 319 (Nov. 1, 2024), p. 118915. doi: [10.1016/j.enconman.2024.118915](https://doi.org/10.1016/j.enconman.2024.118915). (Visited on 06/17/2025) (cited on pages 8, 59).
- [16] Hemin Hu et al. "Thermodynamic Characteristics of Thermal Power Plant with Hybrid (Dry/Wet) Cooling System." In: *Energy* 147 (Mar. 15, 2018), pp. 729–741. doi: [10.1016/j.energy.2018.01.074](https://doi.org/10.1016/j.energy.2018.01.074). (Visited on 03/10/2023) (cited on pages 8, 43, 59).
- [17] Tao Tang et al. "Study on Operating Characteristics of Power Plant with Dry and Wet Cooling Systems." In: *Energy and Power Engineering* 5.4 (4 June 30, 2013), pp. 651–656. doi: [10.4236/epe.2013.54B126](https://doi.org/10.4236/epe.2013.54B126). (Visited on 06/13/2025) (cited on pages 8, 59).

- [18] Wanchai Asvapoositkul and Mantheerapol Kuansathan. "Comparative Evaluation of Hybrid (Dry/Wet) Cooling Tower Performance." In: *Applied Thermal Engineering* 71.1 (Oct. 5, 2014), pp. 83–93. doi: [10.1016/j.applthermaleng.2014.06.023](https://doi.org/10.1016/j.applthermaleng.2014.06.023). (Visited on 03/10/2023) (cited on pages 8, 43, 44, 59).
- [19] G. Barigozzi, A. Perdichizzi, and S. Ravelli. "Performance Prediction and Optimization of a Waste-to-Energy Cogeneration Plant with Combined Wet and Dry Cooling System." In: *Applied Energy* 115 (Feb. 15, 2014), pp. 65–74. doi: [10.1016/j.apenergy.2013.11.024](https://doi.org/10.1016/j.apenergy.2013.11.024). (Visited on 03/10/2023) (cited on pages 8, 43, 59).
- [20] Lidia Martín and Mariano Martín. "Optimal Year-Round Operation of a Concentrated Solar Energy Plant in the South of Europe." In: *Applied Thermal Engineering* 59.1 (Sept. 25, 2013), pp. 627–633. doi: [10.1016/j.applthermaleng.2013.06.031](https://doi.org/10.1016/j.applthermaleng.2013.06.031). (Visited on 06/13/2025) (cited on pages 8, 40, 59).
- [21] Mariano Martín. "Optimal Annual Operation of the Dry Cooling System of a Concentrated Solar Energy Plant in the South of Spain." In: *Energy* 84 (May 1, 2015), pp. 774–782. doi: [10.1016/j.energy.2015.03.041](https://doi.org/10.1016/j.energy.2015.03.041). (Visited on 06/12/2025) (cited on pages 8, 42, 59).
- [22] L. E. Wiles et al. *Description and Cost Analysis of a Deluge Dry/Wet Cooling System*. PNL-2498. Battelle Pacific Northwest Labs., Richland, WA (USA), June 1, 1978. doi: [10.2172/6700397](https://doi.org/10.2172/6700397). (Visited on 08/10/2025) (cited on pages 8, 42, 43, 59).
- [23] F. R. Zaloudek et al. *Study of the Comparative Costs of Five Wet/Dry Cooling Tower Concepts*. BNWL-2122. Battelle Pacific Northwest Labs., Richland, WA (USA), Sept. 1, 1976. doi: [10.2172/7101320](https://doi.org/10.2172/7101320). (Visited on 08/09/2025) (cited on pages 8, 42, 43, 59).
- [24] Shahab Rohani et al. "Optimization of Water Management Plans for CSP Plants through Simulation of Water Consumption and Cost of Treatment Based on Operational Data." In: *Solar Energy* 223 (July 15, 2021), pp. 278–292. doi: [10.1016/j.solener.2021.05.044](https://doi.org/10.1016/j.solener.2021.05.044). (Visited on 06/17/2025) (cited on pages 8, 38, 40, 43, 44, 59).
- [25] Chaouki Ghenai et al. "Performance Analysis and Optimization of Hybrid Multi-Effect Distillation Adsorption Desalination System Powered with Solar Thermal Energy for High Salinity Sea Water." In: *Energy* 215 (Jan. 15, 2021), p. 119212. doi: [10.1016/j.energy.2020.119212](https://doi.org/10.1016/j.energy.2020.119212). (Visited on 01/08/2023) (cited on pages 9, 137).
- [26] Hyuk Soo Son et al. "Pilot Studies on Synergetic Impacts of Energy Utilization in Hybrid Desalination System: Multi-effect Distillation and Adsorption Cycle (MED-AD)." In: *Desalination* 477 (Mar. 1, 2020), p. 114266. doi: [10.1016/j.desal.2019.114266](https://doi.org/10.1016/j.desal.2019.114266). (Visited on 01/07/2023) (cited on pages 9, 137).
- [27] Greg Burgess and Keith Lovegrove. "Solar Thermal Powered Desalination: Membrane versus Distillation Technologies." In: (Jan. 2000) (cited on pages 9, 137).
- [28] F. Silva Pinto and R. Cunha Marques. "Desalination Projects Economic Feasibility: A Standardization of Cost Determinants." In: *Renewable and Sustainable Energy Reviews* 78 (Oct. 2017), pp. 904–915. doi: [10.1016/j.rser.2017.05.024](https://doi.org/10.1016/j.rser.2017.05.024). (Visited on 07/27/2023) (cited on pages 9, 137).
- [29] Lidia Roca et al. "Solar Field Control for Desalination Plants." In: *Solar Energy* 82.9 (Sept. 1, 2008), pp. 772–786. doi: [10.1016/j.solener.2008.03.002](https://doi.org/10.1016/j.solener.2008.03.002). (Visited on 09/10/2025) (cited on pages 9, 161).
- [30] Ramón González, Lidia Roca, and Francisco Rodríguez. "Economic Optimal Control Applied to a Solar Seawater Desalination Plant." In: *Computers & Chemical Engineering* 71 (Dec. 4, 2014), pp. 554–562. doi: [10.1016/j.compchemeng.2014.10.005](https://doi.org/10.1016/j.compchemeng.2014.10.005). (Visited on 09/09/2025) (cited on pages 9, 161, 162).
- [31] Jose A. Carballo et al. "Optimal Operating Conditions Analysis for a Multi-Effect Distillation Plant According to Energetic and Exergetic Criteria." In: *Desalination*. Desalination Using Renewable Energy 435 (June 1, 2018), pp. 70–76. doi: [10.1016/j.desal.2017.12.013](https://doi.org/10.1016/j.desal.2017.12.013). (Visited on 06/17/2022) (cited on pages 9, 161).
- [32] Aicha Chorak et al. "Experimental Characterization of a Multi-Effect Distillation System Coupled to a Flat Plate Solar Collector Field: Empirical Correlations." In: *Applied Thermal Engineering* 120 (June 25, 2017), pp. 298–313. doi: [10.1016/j.applthermaleng.2017.03.115](https://doi.org/10.1016/j.applthermaleng.2017.03.115). (Visited on 09/10/2025) (cited on pages 9, 107, 161).
- [33] Juan D. Gil et al. "Hybrid NMPC Applied to a Solar-powered Membrane Distillation System." In: *IFAC-PapersOnLine*. 12th IFAC Symposium on Dynamics and Control of Process Systems, Including Biosystems DYCOps 2019 52.1 (Jan. 1, 2019), pp. 124–129. doi: [10.1016/j.ifacol.2019.06.048](https://doi.org/10.1016/j.ifacol.2019.06.048). (Visited on 03/18/2024) (cited on pages 9, 162).
- [34] Francesco Biscani and Dario Izzo. "A Parallel Global Multiobjective Framework for Optimization: Pagmo." In: *Journal of Open Source Software* 5.53 (2020), p. 2338. doi: [10.21105/joss.02338](https://doi.org/10.21105/joss.02338) (cited on pages 10, 25–27).
- [35] Caio Felippe Curitiba Marcellos et al. *PyEqulon: A Python Package For Automatic Speciation Calculations of Aqueous Electrolyte Solutions*. May 2021. Pre-published (cited on pages 10, 155, 195).
- [36] John A. Sokolowski and Catherine M. Banks. *Principles of Modeling and Simulation: A Multidisciplinary Approach*. John Wiley & Sons, Sept. 20, 2011. 211 pp. (cited on pages 11, 13).

- [37] Jiri Nossent, Pieter Elsen, and Willy Bauwens. "Sobol'sensitivity Analysis of a Complex Environmental Model." In: *Environmental Modelling & Software* 26.12 (2011), pp. 1515–1525 (cited on pages 12, 18).
- [38] Carl Edward Rasmussen and Christopher K. I. Williams. *Gaussian Processes for Machine Learning*. Adaptive Computation and Machine Learning. Cambridge, Mass: MIT Press, 2006. 248 pp. (cited on pages 14, 15).
- [39] A. Gelman et al. *Bayesian Data Analysis, Third Edition*. Chapman & Hall/CRC Texts in Statistical Science. Taylor & Francis, 2013 (cited on page 15).
- [40] Martin T. Hagan et al. *Neural Network Design*. Martin Hagan, 2014. 800 pp. (cited on pages 15, 16).
- [41] Mark Hudson Beale, Martin T Hagan, and Howard B Demuth. "Neural Network Toolbox." In: *User's Guide, MathWorks* 2 (2010), pp. 77–81 (cited on page 16).
- [42] Lonnie Hamm, B. Wade Brorsen, and Martin T. Hagan. "Comparison of Stochastic Global Optimization Methods to Estimate Neural Network Weights." In: *Neural Processing Letters* 26.3 (Dec. 1, 2007), pp. 145–158. doi: [10.1007/s11063-007-9048-7](https://doi.org/10.1007/s11063-007-9048-7). (Visited on 03/16/2024) (cited on page 16).
- [43] Leo Breiman. "Random Forests." In: *Machine Learning* 45.1 (Oct. 1, 2001), pp. 5–32. doi: [10.1023/A:1010933404324](https://doi.org/10.1023/A:1010933404324). (Visited on 03/13/2024) (cited on page 17).
- [44] Jerome H. Friedman. "Greedy Function Approximation: A Gradient Boosting Machine." In: *The Annals of Statistics* 29.5 (Oct. 2001), pp. 1189–1232. doi: [10.1214/aos/1013203451](https://doi.org/10.1214/aos/1013203451). (Visited on 08/19/2025) (cited on page 17).
- [45] M. D. McKay, R. J. Beckman, and W. J. Conover. "A Comparison of Three Methods for Selecting Values of Input Variables in the Analysis of Output from a Computer Code." In: *Technometrics* 21.2 (1979), pp. 239–245. doi: [10.2307/1268522](https://doi.org/10.2307/1268522). (Visited on 10/13/2025) (cited on page 18).
- [46] Andrea Saltelli, K. Chan, and E. M. Scott. *Sensitivity Analysis: Gauging the Worth of Scientific Models*. John Wiley & Sons, Oct. 3, 2000. 515 pp. (cited on page 18).
- [47] Xiaojun Wang et al. "Structural Design Optimization Based on the Moving Baseline Strategy." In: *Acta Mechanica Solida Sinica* 33.3 (June 1, 2020), pp. 307–326. doi: [10.1007/s10338-019-00144-0](https://doi.org/10.1007/s10338-019-00144-0). (Visited on 08/24/2025) (cited on page 21).
- [48] R. Farmani and J.A. Wright. "Self-Adaptive Fitness Formulation for Constrained Optimization." In: *IEEE Transactions on Evolutionary Computation* 7.5 (Oct. 2003), pp. 445–455. doi: [10.1109/TEVC.2003.817236](https://doi.org/10.1109/TEVC.2003.817236). (Visited on 03/31/2025) (cited on pages 23, 27).
- [49] Kalyanmoy Deb. "Multi-Objective Optimisation Using Evolutionary Algorithms: An Introduction." In: *Multi-Objective Evolutionary Optimisation for Product Design and Manufacturing*. Springer, 2011, pp. 3–34 (cited on page 23).
- [50] Andreas Wächter and Lorenz T. Biegler. "On the Implementation of an Interior-Point Filter Line-Search Algorithm for Large-Scale Nonlinear Programming." In: *Mathematical Programming* 106.1 (Mar. 1, 2006), pp. 25–57. doi: [10.1007/s10107-004-0559-y](https://doi.org/10.1007/s10107-004-0559-y). (Visited on 08/19/2025) (cited on page 24).
- [51] Tamara G. Kolda, Robert Michael Lewis, and Virginia Torczon. "Optimization by Direct Search: New Perspectives on Some Classical and Modern Methods." In: *SIAM Review* 45.3 (2003), pp. 385–482. doi: [10.1137/S003614450242889](https://doi.org/10.1137/S003614450242889) (cited on page 24).
- [52] John H. Holland. *Adaptation in Natural and Artificial Systems: An Introductory Analysis with Applications to Biology, Control, and Artificial Intelligence*. The MIT Press, Apr. 29, 1992. (Visited on 08/19/2025) (cited on pages 24, 25).
- [53] Ingo Rechenberg. "Evolution Strategy: Nature's Way of Optimization." In: *Optimization: Methods and Applications, Possibilities and Limitations*. Ed. by H. W. Bergmann. Berlin, Heidelberg: Springer, 1989, pp. 106–126. doi: [10.1007/978-3-642-83814-9_6](https://doi.org/10.1007/978-3-642-83814-9_6) (cited on pages 24, 25).
- [54] Hans-Paul Schwefel. *Numerical Optimization of Computer Models*. USA: John Wiley & Sons, Inc., May 1981. 398 pp. (cited on pages 24, 25).
- [55] Nikolaus Hansen. "The CMA Evolution Strategy: A Comparing Review." In: *Towards a New Evolutionary Computation: Advances in the Estimation of Distribution Algorithms*. Ed. by Jose A. Lozano et al. Berlin, Heidelberg: Springer, 2006, pp. 75–102. doi: [10.1007/3-540-32494-1_4](https://doi.org/10.1007/3-540-32494-1_4). (Visited on 08/19/2025) (cited on page 25).
- [56] Michel Gendreau and Jean-Yves Potvin, eds. *Handbook of Metaheuristics*. Vol. 146. International Series in Operations Research & Management Science. Boston, MA: Springer US, 2010. (Visited on 01/02/2024) (cited on pages 25, 27).
- [57] Martin Schlüter, Jose A. Egea, and Julio R. Banga. "Extended Ant Colony Optimization for Non-Convex Mixed Integer Nonlinear Programming." In: *Computers & Operations Research* 36.7 (July 1, 2009), pp. 2217–2229. doi: [10.1016/j.cor.2008.08.015](https://doi.org/10.1016/j.cor.2008.08.015). (Visited on 08/19/2025) (cited on page 26).

- [58] J. Kennedy and R. Eberhart. "Particle Swarm Optimization." In: *Proceedings of ICNN'95 - International Conference on Neural Networks*. ICNN'95 - International Conference on Neural Networks. Vol. 4. Nov. 1995, 1942–1948 vol.4. doi: [10.1109/ICNN.1995.488968](https://doi.org/10.1109/ICNN.1995.488968). (Visited on 08/19/2025) (cited on page 26).
- [59] Ahmed G. Gad. "Particle Swarm Optimization Algorithm and Its Applications: A Systematic Review." In: *Archives of Computational Methods in Engineering* 29.5 (Aug. 1, 2022), pp. 2531–2561. doi: [10.1007/s11831-021-09694-4](https://doi.org/10.1007/s11831-021-09694-4). (Visited on 08/19/2025) (cited on page 26).
- [60] Rainer Storn and Kenneth Price. "Differential Evolution – A Simple and Efficient Heuristic for Global Optimization over Continuous Spaces." In: *Journal of Global Optimization* 11.4 (Dec. 1, 1997), pp. 341–359. doi: [10.1023/A:1008202821328](https://doi.org/10.1023/A:1008202821328). (Visited on 08/20/2025) (cited on page 26).
- [61] Janez Brest et al. "Self-Adapting Control Parameters in Differential Evolution: A Comparative Study on Numerical Benchmark Problems." In: *IEEE Transactions on Evolutionary Computation* 10.6 (Dec. 2006), pp. 646–657. doi: [10.1109/TEVC.2006.872133](https://doi.org/10.1109/TEVC.2006.872133). (Visited on 08/20/2025) (cited on page 26).
- [62] Saber M. Elsayed, Ruhul A. Sarker, and Daryl L. Essam. "Differential Evolution with Multiple Strategies for Solving CEC2011 Real-World Numerical Optimization Problems." In: *2011 IEEE Congress of Evolutionary Computation (CEC)*. 2011 IEEE Congress on Evolutionary Computation (CEC). New Orleans, LA, USA: IEEE, June 2011, pp. 1041–1048. doi: [10.1109/CEC.2011.5949732](https://doi.org/10.1109/CEC.2011.5949732). (Visited on 08/20/2025) (cited on page 26).
- [63] A. Corana et al. "Minimizing Multimodal Functions of Continuous Variables with the "Simulated Annealing" Algorithm—Corrigenda for This Article Is Available Here." In: *ACM Trans. Math. Softw.* 13.3 (Sept. 1, 1987), pp. 262–280. doi: [10.1145/29380.29864](https://doi.org/10.1145/29380.29864). (Visited on 08/19/2025) (cited on page 27).
- [64] Zong Woo Geem, Joong Hoon Kim, and G.V. Loganathan. "A New Heuristic Optimization Algorithm: Harmony Search." In: *SIMULATION* 76.2 (Feb. 1, 2001), pp. 60–68. doi: [10.1177/003754970107600201](https://doi.org/10.1177/003754970107600201). (Visited on 06/16/2025) (cited on page 27).
- [65] E. F. Camacho and C. Bordons. *Model Predictive Control*. Red. by Michael J. Grimble and Michael A. Johnson. Advanced Textbooks in Control and Signal Processing. London: Springer, 2007. (Visited on 03/12/2024) (cited on page 29).
- [66] Karl J Hägglund and Tore Åström. *Advanced PID Control*. Research Triangle Park, NC: ISA-The Instrumentation, Systems, and Automation Society, 2006 (cited on pages 29, 84).
- [67] Riccardo Scattolini. "Architectures for Distributed and Hierarchical Model Predictive Control – A Review." In: *Journal of Process Control* 19.5 (May 1, 2009), pp. 723–731. doi: [10.1016/j.jprocont.2009.02.003](https://doi.org/10.1016/j.jprocont.2009.02.003). (Visited on 08/21/2025) (cited on page 30).
- [68] Carrie Schoeneberger et al. "Solar for Industrial Process Heat: A Review of Technologies, Analysis Approaches, and Potential Applications in the United States." In: *Energy* 206 (2020), p. 118083. doi: [10.1016/j.energy.2020.118083](https://doi.org/10.1016/j.energy.2020.118083). (Visited on 08/07/2025) (cited on page 35).
- [69] IEA SHC. *Solar Heat Worldwide 2025*. 2025 (cited on page 36).
- [70] Richard Thonig and Johan Lilliestam. "Concentrating Solar Technology Policy Should Encourage High Temperatures and Modularity to Enable Spillovers." In: *AIP Conference Proceedings* 2815.1 (Oct. 6, 2023), p. 050005. doi: [10.1063/5.0149423](https://doi.org/10.1063/5.0149423). (Visited on 06/13/2025) (cited on page 36).
- [71] Mark Mehos et al. "Concentrating Solar Power Best Practices Study." In: (2020). (Visited on 08/05/2025) (cited on page 36).
- [72] Mark Mehos et al. "Concentrating Solar Power Gen3 Demonstration Roadmap." In: (2017). doi: [10.2172/1338899](https://doi.org/10.2172/1338899). (Visited on 08/02/2025) (cited on page 36).
- [73] Stefan Pfenninger et al. "Potential for Concentrating Solar Power to Provide Baseload and Dispatchable Power." In: *Nature Climate Change* 4.8 (Aug. 2014), pp. 689–692. doi: [10.1038/nclimate2276](https://doi.org/10.1038/nclimate2276). (Visited on 08/08/2025) (cited on page 36).
- [74] Christian Binz et al. "Toward Technology-Sensitive Catching-Up Policies: Insights from Renewable Energy in China." In: *World Development* 96 (Aug. 1, 2017), pp. 418–437. doi: [10.1016/j.worlddev.2017.03.027](https://doi.org/10.1016/j.worlddev.2017.03.027). (Visited on 08/08/2025) (cited on page 36).
- [75] Johan Lilliestam et al. "The Near- to Mid-Term Outlook for Concentrating Solar Power: Mostly Cloudy, Chance of Sun." In: *Energy Sources, Part B: Economics, Planning, and Policy* 16.1 (2021), pp. 23–41. doi: [10.1080/15567249.2020.1773580](https://doi.org/10.1080/15567249.2020.1773580) (cited on pages 36–38, 90).
- [76] Nuno Bento and Charlie Wilson. "Measuring the Duration of Formative Phases for Energy Technologies." In: *Environmental Innovation and Societal Transitions* 21 (Dec. 1, 2016), pp. 95–112. doi: [10.1016/j.eist.2016.04.004](https://doi.org/10.1016/j.eist.2016.04.004). (Visited on 08/08/2025) (cited on page 36).

- [77] Pere Mir Artigues, Pablo del Río González, and Nàtalia Caldés. *The Economics and Policy of Concentrating Solar Power Generation*. Springer Nature, 2019. (Visited on 08/08/2025) (cited on page 36).
- [78] Thomas M. Schmitt. "(Why) Did Desertec Fail? An Interim Analysis of a Large-Scale Renewable Energy Infrastructure Project from a Social Studies of Technology Perspective." In: *Local Environment* 23.7 (July 3, 2018), pp. 747–776. doi: [10.1080/13549839.2018.1469119](https://doi.org/10.1080/13549839.2018.1469119). (Visited on 08/08/2025) (cited on page 37).
- [79] IRENA. *Renewable Power Generation Costs in 2024*. 978-92-9260-669-5. Abu Dhabi, July 22, 2025. (Visited on 08/02/2025) (cited on pages 37, 38).
- [80] Javier Bonilla et al. "Feasibility and Practical Limits of Full Decarbonization of the Electricity Market with Renewable Energy: Application to the Spanish Power Sector." In: *Energy* 239 (Jan. 15, 2022), p. 122437. doi: [10.1016/j.energy.2021.122437](https://doi.org/10.1016/j.energy.2021.122437). (Visited on 08/09/2025) (cited on page 37).
- [81] IEA. "Net Zero by 2050 - A Roadmap for the Global Energy Sector." In: (2021) (cited on page 37).
- [82] IRENA. "World Energy Transitions Outlook 2024: 1.5°C Pathway." In: (2024) (cited on page 37).
- [83] Johan Lilliestam et al. "Scaling up CSP: How Long Will It Take?" In: *AIP Conference Proceedings* 2815.1 (Oct. 6, 2023), p. 050003. doi: [10.1063/5.0148709](https://doi.org/10.1063/5.0148709). (Visited on 06/13/2025) (cited on page 37).
- [84] China Solar Thermal Alliance. *Blue Book of China's Concentrating Solar Power Industry 2024*. 2024 (cited on pages 37, 42).
- [85] Franziska Schöniger et al. "The Need for Dispatchable RES: A Closer Look at the Future Role of CSP in Europe." In: *Renewable Energy Based Solutions*. Ed. by Tanay Sıdkı Uyar and Nader Javani. Cham: Springer International Publishing, 2022, pp. 219–239. doi: [10.1007/978-3-031-05125-8_8](https://doi.org/10.1007/978-3-031-05125-8_8). (Visited on 06/13/2025) (cited on page 38).
- [86] Tarun Kumar Aseri, Chandan Sharma, and Tara C. Kandpal. "Condenser Cooling Technologies for Concentrating Solar Power Plants: A Review." In: *Environment, Development and Sustainability* 24.4 (Apr. 2022), pp. 4511–4565. doi: [10.1007/s10668-021-01678-5](https://doi.org/10.1007/s10668-021-01678-5). (Visited on 06/15/2025) (cited on pages 38, 41, 42, 45).
- [87] Samantha Kuzma et al. "Aqueduct 4.0: Updated Decision-Relevant Global Water Risk Indicators." In: (Aug. 16, 2023). (Visited on 08/09/2025) (cited on pages 39, 99).
- [88] J Meldrum et al. "Life Cycle Water Use for Electricity Generation: A Review and Harmonization of Literature Estimates." In: *Environmental Research Letters* 8.1 (Mar. 2013), p. 015031. doi: [10.1088/1748-9326/8/1/015031](https://doi.org/10.1088/1748-9326/8/1/015031). (Visited on 06/13/2025) (cited on page 40).
- [89] Antonio Colmenar-Santos et al. "Water Consumption in Solar Parabolic Trough Plants: Review and Analysis of the Southern Spain Case." In: *Renewable and Sustainable Energy Reviews* 34 (June 1, 2014), pp. 565–577. doi: [10.1016/j.rser.2014.03.042](https://doi.org/10.1016/j.rser.2014.03.042). (Visited on 06/02/2023) (cited on page 40).
- [90] Philipp Habl, Ana Blanco-Marigorta, and Berit Erlach. "Exergoeconomic Comparison of Wet and Dry Cooling Technologies for the Rankine Cycle of a Solar Thermal Power Plant." In: () (cited on page 40).
- [91] Richard Thonig, Alina Gilmanova, and Johan Lilliestam. *CSP.Guru 2023-07-01*. Zenodo, July 1, 2023. (Visited on 05/31/2025) (cited on pages 40, 42, 45, 90).
- [92] Javier Bonilla et al. "CSP Data: A Data Discovery Web Application of Commercial CSP Plants." In: (July 2024) (cited on pages 40, 42, 90).
- [93] Patricia Palenzuela, Diego-César Alarcón-Padilla, and Guillermo Zaragoza. *Concentrating Solar Power and Desalination Plants*. Oct. 9, 2015 (cited on pages 40, 104, 109, 139, 141, 145).
- [94] C. Turchi. *Parabolic Trough Reference Plant for Cost Modeling with the Solar Advisor Model (SAM)*. NREL/TP-550-47605, 983729. July 1, 2010, NREL/TP-550-47605, 983729. doi: [10.2172/983729](https://doi.org/10.2172/983729). (Visited on 08/09/2025) (cited on page 40).
- [95] J Maulbetsch. *Comparison of Alternate Cooling Technologies for U.S. Power Plants: Economic, Environmental, and Other Tradeoffs*. 1005358. Palo Alto, CA: EPRI, Aug. 2004 (cited on pages 41, 42, 44, 45).
- [96] J Maulbetsch. *Economic Evaluation of Alternative Cooling Technologies*. 1024805. Palo Alto, CA: Electric Power Research Institute (EPRI), Jan. 2012. (Visited on 08/09/2025) (cited on pages 41–43, 45, 59).
- [97] T Jászay. "Indudustrial Review-Aus Der Industrie. The Air-Cooled Condensing Equipment" System Heller" a Comprehensive Survey." In: *Periodica Polytechnica Mechanical Engineering* 2.4 (1958), pp. 389–402 (cited on page 41).
- [98] A. Balogh and J. Budik. "Heller's Indirect Approach Widens Applicability of Dry Cooling." In: *Modern Power Systems* 26.7 (July 2006), ?? (Cited on page 41).

- [99] O. O. Mil'man and P. A. Anan'ev. "Air-Cooled Condensing Units in Thermal Engineering (Review)." In: *Thermal Engineering* 67.12 (Dec. 1, 2020), pp. 872–891. doi: [10.1134/S0040601520120058](https://doi.org/10.1134/S0040601520120058). (Visited on 08/11/2025) (cited on page 41).
- [100] Nalogh Andras and Szabo Aoltan. "Advanced Heller System Technical Characteristics." 2005 (cited on page 41).
- [101] Kelly Birkinshaw, Marwan Masri, and Robert L Therkelsen. "Comparison of Alternate Cooling Technologies for California Power Plants Economic, Environmental and Other Tradeoffs." In: (Feb. 2002) (cited on page 42).
- [102] M. C. Hu. *Engineering and Economic Evaluation of Wet/Dry Cooling Towers for Water Conservation*. COO-2442-1. United Engineers and Constructors, Inc., Philadelphia, PA (USA), Oct. 31, 1976. doi: [10.2172/7101949](https://doi.org/10.2172/7101949). (Visited on 08/09/2025) (cited on page 42).
- [103] W. V. Loscutoff. *Preliminary Evaluation of Wet/Dry Cooling Concepts for Power Plants*. BNWL-1969. Battelle Pacific Northwest Labs., Richland, Wash. (USA), Dec. 31, 1975. doi: [10.2172/7341661](https://doi.org/10.2172/7341661). (Visited on 08/09/2025) (cited on pages 42, 43).
- [104] Babak Golkar et al. "Determination of Optimum Hybrid Cooling Wet/Dry Parameters and Control System in off Design Condition: Case Study." In: *Applied Thermal Engineering* 149 (Feb. 25, 2019), pp. 132–150. doi: [10.1016/j.applthermaleng.2018.12.017](https://doi.org/10.1016/j.applthermaleng.2018.12.017). (Visited on 06/21/2025) (cited on page 43).
- [105] G. Barigozzi, A. Perdichizzi, and S. Ravelli. "Wet and Dry Cooling Systems Optimization Applied to a Modern Waste-to-Energy Cogeneration Heat and Power Plant." In: *Applied Energy* 88.4 (Apr. 1, 2011), pp. 1366–1376. doi: [10.1016/j.apenergy.2010.09.023](https://doi.org/10.1016/j.apenergy.2010.09.023). (Visited on 03/10/2023) (cited on page 43).
- [106] Patricia Palenzuela et al. "Experimental Assessment of a Pilot Scale Hybrid Cooling System for Water Consumption Reduction in CSP Plants." In: *Energy* 242 (Mar. 1, 2022), p. 122948. doi: [10.1016/j.energy.2021.122948](https://doi.org/10.1016/j.energy.2021.122948). (Visited on 03/10/2023) (cited on page 43).
- [107] SPX. SPX Awarded Contract to Supply Parallel Condensing System For Crescent Dunes Solar Energy Project near Tonopah, Nevada. Mar. 24, 2012. URL: <https://www.powersystemsdesign.com/articles/spx-awarded-contract-to-supply-parallel-condensing-system-for-crescent-dunes-solar-energy-project-near-tonopah-nevada/8/3720> (visited on 08/12/2025) (cited on pages 45, 46).
- [108] Steinbeis 2i GmbH. Blog #29 – Full Scale Testing in Stellenbosch, South Africa | MinwaterCSP. Jan. 27, 2020. URL: <https://www.minwatercsp.eu/blog-29-full-scale-testing-in-stellenbosch-south-africa/> (visited on 08/02/2025) (cited on page 46).
- [109] UNE. *Thermal Performance Acceptance Testing of Mechanical Draught Series Wet Cooling Towers*. manual. UNE. 2004 (cited on page 48).
- [110] CTI. *Code Tower, Standard Specifications. Acceptance Test Code for Water Cooling Towers*. manual. Cooling Technology Institute. 2000 (cited on page 48).
- [111] F. Merkel. "Verdunstungskühlung." In: *VDI Zeitschrift Deutscher Ingenieure, Berlin, Alemania* (1925), pp. 123–128 (cited on page 52).
- [112] H. Jaber and R. L. Webb. "Design of Cooling Towers by the Effectiveness-NTU Method." In: *Journal of Heat Transfer* 111.4 (Nov. 1989), pp. 837–843. doi: [10.1115/1.3250794](https://doi.org/10.1115/1.3250794) (cited on page 52).
- [113] M. Poppe and H. Rögner. "Berechnung von Rückkühlwerken." In: *VDI wärmeatlas* (1991), p. Mi 1 (cited on page 52).
- [114] J.C. Kloppers and D.G. Kröger. "A Critical Investigation into the Heat and Mass Transfer Analysis of Counterflow Wet-Cooling Towers." In: *International Journal of Heat and Mass Transfer* 48.3 (2005), pp. 765–777 (cited on page 52).
- [115] P. Navarro et al. "Critical Evaluation of the Thermal Performance Analysis of a New Cooling Tower Prototype." In: *Applied Thermal Engineering* 213 (2022), p. 118719. doi: [10.1016/j.applthermaleng.2022.118719](https://doi.org/10.1016/j.applthermaleng.2022.118719) (cited on page 52).
- [116] Juan Miguel Serrano et al. "Wet Cooling Tower Performance Prediction in CSP Plants: A Comparison between Artificial Neural Networks and Poppe's Model." In: *Energy* (May 29, 2024), p. 131844. doi: [10.1016/j.energy.2024.131844](https://doi.org/10.1016/j.energy.2024.131844). (Visited on 05/30/2024) (cited on page 52).
- [117] Ashrae. "HVAC Systems and Equipment." In: *Chapter 36 Cooling Towers*. 2004 (cited on page 53).
- [118] Han Zhang et al. "Preliminary Analysis of a Parabolic Trough Concentrating Solar Power System Integrated with Radiative Cooling." In: *International Journal of Low-Carbon Technologies* 19 (Jan. 18, 2024), pp. 1144–1159. doi: [10.1093/ijlct/ctae050](https://doi.org/10.1093/ijlct/ctae050). (Visited on 06/17/2025) (cited on page 54).
- [119] Yunus A. Cengel and Afshin J. Ghajar. *Heat and Mass Transfer*. London: McGraw-Hill Professional, 2014 (cited on page 54).

- [120] D.G. Kröger. *Air-Cooled Heat Exchangers and Cooling Towers*. Air-Cooled Heat Exchangers and Cooling Towers v. 1. Penwell Corporation, 2004 (cited on page 54).
- [121] Volker Gnielinski. "New Equations for Heat and Mass Transfer in Turbulent Pipe and Channel Flow." In: *International chemical engineering* 16.2 (1976), pp. 359–367 (cited on page 55).
- [122] S Kakac, R K Shah, and W Aung. *Handbook of Single-Phase Convective Heat Transfer*. United States: John Wiley and Sons Inc., New York, NY, Dec. 1986 (cited on page 55).
- [123] R. W. Serth. *Process Heat Transfer: Principles, Applications and Rules of Thumb*. 2007 (cited on page 56).
- [124] Warren M. Rohsenow, J. P. Hartnett, and Young I. Cho, eds. *Handbook of Heat Transfer*. 3rd ed. McGraw-Hill Handbooks. New York: McGraw-Hill, 1998. 1 p. (cited on page 56).
- [125] Richard Damania et al. *Uncharted Waters: The New Economics of Water Scarcity and Variability*. Washington, DC: World Bank, Oct. 24, 2017. (Visited on 01/08/2023) (cited on page 60).
- [126] David Wales and Jonathan Doye. "Global Optimization by Basin-Hopping and the Lowest Energy Structures of Lennard-Jones Clusters Containing up to 110 Atoms." In: *The Journal of Physical Chemistry A* 101.28 (July 1, 1997), pp. 5111–5116. doi: [10.1021/jp970984n](https://doi.org/10.1021/jp970984n). (Visited on 06/11/2025) (cited on page 67).
- [127] OpenWeather. *Current Weather and Forecast - OpenWeatherMap*. 2025. URL: <https://openweathermap.org/> (visited on 10/04/2025) (cited on page 83).
- [128] Red Eléctrica de España. *Red Eléctrica – Negocio Eléctrico En España*. 2025. URL: <https://www.ree.es/es> (cited on pages 83, 91).
- [129] Sigurd Skogestad and Chriss Grimholt. "The SIMC Method for Smooth PID Controller Tuning." In: *PID Control in the Third Millennium: Lessons Learned and New Approaches*. Ed. by Ramon Vilanova and Antonio Visioli. Advances in Industrial Control. London: Springer, 2012, pp. 147–175. (Visited on 12/22/2023) (cited on page 84).
- [130] Meteotest AG. *Meteonorm V8.2.0.24079*. URL: <https://meteonorm.com/climate/> (visited on 06/09/2025) (cited on pages 90, 91).
- [131] Bartolomé Ortega Delgado. "Theoretical analysis of high efficient multi-effect distillation processes and their integration into concentrating solar power plants." <http://purl.org/dc/dcmitype/Text>. Universidad de Sevilla, 2016. (Visited on 09/25/2025) (cited on pages 90, 91).
- [132] Hanna Pltomykova et al. "The United Nations World Water Development Report 2020: Water and Climate Change." In: (2020) (cited on page 99).
- [133] Edward Jones et al. "The State of Desalination and Brine Production: A Global Outlook." In: *Science of The Total Environment* 657 (Mar. 20, 2019), pp. 1343–1356. doi: [10.1016/j.scitotenv.2018.12.076](https://doi.org/10.1016/j.scitotenv.2018.12.076). (Visited on 06/29/2022) (cited on pages 99, 141).
- [134] Joyner Eke et al. "The Global Status of Desalination: An Assessment of Current Desalination Technologies, Plants and Capacity." In: *Desalination* 495 (Dec. 1, 2020), p. 114633. doi: [10.1016/j.desal.2020.114633](https://doi.org/10.1016/j.desal.2020.114633). (Visited on 01/05/2023) (cited on page 99).
- [135] Mesfin M Mekonnen and Arjen Y Hoekstra. "Four Billion People Facing Severe Water Scarcity." In: *Science advances* 2.2 (2016), e1500323 (cited on page 99).
- [136] Raphael Semiat. "Energy Issues in Desalination Processes." In: *Environmental Science & Technology* 42.22 (Nov. 15, 2008), pp. 8193–8201. doi: [10.1021/es801330u](https://doi.org/10.1021/es801330u). (Visited on 01/08/2023) (cited on page 99).
- [137] Kerry J. Howe et al. *Principles of Water Treatment*. John Wiley & Sons, Oct. 26, 2012. 674 pp. (cited on page 99).
- [138] Nooshin Shekarchi and Farhad Shahnia. "A Comprehensive Review of Solar-Driven Desalination Technologies for off-Grid Greenhouses." In: *International Journal of Energy Research* 43.4 (2019), pp. 1357–1386. doi: [10.1002/er.4268](https://doi.org/10.1002/er.4268). (Visited on 10/17/2024) (cited on page 99).
- [139] A. Allouhi and K. M. Almohammadi. "Towards Green Desalination: A Multi-Site Analysis of Hybrid Renewable Energy Integration in Saudi Arabian RO Plants." In: *Desalination* 592 (Dec. 21, 2024), p. 118087. doi: [10.1016/j.desal.2024.118087](https://doi.org/10.1016/j.desal.2024.118087). (Visited on 10/17/2024) (cited on page 99).
- [140] Sebastian Schär et al. "Optimization of Sustainable Seawater Desalination: Modeling Renewable Energy Integration and Energy Storage Concepts." In: *Energy Conversion and Management* 293 (Oct. 1, 2023), p. 117447. doi: [10.1016/j.enconman.2023.117447](https://doi.org/10.1016/j.enconman.2023.117447). (Visited on 10/17/2024) (cited on page 99).
- [141] Argyris Panagopoulos. "Study and Evaluation of the Characteristics of Saline Wastewater (Brine) Produced by Desalination and Industrial Plants." In: *Environmental Science and Pollution Research* 29.16 (Apr. 1, 2022), pp. 23736–23749. doi: [10.1007/s11356-021-17694-x](https://doi.org/10.1007/s11356-021-17694-x). (Visited on 10/16/2025) (cited on page 100).

- [142] Argyris Panagopoulos and Katherine-Joanne Haralambous. "Environmental Impacts of Desalination and Brine Treatment - Challenges and Mitigation Measures." In: *Marine Pollution Bulletin* 161 (Dec. 1, 2020), p. 111773. doi: [10.1016/j.marpolbul.2020.111773](https://doi.org/10.1016/j.marpolbul.2020.111773). (Visited on 10/16/2025) (cited on pages 100, 103, 104).
- [143] Pía Hernández et al. "Use of Seawater/Brine and Caliche's Salts as Clean and Environmentally Friendly Sources of Chloride and Nitrate Ions for Chalcopyrite Concentrate Leaching." In: *Minerals* 10.5 (May 2020), p. 477. doi: [10.3390/min10050477](https://doi.org/10.3390/min10050477). (Visited on 10/16/2025) (cited on page 100).
- [144] H. T. El-Dessouky and H. M. Ettouney. *Fundamentals of Salt Water Desalination*. Elsevier, Mar. 20, 2002. 691 pp. (cited on pages 101, 137, 140).
- [145] Bernhard Milow and Eduardo Zarza. "Advanced MED Solar Desalination Plants. Configurations, Costs, Future – Seven Years of Experience at the Plataforma Solar de Almeria (Spain)." In: *Desalination*. Annual Meeting of the European Desalination Society of Desalination Anf the Environment 108.1 (Feb. 1, 1997), pp. 51–58. doi: [10.1016/S0011-9164\(97\)00008-8](https://doi.org/10.1016/S0011-9164(97)00008-8). (Visited on 10/16/2025) (cited on pages 102, 107).
- [146] Diego-César Alarcón-Padilla and Lourdes García-Rodríguez. "Application of Absorption Heat Pumps to Multi-Effect Distillation: A Case Study of Solar Desalination." In: *Desalination* 212.1 (June 25, 2007), pp. 294–302. doi: [10.1016/j.desal.2006.10.014](https://doi.org/10.1016/j.desal.2006.10.014). (Visited on 10/16/2025) (cited on pages 102, 107).
- [147] Akili D. Khawaji, Ibrahim K. Kutubkhanah, and Jong-Mihn Wie. "Advances in Seawater Desalination Technologies." In: *Desalination* 221.1–3 (Mar. 2008), pp. 47–69. doi: [10.1016/j.desal.2007.01.067](https://doi.org/10.1016/j.desal.2007.01.067). (Visited on 11/21/2025) (cited on page 102).
- [148] Andrew T. Bouma, Jaichander Swaminathan, and John H. Lienhard V. "Metrics Matter: Accurately Defining Energy Efficiency in Desalination." In: *Journal of Heat Transfer* 142.12 (Oct. 7, 2020). doi: [10.1115/1.4048250](https://doi.org/10.1115/1.4048250). (Visited on 03/22/2023) (cited on pages 102, 137, 140, 144).
- [149] Amaia Lejarazu-Larrañaga et al. "Thin Film Composite Polyamide Reverse Osmosis Membrane Technology towards a Circular Economy." In: *Membranes* 12.9 (Sept. 7, 2022), p. 864. doi: [10.3390/membranes12090864](https://doi.org/10.3390/membranes12090864). (Visited on 11/21/2025) (cited on page 103).
- [150] Guillermo Zaragoza et al. "Coupling of Nanofiltration with Multi-Effect Distillation for Solar-Powered Seawater Desalination towards Brine Mining and Water Production for Agriculture." In: *Nanofiltration 2022 : Principles, Applications and New Materials*. Achalm, Reutlingen, June 26–30, 2022 (cited on pages 103, 139).
- [151] Argyris Panagopoulos. "Process Simulation and Techno-Economic Assessment of a Zero Liquid Discharge/Multi-Effect Desalination/Thermal Vapor Compression (ZLD/MED/TVC) System." In: *International Journal of Energy Research* 44.1 (2020), pp. 473–495. doi: [10.1002/er.4948](https://doi.org/10.1002/er.4948). (Visited on 01/06/2023) (cited on page 103).
- [152] Haya Nassrullah et al. "Energy for Desalination: A State-of-the-Art Review." In: *Desalination* 491 (Oct. 1, 2020), p. 114569. doi: [10.1016/j.desal.2020.114569](https://doi.org/10.1016/j.desal.2020.114569). (Visited on 04/04/2022) (cited on page 103).
- [153] Jhon Jairo Feria-Díaz et al. "Commercial Thermal Technologies for Desalination of Water from Renewable Energies: A State of the Art Review." In: *Processes* 9.2 (2 Feb. 2021), p. 262. doi: [10.3390/pr9020262](https://doi.org/10.3390/pr9020262). (Visited on 03/21/2022) (cited on page 103).
- [154] Patricia Palenzuela and Diego C. Alarcón-Padilla. "Concentrating Solar Power and Desalination Plants." In: *Solar Resources Mapping: Fundamentals and Applications*. Ed. by Jesús Polo, Luis Martín-Pomares, and Antonio Sanfilippo. Cham: Springer International Publishing, 2019, pp. 327–340. doi: [10.1007/978-3-319-97484-2_14](https://doi.org/10.1007/978-3-319-97484-2_14). (Visited on 10/16/2025) (cited on page 104).
- [155] Khaled Elsaïd et al. "Recent Progress on the Utilization of Waste Heat for Desalination: A Review." In: *Energy Conversion and Management* 221 (Oct. 1, 2020), p. 113105. doi: [10.1016/j.enconman.2020.113105](https://doi.org/10.1016/j.enconman.2020.113105). (Visited on 10/15/2025) (cited on page 105).
- [156] Sarah Brückner et al. "Industrial Waste Heat Recovery Technologies: An Economic Analysis of Heat Transformation Technologies." In: *Applied Energy* 151 (Aug. 1, 2015), pp. 157–167. doi: [10.1016/j.apenergy.2015.01.147](https://doi.org/10.1016/j.apenergy.2015.01.147). (Visited on 01/07/2023) (cited on page 105).
- [157] Alexander Christ, Klaus Regenauer-Lieb, and Hui Tong Chua. "Boosted Multi-Effect Distillation for Sensible Low-Grade Heat Sources: A Comparison with Feed Pre-Heating Multi-Effect Distillation." In: *Desalination*. Energy and Desalination 366 (June 15, 2015), pp. 32–46. doi: [10.1016/j.desal.2014.12.047](https://doi.org/10.1016/j.desal.2014.12.047). (Visited on 01/04/2023) (cited on pages 105, 140).
- [158] A. Gregorzewski et al. "The Solar Thermal Desalination Research Project at the Plataforma Solar de Almeria." In: *Desalination* 82.1–3 (1991), pp. 142–144 (cited on page 107).
- [159] Julián Blanco et al. "The AQUASOL System: Solar Collector Field Efficiency and Solar-Only Mode Performance." In: *Journal of Solar Energy Engineering* 133.011009 (Jan. 28, 2011). doi: [10.1115/1.4003291](https://doi.org/10.1115/1.4003291). (Visited on 10/20/2025) (cited on page 107).

- [160] Gary Ampuño et al. "Modeling and Simulation of a Solar Field Based on Flat-Plate Collectors." In: *Solar Energy* 170 (Aug. 1, 2018), pp. 369–378. doi: [10.1016/j.solener.2018.05.076](https://doi.org/10.1016/j.solener.2018.05.076). (Visited on 03/17/2023) (cited on pages 107, 114, 117).
- [161] Lidia Roca et al. "Modelo de parámetros concentrados para captadores solares planos con reflectores." In: *Jornadas de Automática* 45 (45 July 19, 2024). doi: [10.17979/ja-cea.2024.45.10930](https://doi.org/10.17979/ja-cea.2024.45.10930). (Visited on 08/25/2024) (cited on page 108).
- [162] John A. Duffie and William A. Beckman. "Energy Storage." In: *Solar Engineering of Thermal Processes*. John Wiley & Sons, Ltd, 2013, pp. 373–408. doi: [10.1002/9781118671603.ch8](https://doi.org/10.1002/9781118671603.ch8). (Visited on 07/15/2025) (cited on pages 108, 119).
- [163] Patricia Palenzuela, Diego C. Alarcón-Padilla, and Guillermo Zaragoza. "Experimental Parametric Analysis of a Solar Pilot-Scale Multi-Effect Distillation Plant." In: *Desalination and Water Treatment* 57:48–49 (Oct. 2016), pp. 23097–23109. doi: [10.1080/19443994.2016.1180481](https://doi.org/10.1080/19443994.2016.1180481). (Visited on 09/01/2025) (cited on pages 109, 204).
- [164] Gary Ampuño et al. "Apparent Delay Analysis for a Flat-Plate Solar Field Model Designed for Control Purposes." In: *Solar Energy* 177 (Jan. 1, 2019), pp. 241–254. doi: [10.1016/j.solener.2018.11.014](https://doi.org/10.1016/j.solener.2018.11.014). (Visited on 03/15/2023) (cited on page 114).
- [165] Julio E. Normey-Rico et al. "A Robust Adaptive Dead-Time Compensator with Application to A Solar Collector Field1." In: *IFAC Proceedings Volumes*. IFAC Workshop on Linear Time Delay Systems (LTDS '98), Grenoble, France, 6-7 July 31.19 (July 1, 1998), pp. 93–98. doi: [10.1016/S1474-6670\(17\)41134-7](https://doi.org/10.1016/S1474-6670(17)41134-7). (Visited on 02/19/2024) (cited on page 114).
- [166] Yunus A. Çengel and Afshin J. Ghajar. *Heat and Mass Transfer: Fundamentals & Applications*. Fifth edition. New York, NY: McGraw Hill Education, 2015. 968 pp. (cited on page 122).
- [167] William Morrow Kays and Alexander Louis London. *Compact Heat Exchangers: A Summary of Basic Heat Transfer and Flow Friction Design Data*. McGraw-Hill, 1958. 180 pp. (cited on page 122).
- [168] GPy. *GPy: A Gaussian Process Framework in Python*. URL: <http://github.com/SheffieldML/GPy> (cited on page 127).
- [169] Karan H. Mistry et al. "Entropy Generation Analysis of Desalination Technologies." In: *Entropy. An International and Interdisciplinary Journal of Entropy and Information Studies* 13:10 (2011), pp. 1829–1864. doi: [10.3390/e13101829](https://doi.org/10.3390/e13101829) (cited on pages 137, 195).
- [170] A. Christ, K. Regenauer-Lieb, and H.T. Chua. "Thermodynamic Optimisation of Multi Effect Distillation Driven by Sensible Heat Sources." In: *Desalination* 336:1 (2014), pp. 160–167. doi: [10.1016/j.desal.2013.12.006](https://doi.org/10.1016/j.desal.2013.12.006) (cited on pages 137, 140).
- [171] John H. Lienhard et al. "Thermodynamics, Exergy, and Energy Efficiency in Desalination Systems." In: *Lienhard via Angie Locknar* (2017). (Visited on 04/04/2022) (cited on pages 137, 138, 144, 195).
- [172] M. A. Darwish, Faisal Al-Juwayhel, and Hassan K. Abdulraheim. "Multi-Effect Boiling Systems from an Energy Viewpoint." In: *Desalination* 194:1 (June 10, 2006), pp. 22–39. doi: [10.1016/j.desal.2005.08.029](https://doi.org/10.1016/j.desal.2005.08.029). (Visited on 06/01/2022) (cited on pages 138, 144).
- [173] Muhammad Wakil Shahzad, Muhammad Burhan, and Kim Choom Ng. "A Standard Primary Energy Approach for Comparing Desalination Processes." In: *npj Clean Water* 2:1 (Jan. 7, 2019), pp. 1–7. doi: [10.1038/s41545-018-0028-4](https://doi.org/10.1038/s41545-018-0028-4). (Visited on 07/23/2024) (cited on page 138).
- [174] Doriano Brogioli, Fabio La Mantia, and Ngai Yin Yip. "Thermodynamic Analysis and Energy Efficiency of Thermal Desalination Processes." In: *Desalination* 428 (Feb. 15, 2018), pp. 29–39. doi: [10.1016/j.desal.2017.11.010](https://doi.org/10.1016/j.desal.2017.11.010). (Visited on 01/05/2023) (cited on pages 138, 139).
- [175] K.S. Spiegler and Y.M. El-Sayed. "The Energetics of Desalination Processes." In: *Desalination* 134 (Apr. 1, 2001), pp. 109–128. doi: [10.1016/S0011-9164\(01\)00121-7](https://doi.org/10.1016/S0011-9164(01)00121-7) (cited on pages 138, 195).
- [176] Mostafa H. Sharqawy, John H. Lienhard V, and Syed M. Zubair. "On Exergy Calculations of Seawater with Applications in Desalination Systems." In: *International Journal of Thermal Sciences* 50:2 (Feb. 1, 2011), pp. 187–196. doi: [10.1016/j.ijthermalsci.2010.09.013](https://doi.org/10.1016/j.ijthermalsci.2010.09.013). (Visited on 03/22/2023) (cited on pages 138, 144, 195).
- [177] Mostafa H. Sharqawy, Syed M. Zubair, and John H. Lienhard. "Formulation of Seawater Flow Exergy Using Accurate Thermodynamic Data." In: *Prof. Lienhard via Angie Locknar* (Nov. 2010). (Visited on 04/13/2023) (cited on page 138).
- [178] Karan H. Mistry and John H. Lienhard V. "Effect of Nonideal Solution Behavior on Desalination of a Sodium Chloride (NaCl) Solution and Comparison to Seawater." In: *Karan Mistry* (Nov. 2012). (Visited on 04/22/2023) (cited on page 138).

- [179] Karan H. Mistry and John H. Lienhard. "Generalized Least Energy of Separation for Desalination and Other Chemical Separation Processes." In: *Entropy. An International and Interdisciplinary Journal of Entropy and Information Studies* 15.6 (2013), pp. 2046–2080. doi: [10.3390/e15062046](https://doi.org/10.3390/e15062046) (cited on page 138).
- [180] Gregory P. Thiel et al. "Energy Consumption in Desalinating Produced Water from Shale Oil and Gas Extraction." In: *Desalination. Energy and Desalination* 366 (June 15, 2015), pp. 94–112. doi: [10.1016/j.desal.2014.12.038](https://doi.org/10.1016/j.desal.2014.12.038). (Visited on 03/06/2023) (cited on pages 138, 142, 145, 195).
- [181] Loreto Valenzuela, Rafael López-Martín, and Eduardo Zarza. "Optical and Thermal Performance of Large-Size Parabolic-Trough Solar Collectors from Outdoor Experiments: A Test Method and a Case Study." In: *Energy* 70 (June 1, 2014), pp. 456–464. doi: [10.1016/j.energy.2014.04.016](https://doi.org/10.1016/j.energy.2014.04.016). (Visited on 07/17/2024) (cited on page 138).
- [182] Christoph Prahl, Christoph Happich, and Jesús Fernández. *Protocol for Characterization of Complete Solar Concentrators Using Photogrammetry or Deflectometry*. WP14 – Task 14.2. DLR, Feb. 2018 (cited on page 138).
- [183] Rocío Bayón and Esther Rojas. "Development of a New Methodology for Validating Thermal Storage Media: Application to Phase Change Materials." In: *International Journal of Energy Research* 43.12 (2019), pp. 6521–6541. doi: [10.1002/er.4589](https://doi.org/10.1002/er.4589). (Visited on 07/17/2024) (cited on page 138).
- [184] Karan H. Mistry, Mohamed A. Antar, and John H. Lienhard V. "An Improved Model for Multiple Effect Distillation." In: *Desalination and Water Treatment* 51.4–6 (Jan. 1, 2013), pp. 807–821. doi: [10.1080/19443994.2012.703383](https://doi.org/10.1080/19443994.2012.703383). (Visited on 06/01/2022) (cited on pages 139, 199).
- [185] Heike Glade et al. "Scale Formation of Mixed Salts in Multiple-Effect Distillers." In: *IDA Journal of Desalination and Water Reuse* 2.1 (Jan. 1, 2010), pp. 38–44. doi: [10.1179/ida.2010.2.1.38](https://doi.org/10.1179/ida.2010.2.1.38). (Visited on 06/16/2023) (cited on page 139).
- [186] Kerstin Krömer et al. "Scale Formation and Mitigation of Mixed Salts in Horizontal Tube Falling Film Evaporators for Seawater Desalination." In: *Heat Transfer Engineering* 36.7–8 (May 3, 2015), pp. 750–762. doi: [10.1080/01457632.2015.954961](https://doi.org/10.1080/01457632.2015.954961). (Visited on 07/10/2023) (cited on page 139).
- [187] John W Ryznar. "A New Index for Determining Amount of Calcium Carbonate Scale Formed by a Water." In: *Journal-American Water Works Association* 36.4 (1944), pp. 472–483 (cited on pages 139, 140).
- [188] Andrea Schafer and Anthony Fane. *Nanofiltration: Principles, Applications, and New Materials*. John Wiley \& Sons. 2021 (cited on page 139).
- [189] Karan H. Mistry and John H. Lienhard. "An Economics-Based Second Law Efficiency." In: *Entropy* 15.7 (7 July 2013), pp. 2736–2765. doi: [10.3390/e15072736](https://doi.org/10.3390/e15072736). (Visited on 03/22/2023) (cited on page 140).
- [190] Alexander Christ et al. "Techno-Economic Analysis of Geothermal Desalination Using Hot Sedimentary Aquifers: A Pre-Feasibility Study for Western Australia." In: *Desalination* 404 (Feb. 17, 2017), pp. 167–181. doi: [10.1016/j.desal.2016.11.009](https://doi.org/10.1016/j.desal.2016.11.009). (Visited on 01/05/2023) (cited on page 140).
- [191] Alexander Christ, Klaus Regenauer-Lieb, and Hui Tong Chua. "Application of the Boosted MED Process for Low-Grade Heat Sources – A Pilot Plant." In: *Desalination. Energy and Desalination* 366 (June 15, 2015), pp. 47–58. doi: [10.1016/j.desal.2014.10.032](https://doi.org/10.1016/j.desal.2014.10.032). (Visited on 01/04/2023) (cited on page 140).
- [192] John H. Lienhard V et al. "SOLAR DESALINATION." In: *Annual Review of Heat Transfer* 15 (2012). doi: [10.1615/AnnualRevHeatTransfer.2012004659](https://doi.org/10.1615/AnnualRevHeatTransfer.2012004659). (Visited on 10/17/2024) (cited on page 142).
- [193] Qian Chen et al. "A Zero Liquid Discharge System Integrating Multi-Effect Distillation and Evaporative Crystallization for Desalination Brine Treatment." In: *Desalination* 502 (Apr. 2021), p. 114928. doi: [10.1016/J.DESAL.2020.114928](https://doi.org/10.1016/J.DESAL.2020.114928) (cited on page 143).
- [194] Adrian Bejan. *Advanced Engineering Thermodynamics*. John Wiley & Sons, 2016 (cited on page 144).
- [195] BIPM. *JCGM 100:2008. GUM 1995 with Minor Corrections. Evaluation of Measurement Data – Guide to the Expression of Uncertainty in Measurement*. Joint Committee for Guides in Metrology, 2008. URL: https://www.bipm.org/documents/20126/2071204/JCGM_101_2008_E.pdf/325dcaad-c15a-407c-1105-8b7f322d651c (cited on page 148).
- [196] Ralph C. Smith. *Uncertainty Quantification: Theory, Implementation, and Applications*. SIAM, Dec. 2, 2013. 400 pp. (cited on page 148).
- [197] NIST. "NIST Guidelines for Evaluating and Expressing the Uncertainty of NIST Measurement Results Cover." In: *NIST* (). (Visited on 06/16/2023) (cited on page 148).
- [198] BIPM. *JCGM101:2008. Evaluation of Measurement Data – Supplement 1 to the "Guide to the Expression of Uncertainty in Measurement" – Propagation of Distributions Using a Monte Carlo Method*. Joint Committee for Guides in Metrology, 2008. URL: https://www.bipm.org/documents/20126/2071204/JCGM_101_2008_E.pdf/325dcaad-c15a-407c-1105-8b7f322d651c (cited on page 148).

- [199] Ulli Wolff. "Monte Carlo Errors with Less Errors." In: *Computer Physics Communications* 176.5 (Mar. 2007), p. 383. doi: [10.1016/j.cpc.2006.12.001](https://doi.org/10.1016/j.cpc.2006.12.001). (Visited on 06/19/2023) (cited on page 148).
- [200] Milan Korbel et al. "Steady State Identification for On-Line Data Reconciliation Based on Wavelet Transform and Filtering." In: *Computers & Chemical Engineering* 63 (Apr. 17, 2014), pp. 206–218. doi: [10.1016/j.compchemeng.2014.02.003](https://doi.org/10.1016/j.compchemeng.2014.02.003). (Visited on 12/14/2022) (cited on page 149).
- [201] Taiwen Jiang et al. "Application of Steady-State Detection Method Based on Wavelet Transform." In: *Computers & Chemical Engineering* 27.4 (Apr. 15, 2003), pp. 569–578. doi: [10.1016/S0098-1354\(02\)00235-1](https://doi.org/10.1016/S0098-1354(02)00235-1). (Visited on 01/03/2023) (cited on page 149).
- [202] Taiwen Jiang, Bingzhen Chen, and Xiaorong He. "Industrial Application of Wavelet Transform to the On-Line Prediction of Side Draw Qualities of Crude Unit." In: *Computers & Chemical Engineering* 24.2 (July 15, 2000), pp. 507–512. doi: [10.1016/S0098-1354\(00\)00520-2](https://doi.org/10.1016/S0098-1354(00)00520-2). (Visited on 12/27/2022) (cited on page 149).
- [203] Karl Johan Åström and Tore Hägglund. *PID Controllers: Theory, Design, and Tuning*. ISA - The Instrumentation, Systems and Automation Society, 1995 (cited on page 150).
- [204] John H. Lienhard V. "Energy Savings in Desalination Technologies: Reducing Entropy Generation by Transport Processes." In: *Journal of Heat Transfer* 141.7 (May 17, 2019). doi: [10.1115/1.4043571](https://doi.org/10.1115/1.4043571). (Visited on 03/30/2023) (cited on page 159).
- [205] R. Porrazzo et al. "A Neural Network-Based Optimizing Control System for a Seawater-Desalination Solar-Powered Membrane Distillation Unit." In: *Computers & Chemical Engineering* 54 (July 11, 2013), pp. 79–96. doi: [10.1016/j.compchemeng.2013.03.015](https://doi.org/10.1016/j.compchemeng.2013.03.015). (Visited on 09/09/2025) (cited on page 162).
- [206] Ignacio E. Grossmann. *Advanced Optimization for Process Systems Engineering*. Cambridge Series in Chemical Engineering. Cambridge: Cambridge University Press, 2021 (cited on page 165).
- [207] Rob J. Hyndman and George Athanasopoulos. *Forecasting: Principles and Practice*. 3rd ed. OTexts, 2021 (cited on pages 166, 168).
- [208] CNR. *Mediterranean Sea Surface Temperature Time Series and Trend from Observations Reprocessing*. <https://doi.org/10.48670/moi-00268>. 2024. doi: [10.48670/moi-00268](https://doi.org/10.48670/moi-00268). (Visited on 05/15/2024) (cited on page 175).
- [209] Kenneth S. Pitzer. "Thermodynamics of Electrolytes. I. Theoretical Basis and General Equations." In: *The Journal of Physical Chemistry* 77.2 (Jan. 1, 1973), pp. 268–277. doi: [10.1021/j100621a026](https://doi.org/10.1021/j100621a026). (Visited on 11/13/2023) (cited on page 194).
- [210] M. H. Sharqawy, J. H. Lienhard, and S. M. Zubair. "Thermophysical Properties of Seawater: A Review of Existing Correlations and Data." In: *Desalination and Water Treatment* 16.1–3 (Apr. 2010), pp. 354–380. doi: [10.5004/dwt.2010.1](https://doi.org/10.5004/dwt.2010.1) (cited on page 194).
- [211] Kishor G. Nayar et al. "Thermophysical Properties of Seawater: A Review and New Correlations That Include Pressure Dependence." In: *Desalination* 390 (July 15, 2016), pp. 1–24. doi: [10.1016/j.desal.2016.02.024](https://doi.org/10.1016/j.desal.2016.02.024). (Visited on 04/25/2023) (cited on page 194).
- [212] Simão P. Pinho and Eugénia A. Macedo. "Solubility of NaCl, NaBr, and KCl in Water, Methanol, Ethanol, and Their Mixed Solvents." In: *Journal of Chemical & Engineering Data* 50.1 (Jan. 1, 2005), pp. 29–32. doi: [10.1021/je049922y](https://doi.org/10.1021/je049922y). (Visited on 04/26/2023) (cited on page 195).
- [213] Patricia Palenzuela et al. "Steady State Model for Multi-Effect Distillation Case Study: Plataforma Solar de Almería MED Pilot Plant." In: *Desalination* 337 (Mar. 1, 2014), pp. 31–42. doi: [10.1016/j.desal.2013.12.029](https://doi.org/10.1016/j.desal.2013.12.029) (cited on page 199).
- [214] Hisham El-Dessouky et al. "Steady-State Analysis of the Multiple Effect Evaporation Desalination Process." In: *Chemical Engineering & Technology* 21.5 (1998), pp. 437–451. doi: [10.1002/\(SICI\)1521-4125\(199805\)21:5<437::AID-CEAT437>3.0.CO;2-D](https://doi.org/10.1002/(SICI)1521-4125(199805)21:5<437::AID-CEAT437>3.0.CO;2-D). (Visited on 06/01/2022) (cited on page 199).

Nomenclature

\dot{E}_x	Exergy flow rate	[kW]
A	Area	[m ²]
b	Molality	[mol kg ⁻¹]
B	Benefit	[u.m.]
C	Conductivity, Consumption, Heat capacity	[mS cm ⁻¹ , kW / L, JK ⁻¹ s ⁻¹]
S	Composite score	[u.m.]
D	Diameter	[m]
J	Electrical power consumption, Cost of operation, Cost of cooling	[kW, -]
h	Specific enthalpy	[kJ kg ⁻¹]
s	Specific entropy	[kJ kg ⁻¹]
e	Environment variables, Specific exergy flow	[-, kJ kg ⁻¹]
g	Specific Gibbs free energy	[kJ kg ⁻¹]
h	Enthalpy	[J kg ⁻¹]
HR	Relative humidity	[%]
c_p	Specific heat capacity	[kJ kg ⁻¹ °C ⁻¹]
I	Irradiance	[W m ⁻²]
J	Fitness / Cost function	
k	Thermal conductivity, Step, Coverage factor	[W m ⁻¹ K ⁻¹ , -, -]
L	Length	[m]
L	Level	[mm]
Le	Lewis number	
l	Solar field loop	
\dot{m}	Mass flow rate	[kg s ⁻¹]
Me	Merkel number	
n, N	Number of	
P	Pressure, Price	[mbar, [u.m./€]]
p, p	Point, Path of points	
Q	Thermal energy or heat	[kJ]
q	Volumetric flow rate	[m ³ h ⁻¹]
Q	Thermal power	[kW]
R	Distribution ratio, Fouling resistance	[m ² K W ⁻¹])
w	Salinity, Concentration in terms of mass fraction	[g kg ⁻¹]
T	Temperature, Period, Time	
H	Thermal loss coefficient	[J s ⁻¹ °C ⁻¹]
U	Heat transfer coefficient	[W m ⁻² K ⁻¹]
$u.m.$	Monetary units	[-]
v	Valve position	
V	Volume	[m ³]
\dot{W}	Work of separation of seawater	[kW]
W	Worst case performance	
x	Decision vector	

Greek symbols

β	Temperature gain coefficient	[m]
μ	Chemical potential, Average performance	[kJ kg ⁻¹ , -]
η	Efficiency	[%]
γ	Threshold	
λ	Specific latent heat of phase change	[kJ kg ⁻¹]
θ	Parameters	
ρ	Density	[kg m ⁻³]
σ	Standard-deviation performance	

ϵ	Tolerance, effectiveness
Δ	Variation
ω	Humidity ratio, Actuator value [kg kg ⁻¹ , -]

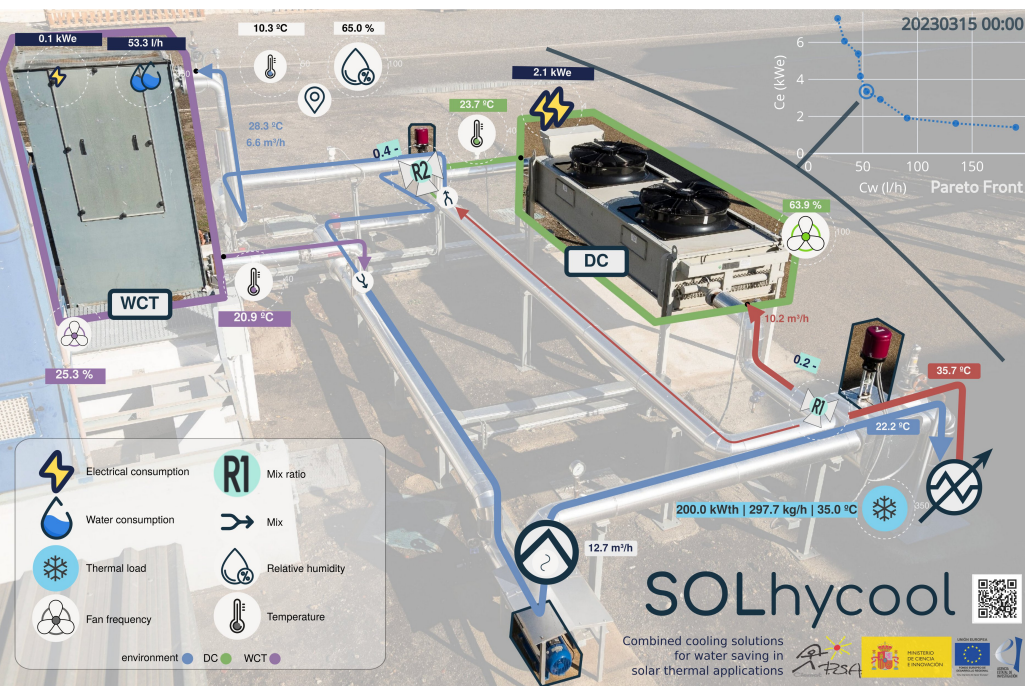
Subscripts

0	Reference system, Dead-state, Initial state
air	Air
amb, ∞	Ambient conditions
aux	Auxiliary systems
$avail$	Available
avg	Average
b	Brine, Bottom
bc	Brine concentration
$least$	Least
bb	Black-box
B	Bottom
c	Surface condenser, Condenser, Cooling water, Cold
cc	Combined cooler
$cond$	Condensate
cv	Controlled variable
cs	Cross-section
d	Distillate
db	Dry bulb
dc	Dry cooler
d	Delay
dis	Discharge
e	Electrical
eq	Equivalent
$eval$	Evaluation
f	Feed water
fsm	Finite-state machine
h	Hot
i	Inner, Iteration, i_{th} element, Integral
in	Inlet
hx, hex	Heat exchanger
med	Multi-effect distillation
sf	Solar field
$3wv$	Three-way valve
sf	Thermal storage
max	Maximum
min	Minimum
min	Minimum
$mode$	Discrete operation mode
$NaCl$	Sodium chloride
o	Outer
$optim$	Optimization
out	Outlet
p	Primary side, Parallel component, Proportional
$c - loop$	Parallel solar field's collectors per loop
$tb - c$	Parallel solar field's collector tube
r	Rejected cooling water
ref	Reference
s	Saturated, Series component, Heat source, Water Source, Secondary side, Sample
$c - s$	Series solar field's collector rows
sat	Saturation
sol	Solute
src	Source
st	State

std Standard deviation
ss Steady-state
streams Discharge streams
t Top
tb Tube
T Top
II Second law
v Vapor
w Water
wb Wet bulb
wct Wet cooling tower
wh Waste heat
wc Worst-case

Superscripts and modifiers

\hat{X} Prediction
 \bar{X} Mean, Upper limit
 \underline{X} Lower limit
 X^* Setpoint
 X_{\uparrow} Start-up
 X_{\downarrow} Shutdown
 $X^{(x)}$ Cumulative X up to step x



Esta investigación abarca dos estudios complementarios sobre dos recursos intrínsecamente vinculados: el agua y la energía. La primera parte se centra en la gestión eficiente de los recursos hídricos para la generación eléctrica en una planta de energía solar concentrada, mientras que la segunda explora el uso eficiente de la energía solar para la producción de agua limpia en un proceso de destilación multi-efecto alimentado con energía solar térmica.

This research encompasses two complementary studies on two intrinsically linked resources: water and energy. The first part focuses on the efficient management of water resources for power generation in Concentrated Solar Power plants, while the second explores the efficient use of solar energy for clean water production in a solar-driven multi-effect distillation plant.